Universitat de Girona

# X-RAY TOMOGRAPHY INVESTIGATION OF THE IMPACT DAMAGE MECHANISMS OF THIN-PLY COMPOSITES AND THE USE OF VEILS TO IMPROVE THEIR IMPACT TOLERANCE

**Santiago García Rodríguez**

Universitat de Girona

Doctoral Thesis

# X-ray tomography investigation of the impact damage mechanisms of thin-ply composites and the use of veils to improve their impact tolerance

Santiago García Rodríguez

2019

Universitat de Girona

Doctoral Thesis

# X-ray tomography investigation of the impact damage mechanisms of thin-ply composites and the use of veils to improve their impact tolerance

Santiago García Rodríguez

2019

Doctoral Program in Technology

Advisor:
Dr. Josep Costa Balanzat
Universitat de Girona

Thesis submitted for the degree of Doctor of Philosophy

**Santiago García Rodríguez**
X-ray tomography investigation of the impact damage mechanisms of thin-ply composites and the use of veils to improve their impact tolerance
Doctoral Thesis, 2019
Doctoral Program in Technology
Advisor: Dr. Josep Costa Balanzat

**Universitat de Girona**
AMADE Research Group
Escola Politècnica Superior
Dept. d'Enginyeria Mecànica i de la Construcció Industrial
Av. Universitat de Girona, 4. Campus Montilivi
17003 Girona

A Don Facundo, Doña Tomasa, el toro, el gallo, el dominguero, Sor Pilar, Migote y otros muchos personajes.

# Preface

This Ph.D. thesis was performed in AMADE, a composites research group at the University of Girona (Spain), during the period of November 2015 to April 2019. The work is part of AIRBUS' AIRNET project, a research program that intends to compare the mechanical performance of several types of thin-ply carbon reinforcement for inclusion in new airplane laminate designs (unidirectional tapes from Hexcel, non-crimp fabrics from Chomarat and woven fabrics from Oxeon and Sakay Ovex). We focused on Chomarat's thin-ply non-crimp fabrics (namely C-PLY$^{TM}$ reinforcements) and the possibility of improving their damage tolerance by interleaving co-polyamide non-woven veils. The thesis was partially funded by the Secretaria d'Universitats i Recerca del Departament d'Empresa i Coneixement de la Generalitat de Catalunya through the pre-doctoral grant 2016FI_B_00551, co-funded itself by the Fondo Social Europeo (FSE).

The entire experimental campaign was performed in the mechanical testing laboratory of the University of Girona, which holds ISO17025 and NADCAP (Non-Metallic Materials) accreditations. The main non-destructive damage inspection technique was, for the first time in the group, X-ray micro-computed tomography. The X-ray equipment was installed by Novadep Scientific Instruments (Valladolid, Spain), while the necessary post-processing tools were developed in collaboration with Dr. Imma Boada and her team (Graphics and Imaging Laboratory, University of Girona), owners of the 3D visualization software "Starviewer".

This work was complemented by a research stay at the μ-VIS X-ray Imaging Centre at the Faculty of Engineering and Physical Sciences, University of Southampton (UK) and one experimental campaign at the European Synchrotron Radiation Facility's ID19 Beamline (Grenoble, France), the latter also being funded by Generalitat de Catalunya.

# Acknowledgments

I express my deepest appreciation to my supervisor, Professor Josep Costa Balanzat, who relentlessly enlightened me during the Ph.D. journey and taught me the art of making difficult things look simple. Without his guidance and imagination, this dissertation would not have been possible.

I extend my gratitude to AMADE's senior researchers and laboratory members, who were always willing to donate their time to contribute to this project. My recognition to Vicky Singery, Julie Fourel, Claude Soubeyrand and Philippe Sanial, who made our collaboration with Chomarat so pleasurable. A thanks to Eusebio Solórzano and Pablo Pérez from Novadep for their support with the X-ray tomography equipment. Special mention to Imma Boada, Antón Barderá, Marc Ruiz and Adrià Julià, who consistenly provided insight into the X-ray tomography post-processing tools. Thank you to Lukas Helfen and Elodie Boller for useful discussions during synchrotron experiments.

I am also indebted to Professor Ian Sinclair, Dr. Mark Mavrogordato, Dr. Kathryn Rankin, Dr. Richard Boardman and Dr. Orestis Katsamenis (µ-VIS X-ray Imaging Centre, University of Southampton): you turned my research stay into a memorable experience.

En lo personal, gracias a todos los compañeros que he encontrado en AMADE, con los cuales he pasado muchas horas a lo largo de estos tres años, y sin los cuales el tiempo hubiera pasado mucho más despacio. Gracias a Laura Compte, Anna Espigol y Nuria Soler por recibirme cada día con una sonrisa. Lo principal, mi familia y amigos, en los cuales no sólo me he apoyado para desarrollar este proyecto, sino que son pilares fundamentales de mi día a día. Gracias a Adrián y Miguel, compañeros de aventura desde el instituto hasta el final de la carrera. Y a Josemi, que pacientemente nos inició en algo que nos apasiona. A Gwen, que hace que cada día me levante más ilusionado que el anterior.

# List of Publications

This thesis is a compendium of peer-reviewed journal papers compliant with the requirements set out by Doctorate School of the University of Girona:

**Paper A** S.M. García-Rodríguez, J. Costa, P. Maimí, V. Singery, A. Sasikumar. On how matrix cracks induce delamination under out-of-plane shear and the associated in-situ effect. Submitted for publication to Composites Science and Technology.

**Paper B** S.M. García-Rodríguez, J. Costa, A. Bardera, V. Singery, D. Trias. A 3D tomographic investigation to elucidate the low-velocity impact resistance, tolerance and damage sequence of thin non-crimp fabric laminates: effect of ply-thickness. Composites Part A: Applied Science and Manufacturing 113 53-65 (2018). doi: `https://doi.org/10.1016/j.compositesa.2018.07.013`

**Paper C** S.M. García-Rodríguez, J. Costa, K.E. Rankin, R.P. Boardman, V. Singery, J.A. Mayugo. Interleaving light veils to minimise the trade-off between mode-I interlaminar fracture toughness and in-plane properties. Submitted for publication to Composites Part A: Applied Science and Manufacturing.

**Paper D** S.M. García-Rodríguez, J. Costa, V. Singery, I. Boada, J.A. Mayugo. The effect interleaving has on thin-ply non-crimp fabric laminate impact response: X-ray tomography investigation. Composites Part A: Applied Science and Manufacturing 107 409-420 (2018). doi: `https://doi.org/10.1016/j.compositesa.2018.01.023`

Other publications related to the thesis but not included in this document are:

- A. Wagih, P. Maimí, N. Blanco, S.M. García-Rodríguez, G. Guillamet, R.P. Issac, A. Turon, J. Costa. Improving damage resistance and load capacity of thin-ply laminates using ply clustering and small mismatch angles. Composites Part A: Applied Science and Manufacturing 117 76-91 (2019). doi: `https://doi.org/10.1016/j.compositesa.2018.11.008`.
- A. Sasikumar, J. Costa, D. Trias, E.V. González, S.M. García-Rodríguez, P. Maimí. Unsymmetrical stacking sequences as a novel approach to tailor damage resistance under out-of-plane impact loading. Composites Science and Technology 173 125-135 (2019). doi: `https://doi.org/10.1016/j.compscitech.2019.02.002`

- A. Sasikumar, S.M. García-Rodríguez, J.J. Arbeláez, D. Trias, J.Costa. On how unsymmetrical laminate designs with tailored ply clusters affect compression after impact strength compared to symmetric baseline. Submitted for publication to Composites Structures.

The journals' classification according to the 2017 Journal Citation Report is:

**Composites Science and Technology**. ISSN: 0266-3538, Impact Factor: 5.160 and ranked 1/26 in the category of Materials Science, Composites ($1^{st}$ quartile).

**Composites Part A: Applied Science and Manufacturing**. ISSN: 1359-835X, Impact Factor: 4.514, ranked 2/46 in the category of Engineering, Manufacturing and ranked 4/26 in the category of Materials Science, Composites ($1^{st}$ quartile).

**Composites Structures**. ISSN: 0263-8223, Impact Factor: 4.101 and ranked 5/26 in the category of Engineering, Manufacturing and ranked 4/26 in the category of Materials Science, Composites ($1^{st}$ quartile).

The outcomes of this thesis were also presented in several conferences:

- S.M. García-Rodríguez, J. Costa, A. Sasikumar, V. Singery. On how ply-thickness affects the short-beam response of thin non-crimp fabric laminates: X-ray tomography investigation. $55^{th}$ Anual Technical Meeting of the Society of Engineering Science (SES2018), Leganés, Madrid, Spain (2018).
  National Conference. Oral presentation.

- S.M. García-Rodríguez, J. Costa, V. Singery, A. Sasikumar. A 3D tomographic investigation to elucidate how thin-ply laminates improve the interlaminar shear strength and the effect of toughening the interfaces with veils. $10^{th}$ European Solid Mechanics Conference (ESMC 2018), Bologna, Italy (2018).
  International Conference. Oral presentation.

- S.M. García-Rodríguez, J. Costa, A. Bardera, I. Boada. Caracterización del patrón de daño en laminados carbono-epoxy sometidos a impacto: tomografía y laminografía computarizada de Rayos-X. XII Congreso Nacional de Materiales Compuestos (MATCOMP 2017), San Sebastián/Donostia (2017).
  National Conference. Oral presentation.

- S.M. García-Rodríguez, V. Singery, Ph. Sanial, J. Costa, Effect of ply-thickness on the impact response of interleaved non-crimp fabric laminates. $17^{th}$ European Conference on Composite Materials (ECCM17), Munich, Germany (2016).
  International Conference. Oral presentation.

Other conferences related to this thesis but not included in this document are:

- A. Sasikumar, S.M. García-Rodríguez, D. Trias, J. Costa. Unsymmetrical laminates: Impact and compression after impact response. 55$^{th}$ Anual Technical Meeting of the Society of Engineering Science (SES2018), Leganés, Madrid, Spain (2018).
  National Conference. Oral presentation.

- S.M. García-Rodríguez, J.A. Artero-Guerrero, J. Pernas-Sánchez, J. Costa, J. Meza, J. López-Puente. The effect cryogenic temperature has on the high velocity impact response of CFRP laminates: X-ray tomography investigation. 4$^{th}$ International Conference on Mechanics of Composites (MECHCOMP2018), Leganés, Madrid, Spain.
  National Conference. Oral presentation.

- A. Sasikumar, D. Trias, S.M. García-Rodríguez, J. Costa. Experimental study to understand the effect of delamination position on impact damage tolerance using unsymmetrical laminates. 18$^{th}$ European Conference on Composite Materials (ECCM18), Athens, Greece (2018).
  International Conference. Oral presentation.

- G. Frossard, R. Amacher, J. Cugnoni, T. Gmür, J. Costa, S.M. García-Rodríguez, J. Botsis. Translaminar fracture of thin-ply composites: hybridization as toughening strategy. 8$^{th}$ International Conference on Composites Testing and Model Indentification (COMPTEST2017), Leuven, Belgium (2017).
  International Conference. Oral presentation.

# Declaration

Universitat de Girona

Dr. Josep Costa Balanzat, Full Professor at the University of Girona, hereby certify that the work entitled *X-ray tomography investigation of the impact damage mechanisms of thin-ply composites and the use of veils to improve their impact tolerance*, submitted by Santiago García Rodríguez in fulfilment of the requirements for the Degree of Doctor of Philosophy, has been conducted under his supervision.

Girona, May 2019,

Dr. Josep Costa Balanzat
Universitat de Girona

# List of Figures

# List of Tables

# Contents

# Abstract

Low-velocity impact is a major concern in carbon fibre reinforced composites as it may impair the mechanical properties of the component and yet is difficult to detect. In an effort to reduce weight and costs, the airline industry is increasingly considering thinner laminates manufactured with out-of-autoclave methods which, in turn, increases impact susceptibility. This is more accentuated when laminates are made with "thin-plies" (i.e. plies thinner than 125 μm), a new generation of carbon reinforcements that, despite improving several mechanical properties, entail brittle damage mechanisms compared to their conventional-ply counterparts. The main purpose of this thesis is two-fold. Firstly, understand how ply-thickness affects the out-of-plane response of thin quasi-isotropic non-crimp fabric laminates (two ply thicknesses are studied: 67 and 134 μm). Secondly, enhance the impact tolerance of the thin-ply system using thermoplastic veils (two types of co-polyamide veil are studied: $V_1$ and $V_2$).

Impact resistance and tolerance were characterized with the drop-weight impact and compression after impact (CAI) experiments. Damage sequence evolution was elucidated by combining interrupted testing (interlaminar shear strength and quasi-static indentation tests) with X-ray micro-computed tomography (μCT) inspections. Interlaminar shear strength (ILSS) experiments provided insight into the interaction between matrix cracks and delamination, whereas quasi-static indentation (QSI) tests replicated the impact damage under controlled deflection. For interleaved laminates, an additional experimental campaign was devised to evaluate the trade-off between CAI strength and other mechanical properties (tensile, compressive and mode-I interlaminar fracture toughness properties). This campaign was accompanied with sub-micron resolution μCT inspections.

The damage sequence of standard- and thin-ply ILSS specimens displayed common qualitative trends. Failure started as a crack tunneling across the central $90^\circ_2$ ply-cluster. The intersection of this crack with the ones developing in the $-45^\circ$ adjacent layers triggered a delamination which, in turn, compromised the load-carrying capacity. The difference was that, for a similar maximum principal stress, the thin-plies required a 32% higher stress to propagate the initial crack, evidencing the so called "in-situ" effect under transverse shear ($\tau_{23}$ in the local coordinates of the

90° plies).

The in-situ effect also controlled the damage sequence of impact and QSI specimens: the thin-plies delayed the onset of shear cracks and delaminations. However, the lower energy dissipated resulted in premature fibre failure and decreased CAI strength for impact at 14 J (27% reduction compared to the standard-ply laminate), which justifies the use of toughening methods.

The key aspect to preserve laminate thickness was the combination of low veil fibre areal weight (4 g/m$^2$) and resin transfer moulding manufacturing (baseline and interleaved configuration configurations fitted within the same mould). The veil fibre diameter was crucial in determining the tensile properties ($V_2$, the veil with thinner fibres, avoided resin accumulation at the interfaces and displayed the same tensile properties as the non-interleaved laminate). Mode-I crack propagation was controlled by the adhesion between the veil fibres and resin. Veils fibres with low adhesion (the $V_1$ fibres) promoted interlaminar crack growth by debonding from the matrix, whereas veil fibres with higher adhesion (the $V_2$ fibres) deviated crack propagation from the 0°/0° interface to the surrounding 0° plies which, in the material system studied, resulted in the highest mode-I initiation and propagation interlaminar fracture toughness (101% and 43% increase). Both veils decreased the compressive strength by up to 9% because of the increase in the ductile phase surrounding the carbon plies. However, $V_2$ recovered the CAI strength of the standard-ply system for impact at 14 J.

We propose a toughening approach that not only enhances the impact tolerance and mode-I interlaminar fracture toughness of the thin-ply baseline laminate — with minimum penalty of in-plane mechanical properties—, but is also cheap, commercially available and easy to incorporate during manufacturing (non-woven veils can be placed manually during the lay-up).

# Resumen

Los impactos a baja velocidad perjudican la integridad estructural de los materiales compuestos reforzados con fibra de carbono porque, además de mermar sus propiedades mecánicas, son muy difíciles de detectar. Dicha susceptibilidad se acentúa con el auge de los laminados "thin-ply" (laminados con capas más delgadas que 125 μm). Las capas delgadas son una nueva generación de materiales compuestos que, a pesar de aumentar las propiedades mecánicas del laminado, incrementan su fragilidad durante el impacto. En su afán por reducir costes, la industria aeronáutica fabrica laminados cada vez más finos, lo cual deteriora aún más la respuesta a impacto. Los objetivos de esta tesis abordan esta problemática. Primero, comprender qué efecto tiene el espesor de capa en la respuesta a impacto de laminados finos y cuasi-isotrópicos de tipo "non-crimp fabric" (se estudian dos espesores de capa: 67 y 134 μm). Segundo, utilizar velos termoplásticos para mejorar la tolerancia al impacto de los laminados manufacturados con capas delgadas (se estudian dos tipos de velo con fibras de co-poliamida: $V_1$ y $V_2$).

La resistencia y tolerancia al impacto se caracterizaron mediante experimentos de impacto por caída y compresión después de impacto. La evolución de los mecanismos de daño bajo cargas fuera del plano se estudió combinando ensayos a niveles de fuerza incremental (en particular, los ensayos de resistencia a cortante interlaminar e indentación cuasi-estática) con inspecciones por tomografía computarizada de rayos-X. Los tests de resistencia a cortante interlaminar proporcionaron información sobre la interacción entre grietas en la matriz y deslaminaciones, mientras que los ensayos de indentación cuasi-estática replican el escenario de impacto bajo condiciones de deflexión controlada. En los laminados con velos, se diseñó una campaña experimental para evaluar el compromiso entre la tolerancia al daño y otras propiedades mecánicas como las de tensión, compresión y tenacidad a la fractura en modo-I. Esta campaña fue complementada con tomografías de resolución nanométrica.

Todas las probetas ILSS presentaron la misma secuencia de fallo independientemente del espesor de capa. La rotura comenzó con una grieta en el clúster de capas a 90° situado en la parte central del laminado. El cruce de esta grieta con las grietas desarrolladas en las capas adyacentes generó una deslaminación que, a su vez, disminuyó la integridad estructural de la probeta (es decir, provocó una caída de

fuerza en la curva fuerza-desplazamiento). La diferencia fue que, para una misma tensión principal máxima, las capas finas requirieron un 32% más de carga para propagar la grieta inicial, lo cual supone una evidencia inequívoca del fenómeno "in-situ" bajo cortante transversal ($\tau_{23}$ en las coordenadas locales de las capas a 90°).

El efecto in-situ también gobernó la secuencia de fallo de las probetas de impacto e indentación: las capas finas retrasaron la aparición de grietas en la matriz y deslaminaciones. Sin embargo, la reducción de energía disipada se tradujo en una rotura de fibras prematura y una tolerancia al impacto menor que la de los laminados con capas convencionales (27% menor tras impacto a 14 J de energía), justificando el uso de agentes de refuerzo.

El aspecto clave para evitar que los velos aumentaran el espesor del laminado con capas delgadas fue la combinación de su bajo gramaje (4 g/m$^2$) con la tecnología de moldeo por transferencia de resina: todos los laminados cupieron en el mismo molde. El diámetro de fibra de los velos estuvo íntimamente ligado a las propiedades de tensión (el velo con fibras más finas, $V_2$, presentó las misma resistencia y módulo elástico que el laminado sin velos). La adhesión entre las fibras del velo y la matriz determinó la localización de la grieta en modo-I. Las fibras del velo con menor adhesión (el velo $V_1$) se despegaron de la resina durante la propagación de la grieta, mientras que las fibras del velo con mayor adhesión (el velo $V_2$) desviaron la propagación de la grieta lejos del velo. Esta desviación incrementó un 101% y 43% la energía necesaria para iniciar y propagar la grieta. Finalmente, ambos tipos de velo disminuyeron la resistencia a compresión hasta un 9% en el caso de $V_2$. Sin embargo, este velo aumentó un 28% la resistencia a la compresión después de impacto (es decir, recuperó la tolerancia al impacto de las probetas con capas convencionales).

En definitiva, se propone una técnica de refuerzo para laminados finos manufacturados con capas delgadas que no es sólo atractiva porque mejore la tolerancia al daño y la tenacidad de fractura (con detrimento mínimo de las propiedades en el plano), sino porque es relativamente barata, fácil de incorporar y se encuentra disponible comercialmente.

# Resum

Els impactes a baixa velocitat perjudiquen la integritat estructural dels materials compostos reforçats amb fibra de carboni perquè, a més de minvar les seves propietats mecàniques, són molt difícils de detectar. Aquesta susceptibilitat s'accentua amb l'auge dels laminats "thin-ply" (laminats amb capes més primes que 125 μm). Les capes primes són una nova generació de materials compostos que, tot i augmentar les propietats mecàniques del laminat, incrementen la seva fragilitat durant l'impacte. Amb la voluntat de reduir costos, la indústria aeronàutica fabrica laminats cada cop més fins, la qual cosa deteriora encara més la resposta a impacte. Els objectius d'aquesta tesi aborden aquesta problemàtica. Primer, comprendre quin efecte té el gruix de capa en la resposta a impacte de laminats fins i quasi-isotròpics de tipus "non-crimp fabric" (s'estudien dos gruixos de capa: 67 i 134 μm). Segon, utilitzar vels termoplàstics per millorar la tolerància a l'impacte dels laminats manufacturats amb capes primes (s'estudien dos tipus de vel amb fibres de co-poliamida: $V_1$ i $V_2$).

La resistència i tolerància a l'impacte es van caracteritzar mitjançant experiments d'impacte per caiguda i compressió després d'impacte. L'evolució dels mecanismes de dany sota càrregues fora del pla es va estudiar combinant assajos a nivells de força incremental (en particular, els assajos de resistència a tallant interlaminar i indentació quasi-estàtica) amb inspeccions per tomografia computeritzada de raigs-X. Els tests de resistència a tallant interlaminar van proporcionar informació sobre la interacció entre esquerdes a la matriu i delaminacions, mentre que els assajos d'indentació quasi-estàtica repliquen l'escenari d'impacte sota condicions de deflexió controlada. En els laminats amb vels, es va dissenyar una campanya experimental per avaluar el compromís entre la tolerància al dany i altres propietats mecàniques com les de tensió, compressió i tenacitat a la fractura en mode-I. Aquesta campanya va ser complementada amb tomografies de resolució nanomètrica.

Totes les provetes ILSS van presentar la mateixa seqüència de fallada independentment del gruix de capa. El trencament va començar amb una esquerda en el clúster de capes a 90° situat a la part central del laminat. L'encreuament d'aquesta esquerda amb les esquerdes desenvolupades en les capes adjacents va generar una deslaminació que, al seu torn, va disminuir la integritat estructural de la proveta (és a dir, va provocar una caiguda de força a la corba força-desplaçament). La

diferència va ser que, per a una mateixa tensió principal màxima, les capes fines van requerir un 32% més de càrrega per propagar l'esquerda inicial, la qual cosa suposa una evidència inequívoca del fenomen "in-situ" sota tallant transversal ($\tau_{23}$ en les coordenades locals de les capes a 90°).

L'efecte in-situ també va governar la seqüència de fallada de les provetes d'impacte i indentació: les capes fines van retardar l'aparició d'esquerdes en la matriu i delaminacions. No obstant això, la reducció d'energia dissipada es va traduir en un trencament de fibres prematura i una tolerància a l'impacte menor que la dels laminats amb capes convencionals (27% menor després impacte a 14 J d'energia), justificant l'ús d'agents de reforç.

L'aspecte clau per evitar que els vels augmentessin el gruix del laminat amb capes primes va ser la combinació del seu baix gramatge (4 g/m$^2$) amb la tecnologia d'emmotllament per transferència de resina: tots els laminats van cabre en el mateix motlle. El diàmetre de fibra dels vels va estar íntimament lligat a les propietats de tensió (el vel amb fibres més fines, $V_2$, va presentar les mateixa resistència i mòdul elàstic que el laminat sense vels). L'adhesió entre les fibres del vel i la matriu va determinar la localització de l'esquerda en mode-I. Les fibres del vel amb menor adhesió (el vel $V_1$) es van desenganxar de la resina durant la propagació de l'esquerda, mentre que les fibres del vel amb major adhesió (el vel $V_2$) van desviar la propagació de l'esquerda lluny del vel. Aquesta desviació va incrementar un 101% i 43% l'energia necessària per iniciar i propagar l'esquerda. Finalment, els dos tipus de vel van disminuir la resistència a compressió fins a un 9% en el cas de $V_2$. No obstant això, aquest vel va augmentar un 28% la resistència a la compressió després d'impacte (és a dir, va recuperar la tolerància a l'impacte de les provetes amb capes convencionals).

En definitiva, es proposa una tècnica de reforç per a laminats fins manufacturats amb capes primes que no és només atractiva perquè millori la tolerància al dany i la tenacitat de fractura (amb detriment mínim de les propietats en el pla), sinó perquè és relativament barata, fàcil d'incorporar i es troba disponible comercialment.

# Introduction 1

## 1.1 Contextual background

A *composite* material is the combination of two or more constituents, usually a matrix and a reinforcement, to produce a new system with intermediate properties. For example, long carbon fibre reinforced epoxy composites combine the high strength and stiffness of carbon with the increased elongation to failure of the epoxy resin. Carbon fibre reinforced epoxy composites are typically stacked in multiple layers – also known as "plies" – to form a *laminate*, where the fibre orientation of each ply is tailored according to preferred loading directions.

Carbon-epoxy laminates are attractive materials for the airline industry mainly because of their high specific stiffness and strength compared to metals (Fig 1.1). New manufacturing approaches, such as the *tow spreading method*, allow plies thinner than 125 μm (so-called "thin-plies") to be produced and, in turn, these are attracting growing interest because they enhance the strength, fatigue life and design space of their conventional-ply counterparts [2–4]. In contrast, one of the main drawbacks of composite laminates is their susceptibility to low-velocity impact [5–7]. This type of impact induces damage that, besides compromising the load-carrying capacity of the structure, is very difficult to detect (damage occurs inside the laminate with little evidence on the impacted surface) [5, 8, 9]. In an effort

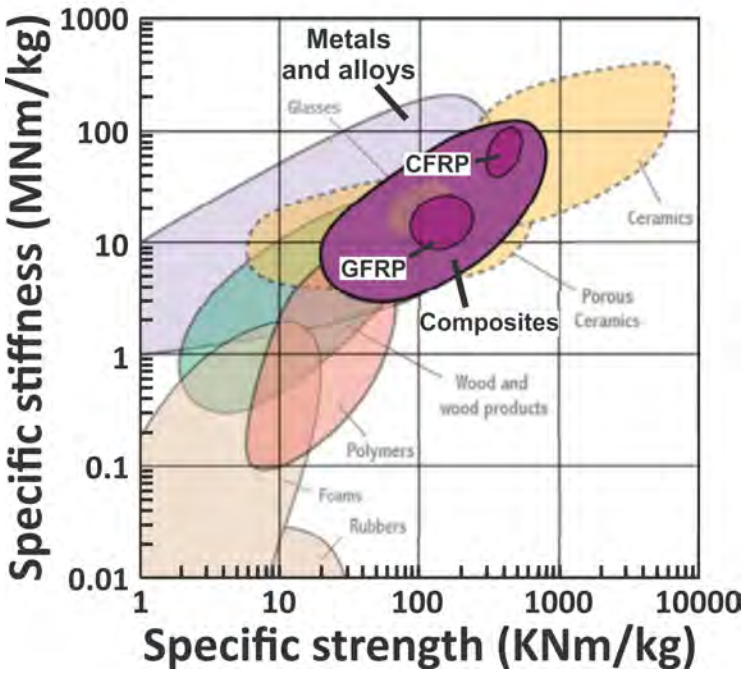


**Figure 1.1:** Ashby diagram comparing the specific stiffness and strength of several types of material, where CFRP and GFRP stand for carbon- and glass-fibre reinforced polymer, reproduced from [1].

to reduce weight and costs, the airline industry manufactures thin laminates using out-of-autoclave methods which, in turn, increases even more impact susceptibility [10]. Considering airplanes will continue in operation after low-velocity impacts, the component should preserve structural integrity throughout the flight, which is typically characterized in terms of the compression after impact (CAI) experiment [11, 12].

## 1.2 Motivation and Objectives

Thin-plies are potential candidates to take part in thin aircraft fuselage skins, not only because the increased design space, but also because they enhance certain mechanical properties compared to their conventional-ply counterparts [2–4]. However, thin-ply laminates display brittle failure mechanisms (particularly extensive fibre failure during low-velocity impact [3]), which could deteriorate CAI strength (unfortunately, there is few information regarding the impact response of thin laminates made with thin-plies).

A cost-effective strategy to overcome the brittleness of thin-plies is interleaving thermoplastic non-woven veils [10]. Incorporating polyamide veils increases the interlaminar fracture toughness, impact resistance and CAI strength of the non-interleaved baseline laminate (the improvement accentuates by increasing veil fibre areal weight) [10, 13–18]. However, an excessive veil fibre areal weight severely compromises laminate thickness, tensile and compressive properties [18, 19]. Based on these observations, a practical balance between laminate thickness, CAI strength and in-plane mechanical properties should rely on veils with relatively low fibre areal weight.

The objective of this thesis is two-fold. Firstly, understand how ply-thickness affects the out-of-plane response of thin quasi-isotropic non-crimp fabric laminates (two ply-thicknesses are studied: 67 and 134 μm). Secondly, enhance the impact tolerance of the thin-ply system using light (4 g/m$^2$) non-woven veils (two types of co-polyamide veil are studied). The successful accomplishment of the main objectives depends on several sub-objectives:

1. Compare the damage sequence evolution of thin quasi-isotropic interlaminar shear strength specimens made with standard- or thin-ply non-crimp fabrics. Provide insight into the interaction between matrix cracks and delamination. Identify the damage mechanisms underlying the load drops observed in the force-displacement curves. Reveal the damage modes triggering ultimate failure. Explain the associated in-situ effect.

2. Compare the damage sequence of thin quasi-isotropic impact specimens

made with standard- or thin-ply non-crimp fabrics. Identify the damage mechanisms underlying the load drops observed in the force-displacement curves. Characterize their low-velocity impact resistance and tolerance.

3. Evaluate (preliminarily) the mechanical performance of interleaved laminates. Characterize their tensile, compressive and mode-I interlaminar fracture toughness properties (the latter devoting particular attention to the damage mechanisms developing in the fracture process zone). Identify the key-veil parameters affecting the microstructure of the thin-ply baseline laminate. Evaluate the compatibility between veil fibres and resin. Connect veil fibre architecture with mechanical properties.

4. Compare the low-velocity impact resistance, tolerance and damage sequence of baseline and interleaved laminates.

Table 1.1 connects the objectives 1, 2, 3 and 4 with the known facts and open questions detailed in the state-of-the-art review (Chapter 2).

## 1.3 Thesis structure

This thesis is a compendium of the papers A-D in the list of publications (the reader is referred to the page vii).

Chapter 2 is a detailed state-of-the art review that provides the foundation necessary to go through the papers. This review describes known theories as well as emphasizes the knowledge gaps that needs to be filled by new research (named "open-questions" in Table 1.1). The end of the most relevant sections includes several bullet points with the main take-home messages.

Chapters 3-6 correspond to the pre-pint version of the papers A-D, each of them fulfilling the objectives 1-4, respectively (Section 1.2 and Table 1.1). Each chapter begins with a brief overview that introduces the scope of the work. Besides this, the nomenclature of the original papers was slightly modified to ensure a coherent flow of information. For the journal version of papers B and D (the ones published at the moment of submission of the thesis document), the reader is refereed to Appendix **??**.

Chapter 7 includes a discussion that brings together all the results, confronts them with existing theories and addresses the open-questions from a global perspective, leading to the conclusions and future work (Chapter 8).

**Table 1.1:** Connection between the objectives of this thesis (Section 1.2) and the known facts and open questions described in the state-of-the-art review (Chapter 2).

| Known facts | Open questions | Objectives |
|---|---|---|
| Ply-strength depends on ply-thickness (also known as "in-situ" effect) | There is no evidence of the in-situ effect under transverse shear | |
| Out-of-plane loads induce shear cracks and delaminations | There is controversy about which damage mechanism triggers the other<br>There is controversy about which damage mechanism compromises the load-carrying capacity<br>There is no unequivocal evidence of how ply-thickness affects damage sequence evolution | 1 |
| Thin-plies increase several in-plane mechanical properties because of the in-situ effect<br>Thin-plies display brittle failure mechanisms | It is unclear how ply-thickness affects thin laminate's impact response | 2 |
| Interleaving polyamide veils with high fibre areal weight enhances impact resistance, tolerance and interlaminar fracture toughness<br>The improvement comes with a reduction of tensile and compressive properties | Few studies incorporate veils with low fibre areal weight<br>Few studies connect veil fibre architecture and mechanical properties<br>No investigation toughens thin-ply laminates | 3&4 |

## 1.4 Nomenclature

Table 1.2 defines the nomenclature necessary to connect the results of papers A-D with the global discussion (Chapters 3-6 and 7).

**Table 1.2:** Nomenclature of the laminates devised for interlaminar shear strength, impact, quasi-static indentation, in-plane (tension and compression) and mode-I interlaminar fracture toughness experiments. Non-crimp fabric blankets are indicated with parenthesis. The bar sign means only one veil in the symmetry plane.

| Laminate | Stacking sequence | Purpose |
|---|---|---|
| $\text{LTHIN}_{\text{ILSS}}$ | $[(45°/0°)/(-45°/90°)]_{4s}$ | Interlaminar shear strenght testing |
| $\text{LTHIN}_{\text{IP}}$ | | Tensile and compressive testing |
| $\text{LTHIN}_{\text{LVI}}$ | | Impact and quasi-static indentation testing |
| $\text{LTHIN}_{G_{\text{IC}}}$ | $[(45°/90°)/(-45°/0°)]_{6s}$ | Mode-I interlaminar fracture toughness testing |
| $\text{LSTANDARD}_{\text{ILSS}}$ | $[(45°/0°)/(-45°/90°)]_{2s}$ | Interlaminar shear strenght testing |
| $\text{LSTANDARD}_{\text{IP}}$ | | Compressive testing |
| $\text{LSTANDARD}_{\text{LVI}}$ | | Impact and quasi-static indentation testing |
| $\text{LV1}_{\text{IP}}$ and $\text{LV2}_{\text{IP}}$ | $[(45°/\text{V}_i/\ 0°)/\text{V}_i/(-45°/\text{V}_i/90°)/\bar{V}_i]_{4s}$ $(i = 1,2)$ | Tensile and compressive testing |
| $\text{LV1}_{\text{LVI}}$ and $\text{LV2}_{\text{LVI}}$ | | Impact and quasi-static indentation testing |
| $\text{LV1}_{G_{\text{IC}}}$ and $\text{LV2}_{G_{\text{IC}}}$ | $[(45°/90°)/(-45°/0°)/\bar{V}_i]_{6s}$ $(i = 1,2)$ | Mode-I interlaminar fracture toughness testing |

# State of the art

# 2

## 2.1 The in-situ effect

The purpose of this section is providing a brief overview of the in-situ phenomenon as well as identifying the knowledge gaps that need to be filled by new experimental evidence. For further details and exhaustive derivations refer to [20–24].

Matrix cracks are the first damage mechanism that develops in carbon/epoxy laminates subjected to mechanical or thermal loads. Matrix cracks are relatively harmless by theirselves (they barely penalize structural integrity [21, 25, 26]). However, they trigger delaminations which severely reduce the component's load-carrying capacity [25, 27, 28]. Based on this observation, it is clear that failure criterion should rely on the accurate prediction of matrix cracking onset.

Ply strength —defined as the load required to propagate a matrix crack— is not a lamina intrinsic property but depends on the orientation of the surrounding layers [25, 31]. Ply-strength is higher when the ply is constrained by laminae with a different orientation. This means that the strength of a ply is higher when embedded in a multidirectional laminate as compared to the same ply in an unidirectional laminate, also known "in-situ" effect [21, 23–25, 27]. What is even more interesting for laminate design is that the in-situ strength (i.e. the ply-strength of laminae embedded in multidirectional laminates) increases further by reducing ply-thickness [21, 25, 27, 28, 31–36] (Fig. 2.1).

Physically based failure criterion account for the in-situ effect using fracture mechan-

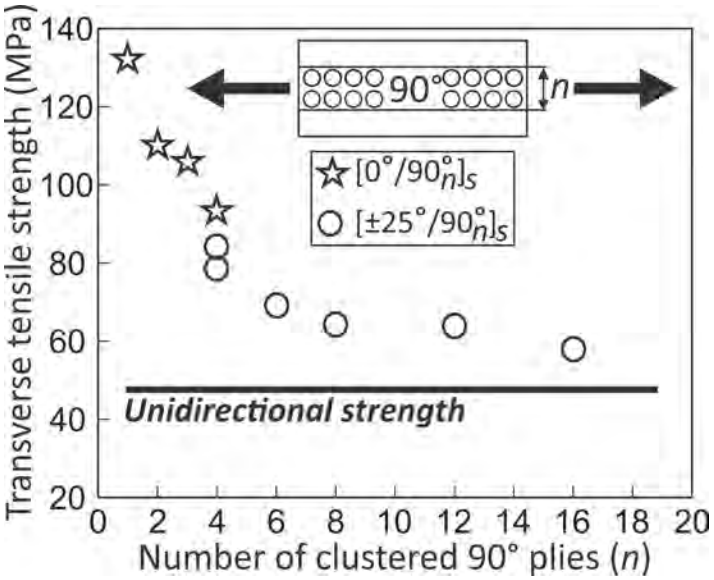


**Figure 2.1:** Relation between the in-situ strength under transverse tension and the thickness of the 90° ply-cluster, adapted from [25, 29, 30].

ics models that predict the relation between ply-thickness, ply fracture toughness and ply in-situ strength. Camanho *et al.* [21] proposed an analytical model to calculate the in-situ strength under transverse tension and in-plane shear. This model is experimentally validated and implemented in continuum damage models such as the one of Maimí *et al.* or Catalanotti *et al.* [37, 38]. However, the topic of debate is how to predict the in-situ strength under other types of loading such as, for example, transverse shear, as there is a lack of unambiguous experimental evidence or experimentally validated analytical expressions (in practice, such values are estimated in accordance with the framework of the corresponding failure criterion [27, 38]).

In a nutshell:

- in-situ strength increases with reduced ply-thickness,
- in-situ strength is accurately predicted under transverse tension and in-plane shear, whereas less information is available under other types of loading such as transverse shear.

## 2.2 Thin-plies

The fact that the in-situ strength depends on ply-thickness aroused the curiosity of the research community: *what if ply-thickness is reduced below the conventional standards?* —Sihn *et al.* [2] defined the conventional limit as 125 µm [2]. "Thin-plies" are a new generation of carbon reinforcements that, despite needing a specific manufacturing process, entail a wide range of design, microstructural and structural benefits compared to their conventional-ply counterparts (Sections 2.2.1-2.2.3). The terms thin- and conventional-ply will be henceforth used for the layers being significantly thinner and thicker than 125 µm, whereas the term standard-ply will be employed for the plies laying in between.

### 2.2.1 Manufacturing process

There are several methods available to manufacture fibre sheets thinner than 125 µm [2, 39–41] (the main requirements are avoiding fibre damage and cost-efficiency [2, 39]). One typical example is the "tow-spreading" technology developed by Industrial Technology Center (Fukui Prefecture, Japan). Fig. 2.2a schematizes the mechanics of their spreading process. The initial step consists on passing an air stream through a carbon tow that is gently positioned on top of two guiding rolls. Since the tow is subjected to relatively low tensile stresses, the fibres sag downwards following the direction of the air flow. The driving force of the spreading method is the difference of pressure between the outer part and the inner parts of the tow (initially, the core fibres have no contact with the air). This pressure difference

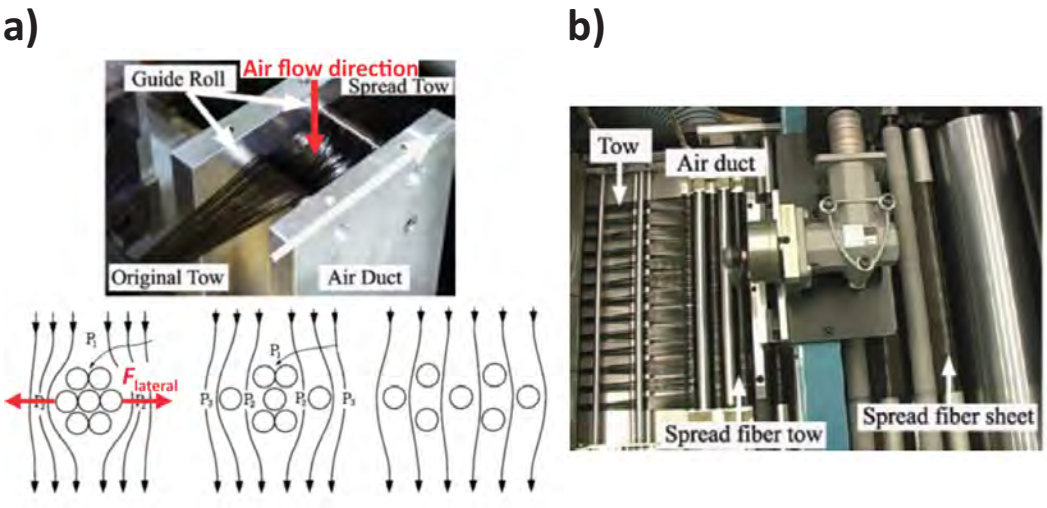


**Figure 2.2:** a) Mechanics of the tow-spreading process. b) Spreading and homogenisation of multiple carbon tows to form a thin-ply sheet, adapted from [39, 43].

induces lateral forces that separate the most external fibres of the tow. The higher the number of spread fibres, the deeper the air penetrates into the tow and the further the spreading process develops [2, 39]. Spreading a single tow results in a thin and narrow fibre bundle. However, forming a thin-ply sheet requires the spreading and homogenisation of several tows at the same time (the spread tows are assembled together using a beam that vibrates perpendicularly to the fibres, Fig. 2.2b).

While current air spreading technology allows the manufacturing of thin-plies (dry or pre-preg) of only 15 µm thickness (i.e. with approximately two carbon fibres through-the-thickness direction [42]), the market is not limited to air-driven approaches: for an example, Chomarat$^{TM}$ spread tows using a collection of vibrating beams (the so called Mayer/Liba's method [41]) —further details are avoided because of confidentiality.

### 2.2.2 Intrinsic benefits

Reducing ply-thickness entails several advantages for the designer. For a fixed stacking sequence, it decreases the nominal thickness (and therefore the weight) of the structure. For a given laminate thickness, it increases the number of layers included within the layup. In other words, thin-plies enlarge the design space. This is particularly important when designing laminates that are already thin [44]. For example, the Airbus A350 fuselage skin is thinner than 2 mm. If it was manufactured with conventional 0.200 mm plies, the designer would count on approximately 10 layers to satisfy the typical design constraints (symmetry, quasi-isotropy, the 10% rule etc. [4, 44–46]). In contrast, reducing ply-thickness increases proportionally the number of plies and provides more freedom to the designer.

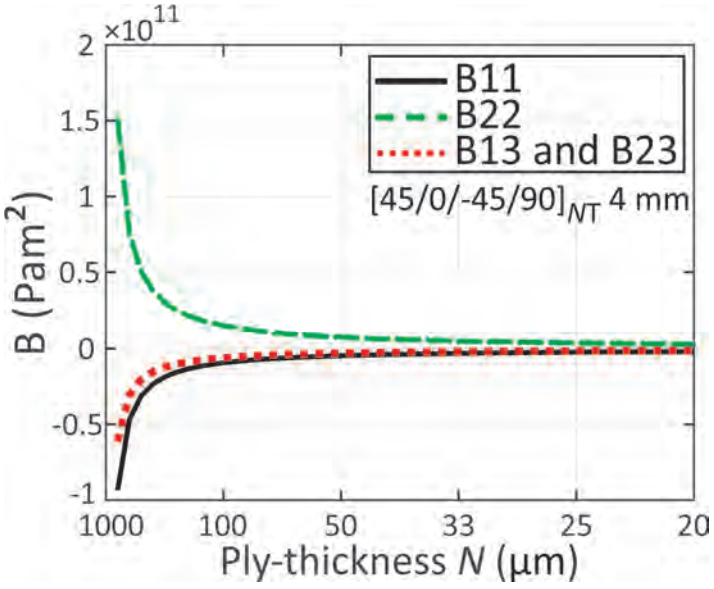


**Figure 2.3:** Relation between the B-terms of a $[45°/0°/-45°/90°]_{NT}$ 4 mm thick asymmetric laminate and ply-thickness. The elastic properties were taken from [47] (T700GC/M21 carbon/epoxy).

More interestingly, not all the classical design constraints are relevant when using thin-plies [46, 48]. Laminate symmetry is usually required to avoid thermal warpage during manufacturing. This symmetry condition ensures that all the components of the extension-bending coupling matrix (also called B matrix) are null and, consequently, in-plane thermal stresses are uncoupled with any out-of-plane deformation [49]. Fig. 2.3 presents how ply-thickness affects the B-terms (particularly $B_{11}$, $B_{22}$, $B_{13}$ and $B_{23}$) of a $[45°/0°/-45°/90°]_{NT}$ 4 mm thick asymmetric laminate. It is evident that the B-terms tend to zero as ply-thickness decreases. In practice, this means that laminates made of sufficiently thin-plies (around 33 µm for the studied configuration) can be both asymmetric and free of thermal warping. Besides relaxing design constraints, asymmetry allows for continuous layup, which would probably reduce the amount of stacking errors [46].

From a microstructural point of view, the quality of composite laminates also depends on ply-thickness [4]. On one hand, the thinner plies contain statistically less defects [50]. On the other hand, fibres in thin-plies are better aligned and more evenly dispersed because of the tow-spreading process [3] (Fig 2.4). This affects the mechanical response (refer to Section 2.2.3) as well as improves the surface finish: enhanced fibre dispersion leads to better surface uniformity and less paint necessary to achieve class A finish [51].

Another advantage relative to the use of thin-plies arises from the manufacturing process. The fact of reducing the fibre areal weight of the tows using a cost-efficient method is already a benefit because, in the textile industry, the light tows (e.g. of 3

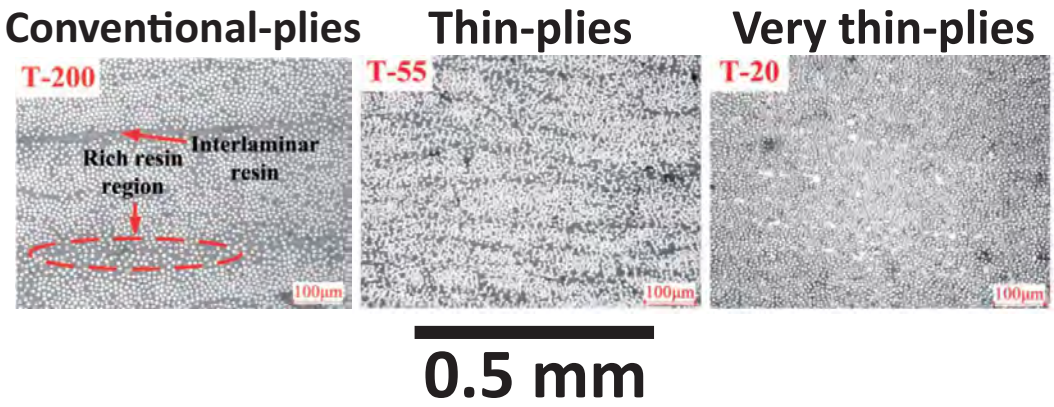


**Figure 2.4:** Microscopic cross-section of unidirectional carbon/epoxy laminates manufactured with conventional-, thin- and very thin-plies (of 200, 55 and 20 μm ply-thickness), adapted from [52].

K) are more expensive than their heavy counterparts (e.g. of 21 K). For example, Chomarat$^{TM}$ uses its proprietary spreading method to decrease the areal weight of (carbon or glass) 24 K tows from approximately 250 down to 80 g/m$^2$ [41].

In a nutshell, thin-plies:

- increase design space,
- relax the constraint of mid-plane symmetry,
- improve fibre alignment and dispersion.

### 2.2.3 Structural response

The fact that thin-ply laminates posses a better fibre dispersion than their conventional-ply counterparts proofs particularly relevant for the compressive properties (refer to Fig. 2.4 for insight into the microstructure of thin-plies). Amacher *et al.* [3] compared the compressive strength of unidirectional carbon/epoxy laminates made with conventional-, thin- or very thin-plies (of 300, 100 or 30 g/m$^2$ fibre areal weight). In theory, all the laminates should have a similar compressive strength determined by the resistance of the 0° fibres against fibre buckling [53]. However, the thinner plies displayed a 24% higher compressive strength than the conventional-ply baseline, attributed to the the better fibre alignment and distribution [3]. When embedded in multidirectional laminates, thin-plies also enhance compressive strength [54, 55].

Thin-plies also improve the tensile response of multidirectional carbon/epoxy laminates (both under static and fatigue loading) [2–4, 54–59]. Tensile failure of conventional-ply quasi-isotropic laminates develops progressively in the form of matrix cracks, matrix cracks induced delaminations (MCID), free-edge delaminations and, finally, catastrophic fibre failure [3, 60]. The benefit of using thin-plies is two-fold. On one hand, thin-plies delay the onset of matrix cracking because of

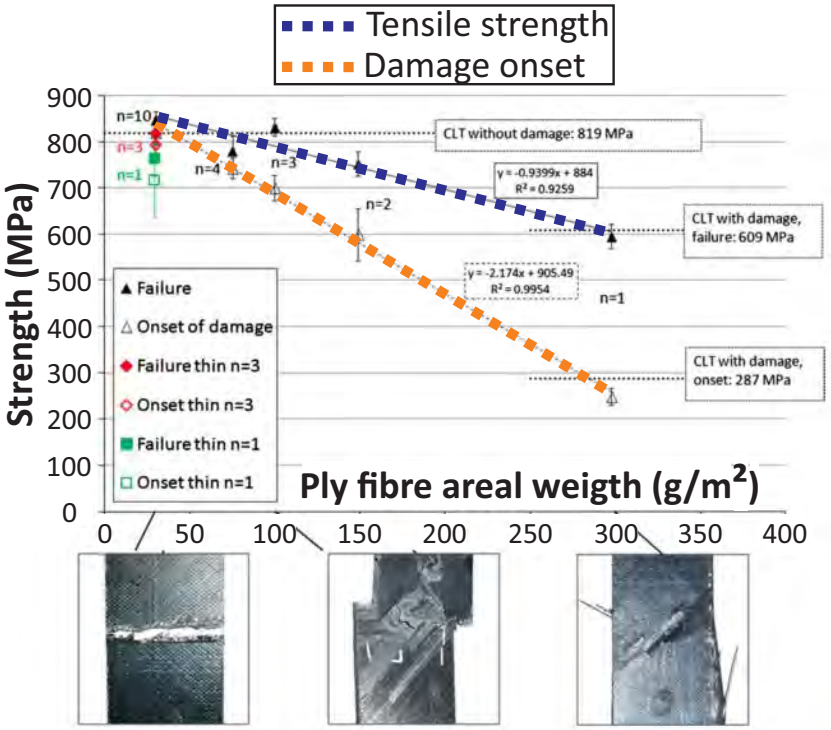


**Figure 2.5:** Tensile strength and onset of damage of $[45°/90°/-45°/0°]_{ns}$ carbon/epoxy specimens made with several ply-thicknesses ranging from conventional (300 g/m$^2$, $n = 1$) to very thin (30 g/m$^2$, $n = 10$), adapted from [3].

the in-situ effect [21, 25] (as monitored by Amacher *et al.* [3] and Cugnoni *et al.* [4]). On the other hand, the thinner the ply is, the lower the free-edge interlaminar shear stress are and the smaller the size of free-edge delaminations becomes (as demonstrated by Camanho *et al.* [61] and Guillamet *et al. et al.* [60, 62]). Overall, thin-plies delay the onset and reduce the intensity of matrix cracks and delamination, which results in a higher tensile strength and, on the negative side, a more brittle failure (Fig. 2.5).

The same tendency applies for open-hole specimens subjected to (static or fatigue) tension: thin-plies delay the onset of damage emerging from the hole [2–4, 46, 63, 64]. The conventional-ply samples develop extensive matrix cracking and delamination, whereas the thin-ply counterparts feature a single macroscopic crack with no subcritical damage [3, 63]. Based on this observation, it is clear that the thinner plies have a higher damage resistance. However, this may result in a lower nominal strength because, in certain open-hole configurations, matrix cracks and delaminations dissipate part of the stress concentration around the hole [2–4, 46, 63, 64] —this strength reduction occurs for open-hole geometries where the ligament between the hole and the free-edge is wide enough to allow for damage propagation [63]. Under compression, the strength of open-hole specimens is controlled by the compressive stability of the 0° layers [3] i.e., the thin-plies enhance

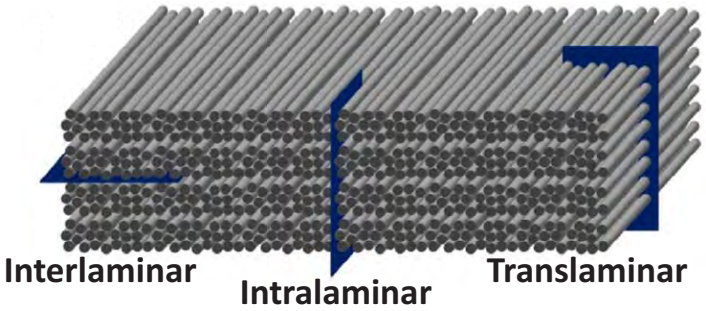


**Figure 2.6:** Definition of inter-, intra- and translaminar fracture toughness, adapted from [69].

the open-hole compressive strength [3, 54].

The thin-ply laminates improve the interlaminar shear strength (ILSS) of quasi-isotropic specimens [52, 65]. Kalfon-Cohen *et al.* [65] compared the ILSS strength of $[0°/90°/\pm 45°]_{ns}$ standard- ($n$=2) and thin-ply ($n$=6) short-beam specimens (162 and 54 µm ply-thickness). The thin-ply coupons displayed a 10% higher strength than their standard-ply counterparts, which is in accordance with the results of Huang *et al.* [52]. Unfortunately, the reason why thin-plies enhance ILSS strength remain unclear because both studies lack details about the damage sequence evolution. For unidirectional laminates, ILSS strength is unaffected by ply-thickness (at least for the M40JB/TP80ep material system [3]). Finally, it is worth noting that thin-plies demonstrate a higher strength under four-point bending (at the cost of a brittler failure [40]) and, moving from the coupon to the component level, a better performance in bolted-joints [3, 46].

While thin-plies increase the damage resistance and, in some cases, the nominal strength compared to their conventional-ply counterparts, they raise some concerns regarding the fracture toughness (inter-, intra- and translaminar fracture toughness, Fig 2.6) [66–69]. Frossard *et al.* [67, 69] characterized the mode I inter- and intralaminar fracture toughness of unidirectional double cantilever beam (DCB) specimens made of standard-, thin- and very thin-plies (150, 75 and 30 µm ply-thickness). Teixeira *et al.* [68] and Frossard *et al.* [66] characterized the translaminar fracture toughness of cross-ply [66, 68] and quasi-isotropic [66] compact-tension specimens with varying 0° ply-thickness (ranging from 150 to 30 µm). In all the experiments, the systems with thinner plies displayed a lower critical energy release rate, which the authors attributed the better fibre dispersion and alignment (thin-plies induced less fibre bridging in DCB specimens and shorter 0° pull-out bundles in compact tension experiments).

In a nutshell, thin-plies:

- reduce matrix cracking and delamination under in-plane loading,

- improve compressive strength,
- improve tensile strength,
- improve fatigue life,
- improve interlaminar shear strength,
- improve four-point bending and bolt-bearing strengths,
- decrease fracture toughness,
- display a brittle failure.

## 2.3 Low-velocity impact

Composite aircraft components are exposed to foreign body impacts [5, 8]. The velocity of such impacts ranges from relatively low (e.g. a tool dropped on a wing during maintenance) to the ballistic-velocity impact of hail on aircraft's fuselage skin [5–8, 70–73]. The nature of the impact event is classified in terms of the impactor-to-target mass ratio. "Ballistic" or "high-velocity" impact applies to light impactors that cause a dynamic response governed by transient waves (e.g. the hail). "Low-velocity impact" (LVI) applies to heavier impactors which deflect the laminate quasi-statically (e.g. the tool) [5, 8, 70, 74–78]. Ballistic- and high-velocity impacts induce severe damage which penalizes the load-carrying capacity but, on the positive side, are easy to detect by visual inspection (they often perforate the laminate) [8, 75, 77]. In contrast, the main threat of LVI is not only the damage itself (which also impairs mechanical properties), but the possibility that such damage would remain undetected during visual inspection (damage occurs inside the laminate with little evidence on the impacted surface, Fig. 2.7) [5, 8, 9, 76, 79–82]. The aircraft industry defines the so-called Barely Visible Impact Damage threshold (BVID) in terms of the dent depth left behind by the impactor (a dent depth between 0.25-0.50 mm is in danger of going unnoticed during visual inspection and is therefore

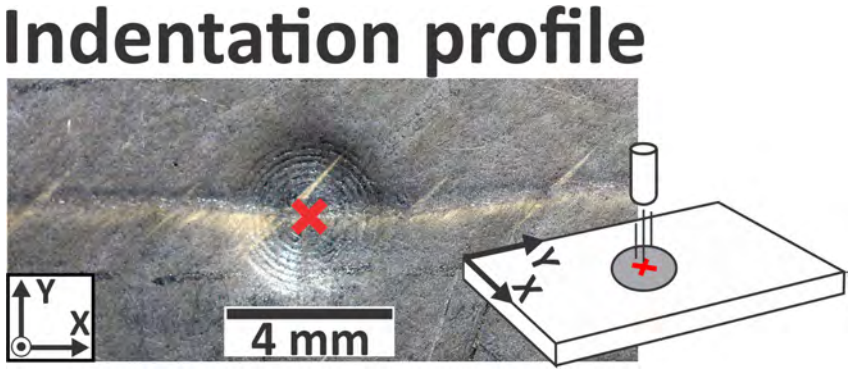


**Figure 2.7:** Permanent indentation left behind by an 8 J low-velocity impact (LVI) on the surface of a $[45°/0°/-45°/90°]_{2s}$ 2.2 mm thick carbon/epoxy laminate.

considered BVID [11, 12]). The threat posed by BVID results in conservative laminate design, which increases the weight of the structure and consequently mitigates the main advantage of composites over metals: their lightness [9].

A standard apparatus to simulate LVIs in a laboratory scale is the drop-weight impact tower [83]. This experiment drops an impactor under free fall onto a clamped composite plate (impactor weight, height and potential energy are known a priori). The impactor is instrumented to monitor the force and deflection developed during the impact event. The standard size of the plate is 100 x 150 mm (width and length). Laminate's impact performance is evaluated using two parameters: impact resistance and impact tolerance [5, 8, 84–90]. Impact resistance is the ability to resist damage formation (damage consists mainly of matrix cracks, delamination and fibre failure), while impact tolerance is the ability to withstand loads after the impact event [85]. Impact resistance is compared by extracting information of the load-displacement curve (e.g. the threshold load, the maximum load, etc. [76, 86–89]) or by measuring delamination size [5, 8, 76, 86–89, 91, 92]. Delamination size is the damage area measured with non-destructive inspection techniques such as C-scan or X-ray tomography (μCT) (Fig. 2.8). C-scan provides a top view of all the delaminations developed across the thickness of the laminate, while μCT provides more sophisticated views (2D or 3D) where matrix cracks and delamination can be ascribed to their correspondent ply or interface. Impact tolerance is characterized using the compression after impact (CAI) test [5, 8, 70, 76, 86, 87, 89–91, 93]. This experiment subjects the whole impacted coupon to plain compression. In aircraft industry, CAI strength has a decisive influence for material screening purposes. The reason for imposing a compressive load rather than other type of in-plane

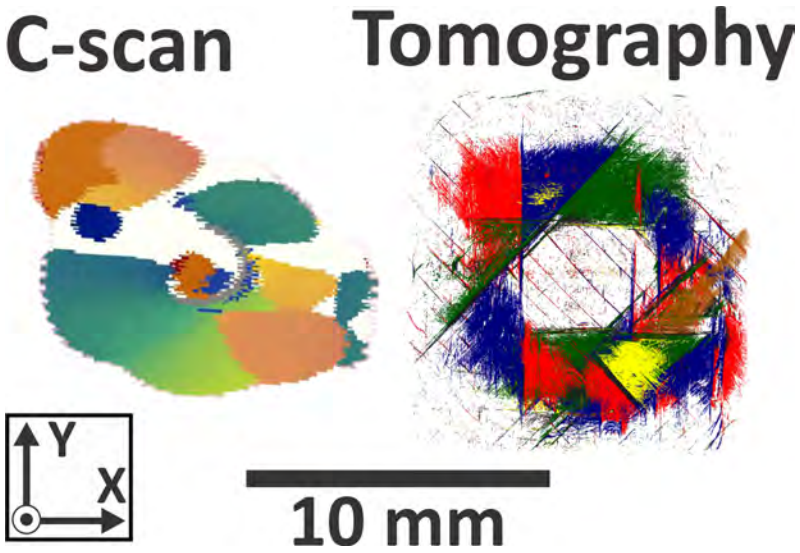


**Figure 2.8:** Projected damage area of the impact specimen described in Fig. 2.7 as inspected with a) C-scan and b) X-ray micro-computed tomography (μCT).

or flexural solicitation is that compressive strength is the most reduced by LVI damage (delamination induces premature buckling which severely reduces pristine compressive strength) [5, 8, 84, 90]. Fig. 2.9 presents the linear relation between C-scan damage size and increased impact energy as observed in several types of thick conventional-ply laminates [86]. Fig. 2.10 displays how CAI strength decreases with increased projected damage area [90]—such reduction is expected to level-off to an asymptotic value when the energy is high enough to cause laminate perforation [5, 8, 90]. It is worth noting that residual compressive strength can be as low as 30% of the pristine value [91].

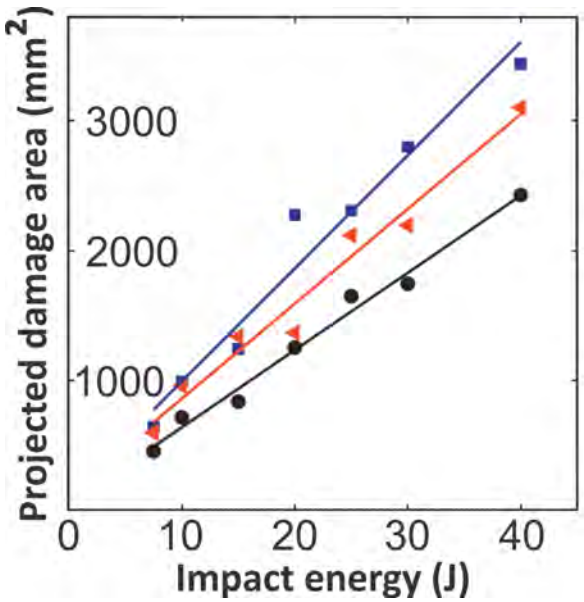


**Figure 2.9:** Projected damage area vs. applied impact energy for several types of thick conventional-ply laminate, adapted from [86].

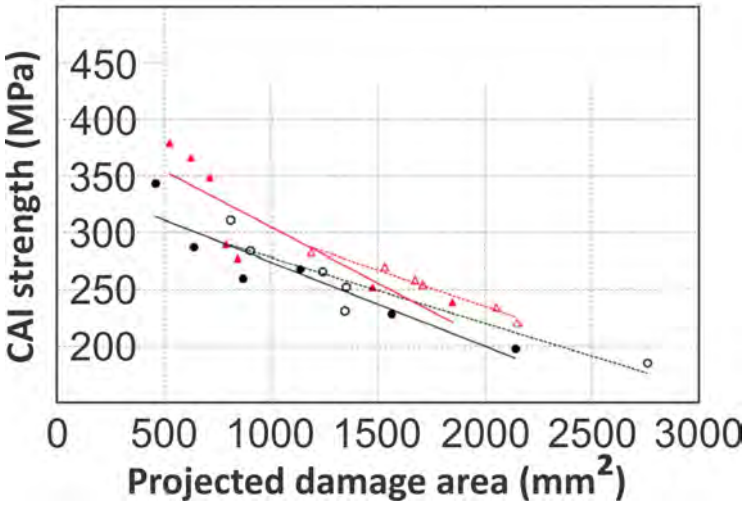


**Figure 2.10:** Compression after impact (CAI) strength vs. projected damage area for several types of thick conventional-ply laminate, adapted from [90].

Impacting a composite plate induces a complex stress state perfectly reflected by the typical *post mortem* damage scenario (Fig. 2.11) [5, 8]. (the reader is referred to Zhang *et al.* [94] for a detailed explanation about the stress state induced by LVI). Contact stresses caused by the impactor induce fibre breakage in the top part of the laminate (*i*). Interlaminar shear stresses in the inner part of the laminate cause 45° matrix cracks ("shear cracks" [5, 95]) and delaminations (*ii* and *iii*). The XY view of Fig. 2.11 details the morphology of those damage mechanisms: shear cracks follow the orientation of the damaged ply, whereas delaminations arise from the intersection of shear cracks with dissimilar orientation [96]. Bending tensile stresses develop 90° matrix cracks ("tensile cracks" [5, 95]) in the bottom part of the laminate (*iv*). Finally, compressive stress results in an "undamaged cone" immediately underneath the impactor (pure compression mitigates the initiation of delamination, Fig. 2.11).

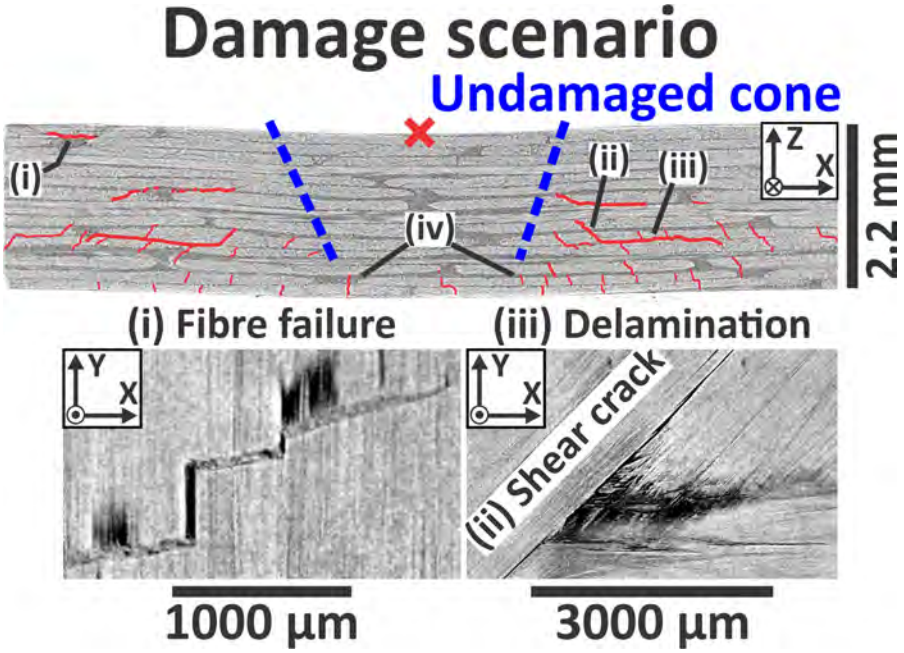


**Figure 2.11:** µCT slice depicting the damage scenario of the impact specimen described in Fig. 2.7: i) is the fibre failure, ii) is the shear crack, iii) is the delamination and iv) are the tensile cracks.

### 2.3.1 Quasi-static indentation

Improving impact resistance and tolerance must depart from the understanding of the damage sequence evolution developed during LVI (i.e. the succession of damage mechanisms that leads to the *post-mortem* damage scenario in Fig. 2.11). Unfortunately, current NDI techniques are unable to elucidate impact damage progression because of the high strain-rate of the experiment (in the order of 10 $s^{-1}$ [92]). The idea of quasi-static indentation experiments is to mimic drop-weight

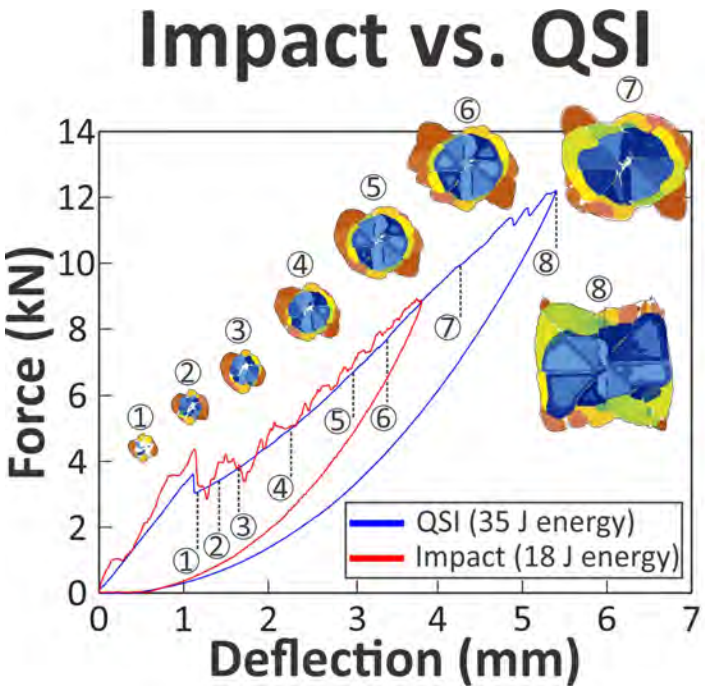


**Figure 2.12:** Qualitative comparison of the load-displacement curves of impact and quasi-static indentation (QSI) experiments, where the points 1-8 refer to the load level at which the QSI tests were arrested for C-scan inspection, adapted from [49].

impact tests under controlled conditions [79, 85, 92, 95–99]. To this purpose, QSI fixtures use a displacement-controlled indenter instead of a free fall impactor (QSI cross-head displacement rates oscillate from 0.5 to 25 mm/min [79, 85, 92, 95–99]). The advantage is that QSI can be interrupted at incremental force (or displacement) levels to gain insight into damage morphology by performing C-scan or μCT inspections after each incremental experiment (Fig. 2.12) [49, 95, 96].

Many investigations demonstrate that impact and QSI tests yield comparable results in terms of the load displacement curves and C-scan projected damage areas (the former being qualitatively illustrated by Fig. 2.12) [79, 85, 92, 100–106]. The reason for this correlation is that, despite the different strain-rate of both experiments, LVI deflects the laminate quasi-statically (for further details concerning the definition of LVI refer to Section 2.3) [5, 8, 70, 74–78].

The damage sequence developed during QSI experiments depends upon the specimen's thickness-to-length ratio. For a given set-up configuration, the thicker laminates ("thick laminates") are stiffer than their thinner counterparts, which means that shear dominates over bending deflection [5, 77, 85, 96, 107]. In contrast, the thinner laminates ("thin laminates") are more flexible, which entails higher bending deflections and associated in-plane stresses in the non-impacted surface [5, 79, 85, 96, 107].

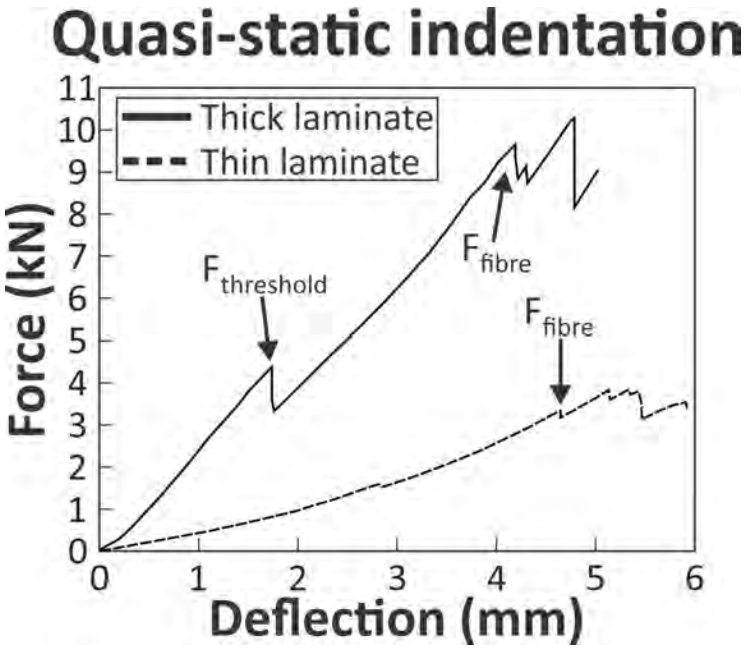


**Figure 2.13:** QSI force-response of "thick" and "thin" laminates (thick and thin are the laminates with a relatively high and low thickness-to-length ratio, respectively), adapted from [96].

The QSI load-displacement curves of thick conventional-ply carbon/epoxy quasi-isotropic laminates display similar tendencies (refer to the continuous line of Fig. 2.13) [49, 85, 92, 95, 96, 107]. First, the load grows linearly until a local maximum ($F_{threshold}$), followed by load drop and a decrease of the bending stiffness. Such load drop is often attributed to the onset of delamination propagation (delaminations divide the laminate in several sub-laminates with lessened bending stiffness) [5, 49, 85, 92, 96, 107]. In contrast, Wagih *et al.* [95] related the drop-off to the sudden propagation of multiple matrix cracks. After the load oscillation, the force continuous to grow non-linearly until another local maximum ($F_{fibre}$) and a subsequent multiple load drops. $F_{fibre}$ is unequivocally attributed to the development of fibre failure across the thickness of the laminate, ultimately resulting into laminate penetration [49, 85, 92, 95, 96, 107]. The main difference between thick and thin laminates is that, for the thinner coupons, bending- dominates over shear-deflection which increases the non-linearity of the force-displacement curve and obscures the development of $F_{threshold}$ (refer to the dashed line of Fig. 2.13) [85, 96, 107, 108]. This means that shear cracks and delamination propagate with no clear evidence in the load-displacement curve. $F_{fibre}$ is also attributed to development of fibre failure but, owing to the high deflections, the fibres start to fail in the non-impacted surface (when bending in-plane stresses overcome the tensile strength of the fibres) [5, 85, 96, 107, 108].

Overall, impact damage sequence depends upon the specimen's thickness-to-length

ratio. In thick laminates, shear cracks and delaminations propagate progressively from the top to the bottom of the specimen followed by catastrophic fibre failure trough the thickness. In thin laminates, shear cracks and delaminations propagate bottom-to-top and fibre breakage starts to develop in the non-impacted surface. In both cases, the intricate mosaic of shear cracks and delaminations results in the so-called C-scan "spiral staircase" profile (Fig. 2.8 and Fig. 2.12, points 1-7) [5, 8, 107, 109].

To conclude this section, it is worth noting that, to the author's knowledge, most of the LVI and QSI studies focus on thick laminates because those are the ones recommended by ASTM standards [83, 93]. The reason is that thin laminates bring complexities during subsequent CAI experiments because they require antibuckling devices [110–112]. Therefore, it is evident that further efforts should be devoted to gain understanding into the impact and post-impact responses of thin laminates.

In a nutshell,

- there is controversy, and lack of unambiguous experimental evidence, whether shear cracks precede delamination during impact or which damage mechanism compromises the load-carrying capacity,
- impact damage sequence depends on the specimen's thickness-to-length ratio (thick versus thin laminates),
- non-standard thin laminate's impact response claims further investigation.

### 2.3.2 Thin-ply impact response

While the research community is gaining a solid understanding of thin-ply laminate's in-plane response (Section 2.2.3), few works investigate their impact resistance, tolerance and damage sequence evolution. This section compares the impact response of thick and thin laminates made with conventional- or thin-plies.

Limited studies suggest that, for thick quasi-isotropic laminates impacted at relatively low energies (6.7 J/mm), the thin-ply specimens display a similar C-scan projected damage area and a higher CAI strength than these of their conventional-ply counterparts [2, 54]. A relevant observation is that, despite the similar damage area, only the conventional-ply laminates feature the typical "spiral staircase" damage profile. Cugnoni *et al.* [4] also reported that decreasing thick laminate's ply-thickness (from 255 to 67 μm) enhanced CAI strength (by 40%). However, the percentage improvement should be taken with caution since both laminates were toughened with thermoplastic particles at the interfaces.

Saito *et al.* [113] provided insight into the impact damage mechanisms developed

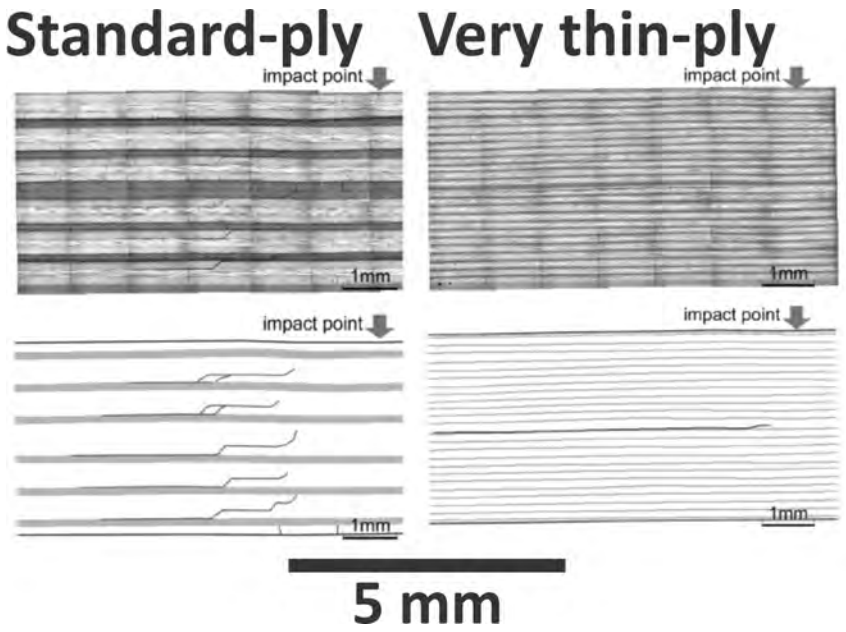


**Figure 2.14:** Microscopic image depictig the impact damage scenario of $[45°/0°/-45°/90°]_{ns}$ thick laminates made with standard- (145 µm, $n = 3$) or very thin-plies (38 µm, $n = 12$). The impact energy was very low (0.75 J/mm), adapted from [113].

in $[45°/0°/-45°/90°]_{ns}$ thick laminates made with standard- (145 µm, $n = 3$) or very thin-plies (38 µm, $n = 12$). (Fig. 2.14). The impact energy was very low (0.75 J/mm). The standard-ply samples developed a shear crack in most of the 90° and 45° layers as well as one delamination in the interfaces between off-axis plies (i.e. the 90° and 45° plies). In contrast, shear cracks and delamination localized into the central section of the thin-ply coupons (where transverse shear stress is maximum across the thickness [114]).

Wagih *et al.* [99] extended the work of Saito *et al.* [113] to a wider range of out-of-plane energies by combining incremental QSI experiments with C-scan/optical microscopy inspections. They tested carbon/epoxy $[((45°/-45°)/(0°/90°))_n]_s$ thick plain-weave fabric laminates made with thin- (80 µm, $n = 7$) or very thin-yarns (40 µm, $n = 14$). For the lowest QSI energy levels, the specimens with very thin-plies delayed/reduced the onset of shear cracks and delaminations (in agreement with the observations of Saito *et al.* [113]). For the highest energies, the lower energy dissipation resulted in premature fibre failure and a decreased load-carrying capacity. In other words, the specimens with thinner plies delayed/reduced the onset of damage at the expense of a brittler failure.

The tendency observed by Wagih *et al.* [99] also applies for thin laminates: thin-plies delay the onset of damage at the cost of premature fibre failure [3, 98]. The difference is that, since thin laminates suffer higher bending deflections than thick laminates [107], fibre breakage concentrates in the back surface (Fig. 2.15).

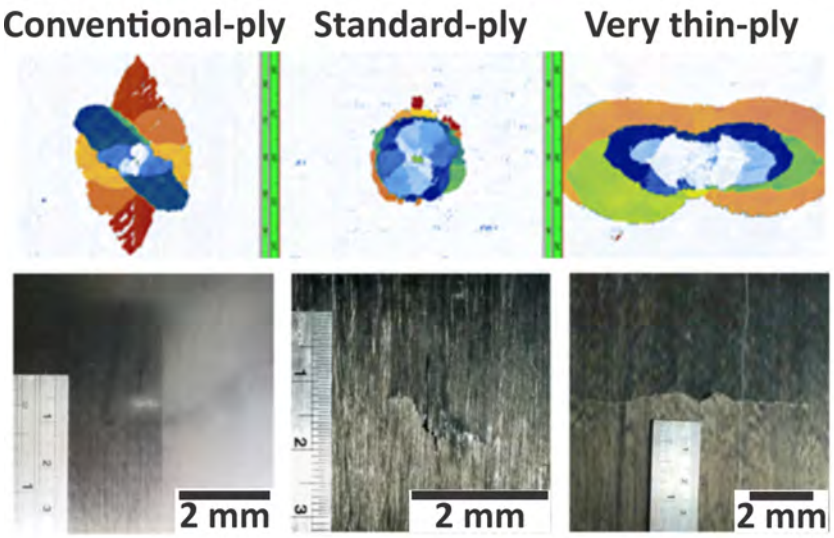


**Figure 2.15:** Non-impacted surface of $[45°/90°/-45°/0°]_{ns}$ thin laminates made of conventional- (300 g/m$^2$, $n$= 1), standard- (100 g/m$^2$, $n$= 3) or very thin-plies (30 g/m$^2$, $n$= 10). The impact energy was 4.8 J/mm, adapted from [3].

In a nutshell, thin-plies:

- reduce matrix cracking and delamination under low-velocity impact,
- display a brittle failure with extensive fibre breakage.

## 2.4 Interleaving thermoplastic veils

From and industrial point of view, damage tolerance can be enhanced using toughening methods that are cheap, easy to handle and suited for out-of-autoclave manufacturing. Nash *et al.* [16] classified toughening methods in three groups: through-the-thickness reinforcements, bulk resin modification and interlaminar toughening. The first group includes Z-pins and stitching, which knock down certain in-plane mechanical properties and, in some cases, are incompatible with resin infusion [10, 13, 16, 18]. The second group increases the fracture toughness of the resin by dissolving/dispersing a thermoplastic agent, which increases resin viscosity [10, 13]. The third group incorporates a toughening system such as thermoplastic particles or thin films at the interfaces. However, the particles may migrate during infusion and the films inhibit through-thickness resin flow. We interleaved our laminates using thermoplastic "non woven veils" (more specifically, using co-polyamide non-woven veils). These are thin webs made of dispersed micro-fibres [15] (Fig 2.16). The main advantages are that they are commercially available, relatively cheap, can be manually placed during lay-up and allow resin infusion through the z-direction (the veils are permeable networks).

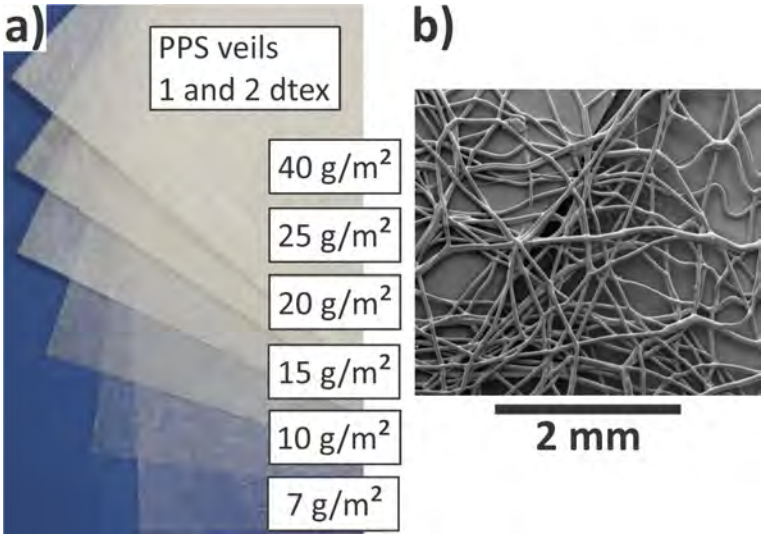


**Figure 2.16:** a) Set of polyphenylenesulfide (PPS) veils b) SEM image of a co-polyamide (CoPA) veil, reproduced from [115, 116] —the CoPA veils used in this study are not shown because of confidentiality.

### 2.4.1 Preliminary considerations

Selecting the appropriate veil for each particular application is a complex decision because of the wide range of veil fibre architectures that are commercially available (refer to [13] for a list of suppliers). Design parameters include veil fibre material, fibre areal weight, fibre diameter, fibre melting temperature, fibre distribution, etc. This section provides an overview of the main aspects considered for veil selection. Sections 2.4.3-2.4.5 will focus on how some of these aspects affect mechanical performance.

**Cost.** Thermoplastic veils are cheaper than their carbon sheet counterparts. Zhu *et al.* [117] manufactured vacuum infused laminates using thermoplastic (polypropylene or high-density polyethylene) interleaves. The price of the veils was approximately 5€/kilogram, increasing the total manufacturing costs by 7%. In contrast, incorporating carbon sheets would have raised costs by more than two orders of magnitude (carbon veils for aerospace structures cost about 1200€/Kg [118]).

**Veil fibre areal weight.** (Weight per unit area of veil). Ramírez *et al.* [15] reported that the thickness of their thermoplastic veils systems increased linearly with improved veil fibre areal weight. Therefore, veil fibre areal weight should be carefully controlled to avoid compromising nominal laminate thickness (as occurs elsewhere [14, 16–19, 119–121]). This is particularly relevant for out-of-autoclave manufacturing methods where the thickness of the laminate is not determined by two mould halves (e.g. vacuum assisted resin transfer moulding [18]). Beylergil *et al.* [18] interleaved a vacuum-infused carbon/epoxy laminate with 50 g/m$^2$ polyamide (PA) veils. Interleaving increased the nominal thickness by 38% and decreased the

fibre volume fraction by 33% compared to the non-interleaved system. In contrast, Walker *et al.* [122] incorporated 2.2 g/m$^2$ PA veils with no associated increase of laminate thickness (laminates were manufactured by compression moulding). Another disadvantage of interleaving heavy veils is that they difficult resin infusion in the z-direction and consequently lead to porosity [16, 19]. In addition to this, the higher veil fibre areal weight is, the greater moisture absorption becomes (polyamide is hydrophilic [14, 17, 120, 123]).

**Adhesion between veil fibres and resin**. Veil fibres with a relatively poor adhesion will easily debond from the matrix, whereas veil fibres with a better adhesion will improve wetting efficiency and display a higher interfacial strength [10, 13, 18, 124–127]. One factor that controls the adhesion between veil fibres and resin is the relative polarity of the constituents [13, 18, 126–128]. For example, both semycristalline PA fibres and epoxy resin are polar and thus likely to form hydogen bonds at the molecular level [13, 18]. Kuwata *et al.* [115] indicated that veil fibre-resin adhesion is also affected by veil fibre diameter. Quantitative methods to evaluate adhesion include Fourier-transform infrared spectroscopy and contact angle measurements (for further details of these techniques refer to [125, 126, 129]).

**Veil fibre integrity.** (After-manufacturing shape of veil fibres). Two factors help to preserve the initial shape of veil fibres after consolidation within the laminate. Firstly, the fibres should be thermally stable until the resin achieves certain viscosity so that, even if the fibres start to yield, the resin will be viscous enough to lock-in their position [13, 130] (if the melting temperature of veil fibres is lower than the gel point of the resin the fibres will agglomerate during curing, Fig. 2.17). The second factor is keeping veil fibres from moving during resin infusion, which can be achieved by "heat bonding" the veils to the dry reinforcements [13, 117] (if veil fibre integrity wants to be preserved, bonding temperature and time should be carefully controlled).

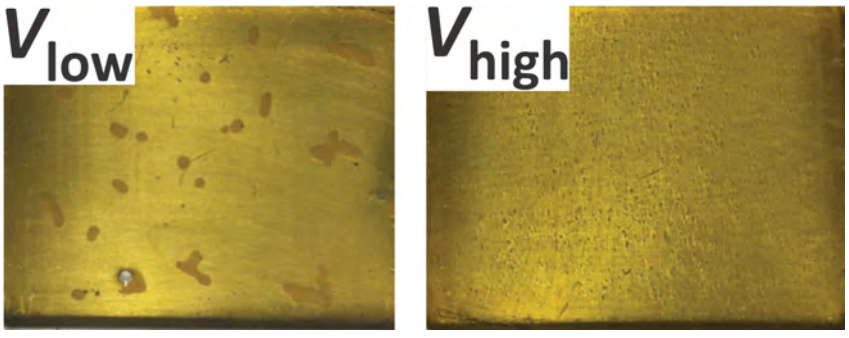


**Figure 2.17:** Shape of two types of co-polyamide veil fibres ($V_{low}$ and $V_{high}$) after curing with a benzoxazine resin. The melting temperatures of $V_{low}$ and $V_{high}$ are 96 and 178 °C. The gel temperature and time of the resin are 180°C and 3-4 min., reproduced from [130].

In a nutshell:

- interleaving veils with a relatively high fibre areal weight increases laminate thickness,
- to preserve the initial shape of veil fibres after consolidation, the melting temperature of the fibres should be higher (or close to) the gel point of the resin.

### 2.4.2 Geometrical description of veils

Disordered fibrous materials are frequently modelled with the aim of predicting certain structural properties in terms of network parameters such as fibre linear density, fibre surface area, porosity, etc. [15]. The main assumption is that fibres follow a 2D stochastic distribution where the orientation of any fibre is independent to that of the others [131]. These models are widely used to design paper or gas filters [116]. However, only a couple of references deal with the veils used in laminated composites [15, 131]. The only purpose of the present section is reviewing basic definitions useful to describe veil fibre architecture (for further details the reader is referred to [15, 116, 131, 132]). Sections 2.4.3-2.4.5 will focus on the effect veil fibre architecture has upon mechanical properties.

In veil fibres with circular cross-section, the linear density $\delta$ depends on the fibre diameter $\omega$ and the polymer density $\rho$ —linear density is the mass per unit length of veil fibre, the typical European unit being dtex (g/10 km of filament):

$$\delta = \frac{\pi \omega^2 \rho}{4} \tag{2.1}$$

The veil fibre specific surface area $S_f$ ($m^2$/kg) follows:

$$S_f = \frac{\pi \omega}{\delta} = \frac{4}{\rho \omega} \tag{2.2}$$

The veil mean coverage $\bar{c}$ is the ratio of the veil fibre areal weight ($\bar{\beta}$, as measured with a weighing scale) to that of the constituent fibres ($\beta_f = \delta/\omega$):

$$\bar{c} = \frac{\bar{\beta}}{\beta_f} = \frac{\bar{\beta}\omega}{\delta} = \frac{4\bar{\beta}}{\pi \omega \rho} \tag{2.3}$$

This parameter gives information about expected number of veil fibres covering each point of the plane of support. For a given $\omega$, $\bar{c}$ increases linearly with veil fibre areal weight. For a fixed $\bar{\beta}$, $\bar{c}$ is inversely proportional to the veil fibre diameter. The mean coverage is a specially relevant parameter since it provides information of both veil and individual veil fibres.

### 2.4.3 Interlaminar fracture toughness

Kuwata *et al.* [115] characterised the mode-I interlaminar fracture toughness ($G_{IC}$) of unidirectional DCB specimens interleaved with a single thermoplastic veil at the centre of the stack (the veils were made of CoPA, polyester PE, carbon or carbon/PE fibres). Each veil was interleaved in several types of carbon fabric (5-harness satin, plain weave and unidirectional non-crimp fabrics) which, in turn, were infused with two types of resin (epoxy and vinyl ester). In most cases, the specimens interleaved with thermoplastic veils (the CoPA and PE veils) displayed a higher $G_{IC}$ than the ones toughened with carbon interleaves, which Kuwata [124] attributed to their lower adhesion with the matrix. Veil fibres with a relatively low adhesion (the CoPA and PE fibres) pull out from the matrix and dissipate part of the fracture energy by fibre bridging and fibre pull-out. In contrast, veil fibres with a higher adhesion (the carbon fibres) remain embedded within the resin and result in the lowest $G_{IC}$ values —this line of reasoning is also be valid for other type of interlaminar toughening techniques such as thermoplastic particles [133].

Ramírez *et al.* [15] focused on how $G_{IC}$ depends on veil fibre areal weight and fibre linear density. They interleaved unidirectional carbon/epoxy specimens with polyetheretherketone (PEEK) or polyphenylenesulfide (PPS) thermoplastic veils. The PPS webs had a fibre areal weight ranging from 9 to 35 g/m$^2$ and, for a given $\bar{\beta}$, two linear densities: 1 or 2 dtex. Mode-I interlaminar fracture toughness increased with improved veil fibre areal up to a plateau (which is in agreement with the observations of O'Donovan *et al.* [128], Beylergil *et al.* [18] and Fitzmaurize *et al.* [127]) and, for a given veil fibre areal weight, the fibres with lower linear density

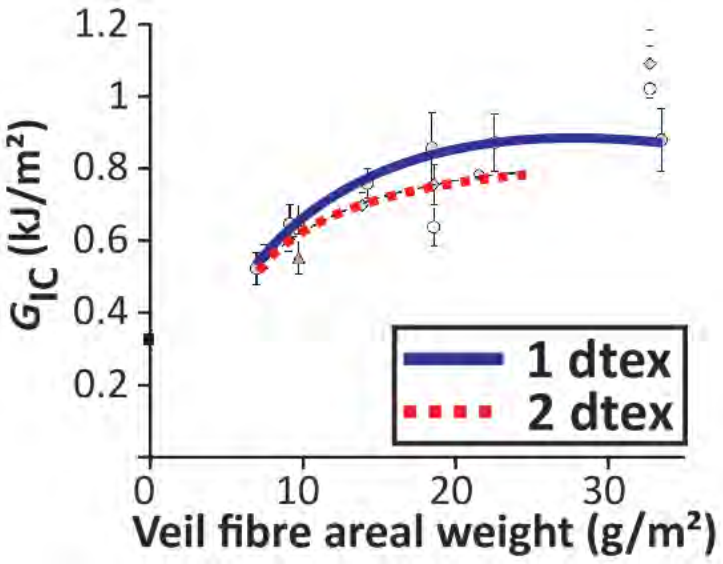


**Figure 2.18:** Mode-I interlaminar fracture toughness ($G_{IC}$) vs. veil fibre areal weight ($\bar{\beta}$) and fibre linear density ($\delta$), adapted from [15].

(i.e. the thinner fibres, Eq. 2.1) performed better (Fig. 2.18). The authors connected both improvements to an increase of the mean coverage of the network (Fig. 2.19): the higher $\bar{c}$ is, the greater amount of fibre bridging develops.

Many other authors report that thermoplastic veils enhance $G_{IC}$ by fibre bridging, pull-out and plastic deformation of the ductile fibres [10, 14, 18, 19, 115, 119, 120, 123, 126, 128, 134–136]. Tables 2.1-2.2 connect veil fibre architecture and $G_{IC}$. It is unequivocally inferred that interleaving PA webs with veil fibre areal weight and fibre diameter values ranging from 7-50 g/m$^2$ and 10-59 µm enhances mode-I interlaminar fracture toughness. By contrast, Saz-Orozco *et al.* [126] reported that a polyethylene terephthalate (PET) veil deviated crack propagation from the resin rich interlayer (full of veil) to the interface between glass fibres/matrix (depleted of veil), which left the baseline $G_{IC}$ unaffected (Fig. 2.20). The PET fibres deviated crack propagation away from the veil because they have a high adhesion with vynil ester resin [124, 126].

Mode-II interlaminar fracture toughness ($G_{IIC}$) also increases with improved veil mean coverage [15]. However, the toughening mechanism are more complex, less dependant on fibre bridging and more related to the ability of the matrix to yield in shear and interact with the deformation of the veil fibres [115]. For an example, Nash *et al.* [17] reported that interleaving a PA veil of 34 g/m$^2$ fibre areal weight and 23 µm fibre diameter enhanced the $G_{IIC}$ of the carbon/benzoxazine non-interleaved laminate by crack pinning, fibre debonding and fibre plastic deformation. Since $G_{IC}$ is typically lower than $G_{IIC}$ (e.g. refer to the the results of [15, 120, 123, 135, 136]), the experimental campaign of this thesis will focus on mode-I fracture toughness as a "worst-case" scenario.

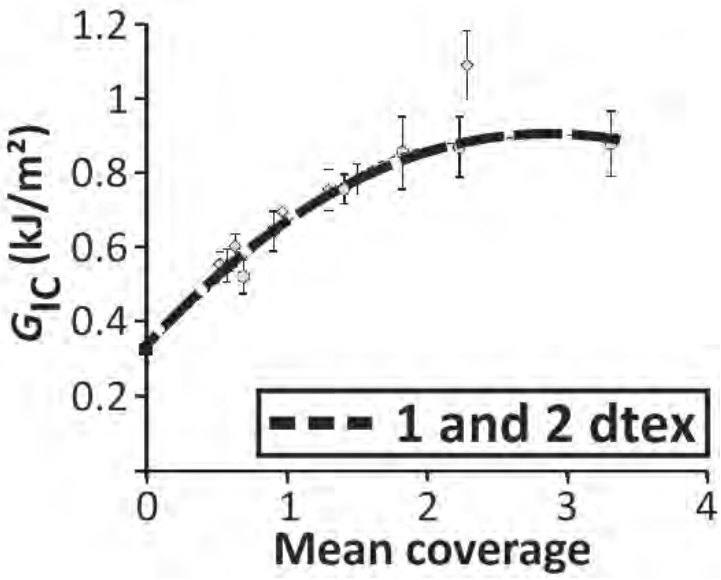


**Figure 2.19:** $G_{IC}$ vs. veil mean coverage ($\bar{c}$), adapted from [15].

**Table 2.1:** Fibre architecture of thermoplastic micro-fibre veils used for mode-I interlaminar fracture toughness testing (for the corresponding $G_{IC}$ results refer to Table 2.2).

| Reference | Laminate | Veil | $\bar{\beta}$ (g/m$^2$) | $\omega$ (µm) | $\rho$ (g/m$^3$)[1] |
|---|---|---|---|---|---|
| Kuwata [115, 137] | Carbon/epoxy (non-crimp and plain-weave fabrics) Carbon/vynil ester (non-crimp and plain-weave fabrics) | CoPA | 21 | 59 | 1.14 |
| Barjasteh [120] | Carbon/benzoxazine | PA12 | 12 | 17[2] | 1.25 |
| Saz-Orozco [126] | Glass/vynil ester | PA66 | 17 | 25 | 1.14 |
| O'Donovan [128] | Glass/polyester | PA66 | 9 | 11.5 | 1.32 |
| Ramírez [15] | Carbon/epoxy | PEEK | 9 | 11.5 | 1.32 |
| Ni [136] | Carbon/epoxy | Aramid | 16 | 15 | 1.44 |
| Kuwata [115, 137] | Carbon/epoxy Carbon/vynil ester | CoPE | 23 | 12 | 1.38 |
| Wong [138] | Carbon/epoxy | Kevlar | 26 | 12 | 1.44 |
| Fitzmaurize [127] | Glass/polyester | PET | 45 | 20 | 1.41 |
| Saz-Orozco [126] | Glass/vynil ester | PET | 45 | 20 | 1.41 |
| Beylergil [18] | Carbon/epoxy | PA66 | 17 | 19.90 | 1.14 |
| | | | 50 | | |
| Ramírez [15] | Carbon/epoxy | PPS | 7 to 35 | 10 | 1.30 |
| | | | 8 to 22 | 14 | |

[1] taken from [139, 140]
[2] measured from a picture in [120]

To the author's knowledge, only one reference deals with the effect veil fibre integrity (i.e. the after-manufacturing shape of veil fibres) has on interlaminar fracture toughness [130]. This study was performed using the veils presented in Fig. 2.17 ($V_{low}$ fibres agglomerated during manufacturing, while $V_{high}$ fibres preserved their initial shape). The veil with fibrous architecture resulted in the highest mode-II interlaminar fracture toughness ($V_{high}$ and $V_{low}$ enhanced $G_{IIC}$ by 172% and 8%). In contrast, $V_{high}$ displayed a lower $G_{IC}$ than $V_{low}$ (both veils improved the property by 45% and 92%). The author suspected that, in mode-I, $V_{high}$ deviated part of the crack to the interfacial region (Fig. 2.20).

In a nutshell:

- interleaving PA veils improves mode-I interlaminar fracture toughness by fibre bridging, pull-out and plastic deformation,
- the enhancement increases with improved veil mean coverage (i.e. for a given veil system, by increasing veil fibre areal weight or decreasing veil fibre diameter, Eq. 2.3).

**Table 2.2:** $G_{IC}$ improvement associated to the thermoplastic veils presented in Table 2.1.

| Reference | Laminate | Veil | $\bar{c}$ | $G_{IC}$ vs. baseline |
|---|---|---|---|---|
| Kuwata [115, 137] | Carbon/epoxy | CoPA | 0.39 | ↑ up to 260%[1] |
| | Carbon/vynil ester | | | ↑ up to 19% |
| Barjasteh [120] | Carbon/benzoxazine | PA12 | 0.72 | ↑ 38% |
| Saz-Orozco [126] | Glass/vynil ester | PA66 | 0.76 | ↑ 91% |
| O'Donovan [128] | Glass/polyester | PA66 | 0.76 | ↑ 76% |
| Ramírez [15] | Carbon/epoxy | PEEK | 0.76 | ↑ 76% |
| Ni [136] | Carbon/epoxy | Aramid | 0.94 | ↑ 92% |
| Kuwata [115, 137] | Carbon/epoxy | CoPE | 1.77 | ↑ up to 160% |
| | Carbon/vynil ester | | | ↑ up to 35% |
| Wong [138] | Carbon/epoxy | Kevlar | 1.92 | ↓ 33% |
| Fitzmaurize [127] | Glass/polyester | PET | 2.03 | ↑ 12% (1 veil)<br>↑ 55% (2 veils) |
| Saz-Orozco [126] | Glass/vynil ester | PET | 2.03 | → |
| Beylergil [18] | Carbon/epoxy | PA66 | 0.96 | ↑ 231% |
| | | | 2.80 | ↑ 737% |
| Ramírez [15] | Carbon/epoxy | PPS | 0.68 to 3.43 | ↑ 63% to 172% |
| | | | 0.49 to 2.40 | ↑ 81% to 144% |

[1] only for plain-weave carbon fabrics (decreased in the other cases).

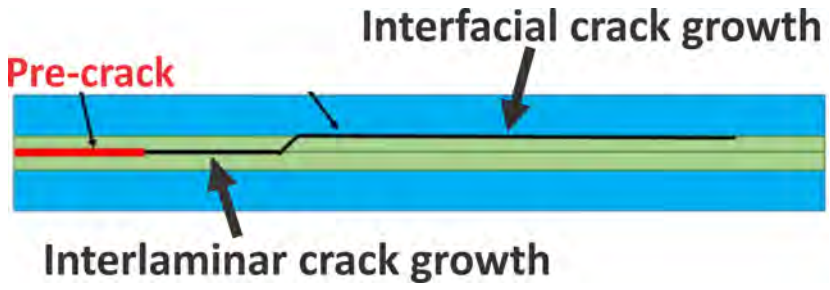


**Figure 2.20:** Crack migration from the interlaminar region (full of veil) to the interfacial region (depleted of veil), reproduced from [127].

### 2.4.4 Impact resistance and tolerance

While interlaminar fracture toughness is widely used for material design and screening purposes, the correlation between $G_c$ and the impact response of interleaved laminates remains unclear. One of the main reasons is the high strain-rate sensitivity of thermoplastics [92, 141]. Masters [142] discussed that the $G_{IC}$ of interleaved laminates correlates poorly with CAI strength, which is supported by the observations of

Nash *et al.* [14, 16]. In contrast, the results of Kuwata *et al.* [124] and Hogg [143] displayed an opposite tendency. In mode-II, Kuwata *et al.* [124] reported a good correlation between $G_{IIC}$ and CAI strength. However, Bull *et al.* [92] evidenced a low correlation between $G_{IIC}$ and projected damage area. Therefore, it is expected that thermoplastic veils provide different toughening mechanisms during mode-I interlaminar fracture toughness than during impact and CAI experiments.

Another source of uncertainty is that interleaving may increase laminate thickness [16, 117, 121, 124, 125, 136, 143, 144] (impact specimens typically incorporate a high number of reinforced interfaces). In this case, baseline and interleaved laminates would have a different bending stiffness, which is less than ideal to isolate the effect that veils have on impact response. To resolve this issue, some authors normalise impact energy to laminate thickness or fibre volume fraction [117, 124, 125, 143, 144].

Tsotsis [13] studied how veil fibre areal weight influences the CAI strength of carbon/epoxy $[45°/0°/90°/-45°]_{3s}$ thick laminates interleaved with thermoplastic veils in all the interfaces. He tested three types of veil (polyamide, elastomer EL and a polyester veils) with three fibre areal weights per system (4.4, 8.48 and 12.73 g/m$^2$). The nominal thickness of the non-interleaved laminate was 4.6 mm while, for interleaved configurations, Tsotsis claimed a maximum thickness increase of 0.3 mm (laminates were manufactured using controlled atmospheric resin infusion). CAI strength improved with enhanced PA and EL veil fibre areal weight (by up to 105% and 53%, respectively). In contrast, CAI strength decreased with increasing content of PE veil (by up to 29%), which the author attributed to the lower adhesion between PE fibres and epoxy. Another interesting observation is that the PA veils localized impact damage to under the impact point, which is in agreement with studies where the toughening agent suppress delamination propagation at the cost of premature fibre failure under the impactor [92, 122, 144] (Fig. 2.21). Finally, after several trials in collaboration with the veil manufacturer, Tsotsis [13] improved further CAI strength by reducing the fibre diameter of the PA veils (which, for a given fibre areal weight, is equivalent to increasing veil mean coverage, Eq. 2.3). The optimized 12.73 g/m$^2$ PA veil system improved CAI strength by 118%.

The results of Nash *et al.* [16] suggest that impact response is not only affected by veil mean coverage, but also by the number of reinforced interfaces. The authors interleaved a $[(45°/-45°)/(0°/90°)]_{2s}$ thick NCF laminate with 1, 3 or 7 PA veils (the fibre areal weight and fibre diameter of the veils was 34 g/m$^2$ and 23 μm). The thickness of the specimens ranged from 4.4 mm for the baseline system to 5.1 mm for the configuration with seven veils (laminates were manufactured by vacuum assisted resin transfer moulding). Impact resistance improved with increasing number of

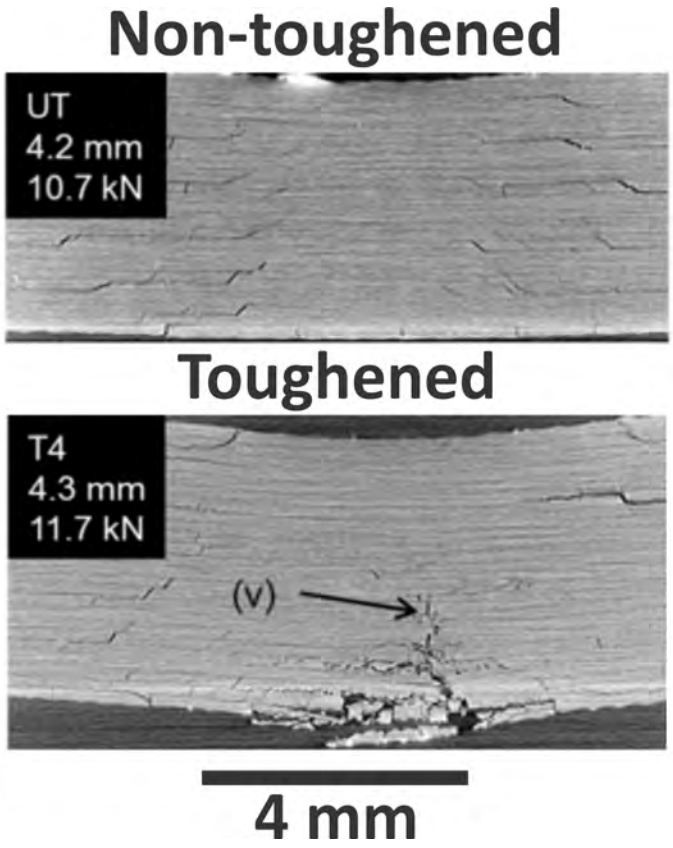


**Figure 2.21:** Impact damage localization caused by toughening thermoplastic particles in the interfaces of a thick carbon/epoxy laminate. "v"indicates the fibre failure, reproduced from [92].

veils (the specimens interleaved with 3 and 7 veils displayed a 16% and 36% lower projected damage area than their non-interleaved counterparts). However, impact tolerance displayed the opposite tendency (the reason for this deterioration remains unclear).

Duarte *et al.* [144] interleaved a $[45°/0°/-45°/90°]_{2s}$ 2 mm thin laminate with polyamide or polyimide (PI) veils in all the interfaces. Both the PA and PI interleaves increased laminate thickness by 13% and 17% (laminates were manufactured in the autoclave) —further details of the veils fibre architecture were not provided. Specimens were impacted at increasing energy levels up to 7 J/mm. Interleaving PA veils increased the damage area and reduced the CAI strength of the non-interleaved system, which the authors attributed to the veil's "open structure" (i.e. the low mean coverage) as well as to the poor adhesion between PA fibres and epoxy. By contrast, interleaving the PI veils did enhance CAI strength by up to 23%. The authors postulated that this is a consequence of the higher shear modulus of the PI fibres delaying fibre buckling during compressive loading. Interestingly, Tsotsis [13] also tested a thermoplastic polyurethane veil under the same hypothesis than Duarte *et al.* [144]. However, the polyurethane veils resulted in a lower CAI strength than their

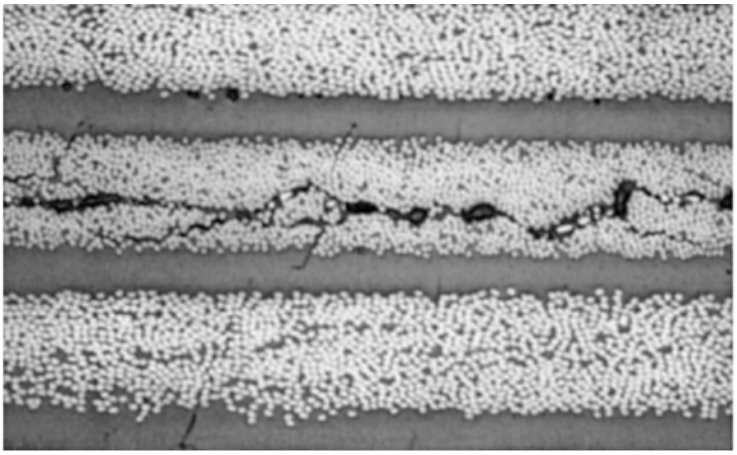

**Figure 2.22:** Intralaminar crack growth displayed by an impact carbon/epoxy specimen interleaved with polyimide veils (ply-thickness was 125 µm), reproduced from [144].

PA counterparts. Finally, a relevant observation made by Duarte *et al.* [144] is that, in the samples interleaved with the PI veils, some of the delaminations propagated inside the plies rather than through the resin interfaces (Fig. 2.22), attributed to the high adhesion between PI fibres and epoxy.

Walker *et al.* [122] used the lightest veils reported for impact applications. They interleaved a $[0°/90°]_5$ 2.4 mm thin laminate with 1.1 and 2.2 g/m$^2$ short-fibre Kevlar and PA veils, respectively. Both interleaved configurations displayed a similar nominal thickness and bending stiffness than the non-interleaved system (where bending stiffness is defined as the elastic region of the impact force-displacement curves). However, interleaving the Kevlar veils deteriorated the baseline's CAI performance [145]. Just recently, Yuan *et al.* [121] improved the impact resistance and CAI strength of a 1.84 mm thin twill weave laminate by interleaving 8 g/m$^2$ veils made of the same short-Kevlar fibres.

In a nutshell:

- interleaving PA veils reduces projected damage area and increases CAI strength,
- the toughening mechanisms are different to the ones reported for mode-I interlaminar fracture toughness testing,
- limited literature suggest that, for relatively low fibre areal weight veils, CAI strength enhances with increasing veil mean coverage.

### 2.4.5 Miscellaneous properties

Beylergil *et al.* [18] own the highest $G_{IC}$ improvement of Tables 2.1-2.2 (231% and 737% for the 17 and 50 g/m$^2$ veils). However, in material science, every en-

hancement has an associated cost, in particular toughness and strength are mutually exclusive [146]. The authors characterised the tensile and compressive properties of a $[0°]_4$ carbon/epoxy laminate interleaved with the 17 or 50 g/m$^2$ veils in all of the interfaces. Both the tensile and compressive moduli decreased with increasing veil fibre areal weight ($E_{11}$ by up to 34%, $E_{22}$ by up to 23.7%, $G_{12}$ by up to 21% and the compressive modulus by up to 13%), and so did the tensile and compressive strength (by up to 41% and 13%). The authors attributed the deterioration of the tensile properties to the higher thickness (and therefore lower fibre volume fraction) of the interleaved laminates. This is in agreement with the tendencies observed by Miller *et al.* [19]. They interleaved a $[0°/90°/90°/0°]_{2s}$ carbon/epoxy laminate with a 15 or 45 g/m$^2$ polyurethane (PU) veil in every second interface. The tensile modulus and strength decreased with increasing content of PU (by up to 40% and 56%), also attributed to the lower fibre volume fraction of the laminates. Besides this, the veils deteriorated the compressive moduli and strength by up to 11% and 56%. Sohn *et al.* [119] and Wong *et al.* [138] also reported that interleaving PA veils (of 18 and 26 g/m$^2$) impairs the tensile and compressive properties of the non-interleaved baseline laminate.

Regarding other mechanical properties, interleaving unidirectional or cross-ply laminates with relatively high fibre areal weight thermoplastic veils also compromises three-point bending modulus [14, 18, 127, 128, 136] (often attributed to the lower fibre volume of the interleaved laminates [14, 18, 136]). In contrast, interleaving unaffects the glass transition temperature [14, 18, 127, 128] and improves the damping ratio (tan $\delta$) [127, 128, 136]. Finally, there is no clear tendency regarding the flexural or interlaminar shear strengths [14, 18, 127, 128, 136, 138].

To conclude this section it is worth noting that non-woven veils are not only used to improve interlaminar fracture toughness or impact response, as they can also enhance ballistic impact resistance [19], reduce delamination induced by pull-off loads [147, 148], improve the adhesion of repair patches [134], etc. Moreover, they can be functionalized (e.g. by loading graphene/graphite particles or silver nano-wires [120, 135]) to improve electrical conductivity.

In a nutshell, interleaving PA veils:

- reduces in-plane and flexural mechanical properties,
- reduces the properties further with increasing veil fibre areal weight.

# Paper A

# 3

## On how matrix cracks induce delamination under out-of-plane shear and the associated in-situ effect

S.M. García-Rodríguez[a], J. Costa[a,*], P. Maimí[a], V. Singery[b], A. Sasikumar[a]

[a]AMADE, Polytechnic School, University of Girona, Av. Universitat de Girona, 4. 17003 Girona, Spain

[b]Chomarat, 39 Avenue de Chabannes, 07160, Le Cheylard, France

Submitted for publication in *Composite Science and Technology*

* Corresponding author

### Overview

Paper A compares the damage sequence evolution of thin $[45°/0°/-45°/90°]_{ns}$ interlaminar shear strength (ILSS) specimens made with standard- ($n = 2$) or thin-ply ($n = 4$) non-crimp fabrics (named $\text{LSTANDARD}_{\text{ILSS}}$ and $\text{LTHIN}_{\text{ILSS}}$, Table 1.2). The aim of this paper is to fulfil the objective 1 in Section 1.2 as well as addressing the corresponding open questions in Table 1.1. The ILSS experiment loads a *short*-beam specimen in three-point bending (*short* signifies of 10 mm x 20 mm width and length [149]). Damage sequence is elucidated by combining interrupted testing with X-ray micro-computed tomography (µCT) inspections. The main advantage of this experiment is the reduced size of the samples, which enables to perform as many incremental tests as necessary to gain insight into the interaction between matrix cracks and delaminations (for further details regarding this open question refer to Table 1.2). The reduced width of the specimens is also an advantage for µCT inspections (the lower the width is, the lower the noise and pixel size may become [150]). Finally, it is worth noting that the ILSS test is normally used to characterize the in-plane shear strength ($\tau_{12}^{ILSS}$) of unidirectional laminates with fibres parallel to the beam axis (where $\tau_{13} = \tau_{12}$ because of laminae orthotropy [151]). However, the specimens containing off-axis plies are subjected to a different stress state, in particular a combination of in-plane and transverse shear ($\tau_{12}$ and $\tau_{23}$) for the $\pm 45°$ plies and pure $\tau_{23}$ for the 90° layers.

**Abstract**

Failure of composite laminates, in load cases where out-of-plane shear prevail, involves shear cracks and delaminations, and yet it is unclear which damage mechanism triggers the other or how it depends on ply-thickness. Combining interrupted interlaminar shear strength tests with X-ray tomography inspections, we compared the damage sequence of $[45°/0°/-45°/90°]_{ns}$ short-beam specimens manufactured with standard- ($n = 2$) or thin-ply ($n = 4$) non-crimp fabrics (fibre areal weights of 134 and 67 gsm per ply). Failure manifested as a load drop in the force-displacement curve. In both materials, the onset of instability was associated to a shear crack tunnelling across the central $90^{\circ}_{2}$ ply-cluster. The intersection of this crack with the ones developing in the adjacent layers induced a delamination which, in turn, activated the load drop. A 3D numerical model predicted that, for the same applied load, the ply-cluster of both laminates would display a similar maximum principal stress distribution. However, the thin-ply samples improved the interlaminar shear strength by 32%, evidencing the so called in-situ effect: the resistance to matrix cracking under out-of-plane shear ($\tau_{23}$ in the local coordinates of the 90° plies) increases when ply-thickness is reduced.

*Keywords*: Thin-ply, B. Matrix cracking, C. Damage mechanics, D. Non-destructive testing

## 3.1 Introduction

Understanding the onset and progression of failure mechanisms at ply level is crucial for robust composite design. The external load required to propagate a matrix crack in a unidirectional ply increases when the layer is embedded in a multidirectional laminate, also known as the *in-situ* effect [20–25, 35, 152–154]. The in-situ strength depends on the orientation of the constraining layers, the ply-location within the laminate and, more importantly, increases with decreased ply-thickness [21, 25]. This is why *thin-ply* laminates enhance certain mechanical properties relative to their standard-ply counterparts [2–4, 40, 54, 55, 60, 63, 64]. Camanho *et al.* [21] proposed an analytical failure criteria based on Fracture Mechanics that calculates the in-situ strength under transverse tension and in-plane shear. Other works assume that the out-of-plane (also called "transverse") shear strength also depends on ply-thickness [23, 38, 77, 155, 156]. However, to the authors' knowledge, experimental studies that evidence the in-situ phenomenon under out-of-plane shear are scarce.

Kalfon-Cohen *et al.* [65] compared the interlaminar shear strength of $[0°/90°/\pm 45°]_{ns}$ standard- ($n = 2$) and thin-ply ($n = 6$) specimens (162 and 54 μm ply-

thickness). The thin-ply laminates increased ILSS strength by 10% relative to the thicker ply counterparts, which is in accordance with the results of Huang *et al.* [52]. Unfortunately, the previous studies lacked insight into the damage sequence, making it difficult to draw conclusions about the mechanisms behind the improvement. We have performed such an investigation using the interlaminar shear strength (ILSS) test. This experiment is widely used to measure interlaminar shear strength because it is much simpler than the alternative shear methods [151, 157–159]. The ILSS test loads *short-beam* specimens in three-point bending, where *short* refers to a relatively low span length-to-thickness ratio. The low aspect ratio maximizes out-of-plane shear and minimizes bending stresses [160]. Away from the loading roll and the side supports, the shear stress varies parabolically from zero at the surfaces to a maximum at the specimen mid-plane [160, 161].

We describe the damage sequence of quasi-isotropic ILSS specimens, identify the damage mode triggering catastrophic failure and explain the associated in-situ effect. We performed a series of interrupted ILSS tests on $[(45°/0°)/(-45°/90°)]_{ns}$ non-crimp fabric (NCF) laminates (fibre areal weights of 134 or 67 gsm per unidirectional ply) followed by *ex-situ* X-ray micro-computed tomography (μCT) inspections. The latter provided ply-by-ply information as to how matrix cracks and delamination evolve with respect to the load events observed in the force-displacement curve. A 3D finite-element model explained some of the μCT observations. In both materials, a matrix crack resulting from a similar $\tau_{23}$ stress distribution initiated unstable failure. In contrast, the thin-ply laminate enhanced the interlaminar shear strength by 32%.

## 3.2 Materials and Methods

### 3.2.1 Materials

We used (0°/45°) and (0°/−45°) non-crimp fabrics made of T700 GC carbon and polyester stitches. They are commercialized by Chomarat under the brand name C-PLY$^{TM}$. The fibre areal weight of the blankets was 268 or 134 gsm (134 and 67 gsm per unidirectional ply). NCFs reduce labour costs because they lay several layers in one-axis, which is ideal for handling plies of reduced thickness [48]. Two types of quasi-isotropic $[(45°/0°)/(-45°/90°)]_{ns}$ laminate were designed by, if necessary, flipping over and/or rotating the fabrics: one with the thin-plies ($n = 4$, $\text{LTHIN}_{\text{ILSS}}$) and other with the standard-plies ($n = 2$, $\text{LSTANDARD}_{\text{ILSS}}$). They were manufactured by resin transfer moulding using HexFlow® RTM6 epoxy resin (for details of the process refer to [162]). The average thickness values of the $\text{LSTANDARD}_{\text{ILSS}}$ and $\text{LTHIN}_{\text{ILSS}}$ tested specimens were 2.15±0.007 and

2.15±0.004 mm (all the samples were cut from the same region of the corresponding panel), where ± means standard deviation. Their average fibre volume fractions were 55.21±0.82% and 54.81±1.97% (five samples per laminate were measured following the standard EN 2564:1998 [163]).

### 3.2.2 Interlaminar shear strength test

Testing was performed using an electromechanical MTS INSIGHT®100 machine with a 10 kN load cell. 10 x 20 mm coupons were subjected to three-point bending in accordance with the standard ASTM D2344/D2344M-16 [164]. The loading roll and side supports were steel cylinders of 6 and 3 mm in diameter. The span length between supports was 8 mm, corresponding to a span length-to-thickness ratio of 4 (a nominal sample thickness of 2 mm was assumed for the calculation). Before the experiment, the edges were carefully polished to remove defects induced during cutting. Samples were loaded at 1 mm/min until a load drop-off of at least 30% developed, considered as the final collapse of the specimen [164]. The interlaminar shear strength ($\sigma^{\mathrm{ILSS}}$) was calculated following classical lamination theory (Equation 3.1):

$$\sigma^{\mathrm{ILSS}} = \frac{3F_{\max}}{4wt} \tag{3.1}$$

where $w$ and $t$ are the width and thickness of the specimen and $F_{\max}$ is the maximum force recorded during the test. Besides this, the residual shear strength was calculated by introducing $F_{\mathrm{residual}}$ (the load-carrying capacity after the drop-off, Figure 3.1) instead of $F_{max}$ in Equation 3.1. Seven $\mathrm{LSTANDARD_{ILSS}}$ and six $\mathrm{LTHIN_{ILSS}}$ coupons were tested until failure. In all the cases, one of the free-edges was recorded with an EOS REBEL t2I/EOS 550D video camera.

An additional experimental campaign was devised to illustrate the sequence of damage mechanisms underlying the catastrophic load drop observed in the force-displacement curve of both material systems (Figure 3.1). The following interrupted tests were performed:

1. testing until a force level where the load-displacement curve presents non-linear growth, e.g. approximately 100 N before the onset of the load drop (point $A_i$ in Figure 3.1, $i = S, T$),
2. testing until a force level immediately preceding the onset of the load drop (point $B_i$ in Figure 3.1, $i = S, T$),
3. testing until a force level immediately after the onset of the load drop, where the slope of the load-displacement curve changes from having a positive to a negative value (point $C_i$ in Figure 3.1, $i = S, T$).

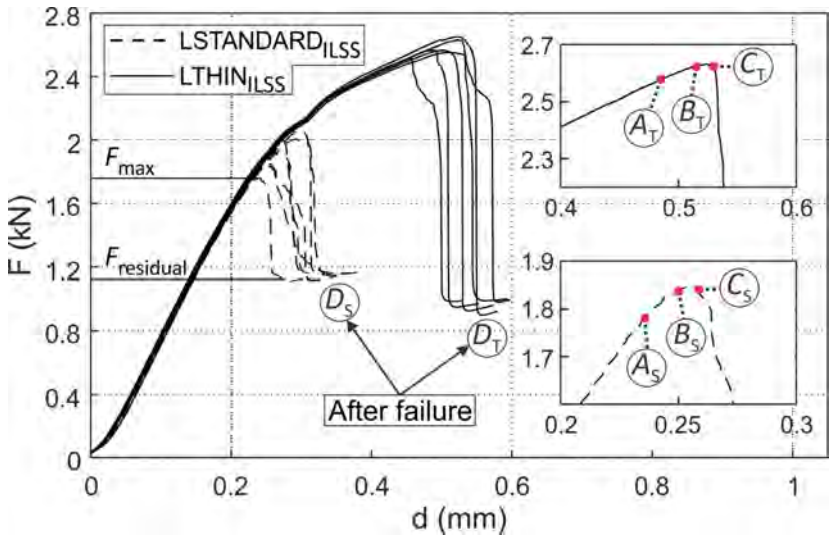


**Figure 3.1:** Load-displacement curves of LSTANDARD$_{ILSS}$ and LTHIN$_{ILSS}$ interlaminar shear strength (ILSS) specimens tested until failure. The zoomed portions of the image illustrate representative load drops developed in each of the materials, where the dots $A_i$, $B_i$ and $C_i$ ($i = S,T$) refer to the force level at which the interrupted tests were arrested.

*Ex-situ* X-ray μCT ascribed the damage mechanisms developed in $A_i$, $B_i$ and $C_i$ ($i = S,T$) specimens to their ply/interface position. To ensure repeatability of the experiments, a minimum of two samples presenting similar damage mechanisms were observed in each of the points ($A_i$, $B_i$ and $C_i$). The loading rate was 1 mm/min, whereas the unloading speed was increased to 50 mm/min to minimize further damage propagation caused by creep. The entire campaign was performed at 23±2 °C and 50±5% humidity in the mechanical testing laboratory of the University of Girona. The laboratory is ISO17025 and NADCAP (non-metallic materials) accredited.

### 3.2.3 X-ray tomography inspection

Each sample subjected to interrupted testing as well as two failed specimens per batch were inspected using μCT (for details about the inspection equipment refer to [162]). In all cases, the inspections were focused on the volume limited by the side supports. The scanning parameters were 55 kV, 80 μA, 1.5 s exposure time and 1400 projections (3 integrations/projection). The pixel size oscillated between approximately 4–5 μm, corresponding to a field of view of 9–11.2 mm. The use of contrast agents was avoided to observe matrix cracks and delaminations regardless of their interconnection. The μCT slices of some specimens were post-processed (damage was segmented from the rest of the specimen) and rendered in 3D following the methodology detailed in a recent study by the authors [165].

### 3.2.4 Numerical model

A fully 3D linear-elastic FEM model was implemented in Abaqus/Implicit to compare the stress distribution in certain key-locations of the standard- and thin-ply samples. The model's geometry, mesh and boundary conditions are depicted in Figure 3.2. The loading nose and bottom supports were simulated because their size is comparable to that of the beam and therefore they affect the stress distribution [160]. The base of the cylinders had all the degrees of freedom constrained except for the vertical displacement of the loading roll. In the laminate, three solid rigid movements were naturally suppressed owing to the contact with the steel noses: the vertical displacement ($u_z$) and the rotation about the $x$- and $y$-axes ($R_x/R_y$). The three remaining ($u_x$, $u_y$ and $R_z$) were constrained by (a) fixing $u_x$ in the line of nodes resulting from the intersection of the horizontal plane at the mid-thickness and the vertical plane at the mid-width of the specimen and (b) fixing $u_y$ in the node at the centre of the rectangular prism (all the former nodes belong to the central $90^\circ_2$ ply-cluster).

Composite plies were modelled using Abaqus-defined C3D8R solid elements with reduced integration [166]. Describing out-of-plane problems with linear elements requires several elements through the thickness of each ply (in particular, six elements

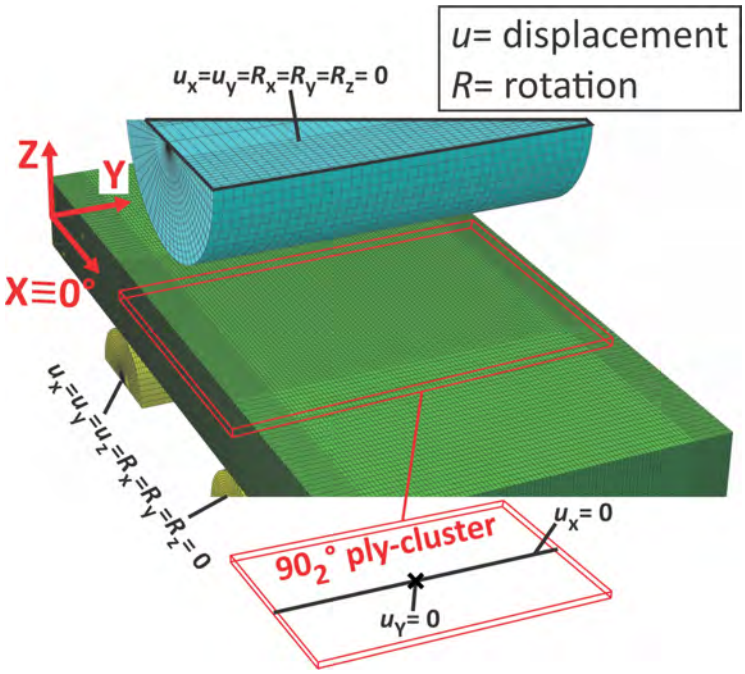


**Figure 3.2:** Numerical model of $\text{LSTANDARD}_{\text{ILSS}}$ and $\text{LTHIN}_{\text{ILSS}}$ ILSS specimens: set-up, mesh and boundary conditions (for visualization purposes, the loading roll has been separated a few millimetres away from the laminate). The only difference between both materials was the number of plies and the number elements included through the thickness of each ply (six and three for the standard- and thin-ply samples).

for $\text{LSTANDARD}_{\text{ILSS}}$ and three for $\text{LTHIN}_{\text{ILSS}}$). The element length was 0.1 mm between the side supports and 0.2 mm outside from this region. The element width was 0.1 mm except for the first millimetre closest to each edge, which was reduced to 0.05 mm in order to capture free-edge effects accurately. This lead to a total of 1.612.800 elements/laminate. The outer volume of the cylinders was modelled with C3D8R solid elements approximately 0.3 mm in maximum size. To avoid mesh distortion, the core was simulated with C3D6 wedge elements. Contact between the cylinders and the composite was simulated using the Abaqus "Hard Contact" algorithm without friction [166].

The elastic properties of the T700/RTM6 plies were taken from Arteiro *et al.* [46] (who characterized 75 g/m$^2$ C-PLY$^{\text{TM}}$ NCF prepregs with an epoxy resin from Aldila). The steel cylinders were isotropic and significantly more rigid than the composite material (elastic modulus of 210 GPa and Poisson's ratio of 0.3). In both laminates, a force-step of 2000 N (approximately the average failure load of $\text{LSTANDARD}_{\text{ILSS}}$, Figure 3.1) was applied in the upper surface of the loading roll.

## 3.3 Results

Figure 3.1 presents the load-displacement curves for the $\text{LSTANDARD}_{\text{ILSS}}$ and $\text{LTHIN}_{\text{ILSS}}$ ILSS specimens tested until failure. The zoomed portions of the figure illustrate representative load drops developed in each of the materials, where the points $A_i$, $B_i$ and $C_i$ ($i = S, T$) stand for the force level at which the tests were stopped for μCT inspection. Both the standard- and thin-ply laminates exhibited qualitatively the same force response: linear load growth followed by a non-linear region and, suddenly, a catastrophic load drop. Despite the similarities, $\text{LTHIN}_{\text{ILSS}}$ displayed a 32% higher interlaminar shear strength (90.19±1.64 versus 68.58±4.20 MPa) and a 20% lower residual shear strength (33.47±1.4 versus 40.29±0.77 MPa) than $\text{LSTANDARD}_{\text{ILSS}}$. In addition to this, the thin-ply samples consistently displayed a load oscillation around 2.2 kN. This was attributed to an undesired movement between the loading roll and the specimen: a μCT inspection of coupons tested until 2.3 kN featured no evidence of damage.

Figure 3.3 depicts the *post-mortem* damage scenario developed in the $\text{LSTANDARD}_{\text{ILSS}}$ and $\text{LTHIN}_{\text{ILSS}}$ ILSS specimens as recorded at one of the free-edges. In all cases, failure was confined to between the loading roll and one of the side supports, in particular a few millimetres away from the loading axis where high compressive stresses occur. Both materials presented intra- (45° matrix cracks) and inter-laminar (delamination) damage, whereas the thin-ply laminate exhibited more delaminated interfaces than the standard-ply did (seven versus three).

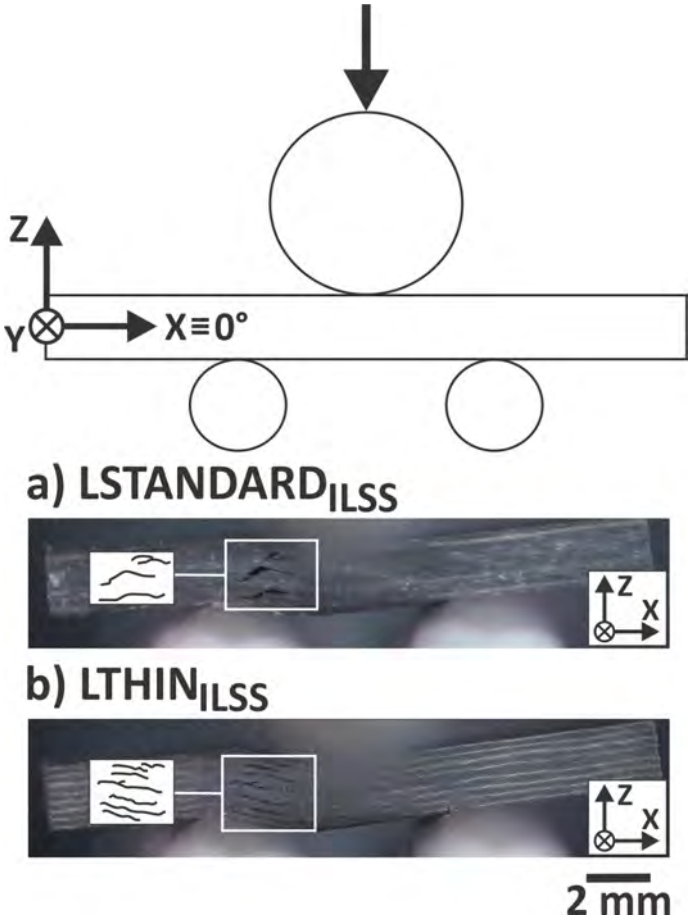


**Figure 3.3:** Failure scenario of LSTANDARD$_{ILSS}$ and LTHIN$_{ILSS}$ ILSS specimens as recorded at one of the free-edges.

Figure 3.4 illustrates the failure mechanisms developed in LSTANDARD$_{ILSS}$ as captured via μCT inspection of ($B_S$-$C_S$) the interrupted tests and ($D_S$) the specimens tested until failure. Samples loaded until $A_S$ (the non-linear region of the load-displacement curve, Figure 3.1) exhibited no evidence of damage and therefore were not included in the figure. Samples loaded until $B_S$ (the force level just before the onset of the load drop) featured a 45° matrix crack ("shear crack" [5]) tunnelling from one of the free-edges to a few millimetres inside the width of the central $90^{\circ}_2$ ply-cluster (the 45° orientation was preserved through the entire length- of the crack). In $C_S$ (the force level immediately after the onset of the load drop), damage propagated in the $-45°/90^{\circ}_2/-45°$ and $45°/90°/-45°$ ply-groups at the central and bottom parts of the laminate (μCT cross-section of Figure 3.4$C_S$). Both regions displayed a similar scenario: (1) one shear crack in the 90° ply (or $90^{\circ}_2$ ply-cluster), (2) multiple shear cracks in the adjacent ±45° layers and (3) one delamination in every interface between off-axis plies (the $\pm 45°/90°$ and $90°/-45°$ interfaces; the coloured images of Figure 3.4$C_S$ depict a top view of representative matrix cracks and delaminations). On the other hand, only the damage located in the central part of the laminate propagated across the entire width of the sample (e.g. the matrix crack

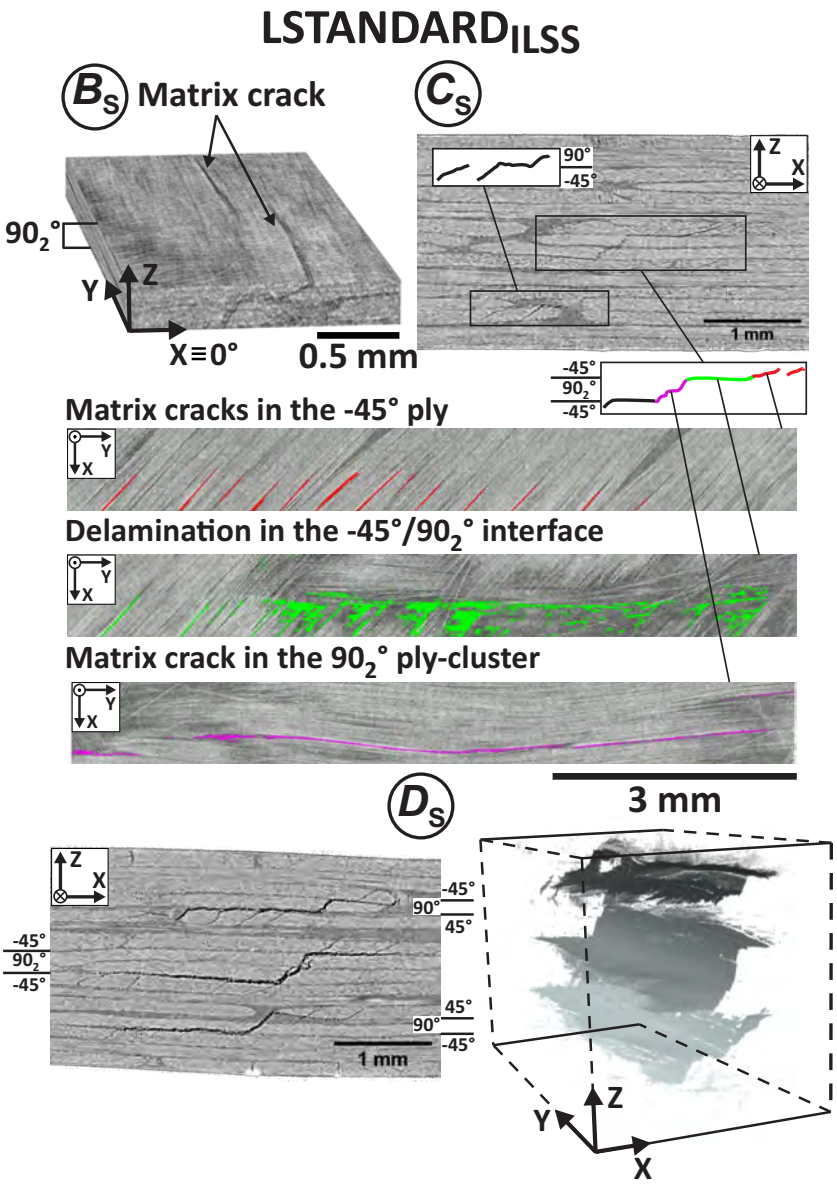


**Figure 3.4:** X-ray micro-computed tomography (μCT) images representing the damage scenario of LSTANDARD$_{ILSS}$ ILSS specimens tested until $B_S$) a force level immediately preceding the onset of the load drop, $C_S$) a force level just after the onset of the load drop and $D_S$) failure. (For interpretation of the references to colour in this figure, the reader is referred to the web version of this article.)

in the bottommost 90° layer spanned three quarters of the total width). Inspection of failed specimens showed matrix cracking in every off-axis layer (Figure 3.4$D_S$); particularly, one shear crack in the 90° plies and multiple shear cracks in the ±45° layers. Besides this, one delamination developed in every interface between off-axis plies.

The thin-ply coupons loaded until $B_T$ also featured a shear crack tunnelling from one of the free-edges of the $90^{\circ}_2$ ply-cluster (Figure 3.5$B_T$). In $C_T$, damage concentrated in the $-45°/90^{\circ}_2/-45°$ off-axis group at the mid-section of the laminate, where

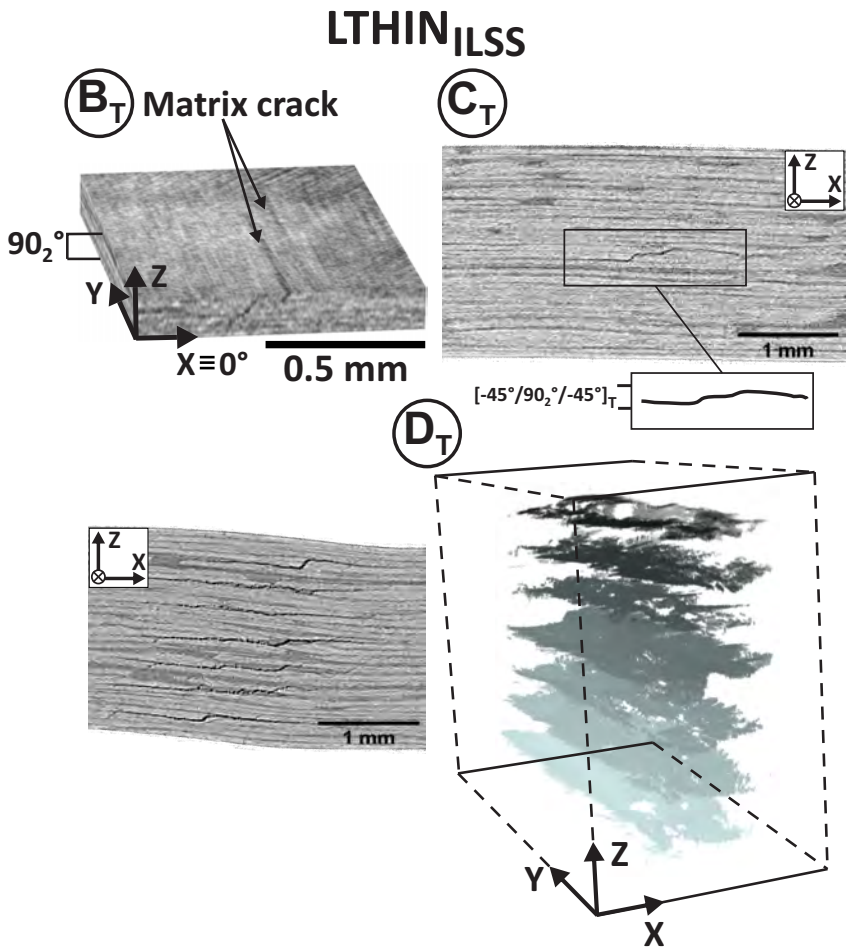


**Figure 3.5:** µCT images representing the damage scenario of LTHIN$_{ILSS}$ ILSS specimens tested until $B_T$) a force level immediately preceding the onset of the load drop, $C_T$) a force level just after the onset of the load drop and $D_T$) failure.

we observed qualitatively the same damage mechanisms as in LSTANDARD$_{ILSS}$. After failure (Figure 3.5$D_T$), matrix cracking extended to every off-axis layer (one shear crack in the 90° plies and multiple shear cracks in the ±45° layers), and one delamination developed in every interface between off-axis plies. Finally, it is worth noting that fibre crushing developed underneath the loading roll of the LSTANDARD$_{ILSS}$ and LTHIN$_{ILSS}$ specimens loaded until $C_i$ and $D_i$ ($i = S, T$), i.e. once shear failure had already initiated. This is attributed to the compressive stress concentration induced by the loading device.

Matrix cracks initiate in planes perpendicular to the maximum principal stress direction [167]. Figure 3.6 presents the maximum principal stress distribution in certain key-locations of the $90^{\circ}_2$ ply-cluster of LSTANDARD$_{ILSS}$ and LTHIN$_{ILSS}$ (the ply where the first matrix crack developed, Figures 3.4$B_S$ and 3.5$B_T$). The load applied was 2000 N, approximately the average failure load of the system with thicker plies (Figure 3.1). The maximum principal stress of both laminates took an orientation of −45° relative to the $x$-$z$ coordinate system, presenting a maximum

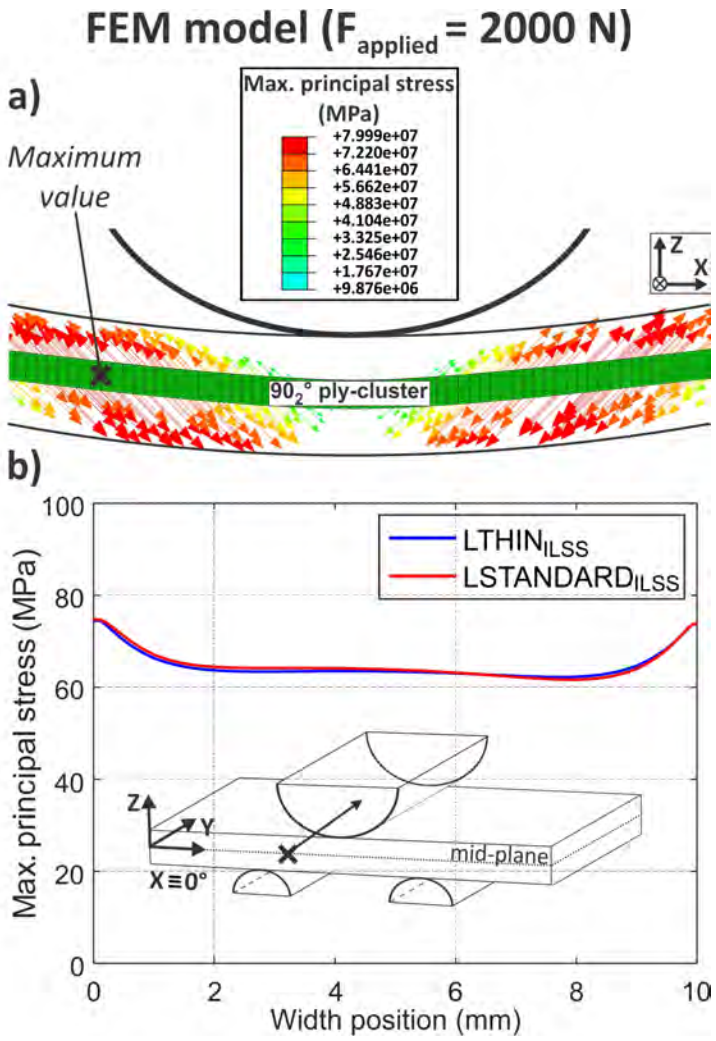


**Figure 3.6:** Maximum principal stress distribution in certain key locations of the central $90_2^\circ$ ply-cluster of $\text{LSTANDARD}_{\text{ILSS}}$ and $\text{LTHIN}_{\text{ILSS}}$ a) at the free-edge b) through-the-width distribution in the $x$-coordinate with maximum stress. (For interpretation of the references to colour in this figure, the reader is referred to the web version of this article.)

value at the free-edge and 2.3 mm away from the loading axis (Figure 3.6a). At this point, both materials displayed a similar stress distribution through-the-width of the sample (Figure 3.6b). (Note that the stress distribution was diagonally symmetric with respect to the $y$-$z$ plane at the mid-length of the beam). Finally, the stress decayed rapidly with increasing distance from the edges, attributed to the so-called "free-edge effect" [60, 62, 168] (Figure 3.6b).

## 3.4 Discussion

The sequence of failure events developed in $\text{LSTANDARD}_{\text{ILSS}}$ and $\text{LTHIN}_{\text{ILSS}}$ displayed common qualitative trends. First, a shear crack started to tunnel from one of the free-edges of the central $90_2^\circ$ ply-cluster (Figures 3.4-3.5$B_i$). The intersection

of this crack with multiple shear cracks in the adjacent $-45°$ layers, induced delamination in the corresponding $-45°/90°_2$ and $90°_2/-45°$ interfaces (Figures 3.4-3.5$C_i$). Eventually, the stress redistribution in the central part of the laminate extended the damage through the thickness of the samples. The same damage scenario developed in all the off-axis groups (i.e. the $\pm 45°/90°/\pm 45°$ ply-groups): matrix cracking in the $90°$ and $\pm 45°$ layers accompanied by one delamination in the interfaces between off-axis plies (Figure 3.4-3.5$D_i$). Obviously, the difference was that $\text{LTHIN}_{\text{ILSS}}$ presented a higher number of damaged groups than $\text{LSTANDARD}_{\text{ILSS}}$ (seven versus three).

Despite the symmetry of the maximum principal stress distribution, damage was confined to between the loading roll and one of the bottom supports (Figure 3.3). This is because failure comes instantaneously as the first shear crack develops in the weakest side of the specimen (materials are not perfectly homogeneous).

The μCT inspections provided understanding into the failure events underlying the force response of $\text{LSTANDARD}_{\text{ILSS}}$ and $\text{LTHIN}_{\text{ILSS}}$. The specimens loaded until point $A_i$ (the non-linear region of the force-displacement curve, Figure 3.1) evidenced no sign of damage. Therefore, the non-linearity is attributed to both matrix yielding and fibre rotations [169]. The coupons loaded until point $B_i$ (the force level preceding the onset of the load drop) displayed a shear crack tunneling across the width of the $90°_2$ ply-cluster. The intersection of this crack with those developing in the adjacent layers induced delamination which, in turn, penalized the load-carrying capacity (point $C_i$ in Figures 3.1 and 3.4-3.5). More than inducing the initial delamination, the shear crack triggered an instantaneous failure (refer to the transition from the points $B_i$ to $D_i$ in Figures 3.1 and 3.4-3.5). That is, this shear crack controls the interlaminar shear strength of the samples.

The numerical calculations demonstrated that, for the same applied load, $\text{LSTANDARD}_{\text{ILSS}}$ and $\text{LTHIN}_{\text{ILSS}}$ exhibited nearly the same maximum principal stress distribution across the width of the $90°_2$ ply-cluster (Figure 3.6b). However, the thin-ply batch improved the interlaminar shear strength by 32% compared to the standard-ply baseline (Figure 3.1). This means that $\text{LTHIN}_{\text{ILSS}}$ coupons delayed the propagation of the initial crack tunnelling across the central $90°$ ply-cluster. In other words, decreasing the thickness of the $90°$ layers improves its resistance to matrix cracking under out-of-plane shear ($\tau_{23}$ in the coordinate system of the $90°$ plies), attributed to the in-situ effect [20–22, 25]. Recent micromechanical models explain that, whereas fibre-matrix debonding occur at the same applied strain in the standard- and thin-plies, the thinner plies delay the onset of crack propagation because the strong confinement exerted by the neighbouring layers restrains the coalesence of those debonding events into matrix cracks [23, 24, 152, 154, 170]

The improvement of interlaminar shear strength in the thin-ply laminate is quantitatively consistent with existing 3D failure criteria [38]. The in-situ out-of-plane shear strength $S_T^{is}$ is assumed to be proportional to the in-situ longitudinal shear strength $S_L^{is}$ with a constant factor that depends on the fracture angle and a friction coefficient [38]. Assuming a linear shear stress-strain curve, $S_L^{is}$ is inversely proportional to the square root of the thickness of the ply [21]. Considering the interlaminar shear strength of $\text{LSTANDARD}_{\text{ILSS}}$ (68.58 MPa) and the ply-thickness values of $\text{LSTANDARD}_{\text{ILSS}}$ and $\text{LTHIN}_{\text{ILSS}}$ (134 and 67 μm), the theoretical strength of $\text{LTHIN}_{\text{ILSS}}$ is 96.99 MPa, which is only 7% higher than the measured value (90.19 MPa) and, given the scatter, compliant with the experimental results. Olsson R. [77] proposed that the out-of-plane shear strength should also be inversely proportional to the square root of ply-thickness.

Provided that out-of-plane shear stresses prevail, the fracture angle of the first shear crack (perpendicular to the principal stresses) indicates that the in-situ transverse shear strength $S_T^{is}$ is higher than the in-situ transverse tensile strength $Y_T^{is}$ [38].

Finally, it is worth noting that, if the specimens were unidirectional, out-of-plane shear strength would be independent of ply-thickness (the in-situ effect only applies for multidirectional laminates, plus failure would be governed by $\tau_{13}$ stresses where there is no influence of the in-situ effect) [3, 77].

The observation of shear cracks inducing delamination during ILSS experiments can be generalized to other loading scenarios where out-of-plane stresses govern the damage evolution such us, for example, the unfolding test. The latter subjects a curved laminate to four-point bending. Failure of unidirectional laminates is typically attributed to delamination caused by $\sigma_{33}$ stresses, a case in which the strength is independent of the laminate thickness [171]. However, when the stacking sequence includes off-axis plies, analytical models fail to explain why and how the strength may vary with the thickness of the sample [172]. González-Cantero *et al.* [172] argued that damage starts as an intralaminar crack that propagates to delamination and causes instantaneous failure (they observed 45° cracks by taking a picture of the free-edge of failed specimens). Our observations in Figures 3.1 and Figures 3.4-3.5 sustain their hypothesis.

The same concept applies to out-of-plane loading cases where shear cracks and delamination initiate away from the free-edges (e.g. low-velocity impact and quasi-static indentation). Abisset *et al.* and Sun *et al.* [96, 173] studied the quasi-static indentation (QSI) response of carbon/epoxy $[45°/0°/90°/-45°]_{2s}$ two-mm thick samples (50 x 75 mm in-plane dimensions). Just after the onset of the load drop, they observed a matrix crack in the central $-45_2^{\circ}$ ply-cluster linking up to a delamination

in the adjacent $90°/-45°$ and $-45°/90°$ interfaces. This is in accordance with the damage scenario observed in $\text{LSTANDARD}_{\text{ILSS}}$ and $\text{LTHIN}_{\text{ILSS}}$ (i.e. one matrix crack in the central $90^{\circ}_{2}$ ply-cluster concatenating delamination in each of the adjacent interfaces, Figures 3.4-3.5C). Therefore, it is believed that the shear crack induced the delamination and the delamination triggered the drop-off.

## 3.5 Conclusions

We compared the damage sequence and interlaminar shear strength of $[45°/0°/-45°/90°]_{ns}$ short-beam specimens manufactured with standard- ($n = 2$) or thin-ply ($n = 4$) non-crimp fabrics (fibre areal weights of 134 and 67 gsm per ply). Damage initiation and growth was detailed by performing interrupted ILSS tests followed by *ex-situ* X-ray micro-computed tomography inspections. A 3D finite-element model compared the stress distribution in certain key locations of the standard- and thin-ply systems.

Failure manifested as a load drop in the force-displacement curve. The damage sequence of both materials exhibited common qualitative trends. A few newtons before the drop-off, a 45° shear crack tunnelled across from one of the free-edges of the central $90^{\circ}_{2}$ ply-cluster. The intersection of this crack with multiple shear cracks in the adjacent $-45°$ layers induced delamination which, in turn, activated the load drop. Eventually, the stress redistribution extended the damage through the thickness of the coupons. Based on the observations, it is concluded that (a) the shear crack tunnelling across the $90^{\circ}_{2}$ ply-cluster controls the interlaminar shear strength of the specimens (b) the intersection of cracks with dissimilar orientation induces delamination and (c) it is the delamination that penalizes the load-carrying capacity.

Matrix cracks initiate in planes perpendicular to the maximum principal stress. Despite both laminates presenting a similar maximum principal stress distribution in the $90^{\circ}_{2}$ ply-cluster, the catastrophic crack initiated at 32% higher load in the thin-ply laminate, in very good agreement with existing failure criteria accounting for in-situ effects. In other words, our findings provide the first unambiguous experimental evidence of the in-situ phenomenon under out-of-plane shear: decreasing ply-thickness increases the resistance to matrix cracking under $\tau_{23}$ stress.

# Paper B

# 4

## A 3D tomographic investigation to elucidate the low-velocity impact resistance, tolerance and damage sequence of thin non-crimp fabric laminates: effect of ply-thickness

S.M. García-Rodríguez[a], J. Costa[a,*], A. Bardera[b], V. Singery[c], D. Trias[a]

[a]AMADE, Polytechnic School, University of Girona, Av. Universitat de Girona, 4. 17003 Girona, Spain

[b]Graphics and Imaging Laboratory, University of Girona, Av. Universitat de Girona, 4. 17003 Girona, Spain

[c]Chomarat, 39 Avenue de Chabannes, 07160, Le Cheylard, France

Published in *Composites Part A: Applied Science and Manufacturing* 113 53-65 (2018). doi: https://doi.org/10.1016/j.compositesa.2018.07.013

* Corresponding author

**Overview**

Paper B compares the impact response of thin $[45°/0°/-45°/90°]_{ns}$ laminates made with standard- ($n = 2$) or thin-ply ($n = 4$) non-crimp fabrics (named $\text{LSTANDARD}_{\text{LVI}}$ and $\text{LTHIN}_{\text{LVI}}$, Table 1.2). The aim of this paper is to fulfil the objective 2 in Section 1.2 as well as addressing the corresponding open question in Table 1.1. Impact resistance and tolerance are characterized with the drop-weight impact and compression after impact experiments, while damage sequence is elucidated by combining QSI testing with X-ray micro-computed tomography inspections. The pristine compressive strength of the standard- and thin-ply laminates is also characterized for reference purposes (the compressive specimens being named $\text{LSTANDARD}_{\text{IP}}$ and $\text{LTHIN}_{\text{IP}}$, Table 1.2). To the author's knowledge, this is the first study that provides comprehensive insight into the impact resistance and tolerance of thin laminates made with thin-plies.

**Abstract**

While thin-plies delay the onset of matrix cracking and improve certain in-plane mechanical properties, the effect they have on the out-of-plane response remains unclear. We compared the impact resistance, tolerance and sequence of failure events of thin laminates manufactured with thin- or standard-ply non-crimp fabrics (fibre areal weight of 67 and 134 gsm per ply). Damage initiation and propagation was detailed using (a) quasi-static indentation and impact tests at incremental energy levels and (b) X-ray tomography. The analysis revealed the damage mechanisms underlying the observed load drops in the force-displacement curves. In the indented specimens, the 3D post-process ascribed matrix cracks and delaminations to their corresponding plies/interfaces. Standard-ply samples develop more extended delaminations and delay fibre failure, improving the load-carrying capacity and increasing compression after impact (CAI) strength by 27% for impact at 14 J.

*Keywords*: Thin-ply, B. Impact behaviour, C. Damage mechanics, D. CT analysis

## 4.1 Introduction

Impact damage is a major concern in composite laminates as it may impair the mechanical properties of components and is difficult to detect. In service, low energy strikes may generate matrix cracks and delaminations that deteriorate structural integrity [76, 88, 89]. In an attempt to reduce weight and costs, the airline industry aims to manufacture increasingly thinner fuselage and wing skins using out-of-autoclave methods which, in turn, accentuate impact susceptibility [10].

Thin-plies are attracting growing interest as they delay matrix cracking and associated delamination, as well as increase certain in-plane mechanical properties [2, 3, 54, 60, 174, 175]. Their main advantage comes from the in-situ strength [20, 24, 152], however, confining a higher number of plies within the same thickness may also increase the stiffness because of pure structural effects [176]. During impact, damage tolerance may be improved in the thin-plies (Table 4.1).

Yokozeki *et al.* [98] examined the out-of-plane damage sequence of carbon/toughened epoxy $[45°/0°/-45°/90°]_{ns}$ laminates with 2.2 mm nominal thickness. They considered ply-thicknesses of 75 µm (thin, $n = 4$) and 145 µm (standard, $n = 2$). The thin-ply layup presented reduced delamination propagation and premature fibre failure when compared to its standard-ply counterpart. Wagih *et al.* [99] performed quasi-static indentation tests at incremental deflection levels in $[((45°/-45°)/(0°/90°))_n]_s$ plain weave fabric laminates with 4.5 mm nominal

**Table 4.1:** Impact damage resistance and tolerance of carbon/epoxy prepreg thin-ply layups compared to their standard-ply counterparts.

| Reference | Stacking sequence | Ply thickness (µm) | | Laminate thickness (mm) | $\frac{Energy}{thickness}$ (J/mm) | Damage area | $\sigma_{CAI}$ |
|---|---|---|---|---|---|---|---|
| | | thin | standard | | | thin vs. standard | thin vs. standard |
| Saito *et al.* [113] | $[45°/0°/-45°/90°]_{ns}$ | 38<br>$n=12$ | 147<br>$n=3$ | 3.6 | 0.75 | thin>standard (∼30%) | thin>standard (∼23%) |
| Yokozeki *et al.* [54] | $[45°/0°/-45°/90°]_{ns}$ | 70<br>$n=8$ | 140<br>$n=4$ | 4.3 - 4.4 | 6.7 | Similar | thin>standard (∼8%) |
| Yokozeki *et al.* [98] | $[45°/0°/-45°/90°]_{ns}$ | 70<br>$n=4$ | 140<br>$n=2$ | 2.2 | Indentation up to 6mm deflection | Similar | Not considered |
| Sihn *et al.* [2] | Not specified | 40<br>– | 200<br>– | Not specified | Not specified | Similar | Not considered |
| Amacher *et al.* [3] | $[0°/45°/-45°/90°]_{ns}$ | 30<br>$n=10$ | 300<br>$n=1$ | 2.4 | 4.79<br>7.58 | thin>standard (∼50%)<br>thin>standard (∼100%) | Not considered |
| Amacher *et al.* [3] | $[0°/45°/-45°/90°]_{ns}$ | 100<br>$n=3$ | 300<br>$n=1$ | 2.4 | 4.79<br>7.58 | thin>standard (∼50%)<br>thin>standard (∼300%) | Not considered |

thickness. They observed that decreasing the yarn thickness from 80 µm (thin, $n = 7$) to 40 µm (very thin, $n = 14$) also resulted in premature fibre breakage. In both cases, the characterization was limited to 2D inspection and damage tolerance was not assessed.

The objective of this investigation is to (a) understand the impact failure mechanisms and damage sequence of thin carbon/epoxy laminates manufactured with thin- or standard-ply non-crimp fabrics (NCFs) and (b) justify their damage resistance and tolerance based on the observations in (a). We considered "thin" laminates (i.e. approximately 2.2 mm thick, thinner than those recommended by the standard ASTM D7137 [93]) to comply with the demands of the aircraft industry. We devised a low-velocity impact, quasi-static indentation (QSI), standard compression and compression after impact (CAI) test campaign, where damage induced by impact and QSI was inspected using ultrasonic C-scan and X-ray micro-computed tomography (µCT). The latter provided ply-by-ply information as to how matrix cracks, delamination and fibre breakage evolve during out-of-plane events.

## 4.2 Materials and Methods

### 4.2.1 Materials

We used Chomarat's T700 GC carbon bi-axial NCFs, commercially known as C-PLY$^{TM}$. In particular, (0°/45°) and (0°/−45°) blankets of 134 and 268 g/m$^2$ fibre areal weight were considered, corresponding to a fibre areal weight of 67 and 134 gsm per unidirectional ply. NCFs reduce labour costs because they allow several layers to be laid in one-axis, which is ideal for handling plies of reduced thickness [48]. Two types of quasi-isotropic $[(45°/0°)/(-45°/90°)]_{ns}$ layups were designed by, if necessary, flipping over and/or rotating the fabrics: one with the thinner plies ($n = 4$, $\text{LTHIN}_{\text{LVI}}$ and $\text{LTHIN}_{\text{IP}}$), and the other with the thicker plies ($n = 2$, $\text{LSTANDARD}_{\text{LVI}}$ and $\text{LSTANDARD}_{\text{IP}}$). They were manufactured by resin transfer moulding using HexFlow® RTM6 epoxy resin (for details of the process refer to a recent study by the authors [162]). The average thickness values of the thin- and standard-ply tested specimens were 2.29±0.16 and 2.17±0.05 mm, where ± means standard deviation. Their average fibre volume fractions were 54.81±1.97 and 55.21±0.82%, respectively (five samples per laminate were measured following the standard EN 2564:1998 [163]; for the same type of material, specimens with a higher thickness presented the lowest fibre volume fraction values).

### 4.2.2 Experimental tests

Impact tests were carried out in a CEAST Fractovis Plus 7536 drop-weight tower with a 16 mm diameter hemispherical indenter. 100 x 150 mm specimens were positioned over a rectangular cut-out and held in place using four rubber-tipped clamps. For further insight into the impact set-up refer to González *et al.* [88]. The data provided by the drop-weight tower were the impactor force (the latter was instrumented with a load cell) and velocity just before the impact (measured with an optical sensor). This data was used to integrate the displacement and velocity of the impactor during the test, as well as the energy absorbed by the coupons as a function of time [76]. The energy dissipated by each sample was computed by subtracting the energy returned to the impactor (i.e. the elastic energy) to the maximum energy (in all cases within $\pm 0.2$ J of the target energy). The sampling rate was 1000 kHz. QSI experiments utilised the same base plate, indenter geometry and clamping devices in order to achieve boundary conditions comparable to those of the impact test (the purpose was to imitate the chronology of damage events taking place during impact [85, 92, 95, 96]). QSI was conducted in an electromechanical MTS INSIGHT®100 testing machine with a 100 kN load cell. The cross-head displacement rate was 0.5 mm/min to avoid dynamic effects [95, 96]. The energy applied to the system was calculated by integrating the area under the load-displacement curve.

Compression tests were performed using an electromechanical MTS INSIGHT®100 testing machine with a 100 kN load cell. The aim was to quantify the pristine compressive strength of $\text{LTHIN}_{\text{IP}}$ and $\text{LSTANDARD}_{\text{IP}}$. 12.7 x 140 mm specimens were tested using a compression fixture in accordance with the standard ASTM D6641/D6641M-14 [177]. The cross-head displacement rate was 1.3 mm/min. The ultimate compression strength was calculated by dividing the maximum load to failure by the specimen's cross-section measured at the gage region.

CAI tests were conducted using an electromechanical MTS INSIGHT®300 testing machine with a 300 kN load cell. A non-standard CAI device adopted from Remacha *et al.* [112] was used. This fixture enabled the testing of laminates thinner than those recommended by the standard ASTM D7137/D7137M [93], which would otherwise fail by global buckling [112, 178, 179]. The device consisted of two antibuckling plates with three vertical ribs that stabilize the specimen during the test. The central rib includes a 52x42 mm central cut-out to avoid any interference with the damaged zone. The cross-head displacement rate was 0.5 mm/min.

Impact energies were selected to ensure that a considerable amount of damage (i.e. observation of fibre failure in the non-impacted surface of the specimens) developed in $\text{LTHIN}_{\text{LVI}}$ (10 J) and $\text{LSTANDARD}_{\text{LVI}}$ (14 J). The QSI experimental campaign

was divided into four deflection levels, where deflection means the displacement of the indenter during the test [95, 96]. The higher deflection (d= 5.24 mm) corresponds to the load drop developed in $LTHIN_{LVI}$. The smaller deflections (d= 3 mm, d= 4 mm and d= 4.4 mm) were chosen based on the onset of acoustic emissions heard during the testing of both types of laminate. These deflections resulted in applied energies of approximately 2.5, 4, 5.5 and 8 J. Three samples of each laminate were impacted at 10 J, and at least four at 14 J, all of which were eventually tested under CAI. In addition, one specimen per layup was indented to each of the deflections above. The combination of QSI and impact experiments provided information about damage resistance and the sequence of failure events, while the CAI tests gave insight into damage tolerance. Finally, six $LTHIN_{IP}$ and seven $LSTANDARD_{IP}$ samples were tested under pure compression. The entire campaign was performed at 23±2 °C and 50±5% humidity in the mechanical testing laboratory at the University of Girona. The laboratory is ISO17025 and NADCAP (non-metallic materials) accredited.

### 4.2.3 Damage inspection and 3D post-process

All the indented and impacted coupons were inspected by C-scan ultrasonic technique using an OLYMPUS OMNI MX system automatized with a robotic arm. In addition, every indented specimen and representative impacted samples were inspected by µCT (for details about both the C-scan and µCT inspection equipments refer to [162]). During the tomography scans, the use of contrast agents was avoided to observe matrix cracks and delaminations regardless of their interconnection.

In the indented specimens, the entire damage scenario was observed as decided from a previous C-scan. Prior to inspection, the samples were cut into approximately 10 mm width coupons to minimize undesired X-ray absorption perpendicular to the axis of rotation [180]. The scanning parameters were 55 kV, 80 µA, 1.5 s exposure time, 1400 projections (3 integrations/projection) and 5–5.5 µm pixel size, corresponding to a field of view of 11.2–12.32 mm. In the impacted specimens, only a representative region centred at the impact site was captured. The inspection parameters were 70 kV, 75 µA, 2.5 s exposure time, 1400 projections (3 integrations/projection) and 6.5 or 10 µm pixel size for 10 and 14 J impact energy (fields of view of 14.6 and 22.4 mm, respectively).

To provide a comprehensive 3D analysis of the damage scenario developed within indented specimens, the µCT slices were post-processed using Matlab:

1. each sample was sliced into one-pixel-thick planes perpendicular to the thickness direction. A 2D median filter was applied to each of the planes. The objective was to remove image noise while preventing information losses at the planes where delamination occurs (i.e. no pixels were filtered through-the-

thickness),

2. to separate the specimen from the background, a mask was obtained using greylevel thresholding and morphological operators,

3. damage was segmented by setting a user-defined grey value threshold (because of their narrow crack opening, the smaller cracks developed in the thin-ply samples were difficult to segment or post-process),

4. after the segmentation process, the μCT slices presenting image artifacts (i.e. zones with excessive noise or ring artifacts) were cleaned using morphological operators. Then, a more refined manual cleaning was performed slice-by-slice using an in-house routine,

5. each segmented pixel (corresponding to damage developed in the sample) was labelled according to its distance from the indented surface. The purpose was to ascribe the damage to particular plies or interfaces. The former coordinate system was selected to take into account the specimen's curvature after indentation [181], i.e. pixels lying in the same ply/interface have approximately the same scalar value,

6. images were rendered in 3D using the software Starviewer [182]. Matrix cracks were coloured in black, and delaminations coloured based on their interface position (Starviewer software allows pixel scalar values to be coloured using a transfer function).

## 4.3 Results

Figures 4.1a-b present the load-displacement curves of representative $\text{LTHIN}_{\text{LVI}}$ and $\text{LSTANDARD}_{\text{LVI}}$ specimens impacted at 10 and 14 J. In the thin-ply laminate, the load grew non-linearly until a local maximum ($F_i$), followed by a load drop and a decrease in the bending stiffness. In contrast, the $\text{LSTANDARD}_{\text{LVI}}$ samples only presented such a local maximum for impact at 14 J, which occurred at a higher force than in $\text{LTHIN}_{\text{LVI}}$. Table 4.2 summarizes the value of $F_i$ and the magnitude of the associated load drop for each material system/impact energy.

Figures 4.1c-d compare the QSI and impact load-displacement curves of each layup. In both systems, the curve of the coupon indented at d= 5.24 mm overlapped the ones subjected to lower deflections except for the standard-ply sample indented at d= 3 mm, which came from a different panel (with a slightly different volume fraction) than the rest of the specimens from the same batch. In the $\text{LTHIN}_{\text{LVI}}$ sample indented at the highest deflection (applied energy of approximately 8 J), a local maximum force preceded several consecutive load-drops (see $F_q$ at approximately 3.3 kN). In

**Table 4.2:** Value of the local force maximum ($F_i$) and magnitude of the associated load drop observed in the load-displacement curves of $\text{LTHIN}_{\text{LVI}}$ and $\text{LSTANDARD}_{\text{LVI}}$ specimens impacted at 10 and 14 J, $\pm$ refers to the standard deviation between experiments.

| Material type | Impact at 10 J | | Impact at 14 J | |
|---|---|---|---|---|
| | $F_i$ (kN) | Load drop (%) | $F_i$ (kN) | Load drop (%) |
| $\text{LTHIN}_{\text{LVI}}$ | 3.24±0.02 | 19.75±0.55 | 3.41±0.25 | 22.80±1.40 |
| $\text{LSTANDARD}_{\text{LVI}}$ | None | None | 4.83±0.28 | 20.63±8.21 |

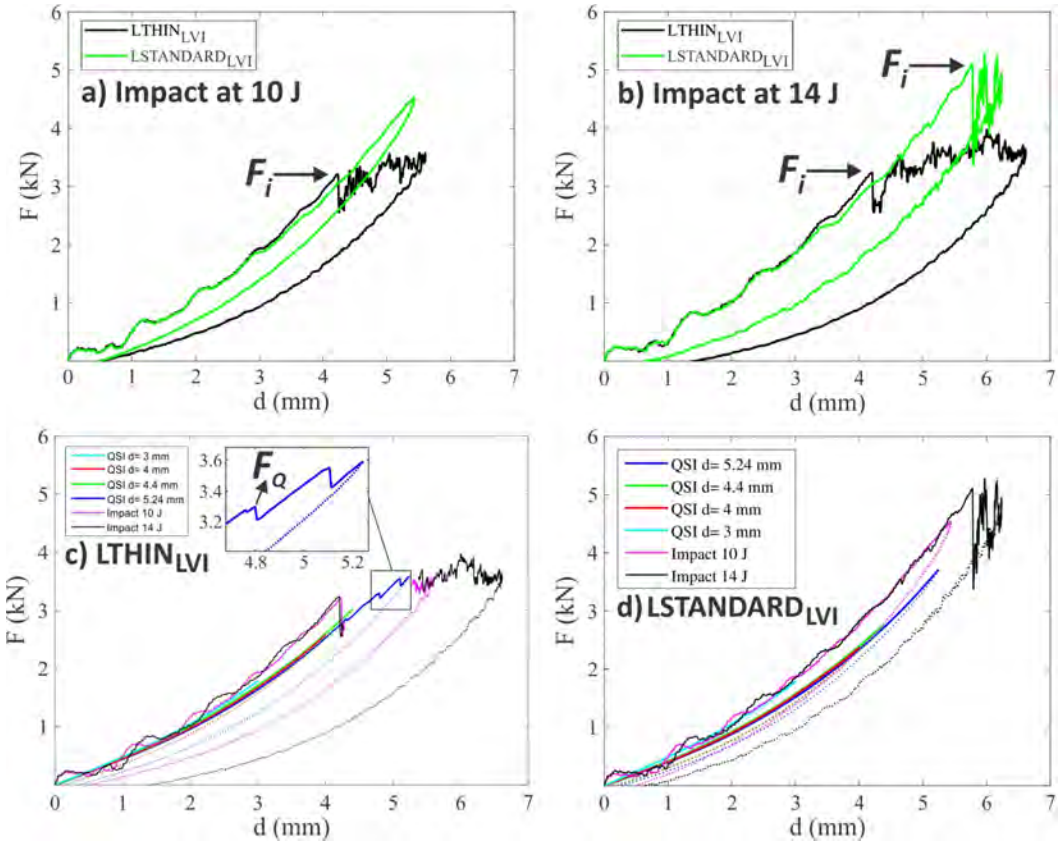


**Figure 4.1:** Load-displacement curves of representative $\text{LTHIN}_{\text{LVI}}$ and $\text{LSTANDARD}_{\text{LVI}}$ specimens impacted at a) 10 J and b) 14 J. 1c-d: Load-displacement curves of indented and representative impacted $\text{LTHIN}_{\text{LVI}}$ and $\text{LSTANDARD}_{\text{LVI}}$ specimens (for visualization purposes, the part of $\text{LTHIN}_{\text{LVI}}$'s impact curves that overlap with those of the quasi-static indentation test were suppressed). (For interpretation of the references to colour in this figure legend, the reader is referred to the web version of this article.)

contrast, the $\text{LSTANDARD}_{\text{LVI}}$ counterpart presented a non-linear response without concomitant load oscillations. Finally, in both materials, the impacted specimens displayed a higher stiffness than the QSI ones owing to the dynamic components of the former test (as observed elsewhere [92]).

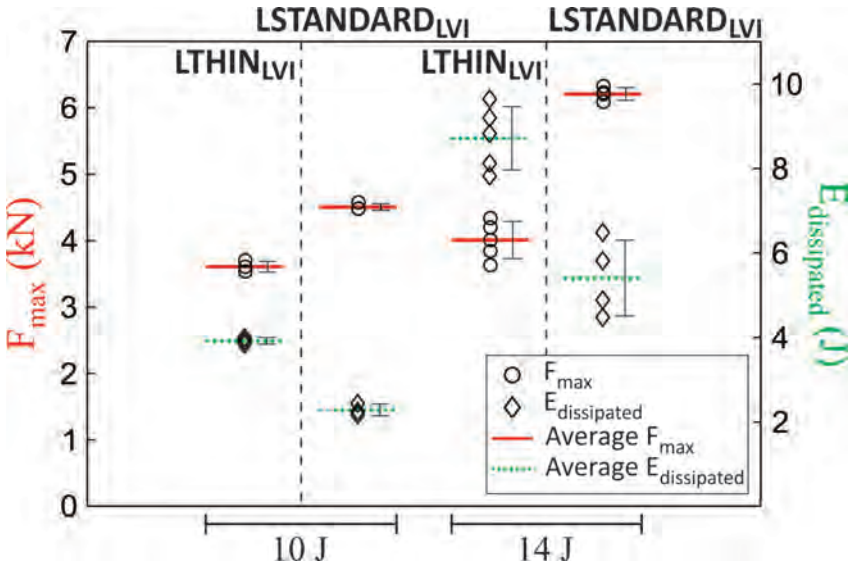


**Figure 4.2:** Maximum load supported and energy dissipated by LTHIN$_{LVI}$ and LSTANDARD$_{LVI}$ specimens impacted at 10 and 14 J - horizontal lines refer to the average value between experiments, whereas vertical bars mean standard deviation.

When an impact load bends a composite plate, part of the energy bounces back as elastic energy and part of it dissipates in the form of damage. We monitored the maximum force supported (i.e. the maximum load value measured during the experiment) and the energy dissipated by the LTHIN$_{LVI}$ and LSTANDARD$_{LVI}$ specimens (Figure 4.2). At both impact energies, LTHIN$_{LVI}$ supported a lower maximum force and dissipated a higher amount of energy than LSTANDARD$_{LVI}$.

Figure 4.3 plots the C-scan projected damage area against the energy applied during QSI and impact tests. In LSTANDARD$_{LVI}$, the damage grew almost linearly with the energy applied during both types of experiment. On the other hand, the LTHIN$_{LVI}$ coupons exhibited very reduced damage until 8.2 J, from which the damage started to grow faster than in the standard-ply system. This tendency agrees well with the results in Figure 4.2, i.e. decreased damage area after impact increases the load-carrying capacity and lessens the energy dissipated though damage propagation.

Figures 4.4-4.8 summarize the damage sequence of LTHIN$_{LVI}$ and LSTANDARD$_{LVI}$. We omitted the coupons indented at d= 4.4 mm as they did not present any new damage forms relative to those indented at the previous deflection step. In addition, Appendix A details the damage mechanisms developed in each ply/interface of the LTHIN$_{LVI}$ and LSTANDARD$_{LVI}$ specimens indented at d= 3 and d= 4 mm, i.e. it compares how damage initiates in both types of laminate (NB: the thin-ply specimen indented at d= 3 mm displayed no significant damage and therefore is not considered in the Appendix A).

The μCT slices evidenced that LTHIN$_{LVI}$ and LSTANDARD$_{LVI}$ presented resin-

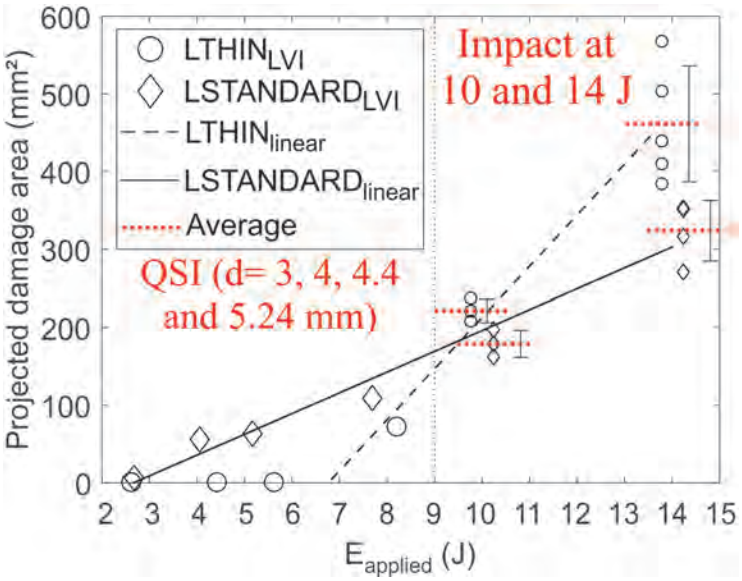


**Figure 4.3:** C-scan projected damage area plotted against the energy applied during quasi-static indentation and impact events. In the impact data, horizontal lines refer to the average value between experiments, whereas vertical bars mean standard deviation.

rich areas (commonly called "resin pockets") dispersed through-the-volume of the laminate. The higher the ply-thickness, the greater the size of the resin pockets (Figures 4.4a and 4.5b).

The LTHIN$_{LVI}$ specimen indented at d= 3 mm featured no damage except for scarce matrix cracks in the bottom part of the laminate (Figure 4.4a) – the top and bottom surfaces will be henceforth defined as the ones lying closest to and farthest from the impactor. In contrast, the standard-ply coupon developed matrix cracks in the seven bottommost plies and one delamination in the first $0°/45°$ interface located under the mid-plane (Figures 4.5a and 4.6b, the delamination is indicated as (i) in Figure 4.5a). We discerned two types of intralaminar cracks, (ii) in Figure 4.5a these are the 90° cracks caused by tensile stresses in the rear part of the laminate ("tensile cracks"[96]), and (iii) in Figure 4.5a these are the 45° cracks induced by shear stresses in the inner part of the laminate ("shear cracks" [95]). Besides this, we observed matrix cracks initiating in resin pockets (see, for example, the first $-45°$ ply located under the mid-plane of the LTHIN$_{LVI}$ specimen indented at d= 4 mm, Figure A.2 in Appendix A).

In the thin-ply material, QSI damage initiated at 4 mm deflection (applied energy of approximately 4 J, Figures 4.4b, 4.6c and 4.7a). It localized in the bottom-half of the laminate, where we observed tensile/shear cracks and delamination in the three $0°/45°$ interfaces under the mid-plane (Figure 4.4b). Another delamination developed through a resin-rich area located below the $90^{\circ}_{2}$ ply-cluster (see the green delamination in Figures 4.6c and 4.7a), where the shear stress distribution is close to

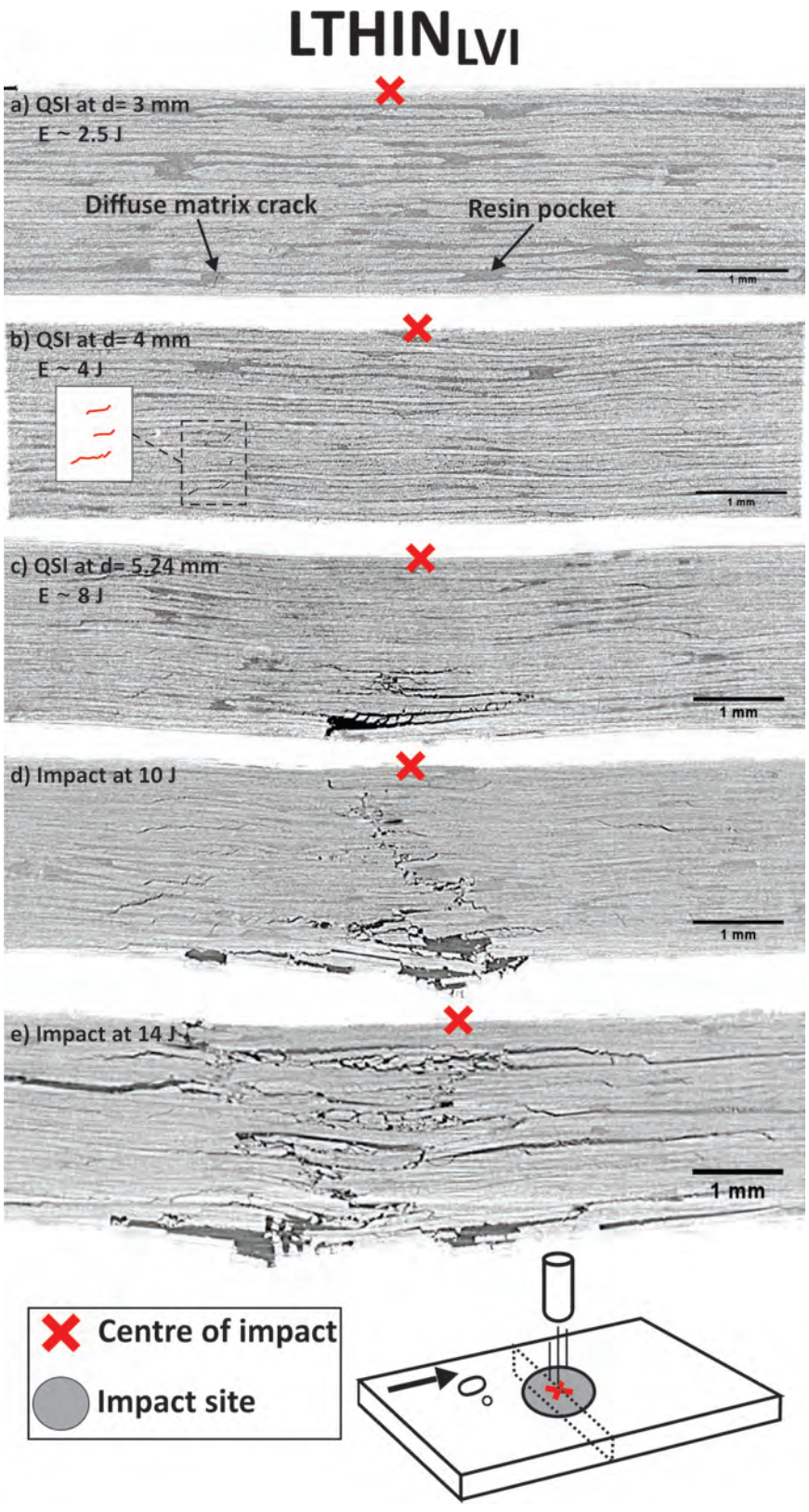


**Figure 4.4:** X-ray micro-computed tomography (μCT) cross-sections of indented and representative impacted LTHIN$_{LVI}$ specimens. The centre of impact is indicated with a cross.

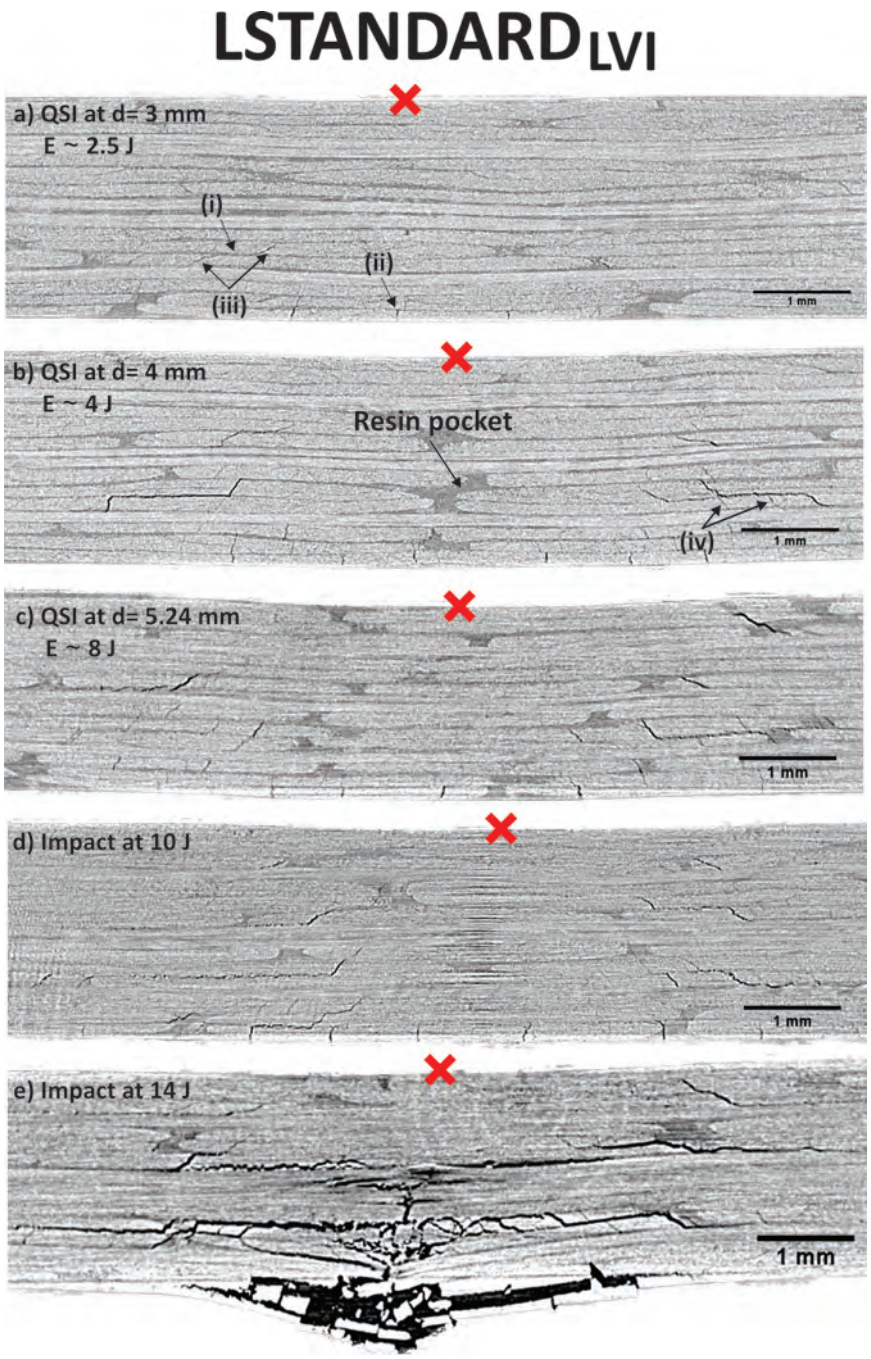


**Figure 4.5:** µCT cross-sections of indented and representative impacted $\text{LSTANDARD}_{\text{LVI}}$ specimens. The centre of impact is indicated with a cross, (i) is the delamination propagating at the first $0°/45°$ interface below the mid-plane, (ii) is the tensile crack, (iii) are the shear cracks and (iv) are the "micro-cracks" developed along with delamination propagation [183, 184].

maximum. In the $\text{LSTANDARD}_{\text{LVI}}$ sample indented at d= 4 mm, damage extended to the bottom three-quarters of the plate (Figures 4.5b and 4.7b). In this region, matrix cracks developed within each ply (see Figure A.3 in Appendix A) and allowed delamination to concatenate resulting in a symmetric "spiral stair-case" profile [96] (Figure 4.7b). At least one pair of matrix cracks with dissimilar orientation confined

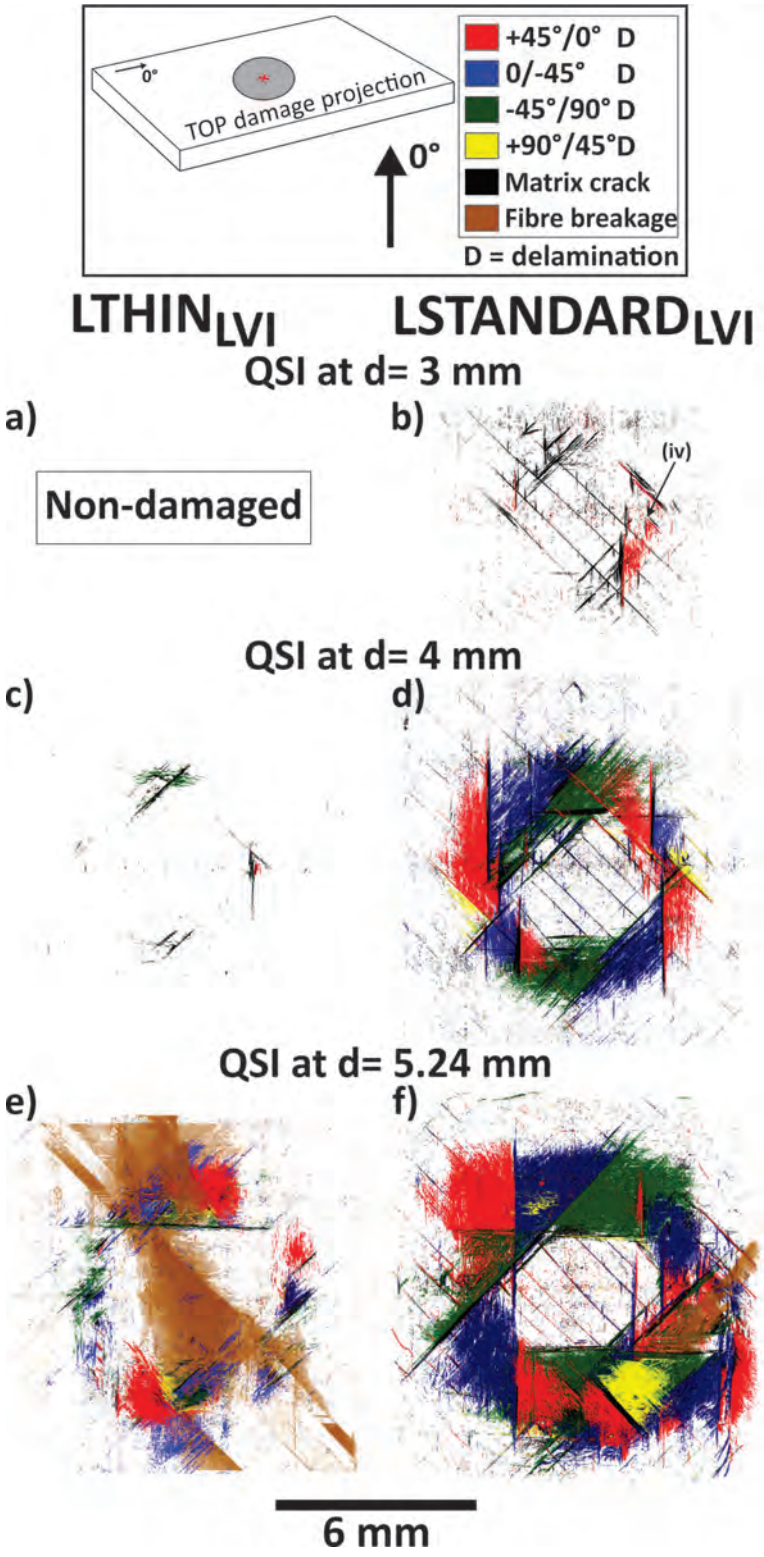


**Figure 4.6:** Projected damage area of indented $LTHIN_{LVI}$ and $LSTANDARD_{LVI}$ specimens obtained through post-process of the μCT slices, (iv) are the "micro-cracks" developed along with delamination propagation [183, 184]. (For interpretation of the references to colour in this figure legend, the reader is referred to the web version of this article.)

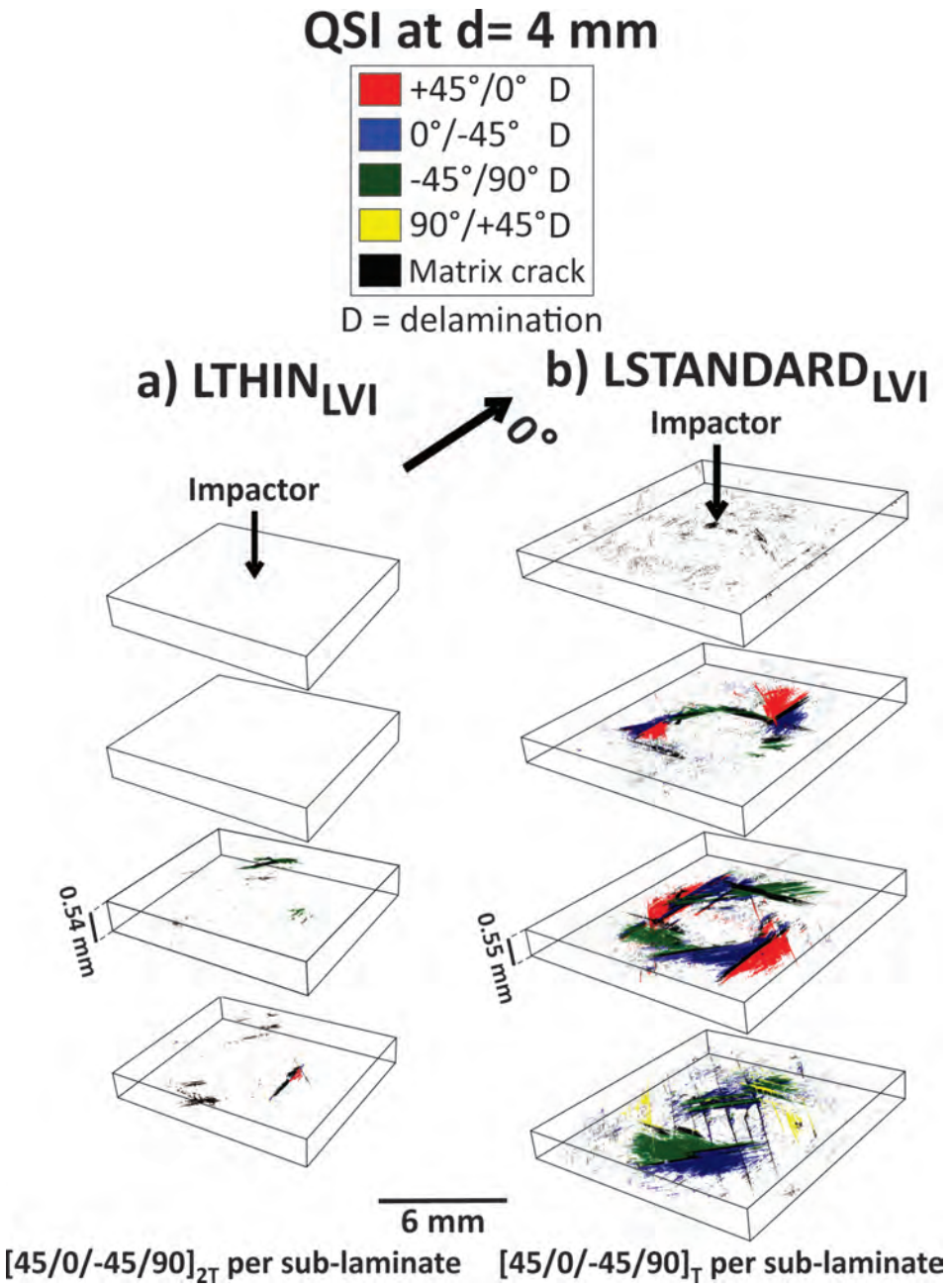


**Figure 4.7:** 3D damage scenario of a) LTHIN$_{LVI}$ and b) LSTANDARD$_{LVI}$ specimens indented at d= 4 mm. For visualization purposes, both images were extruded in the through-the-thickness direction and divided into 4 equally-thick sublaminates. (For interpretation of the references to colour in this figure legend, the reader is referred to the web version of this article.)

delamination propagation (Figure 4.6d), whereas we observed multiple micro-cracks parallel to the "main" cracks [183] ((iv) in Figures 4.5b and 4.6b).

The LTHIN$_{LVI}$ specimen indented at d= 5.24 mm (applied energy of approximately 8 J) presented fibre failure in almost all the plies in the lower half of the laminate

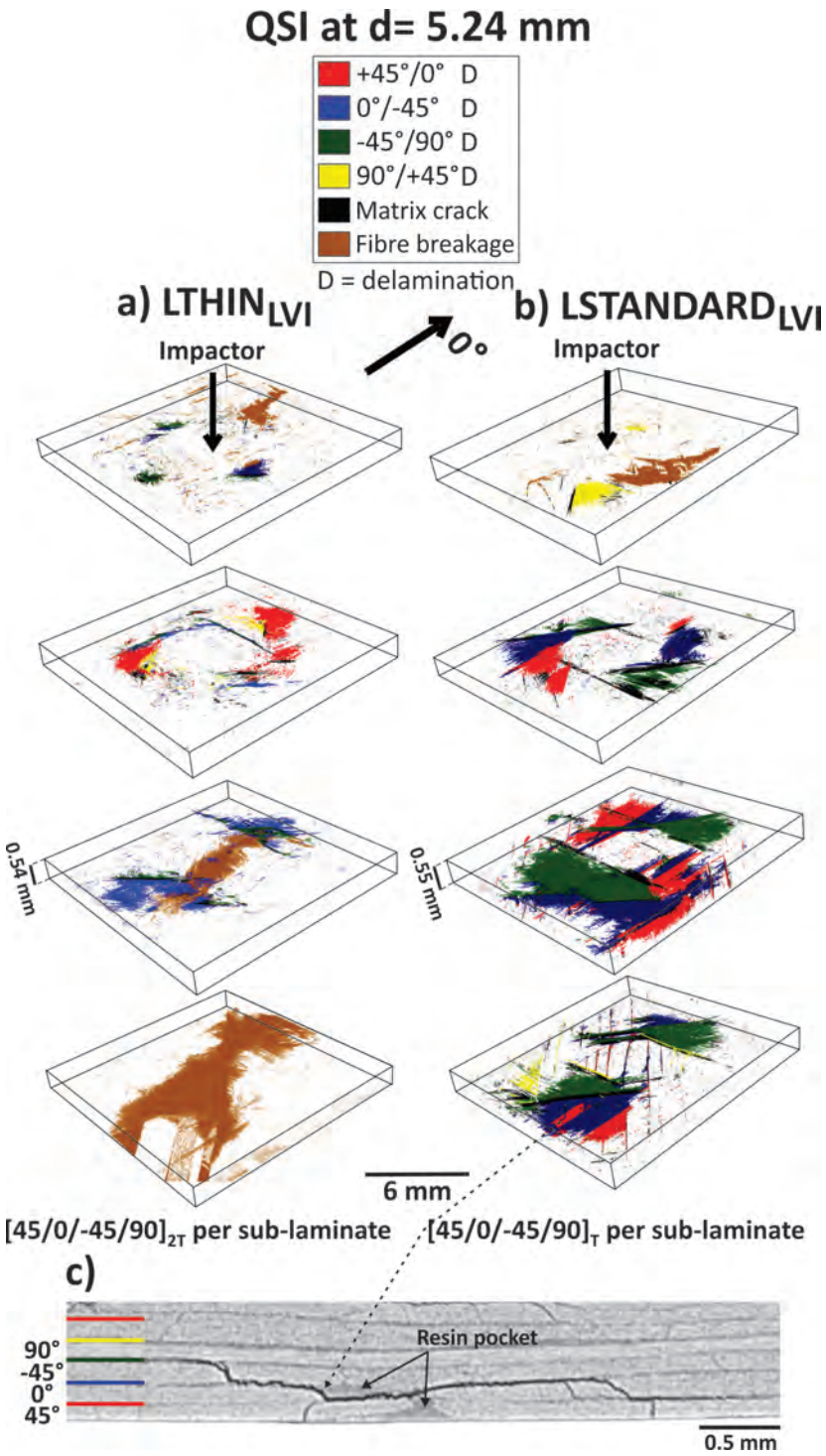


**Figure 4.8:** 3D damage scenario of a) LTHIN$_{LVI}$ and b) LSTANDARD$_{LVI}$ specimens indented at d= 5.24 mm. For visualization purposes, both images were extruded in the through-the-thickness direction and divided into 4 equally-thick sublaminates. 8c: Delamination migration favoured by a transverse crack developed within a resin pocket - the colour of the lines to the left of the picture refer to the interfaces highlighted in the legend. (For interpretation of the references to colour in this figure legend, the reader is referred to the web version of this article.)

(Figures 4.4c and 4.8a). In addition, matrix cracks and delaminations 1–3 mm wide extended from the bottom to the top parts of the plate except for the five interfaces closest to the indenter where fibre crushing occurred because of high compressive stresses (Figure 4.8a). In the $\text{LSTANDARD}_{\text{LVI}}$ sample indented at d= 5.24 mm, delaminations developed in the same interfaces as in the coupon indented at d= 4 mm (Figures 4.7–4.8b), albeit with higher lateral extension (Figures 4.6d and f). Additionally, we observed that the delamination in the bottommost $-45°/0°$ interface migrated to the adjacent $0°/45°$ favoured by a transverse crack developed within a resin pocket (Figure 4.8c).

Once fibre breakage initiated in the $\text{LTHIN}_{\text{LVI}}$ system (Figure 4.4c), it extended through-the-thickness of the laminate (Figure 4.4d) and induced further delamination propagation (Figure 4.4e). The $\text{LSTANDARD}_{\text{LVI}}$ specimens presented fibre breakage solely after impact at 14 J (Figure 4.5e).

Figure 4.9 introduces the compressive strength of pristine and impacted $\text{LTHIN}_{\text{IP}}$, $\text{LTHIN}_{\text{LVI}}$, $\text{LSTANDARD}_{\text{IP}}$ and $\text{LSTANDARD}_{\text{LVI}}$ coupons. Each standard compression specimen failed within the gage section. The failure mode was either "brooming" ($\text{LTHIN}_{\text{IP}}$) or a combination of brooming and delamination ($\text{LSTANDARD}_{\text{IP}}$). In the CAI experiments, all the samples failed by local buckling at the impact site followed by damage propagation perpendicular to the applied load. Despite the scatter presented by coupons of the same batch, $\text{LTHIN}_{\text{IP}}$ improved the standard compressive strength by approximately 3% compared to the standard-ply baseline, typically attributed to the more homogeneous microstructure (i.e. in the case of NCFs, to the reduced size of the resin pockets) or the improved fibre dispersion inherent to the thinner plies [3, 54]. On the other hand, $\text{LTHIN}_{\text{LVI}}$ decreased the CAI strength by 27% for impact at 14 J.

## 4.4 Discussion

The microstructure of NCF laminates presents resin accumulations because the stitching yarns deviate carbon tows from their uniform directions, generating multiple and regularly spaced fibre-free regions [185]. The higher the ply-thickness, the bigger the length of and the distortion induced by the NCF stitches (Figures 4.4a and 4.5b). We observed that resin pockets favoured the initiation of matrix cracks (e.g. see the first $-45°$ ply below the mid-plane of the $\text{LTHIN}_{\text{LVI}}$ specimen indented at d= 4 mm, Figure A.2) and interacted with the propagation of delaminations (Figure 4.8c), which seems obvious as pure epoxy has less resistance than the carbon-epoxy composite.

The load-displacement curves of $\text{LTHIN}_{\text{LVI}}$ and $\text{LSTANDARD}_{\text{LVI}}$ exhibited one or

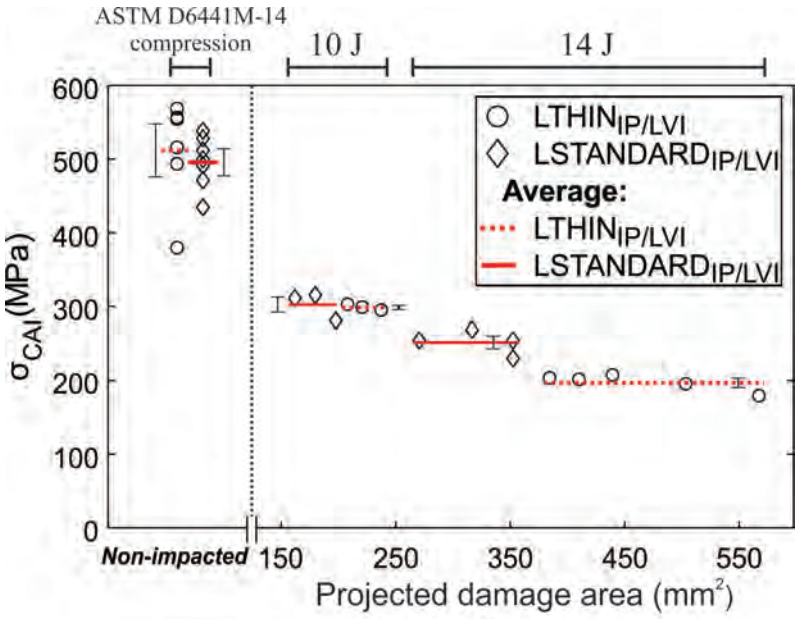


**Figure 4.9:** Compressive strength of pristine and impacted $\text{LTHIN}_{\text{IP}}$, $\text{LTHIN}_{\text{LVI}}$, $\text{LSTANDARD}_{\text{IP}}$ and $\text{LSTANDARD}_{\text{LVI}}$ specimens. Horizontal lines refer to the average value between experiments, whereas vertical bars mean standard deviation.

several consecutive load drops during impact and/or QSI experiments ($F_i$ and $F_q$ in Figure 4.1). According to our $\mu$CT observations, such load drops correspond to the development of fibre failure localized in the bottom half of the laminate (Figures 4.5e and 4.4c). On the other hand, the $\text{LSTANDARD}_{\text{LVI}}$ specimens exhibited extended delamination propagation without associated evidence in the load-displacement curve (Figures 4.1d and 4.5a-d). This arises from the thickness-to-length ratio of the coupons. For small ratios (e.g. thin laminates), bending deflection and non-linear membrane stiffening effects dominate over shear; which may obscure the evidence of delamination onset in the force-displacement curve [85, 107]. In contrast, the curve of thick laminates typically displays a load drop corresponding to the initiation of delamination [92, 96, 99].

The sequence of damage events developed in thin- and standard-ply materials displays common qualitative trends. First, tensile and shear cracks develop in the bottom part of the laminate, accompanied by a delamination in the $0°/45°$ interface ($\text{LSTANDARD}_{\text{LVI}}$) or in the three $0°/45°$ interfaces ($\text{LTHIN}_{\text{LVI}}$) under the mid-plane (Figures 4.4b and 4.5a). Then, shear cracks extend from the bottom to the top and allow delaminations to concatenate through-the-thickness [96] (Figures 4.4c, 4.5b, 4.7b and 4.8a, NB: the exception to this are the 4–5 interfaces under the impactor, where high compressive stresses inhibit delamination propagation). Finally, fibre failure develops in the rear part of the laminate; subsequently evolving towards the top and inducing further damage propagation (Figures 4.4c-e and 4.5e).

The fact that matrix cracks, delaminations and fibre failure grow bottom-to-top is, again, a consequence of the low thickness (and associated high deflections) of the plate [5]. We observed that a pair of long matrix cracks confined delamination (Figure 4.6d). Besides, multiple "micro-cracks" parallel to the long cracks developed along with delamination propagation (e.g. (iv) in Figure 4.5b) [183, 184]. The latter could derive from stress redistributions near the main matrix cracks [186], suggesting that delamination may grow progressively (confined between the smaller cracks) rather than in a single-step process.

The difference between $\text{LTHIN}_{\text{LVI}}$ and $\text{LSTANDARD}_{\text{LVI}}$ is the magnitude of the various damage mechanisms and the energy at which they occur. $\text{LTHIN}_{\text{LVI}}$ displays smaller matrix cracks/delaminations that appear at higher QSI deflections (or energy levels) than those developed in $\text{LSTANDARD}_{\text{LVI}}$ (Figure 4.6a-d), attributed to the improved in-situ strength in transverse tension and shear [20, 24, 152]. When tensile stresses due to bending overcome the tensile strength of the fibres, catastrophic fibre failure occurs [98] (Figure 4.4c). In contrast, $\text{LSTANDARD}_{\text{LVI}}$ dissipates a higher fraction of the applied energy through delamination propagation, delaying the development of fibre breakage to the highest impact energy (Figure 4.5). This results in higher load-carrying capacity (Figure 4.2) and enhanced CAI strength for impact at 14 J (Figure 4.9). Our findings coincide with the results of Amacher *et al.* [3], who observed increased back-face fibre breakage as the laminate's ply-thickness decreased (they impacted coupons of relatively low thickness-to-length ratio).

It is evident that the thin-ply laminate delays the initiation of matrix cracks and delaminations when compared to the standard-ply counterpart. However, these damage modes do not entail a decrease in bending stiffness in the load-displacement curve. In this regard, the standard-ply material displays a greater damage resistance: the load drop (and concomitant stiffness reduction) appears at higher applied energy. Selecting the optimal configuration would depend on the requirements of the structural application. If damage detectability prevails over load-carrying capacity, thin-plies should be used (according to our observations, $\text{LTHIN}_{\text{LVI}}$ will probably suffer an earlier penetration than $\text{LSTANDARD}_{\text{LVI}}$, which can be detected with the naked eye, Figures 4.4-4.5e). In other words, the impact on thin-ply laminates will be detectable at lower applied energies as compared to their standard-ply counterparts. The authors speculate that an optimal balance between damage suppression and CAI strength could be achieved by mixing thin- and standard-plies within the same laminate.

## 4.5 Conclusions

Combining quasi-static indentation and impact tests at incremental energy levels with 3D X-ray tomography, we compared the impact resistance, tolerance and sequence of failure events of thin laminates manufactured with thin- or standard-ply non-crimp fabrics. During the experiments we monitored the force-displacement data to associate load drops with observed damage mechanisms.

The load-displacement curve for both types of material presents a load drop corresponding to the development of fibre breakage localized in the bottom part of the laminate. Prior to the drop, matrix cracks and delaminations propagate with no associated evidence in the load-displacement curve. This is related to the low thickness-to-length ratio of the coupons, whereby bending and non-linear membrane stiffening effects dominate over shear.

The sequence of damage mechanisms developed in thin- and standard-ply laminates presents common qualitative trends (i.e., matrix cracks/delaminations extend from the bottom to the top of the laminate until fibre failure localizes in the rear part in the coupons, which subsequently evolves towards the top and induces further damage propagation). However, the thin-plies delay the onset and reduce the extension of matrix cracks and delaminations. Lessening the energy dissipated through delamination propagation results in premature fibre breakage, decreased load-carrying capacity (by 25% and 55% for impact at 10 and 14 J) and lower CAI strength for impact at 14 J (by 27%).

As a last remark, the impact and QSI tests display a good coherence in terms of the force local maxima ($F_i$ and $F_q$), the projected damage area (which grows linearly with the incremental energy applied in both types of test) and the observed damage sequence. Therefore, for the type of material and range of energies considered in this study, the quasi-static test can be used to infer qualitative information about the damage mechanisms taking place during low-velocity impact.

## 4.6 Appendix A. Ply-by-ply damage analysis

See Figs. A.1-A.3.

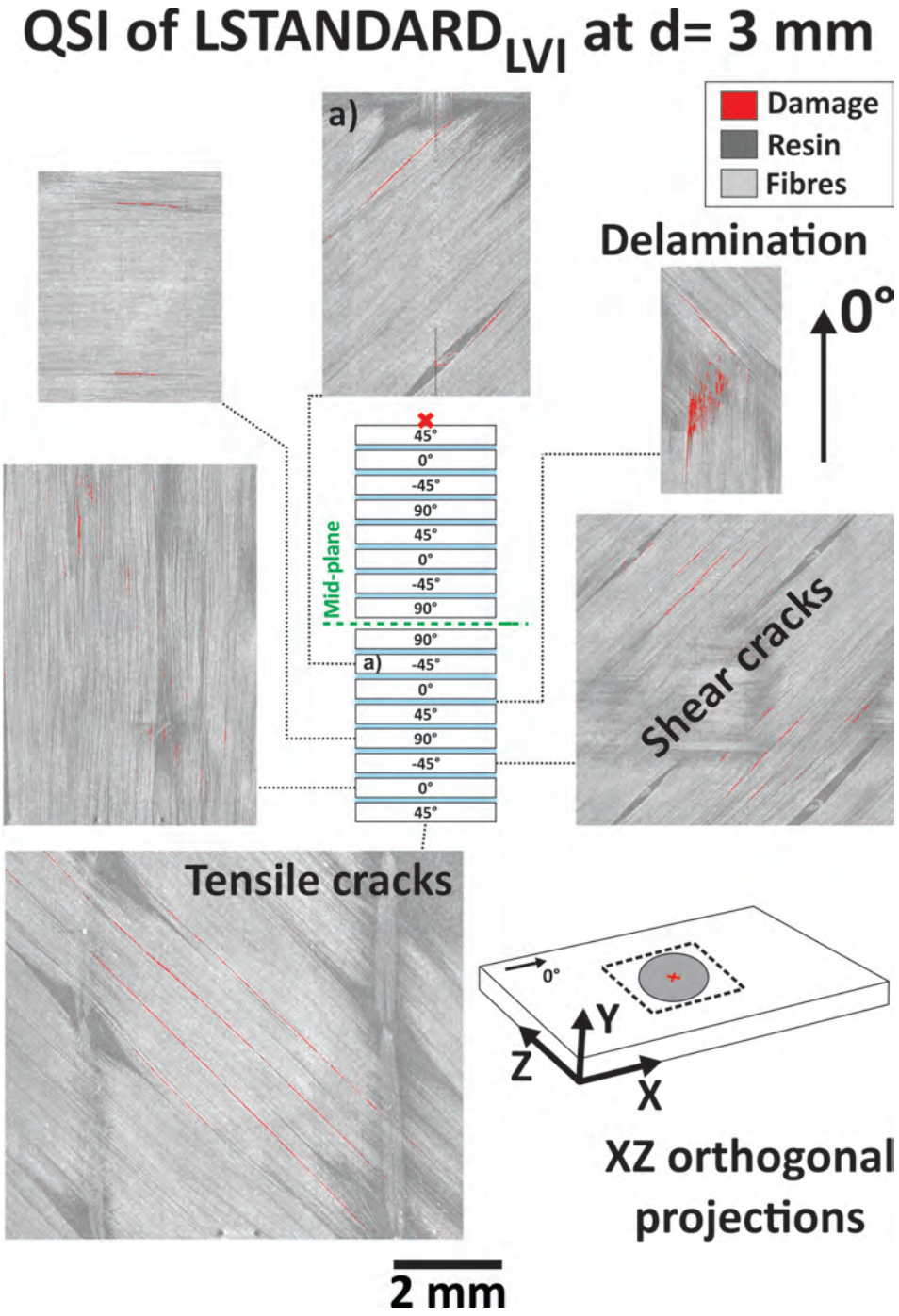


**Figure A.1:** 1 pixel thick XZ orthogonal slices representing the damage developed in each ply/interface of the LSTANDARD$_{LVI}$ specimen indented at d= 3 mm. Resin and carbon fibres appear in darker and lighter shades of grey, whereas matrix cracks/delaminations (originally in black) were segmented and coloured in red. In the sketch depicting the stacking sequence, the centre of impact is indicated with a cross. (For interpretation of the references to colour in this figure legend, the reader is referred to the web version of this article.)

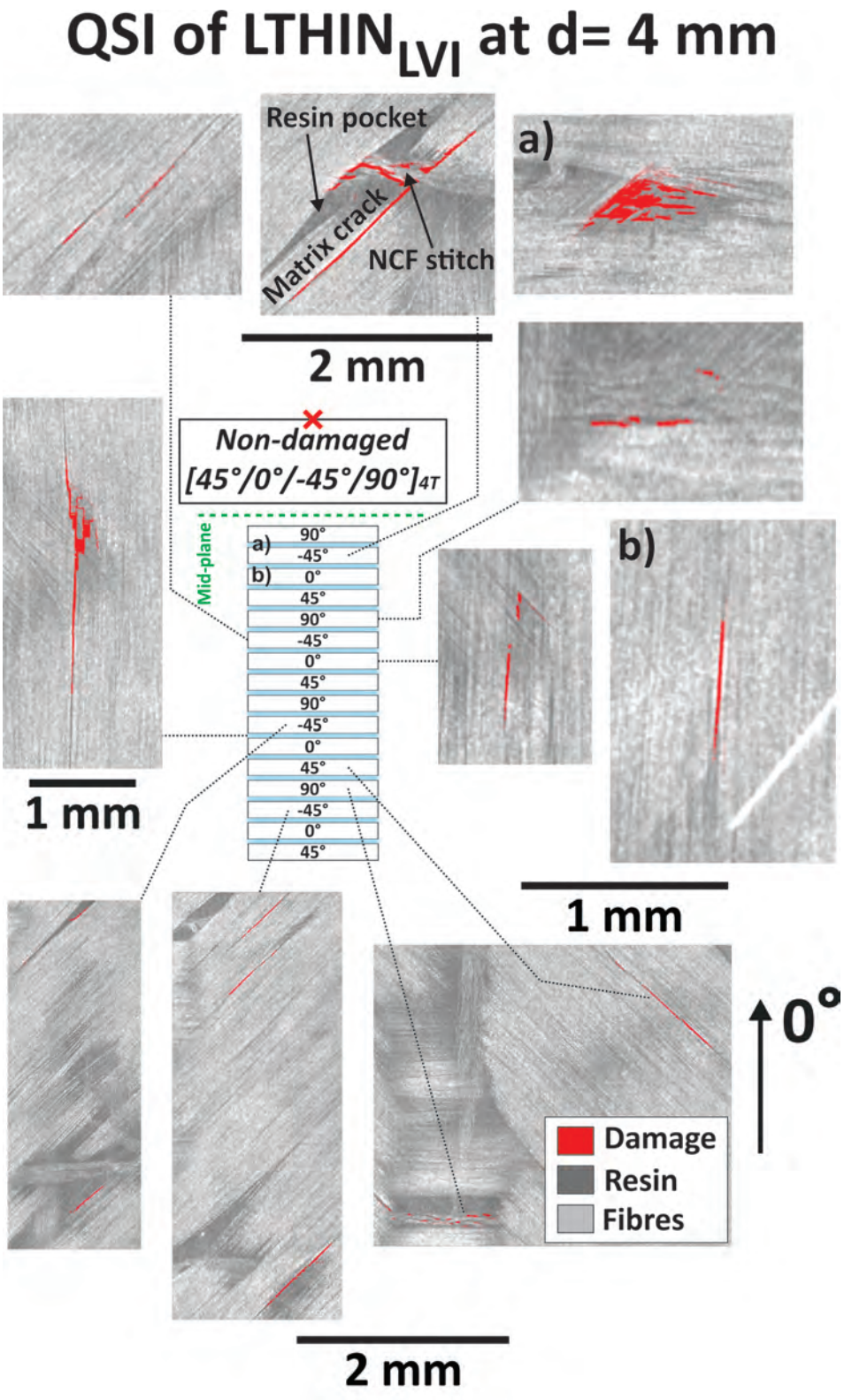


**Figure A.2:** 1 pixel thick XZ orthogonal slices representing the damage developed in each ply/interface of the LTHIN$_{LVI}$ specimen indented at d= 4 mm. Resin and carbon fibres appear in darker and lighter shades of grey, whereas matrix cracks/delaminations (originally in black) were segmented and coloured in red. In the sketch depicting the stacking sequence, the centre of impact is indicated with a cross. (For interpretation of the references to colour in this figure legend, the reader is referred to the web version of this article.)

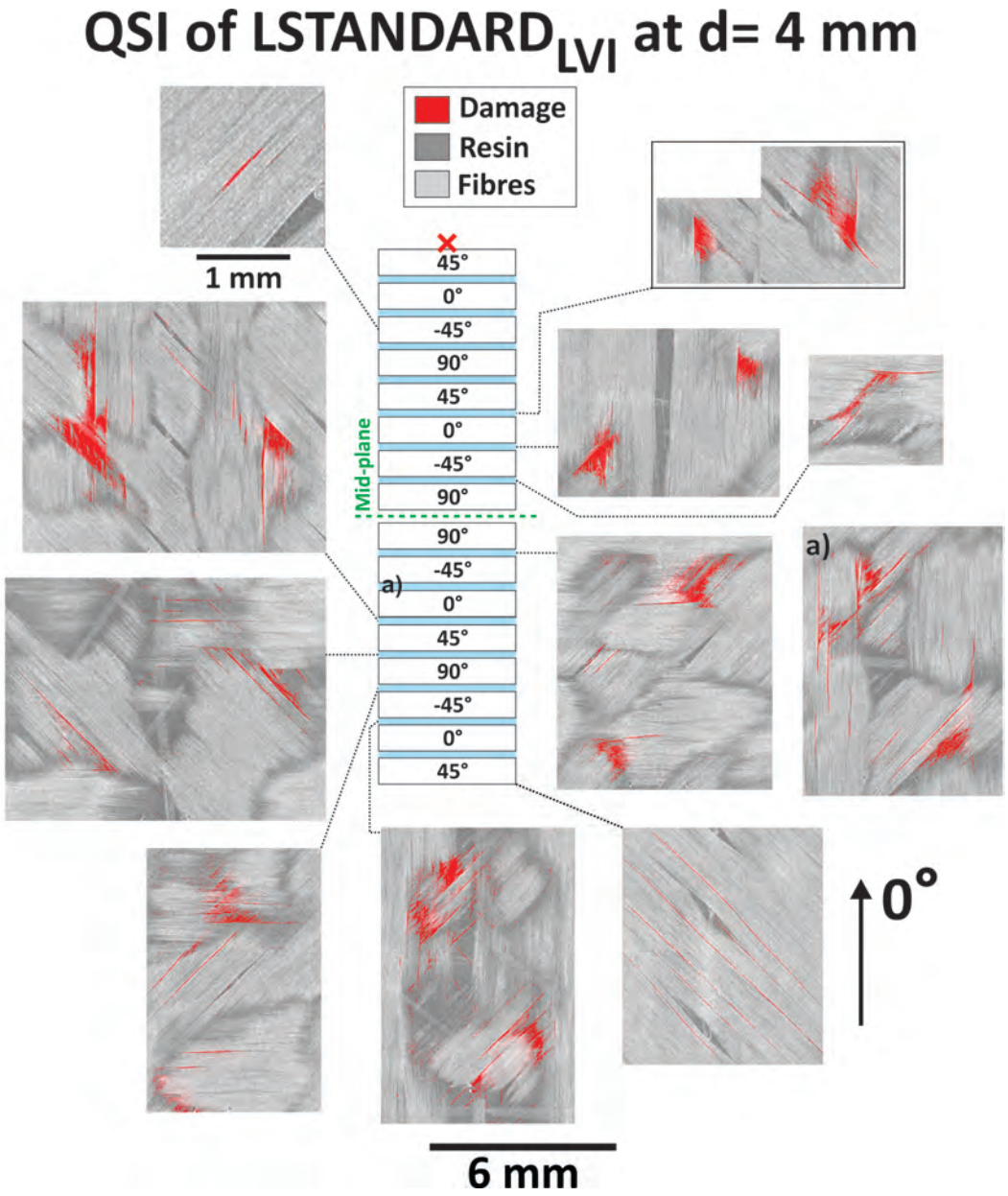


**Figure A.3:** 1 pixel thick XZ orthogonal slices representing the damage developed in each ply/interface of the LSTANDARD$_{LVI}$ specimen indented at d= 4 mm. Resin and carbon fibres appear in darker and lighter shades of grey, whereas matrix cracks/delaminations (originally in black) were segmented and coloured in red. In the sketch depicting the stacking sequence, the centre of impact is indicated with a cross. (For interpretation of the references to colour in this figure legend, the reader is referred to the web version of this article.)

# Paper C

# 5

## Interleaving light veils to minimise the trade-off between mode-I interlaminar fracture toughness and in-plane properties

S.M. García-Rodríguez[a], J. Costa[a,*], K.E. Rankin[b], R.P. Boardman[b], V. Singery[c], J.A. Mayugo[a]

[a]AMADE, Polytechnic School, University of Girona, Av. Universitat de Girona, 4. 17003 Girona, Spain

[b]Faculty of Engineering and Physical Sciences, University of Southampton, Southampton SO17 1BJ, United Kingdom

[c]Chomarat, 39 Avenue de Chabannes, 07160, Le Cheylard, France

Submitted for publication in *Composites Part A: Applied Science and Manufacturing*

* Corresponding author

**Overview**

Paper C compares the tensile, compressive and mode-I interlaminar fracture toughness properties of the thin-ply baseline laminate and laminates interleaved with two types of light (4 g/m$^2$) co-polyamide veil: $V_1$ and $V_2$. In-plane and interlaminar fracture toughness configurations are named LTHIN$_{IP}$, LTHIN$_{G_{IC}}$, LV1$_{IP}$, LV1$_{G_{IC}}$, LV2$_{IP}$ and LV2$_{G_{IC}}$ (for details of the stacking sequences refer to Table 1.2). The aim of this paper is to fulfil the objective 3 in Section 1.2 as well as addressing the corresponding open question in Table 1.1. Paper C uses a novel experimental technique compared to the rest of manuscripts: sub-micron resolution X-ray tomography. Two types of X-ray source were used, a synchrotron X-ray source, and a laboratory source at the μ-VIS X-ray Imaging Centre, Faculty of Engineering and Physical Sciences, University of Southampton (named Zeiss 160 kVp Versa 510 scanner). To the author's knowledge, this is the first study that provides 3D insight into the after-manufacturing state of veil fibres as well as connects veil fibre architecture with mechanical properties.

**Abstract**

Interleaving heavy non-woven veils, commonly used to improve interlaminar fracture toughness, affects laminate thickness and tensile/compressive properties. We manufactured a thin-ply quasi-isotropic baseline laminate and laminates interleaved with two types of light (4 g/m$^2$) co-polyamide veil. For mode-I interlaminar fracture toughness testing, a single veil was incorporated at the centre of the stack. For in-plane testing, a single veil was incorporated into every interface. Submicron resolution X-ray micro-computed tomography provided insight into the after-manufacturing state of the veil fibres as well as into the fracture process zone of the double cantilever beam specimens. The veil fibre diameter was the key parameter determining the tensile properties (the veil with smaller fibre diameter avoided resin accumulation at the interfaces and displayed the same tensile properties as the baseline laminate). Both veils decreased the compressive strength by up to 9% because of the increase in the ductile phase surrounding the carbon plies. Mode-I crack propagation was controlled by the adhesion between the veil fibres and resin. Veils fibres with low adhesion promoted interlaminar crack growth by debonding from the matrix, whereas veil fibres with higher adhesion deviated crack propagation from the 0°/0° interface to the surrounding 0° plies which, in the material system studied, resulted in the highest mode-I initiation and propagation interlaminar fracture toughness (101% and 43% increase).

*Keywords*: Thin-plies, Non-woven veils, B. Mechanical properties, D. CT analysis

## 5.1 Introduction

In an effort to reduce costs, the airline industry is increasingly considering thinner carbon fibre reinforced composite laminates manufactured using out-of-autoclave methods such as resin transfer moulding (RTM). However, infusion techniques demand low-viscosity inherently brittle resins, which lowers the component's damage tolerance [10]. This is even more accentuated when laminates are made of "thin-plies" (i.e. plies thinner than 125 µm [2]). Thin-ply laminates are a new generation of composite materials that, despite improved certain mechanical properties [2–4, 40, 46, 54, 55, 57, 58, 60, 63–65, 187], entail brittle damage mechanisms compared to their conventional-ply counterparts. [3, 67–69, 99, 165].

From an industrial point of view, brittleness can be overcome with toughening methods that are cheap and easy to incorporate during manufacturing. Nash *et al.* [10] wrote a comprehensive review on toughening methods that use a thermoplastic modifier. They classified them into two groups: bulk resin modification and inter-

laminar toughening. The first group increases the fracture toughness of the resin by dispersing/dissolving external agents, which normally increases the viscosity. The second group incorporates a toughening system such as thermoplastic particles or thin films in the interfaces. However, the particles may migrate during resin infusion while the films inhibit through-thickness resin flow. To overcome these difficulties, we used a relatively undeveloped interlaminar toughening approach called interleaving "non-woven veils" [10, 13, 15, 115]. These are thin heterogeneous networks made of dispersed micro-fibres [15]. The main advantages are that they are commercially available, relatively cheap, can be manually placed during the lay-up and allow resin infusion through the z-direction (the veils are permeable) [10].

Interleaving polyamide veils improves the mode-I interlaminar fracture toughness ($G_{IC}$) of the non-interleaved baseline [10, 14, 18, 119, 120, 123, 126, 128, 135, 136]. Kuwata [124] explained that a critical parameter for $G_{IC}$ performance is the adhesion between veil fibres and matrix. Veil fibres with a low adhesion pull out from the matrix and dissipate part of the fracture energy by fibre bridging (as observed in [10, 14, 18, 19, 115, 119, 120, 123, 126, 128, 135, 136]). Veil fibres with a higher adhesion deviate crack propagation away from the veil, which may leave the baseline $G_{IC}$ unaffected [126]. Finally, some authors report a mixture of interlaminar and interfacial crack growth [14, 18, 120, 123, 127].

The $G_{IC}$ of a given interleaved system improves by increasing veil fibre areal weight (i.e. weight per unit area of veil) [15, 18, 127, 128]. For example, Beylergil *et al.* [18] reported a $G_{IC}$ improvement of 231% and 737% by interleaving 17 or 50 g/m$^2$ polyamide (PA) veils. However, in materials science, every enhancement has an associated cost, in particular toughness and strength are mutually exclusive [146]. Beylergil *et al.* [18] characterised the tensile and compressive properties of a carbon/epoxy $[0°]_4$ laminate interleaved with the 17 or 50 g/m$^2$ PA veils in every interface. Both the tensile and compressive moduli decreased with improved veil fibre areal weight ($E_{11}$ by up to 34%, $E_{22}$ by up to 23.7%, $G_{12}$ by up to 21% and the compressive modulus by up to 13%), and likewise the tensile and compressive strength (by up to 41% and 13%). The authors attributed the reduction of tensile properties to the increase in laminate thickness (and thus the decrease in fibre volume fraction) brought about by the veils (both veils increased nominal thickness by up to 38%), which also agrees with the tendencies reported elsewhere [19, 119, 138].

Based on the observations, a practical balance between laminate thickness, mode-I interlaminar fracture toughness and in-plane mechanical properties should rely on veils with relatively low fibre areal weight. We manufactured a thin-ply quasi-isotropic baseline laminate and laminates interleaved with two types of light (4 g/m$^2$)

co-polyamide veils. To the authors' knowledge, 4 g/m$^2$ is the lightest fibre areal weight reported for interlaminar fracture toughness testing (values oscillate from 7 to 50 g/m$^2$ [10, 14, 15, 18, 19, 115, 119, 120, 123, 126–128, 135, 136, 138]). Sub-micron resolution X-ray tomography (μCT) provided comprehensive insight into the after-manufacturing state of the veil fibres as well as into the fracture process zone of the double cantilever beam (DCB) specimens. One of the interleaved configurations enhanced the baseline $G_{IC}$ with no associated reduction of the tensile properties. Besides this, a previous study demonstrated a compression after impact (CAI) strength improvement of up to 28% for impact at 14 J [162].

## 5.2 Materials and Methods

### 5.2.1 Materials

We used (0°/45°) and (0°/−45°) warp-knitted non-crimp fabrics (NCFs) made of T700 GC carbon and 35 dtex polyester yarns, which are commercialized by Chomarat under the brand name C-PLY$^{TM}$. The fibre areal weight of the blankets was 134 g/m$^2$, corresponding to 67 g/m$^2$ per unidirectional ply. NCFs reduce labour costs because they lay several layers in one-axis, which is ideal for handling thin-plies [48].

We used two types of CoPA non-woven veils with the same fibre areal weights (4 g/m$^2$): $V_1$ and $V_2$. Both veils had a different melting temperature. The melting point of $V_2$ was higher than the curing temperature (170 °C) and slightly lower than the laminate's post-curing temperature (180 °C). In contrast, that of $V_1$ was significantly higher than 180 °C. The fibre diameter of $V_1$ and $V_2$ was 37±4 μm and 11±2 μm, respectively, where ± means standard deviation (at least 50 fibres were measured using an optical microscope). For a given veil fibre areal weight, the veil fibre diameter is the parameter that intuitively controls the surface area covered by veil fibres (the smaller the veil fibre diameter is, the more closely packed the network and the higher the surface area covered by veil fibres is [15]). This tendency was verified using an optical microscope. First, different regions of $V_i$ ($i$ = 1,2) were inspected under similar magnification (at least 15 areas of 1 cm$^2$ were observed per veil). Then, the fibres were segmented from the background using Image J [188]. Finally, the percentage area covered by $V_1$ and $V_2$ fibres was calculated: 22±2% and 65±5%. No further details of the veils can be disclosed due to confidentiality.

Laminates were manufactured by resin transfer moulding using HexFlow® RTM6 epoxy resin (for further details of the manufacturing process refer to [162]). Two types of quasi-isotropic baseline laminate were designed by, if necessary, flipping over and/or rotating the NCF blankets. For in-plane testing, we devised a

$[(45°/0°)/(-45°/90°)]_{4s}$ laminate approximately 2.2 mm thick. For mode-I fracture toughness testing, we devised a $[(45°/90°)/(-45°/0°)]_{6s}$ laminate of approximately 3.7 mm thickness. The former is the stacking sequence used for the CAI study [162], whereas the latter is in agreement with interlaminar fracture toughness standards [189, 190]. Both configurations were interleaved with a different number of veils. For mode-I testing, a single veil was placed at the centre of the stack. For in-plane testing, a single veil was incorporated into every interface. Table 5.1 defines the notation and stacking sequence of the laminates. It is worth noting that veils lying within NCF blankets were incorporated during the stitching process. However, the veils outside the NCF blankets were positioned manually during the lay-up.

**Table 5.1:** Laminates devised for in-plane (tension and compression) and mode-I interlaminar fracture toughness experiments. Non-crimp fabric blankets are indicated with parenthesis. The bar sign means only one veil in the symmetry plane.

| Laminate | Stacking sequence | Purpose |
|---|---|---|
| $\text{LTHIN}_{\text{IP}}$ | $[(45°/0°)/(-45°/90°)]_{4s}$ | In-plane testing |
| $\text{LV1}_{\text{IP}}$ | $[(45°/\text{V}_1/0°)/\text{V}_1/(-45°/\text{V}_1/90°)/\bar{V}_1]_{4s}$ | |
| $\text{LV2}_{\text{IP}}$ | $[(45°/\text{V}_2/0°)/\text{V}_2/(-45°/\text{V}_2/90°)/\bar{V}_2]_{4s}$ | |
| $\text{LTHIN}_{G_{\text{IC}}}$ | $[(45°/90°)/(-45°/0°)]_{6s}$ | Mode-I interlaminar fracture toughness testing |
| $\text{LV1}_{G_{\text{IC}}}$ | $[(45°/90°)/(-45°/0°)/\bar{V}_1]_{6s}$ | |
| $\text{LV2}_{G_{\text{IC}}}$ | $[(45°/90°)/(-45°/0°)/\bar{V}_2]_{6s}$ | |

### 5.2.2 Experimental tests

Compression tests were performed using an electromechanical MTS INSIGHT®100 testing machine (MTS systems corporation, USA) with a 100 kN load cell. 12.7 x 140 mm (width and length) specimens were tested using a compression fixture in accordance with the ASTM D6641/D6641M-14 standard [177]. The cross-head displacement rate was 1.3 mm/min. The compression strength was calculated by dividing the maximum load to failure by the specimen's cross-section measured at the gage region. The average thickness of $\text{LTHIN}_{\text{IP}}$, $\text{LV1}_{\text{IP}}$ and $\text{LV2}_{\text{IP}}$ tested specimens was $2.37\pm0.23$, $2.25\pm0.03$ and $2.22\pm0.02$ mm, where $\pm$ means standard deviation. A minimum of 6 specimens were tested per material system.

Tensile tests were carried out using a servo-hydraulic MTS INSIGHT®250 testing machine (MTS systems corporation, USA) with a 250 kN load cell. 25 x 210 mm (width and length) specimens were tested in accordance with the ASTM D3039/D3039M-14 standard [191]. The coupons included 50 mm long glass/epoxy

end tabs. The cross-head displacement rate was 2 mm/min. One strain gage was glued onto the surface of each specimen to monitor for undesirable bending (in all the experiments less than 3%). The tensile strength was calculated by dividing the maximum load to failure by the specimen's cross-section measured at the gage region. The elastic modulus was estimated from the slope of a linear regression in the elastic regime of the load displacement curve (in the range of 0.1-0.3% strain). The average thickness of $\text{LTHIN}_{\text{IP}}$, $\text{LV1}_{\text{IP}}$ and $\text{LV2}_{\text{IP}}$ tested specimens was 2.21±0.02, 2.22±0.01 and 2.18±0.02 mm. A minimum of 8 specimens were tested per material system. The fibre volume fraction of $\text{LTHIN}_{\text{IP}}$, $\text{LV1}_{\text{IP}}$ and $\text{LV2}_{\text{IP}}$ in-plane laminates (both tension and compression) was 53.50±1.63%, 53.53±1.65% and 53.67±1.25% (five samples were measured per laminate following the standard EN 2564:1998 [163]).

Mode-I interlaminar fracture toughness experiments were performed using an electromechanical MTS INSIGHT®5 testing machine (MTS systems corporation, USA), a 5 kN load cell and the side clamped beam hinge system designed by Renart *et al.* (2011) [192]. The width and length of the DCB specimens were 25 and 250 mm, and the length of the teflon insert was approximately 70 mm. Specimens were pre-cracked and subsequently loaded following the guidelines set out in the ASTM D5528/D5528-13 and ISO 15024 standards [189, 193]. The loading and unloading rates were 5 and 25 mm/min. Crack propagation was recorded using an optical system consisting of a high-resolution video camera (EOS REBEL t2I/EOS 550D, Canon Inc, Japan) and a long distance microscope (Questar QM 100 MK III, Questar Corporation, USA). Data was reduced using the modified compliance calibration method [189, 193]. Mode-I initiation interlaminar fracture toughness ($G_{\text{Iinit}}$) was computed using the force and displacement measured at the $5\%/max$ point after pre-cracking [189, 193]. Mode-I propagation interlaminar fracture toughness ($G_{\text{Iprop}}$) was the average toughness of the propagation increments between 20 and 40 mm (where the R-curves were consistently flatter in all of the batches as will be presented in the Results section). The average thickness of the $\text{LTHIN}_{G_{\text{IC}}}$, $\text{LV1}_{G_{\text{IC}}}$ and $\text{LV2}_{G_{\text{IC}}}$ tested specimens was 3.83±0.15, 3.89±0.04 and 3.45±0.18 mm. Six specimens were tested per batch. The entire campaign was performed at 23±2 °C and 50±5% humidity in the mechanical testing laboratory at the University of Girona. The laboratory holds ISO17025 and NADCAP (Non-Metallic Materials) accreditations.

### 5.2.3 X-ray tomography inspection

To gain understanding into the microstructure of the baseline and interleaved systems, $\text{LTHIN}_{\text{IP}}$, $\text{LV1}_{\text{IP}}$ and $\text{LV2}_{\text{IP}}$ were inspected using a sub-micron resolution

μCT ($LV1_{IP}$ and $LV2_{IP}$ incorporate one veil in every interface). Inspections were performed with the Zeiss 160 kVp Versa 510 scanner at the μ-VIS X-ray Imaging Centre, Faculty of Engineering and Physical Sciences, University of Southampton (the equipment has a 2000 x 2000 pixels detector). The scan set up was altered to use a 20X magnifying lens. Prior to inspection, 1 x 1 mm (width and thickness) rectangular parallelepipeds were cut/polished from pristine laminates (high-resolution tomography requires inspecting small volumes and yet, ideally, the object should rotate fully within the field of view FOV [150]). The scanning parameters were 60 kV, 83.3 μA, 5 W, 7 s exposure time, 4001 projections and 783 nm pixel size, corresponding to an FOV of approximately 800 nm (to reduce noise and inspection time, the detector was used in the 2 x 2 binning mode). The source to detector and source to object distances were 16.85 and 9.92 mm, and the specimens were rotated through 360° during the acquisition of the 4001 projection images. It is worth noting that the incident energy was relatively low (60 kVp) in order to enhance the contrast between the CoPA veil fibres and the epoxy matrix (the linear attenuation coefficient of the constituents increases with decreased incident energy [150]), which reduced the flux of photons in the detector and, consequently, increased the inspection time (around 10 h per scan).

The fracture process zone (FPZ) of the DCB specimens was inspected "ex-situ" using the Versa system. Prior to inspection, 2 x 2 mm (width and thickness) rectangular parallelepipeds were cut/polished from the DCB samples (away from the specimens' free-edges). A fast "scout" low-resolution inspection was performed to identify the location of the FPZ (the shape of the matchsticks and the location of the FPZ are sketched in Fig. 5.1). Once the region of interest had been identified, the scan set up was altered to use a 4X magnifying lens and a higher-resolution scan was performed. The scanning parameters were 80 kV, 87.5 μA, 7 W, 2 s exposure time, 2001 projections, 1.22 μm pixel size and 1.24 mm FOV (the detector was used in the 2 x 2 binning mode). The source to detector and source to object distances were 82.35 and 14.9 mm, and the specimens were rotated through 360° during the acquisition of the 2001 projection images. Each inspection lasted for approximately 2 h. In total, at least 3 different $LTHIN_{G_{IC}}$ and $LV1_{G_{IC}}$ specimens (some of them in several positions through the width) as well as all of the $LV2_{G_{IC}}$ DCB samples (two

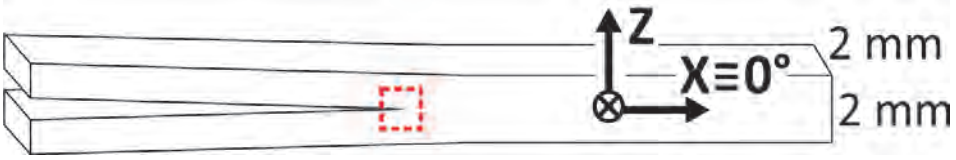


**Figure 5.1:** 2 x 2 mm (width and thickness) matchsticks cut from $LTHIN_{G_{IC}}$, $LV1_{G_{IC}}$ and $LV2_{G_{IC}}$ double cantilever beam (DCB) specimens. The square indicates the location of the fracture process zone (FPZ).

of them in multiple locations) were inspected.

During the microstructure assessment, the contrast between $V_1$ fibres and the epoxy resin was less satisfactory than expected (despite the low incident energy, polyamide and epoxy have similar chemical constituents, plus the veils being very light). To unambiguously observe $V_1$ fibres, one tested DCB LV1$_{G_{IC}}$ specimen was impregnated with a staining agent and subsequently scanned with the European Synchrotron Radiation Facility's ID19 Beamline (ESRF, Grenoble). The aim was that the contrast agent would impregnate and reveal the $V_1$ fibres interacting with the crack tip. The inspection parameters were 26 keV X-ray energy (almost monochromatic), 90 ms exposure time, 3001 projections, 650 nm pixel size, approximately 2 mm FOV and roughly 5 min total inspection time (the specimens were rotated through 360° during the acquisition of the 3001 projection images).

To facilitate the understanding of the images, some of the µCT stacks were post-processed using "Trainable Weka Segmentation" (a machine learning plugin from Image J [194]). The purpose was to classify the constituents of each material using a consistent colour code (Fig. 5.2): yellow for the 0° carbon fibres, cyan for the ±45° carbon fibres, orange for the 90° carbon fibres, green for the NCF stitching yarn fibres, purple for the $V_1$ veil fibres, red for the $V_2$ veil fibres and black for the cracks within the DCB specimens. It is worth noting that, despite their µCT low contrast, the shape of the $V_1$ fibres could be recognised because of the unequivocal debondings between the $V_1$ fibres and the resin, which were also painted in black (e.g. Fig. 5.5).

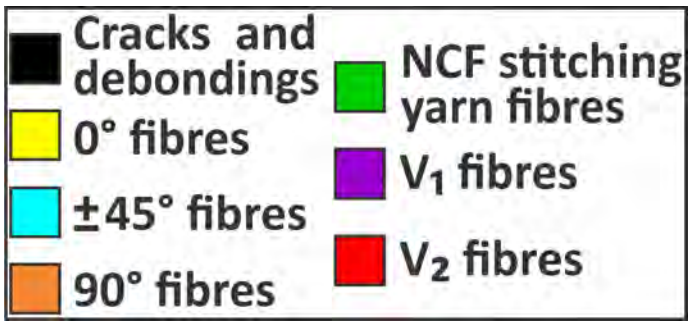


**Figure 5.2:** Colour legend of the post-processed X-ray tomography (µCT) images. NCF means non-crimp fabric. (For interpretation of the references to colour in this figure legend, the reader is referred to the web version of this article).

## 5.3 Results

### 5.3.1 Microstructure

The purpose of NCF stitches is not structural but rather to hold two layers together. However, the stitching yarns cause deviation of the fibres from their unidirectional

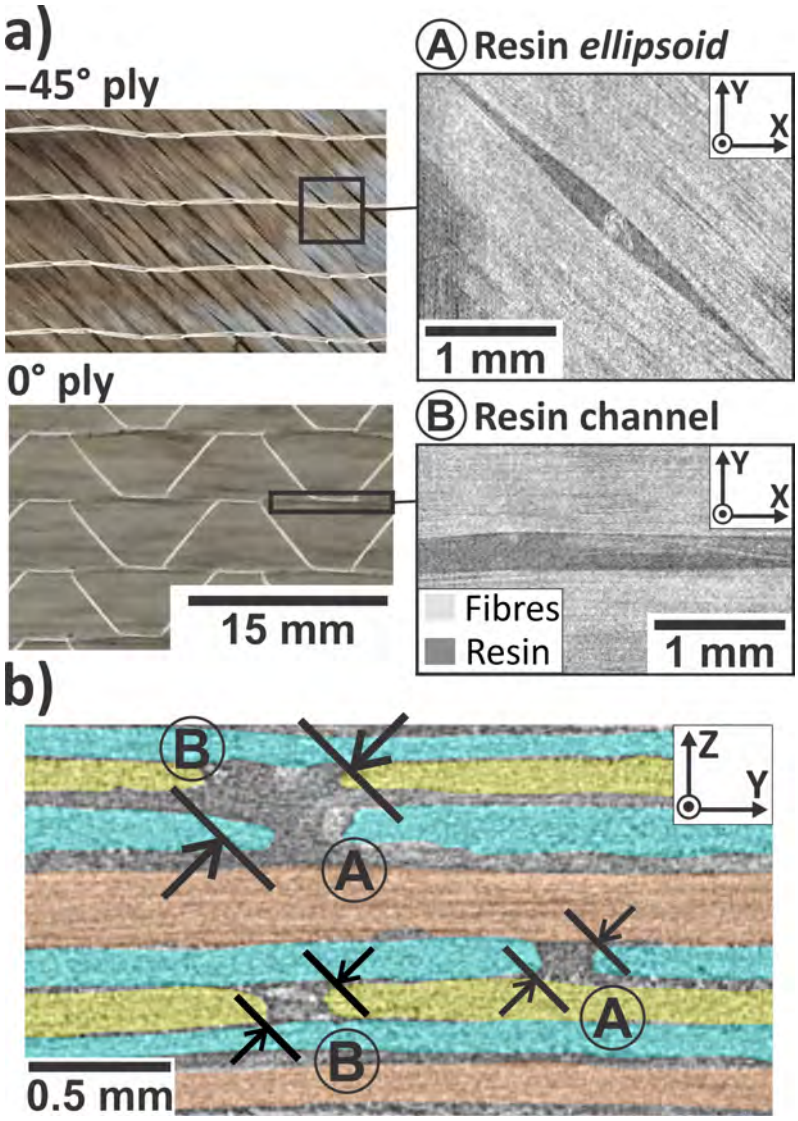


**Figure 5.3:** a) XY and b) XZ views of the resin pockets inherent to (0°/±45°) C-PLY$^{TM}$ NCFs (refer to the coordinate system defined in Fig. 5.1). A and B are the "resin ellipsoids" in the ±45° and the "resin channels" in the 0° plies. (For interpretation of the references to colour in this figure legend, the reader is referred to the web version of this article).

orientations. During resin infusion, the fibre-free regions provide preferential flow paths, resulting in the so-called "resin pockets" after laminate consolidation [195]. Fig. 5.3 describes the types of resin pockets induced by the 33 dtex polyester (PE) yarns that, using a warp-knitting pattern, stitch together the layers of the (0°/±45°) C-PLY$^{TM}$ NCFs. For clarity, μCT images were taken from a $[(45°/0°)/(-45°/90°)]_{2s}$ laminate made with thick-ply C-PLY$^{TM}$ NCFs (the size of the resin pockets increases with increased ply-thickness [165]). Fig 5.3a depicts the resin-rich regions as observed from the XY plane (refer to the coordinate axis defined in Fig. 5.1) i.e., the plane that is parallel to the specimen interfaces. The orientation of the resin

pockets follows the fibre orientation of the stitched ply forming, in the ±45° layers, a "resin ellipsoid" (A, also known as "fish eye" [196]). In the 0° ply, the overlapping of several distortions creates a "resin channel" that separates the 0° tows (B). The stitching yarns impact not only the surface of the fabrics, but also the entire thickness of the ply (Fig. 5.3b). The biggest resin pockets form when a fish eye (A) and a resin channel (B) intersect through the thickness. Besides inducing resin pockets, the stitches increase the interface thickness locally (refer to the interfaces adjacent to the intersection between A and B, Fig. 5.3b).

Figs. 5.4-5.8 illustrate the sub-micron resolution μCT inspections of the pristine $LTHIN_{IP}$, $LV1_{IP}$ and $LV2_{IP}$ specimens. The tomographies revealed no evidence of porosity in any of the laminates. Away from resin pockets, $LTHIN_{IP}$ presented a closely packed microstructure (Fig. 5.4). In contrast, interleaving $V_1$ (the veil with a higher fibre diameter and a more "open" architecture) increased the thickness of the resin rich interfaces (Fig. 5.5). We consistently observed debonding between $V_1$ fibres and the surrounding matrix (refer to the black decohesions in Fig. 5.5). Besides this, some of the $V_1$ fibres deformed the adjacent carbon plies (Fig. 5.6) —the fibre is visible because it was impregnated with a contrast agent. Interleaving $V_2$ (the veil with the smaller diameter fibres and a more packed architecture) only impaired the interface thickness in regions where the $V_2$ fibres agglomerated (refer to the red fibres in Fig. 5.7a). Despite the melting point of $V_2$ being lower than the laminate's post-curing temperature, most of the $V_2$ fibres conserved their initial shape after manufacturing (Fig. 5.8b). However, the $V_2$ fibres lying close to a

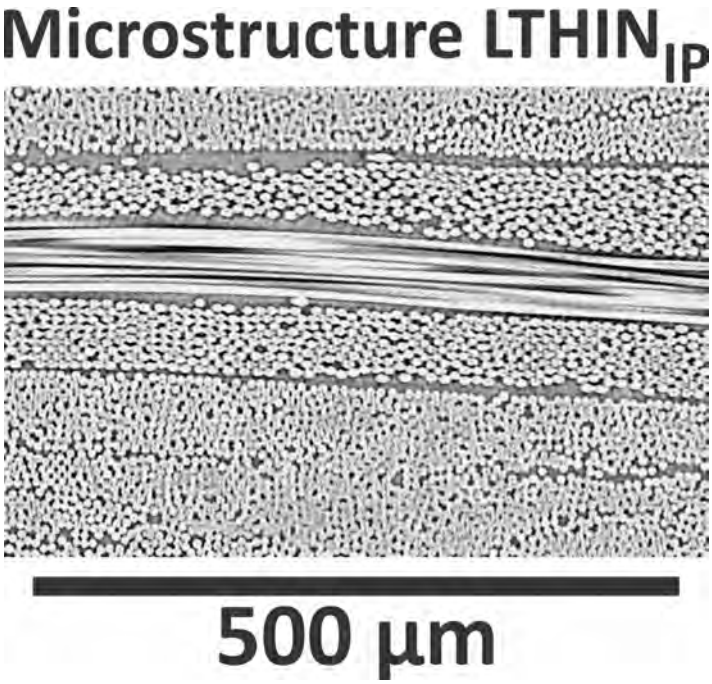


**Figure 5.4:** μCT cross-section depicting the microstructure of $LTHIN_{IP}$.

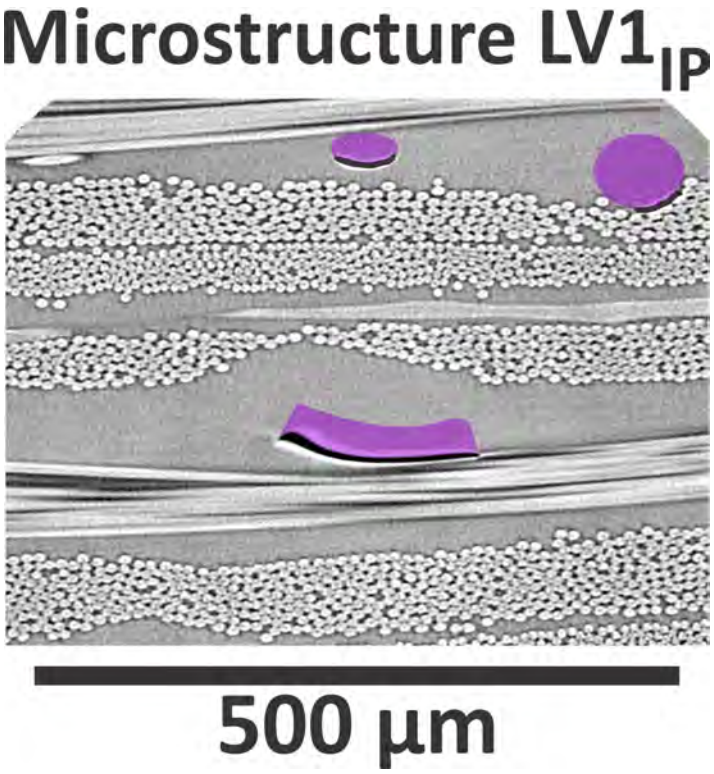


**Figure 5.5:** µCT cross-section depicting the microstructure of $LV1_{IP}$. $V_1$ fibres are coloured purple. Debondings between $V_1$ fibres and resin are coloured black. Despite the low contrast of $V_1$ fibres, their geometry is deduced from the unequivocal shape of the debondings.

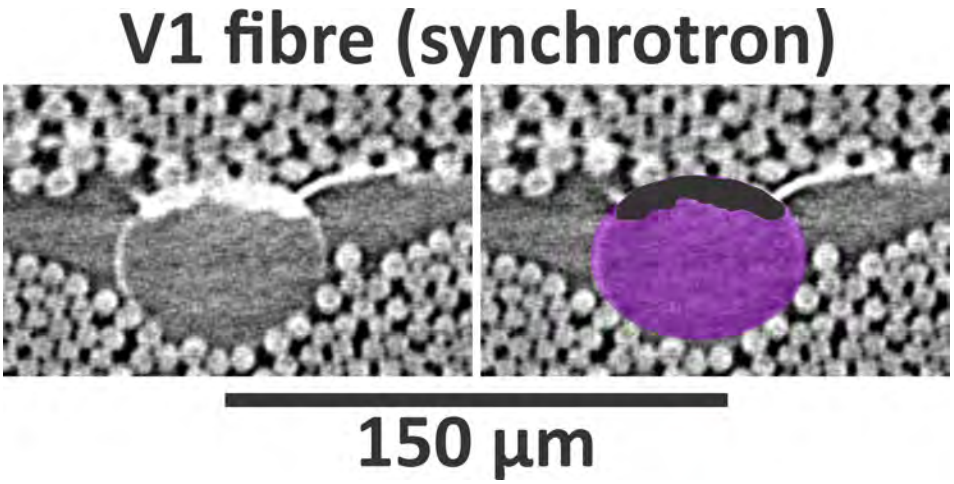


**Figure 5.6:** $V_1$ fibre observed with a synchrotron X-ray source (the fibre was impregnated with a contrast agent). The $V_1$ fibre is coloured purple. The debonding between $V_1$ fibre and the surrounding resin is coloured black.

carbon ply displayed multiple cracks (Fig. 5.8a). Finally, it is worth noting that, regardless of which material system was used, we also observed debonding between some of the stitching yarn fibres and the surrounding resin (for an example, refer to the green fibres in Fig 5.8b).

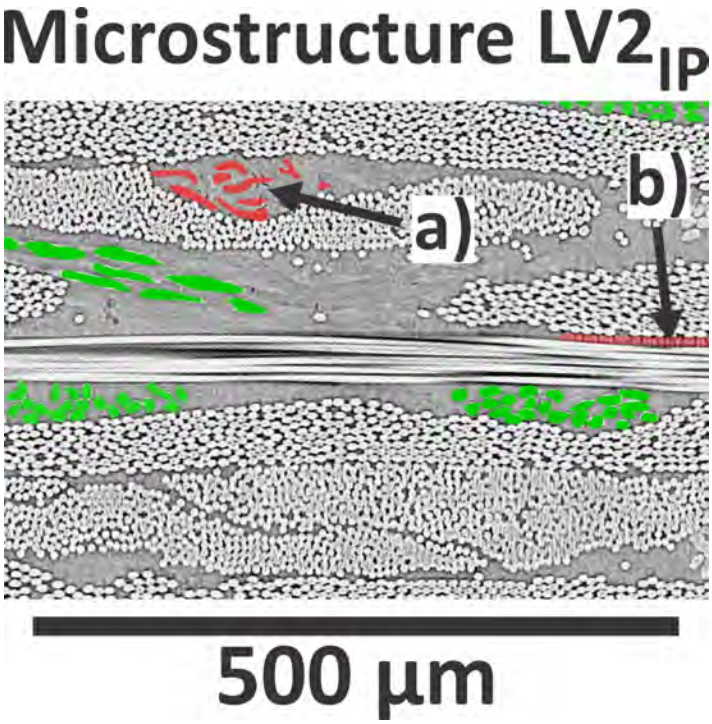


**Figure 5.7:** µCT cross-section depicting the microstructure of $LV2_{IP}$. NCF yarn fibres are coloured green. $V_2$ fibres are coloured red: a) is the accumulation of $V_2$ fibres, b) is the single $V_2$ fibre.

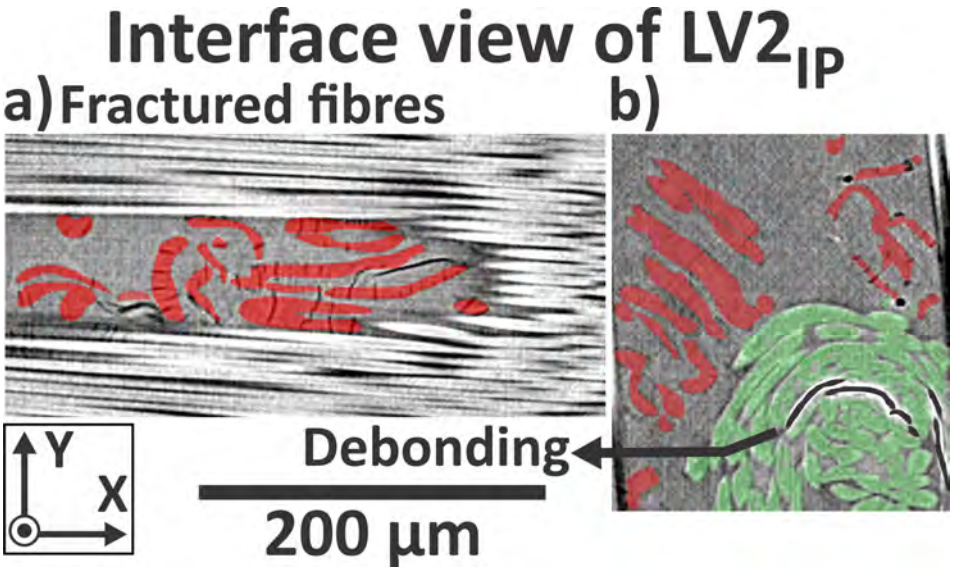


**Figure 5.8:** XY cross-sections depicting the microstructure of $LV2_{IP}$ (XY is the plane parallel to the specimen interfaces, Fig. 5.1). NCF yarn fibres are coloured green. Debonding between yarn fibres and resin are coloured black. $V_2$ fibres are coloured red: a) are the $V_2$ fibres laying close to a carbon tow b) are the $V_2$ fibres laying in a resin rich area.

### 5.3.2 Structural response

Fig. 5.9 summarizes the tensile and compressive properties of $LTHIN_{IP}$, $LV1_{IP}$ and $LV2_{IP}$ laminates. $LV2_{IP}$ displayed a similar tensile strength, strain-to-failure

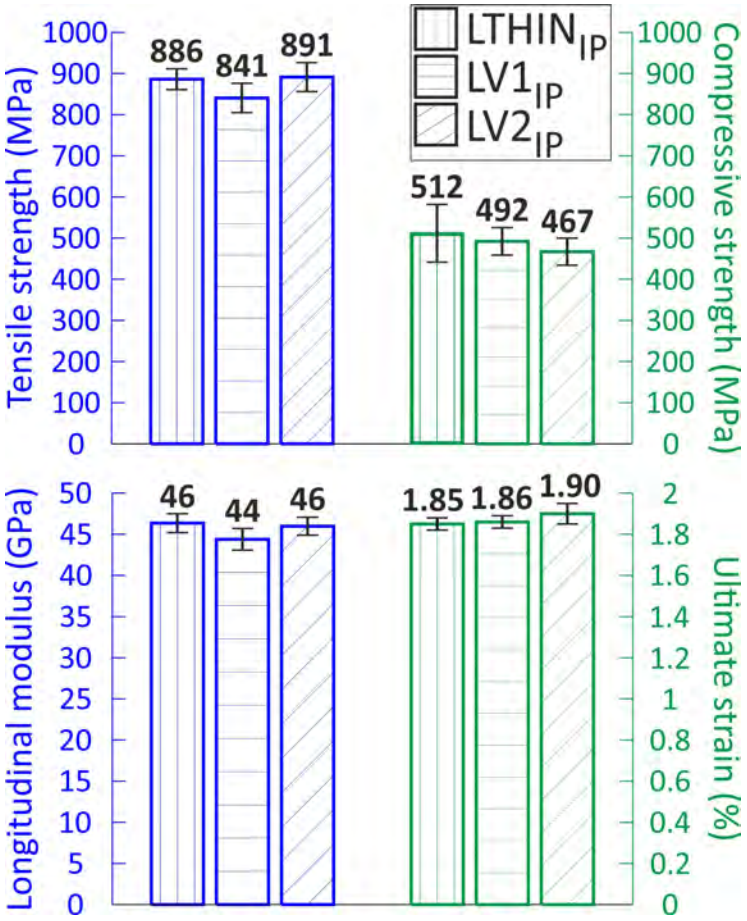


**Figure 5.9:** Tensile and compressive properties of LTHIN$_{IP}$, LV1$_{IP}$ and LV2$_{IP}$.

and longitudinal modulus as that of LTHIN$_{IP}$. In contrast, LV1$_{IP}$ decreased the elastic modulus and ultimate strength by 4% and 5%. LV2$_{IP}$ and some of the LV1$_{IP}$ tensile specimens changed the failure mode from a single crack to several cracks propagating across the width of the non-tabbed region. Regarding the compressive strength, interleaving both types of veil deteriorated the property by up to 9% in the case of LV2$_{IP}$ (and yet most of LV2$_{IP}$ values lay within the scatter of LTHIN$_{IP}$).

Figd. 5.10-5.11 presents the force response and average R-curves of the LTHIN$_{G_{IC}}$, LV1$_{G_{IC}}$ and LV2$_{G_{IC}}$ DCB specimens. Fig. 5.12 includes the average mode-I initiation ($G_{Iinit}$) and propagation ($G_{Iprop}$) interlaminar fracture toughness values. The load displacement curves of LTHIN$_{G_{IC}}$ displayed a range of shapes and propagation forces; the curves with a lower maximum force exhibited a jagged shape (i.e. with multiple load drops), whereas those with higher propagation forces were smoother. The curves of LV1$_{G_{IC}}$ featured a similar tendency than those of LTHIN$_{G_{IC}}$, albeit with higher variation and more intensified load oscillations. The force response of LV2$_{G_{IC}}$ evidenced less variation and smaller load drops than those of LTHIN$_{G_{IC}}$ and LV1$_{G_{IC}}$, resulting in the highest $G_{Iinit}$ and $G_{Iprop}$ of all the systems. LV2$_{G_{IC}}$ enhanced $G_{Iinit}$ and $G_{Iprop}$ by 101% and 43% compared to LTHIN$_{G_{IC}}$. LV1$_{G_{IC}}$ only

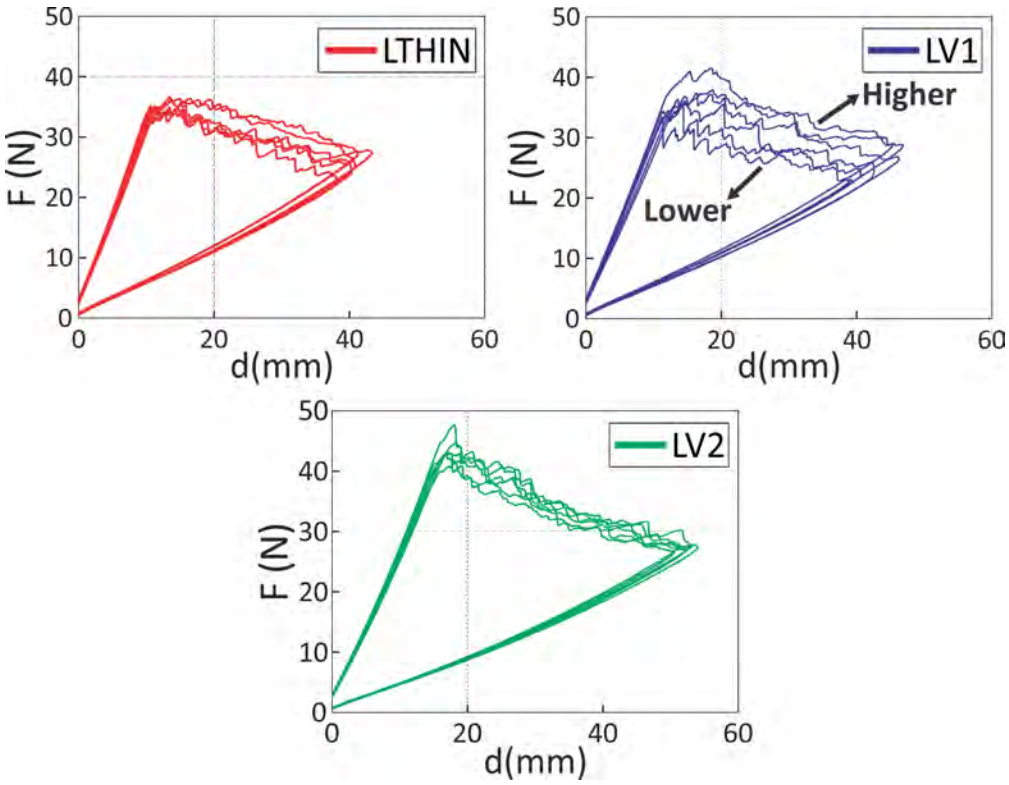


**Figure 5.10:** Force response of the LTHIN$_{G_{IC}}$, LV1$_{G_{IC}}$ and LV2$_{G_{IC}}$ DCB specimens.

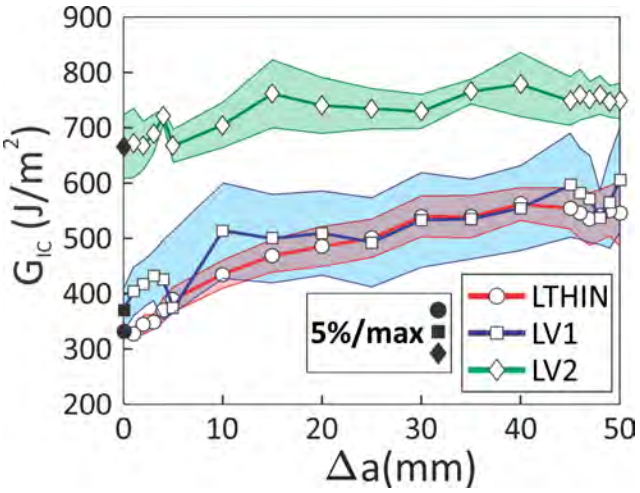


**Figure 5.11:** Average R-curves of the LTHIN$_{G_{IC}}$, LV1$_{G_{IC}}$ and LV2$_{G_{IC}}$ DCB specimens.

improved $G_{\text{Iinit}}$ by 12%.

### 5.3.3 Fracture process zone

Figs. 5.13-5.14 illustrate the sub-micron resolution μCT inspections performed in the FPZ of the LTHIN$_{G_{IC}}$, LV1$_{G_{IC}}$ and LV2$_{G_{IC}}$ DCB specimens. The crack grows towards the reader. In particular, Figs. 5.13a and 5.14 summarize the mode-I propagation mechanisms of LTHIN$_{G_{IC}}$ when inspected in the different y-positions of the same specimen (refer to the coordinate system defined in Fig. 5.1). In Fig.

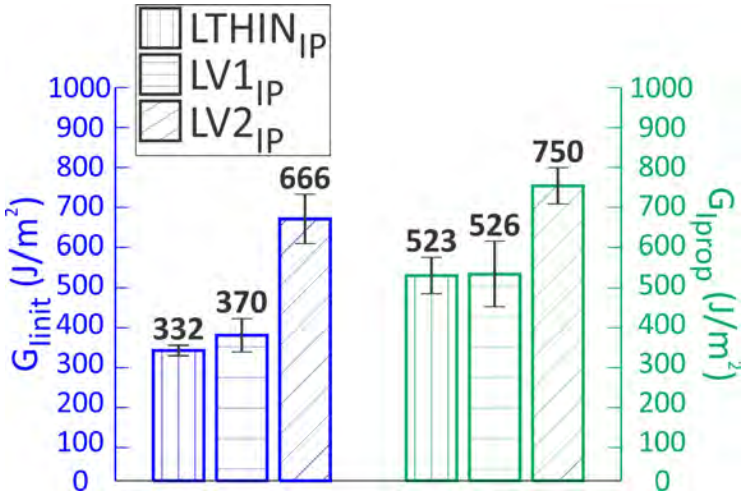


**Figure 5.12:** Mode-I initiation ($G_{\text{Iinit}}$) and propagation ($G_{\text{Iprop}}$) interlaminar fracture toughness of LTHIN$_{G_{IC}}$, LV1$_{G_{IC}}$ and LV2$_{G_{IC}}$.

5.13a, the crack propagates across the 0°/0° interface (the 0° carbon fibres and the crack are coloured yellow and black, respectively). In Fig. 5.14, the crack deviates from the 0°/0° interface through the debonding of the stitching yarn fibres (the yarn fibres are coloured green). The YZ view of the figure displays how, after interaction with the stitching yarn fibres, the unbalanced crack preferrs to propagate inside a 0° carbon tow rather than continuing to face the stitching yarn fibres of the 0°/0° interface. Regarding LV1$_{G_{IC}}$, the crack interacted with both $V_1$ fibres and stitching yarn fibres and yet it was confined to the interfaces (Fig. 5.13b). ($V_1$ fibres are coloured purple). In contrast, the crack of LV2$_{G_{IC}}$ propagated inside the 0° layers (Fig. 5.13c) —except when it interacted with the NCF yarn fibres.

## 5.4 Discussion

We manufactured two types of interleaved laminates with no porosity, the same nominal thickness and a similar fibre volume fraction as the non-interleaved baseline laminate (e.g. the average thickness of LTHIN$_{IP}$, LV1$_{IP}$ and LV2$_{IP}$ varied between 2.21-2.37, 2.22-2.25 and 2.18-2.22 mm, and their average fibre volume fraction was 53.50±1.63%, 53.53±1.65% and 53.67±1.25%). Interleaved laminates displayed a similar nominal thickness because of the combination of low veil fibre areal weight (4 g/m$^2$) and RTM manufacturing: all of the laminates fitted within the same mould. Incorporating the same amount of carbon fibre within a fixed volume results in a similar fibre volume fraction as measured by acid digestion methods [163]. The lack of porosity is also attributed to the low fibre areal weight of the veils (light veils allow through-thickness resin infusion [16, 19]).

Interleaving $V_1$ increased the thickness of the resin interfaces. In contrast, interleaving $V_2$ only increased interface thickness in regions where $V_2$ fibres agglomerated

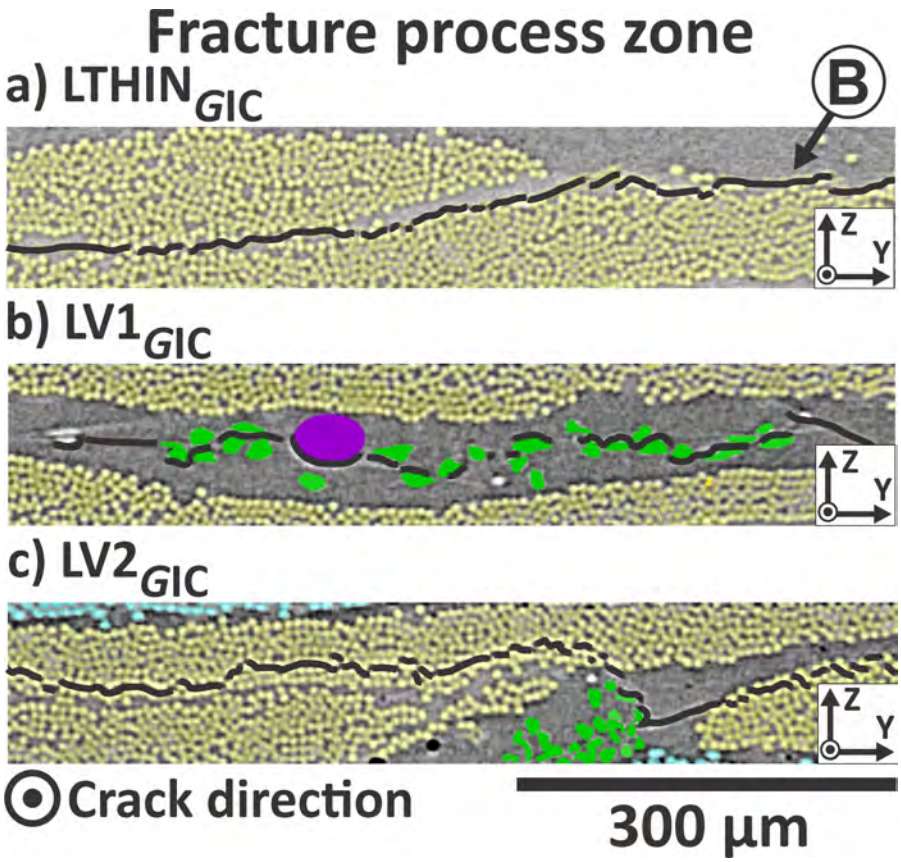


**Figure 5.13:** µCT cross-sections depicting the FPZ of the LTHIN$_{G_{IC}}$, LV1$_{G_{IC}}$ and LV2$_{G_{IC}}$ DCB specimens. The crack grows towards the reader. 0° carbon fibres are coloured yellow. NCF yarn fibres are coloured green. The $V_1$ fibre is coloured purple. Mode-I cracks are coloured black. "B" is the resin channel (refer to Fig. 5.3).

(compare Figs. 5.4-5.5 and 5.7). Despite the melting temperature of $V_2$ being lower than the laminate's post-curing temperature, most of the $V_2$ fibres maintained their original shape after manufacturing (refer to the red fibres in Fig. 5.8b). However, $V_2$ fibres lying close to a carbon tow displayed multiple cracks (Fig. 5.8a). LV1$_{IP}$ accumulates resin in the interfaces because the fibre diameter of $V_1$ (37 µm) is much higher than the interface thickness of LTHIN$_{IP}$ (approximately 10 µm). $V_2$ fibres conserve their inital shape because of the competition between fibre melting and resin gelification (when $V_2$ fibres start to yield, the resin is viscous enough to lock in the position of the fibres [13]). The cracks in veils $V_2$ develop because the stiff carbon tows hinder not only the movement, but also the thermal contraction of the $V_2$ fibres (thermal stresses dissipate in the form of cracks). Therefore, the only possible movement is $V_2$ fibres diffusing along with resin infusion (before curing) [13, 115], which would explain the agglomerations observed in LV2$_{IP}$ (Fig. 5.7a).

We consistently observed debonding between $V_1$ fibres and the surrounding matrix (refer to the purple fibres in Figs. 5.5-5.6). The same observation applied for NCF

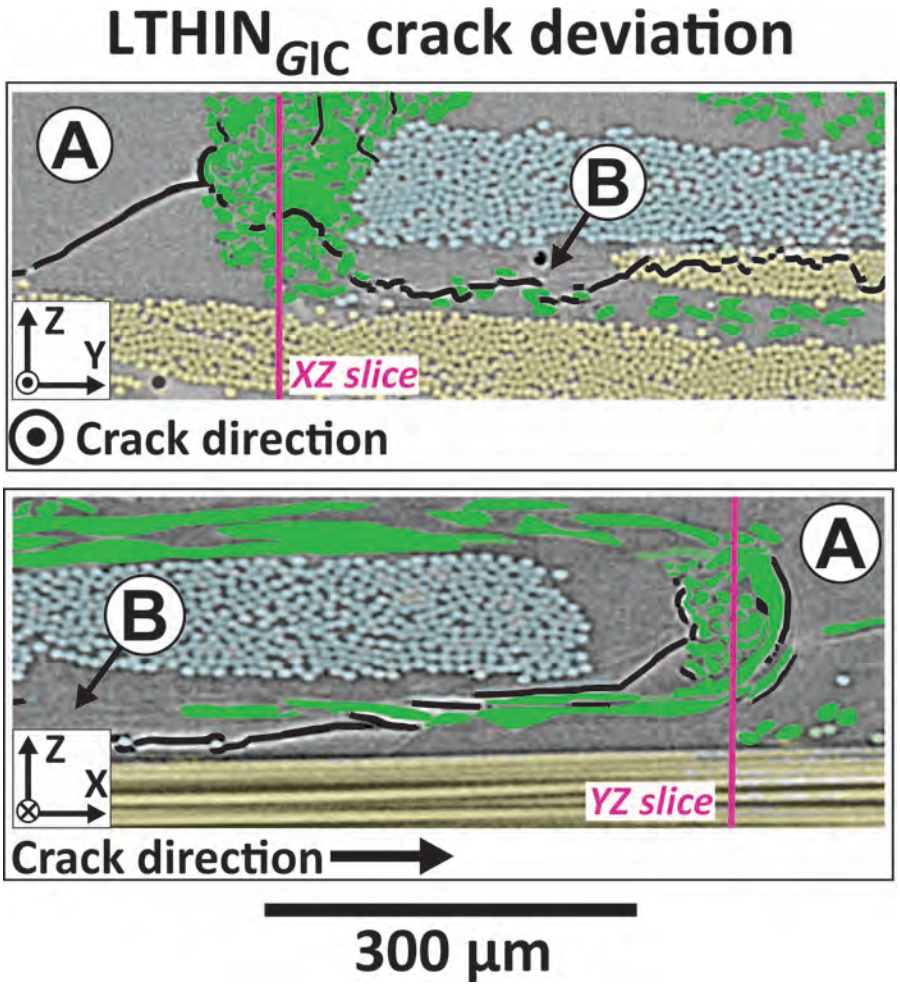


**Figure 5.14:** Interaction between the crack of LTHIN$_{G_{IC}}$ and the NCF yarn fibres. In the YZ view, the crack grows towards the reader. In the XZ view, the crack grows left-to-right. 0° carbon fibres are coloured yellow. −45° carbon fibres are coloured cyan. NCF yarn fibres are coloured green. Mode-I cracks are coloured black. "A" and "B" are the resin ellipsoid and resin channel (refer to Fig. 5.3).

stitching yarn fibres (e.g. the green fibres in Fig. 5.8b). In contrast, the $V_2$ fibres displayed almost no decohesions with the resin (e.g. the red fibres in Fig. 5.8b). Based on the observations, it is clear that $V_2$ fibres have an improved adhesion with epoxy than $V_1$ or stitching yarn fibres do.

LV2$_{IP}$ displayed a similar tensile strength, strain-to-failure and longitudinal modulus as that of LTHIN$_{IP}$. In contrast, LV1$_{IP}$ reduced the tensile modulus and ultimate strength by 4% and 5% (Fig 5.9). The tendencies observed are directly connected to the microstructure of the materials. The tensile properties of LV2$_{IP}$ are similar to these of LTHIN$_{IP}$ because both laminates have a similar nominal thickness, fibre volume fraction and (overall) interface thickness. Provided LV1$_{IP}$ also has a similar nominal thickness and fibre content, the decrease of tensile properties can only be attributed to the larger diameter of $V_1$ fibres: the thick $V_1$ fibres locally compact the

carbon plies and reduce carbon uniformity across the thickness (Fig. 5.6).

LTHIN$_{G_{IC}}$, LV1$_{G_{IC}}$ and LV2$_{G_{IC}}$ featured different crack propagation mechanisms (Figs. 5.13-5.14). Mode-I crack growth is mainly governed by the adhesion between the fibres (the stitching yarn fibres, the $V_1$ fibres or the $V_2$ fibres) and the matrix [124]. Fibres with a suspected low adhesion (the yarn fibres and the $V_1$ fibres) promote crack propagation by fibre-resin debonding [133]. Fibres with a suspected higher adhesion (the $V_2$ fibres) avoid interacting with the crack [126, 133]. Therefore, it seems logical that the crack of LTHIN$_{G_{IC}}$ interacts with the yarn fibres (the green fibres in Fig. 5.14), the crack of LV1$_{G_{IC}}$ interacts with the $V_1$ fibres (the purple fibre in Fig. 5.13b) and the crack of LV2$_{G_{IC}}$ migrates away from the veil (particularly into the 0° layers, Fig. 5.13c). As a result of these interactions, the crack of LV1$_{G_{IC}}$ confines itself to the 0°/0° interface (Fig. 5.13b), the crack of LV2$_{G_{IC}}$ propagates across the 0° plies (Fig. 5.13c) and the crack of LTHIN$_{G_{IC}}$ meanders among the 0°/0° interface and the 0° layers (some of the stitching yarns diverted crack propagation from the resin interlayer into the 0° plies, Figs. 5.13a and 5.14).

LV2$_{G_{IC}}$ enhanced $G_{\text{Iinit}}$ and $G_{\text{Iprop}}$ by 101% and 43% compared to LTHIN$_{G_{IC}}$. LV1$_{G_{IC}}$ only enhanced $G_{\text{Iinit}}$ by 12% (Fig. 5.12). The FPZ observations suggest that $V_1$ fibres dissipate fracture energy as they interact with the crack (Fig. 5.13b). Dissipation mechanisms probably include fibre deformation and fibre pull-out from the matrix [124]. However, LV1$_{G_{IC}}$ did not affect the the baseline $G_{\text{Iprop}}$ because of the low number of $V_1$ fibres interacting with the crack (the surface area covered by $V_1$ was only 22%) [15]. The 101% $G_{\text{Iinit}}$ improvement displayed by LV2$_{G_{IC}}$ is explained if, during initiation, the crack required extra energy to circumvent $V_2$ fibres and penetrate into the 0° plies. This would correlate with the observations of the FPZ and justifies why the improvement of $G_{\text{Iprop}}$ is smaller than that of $G_{\text{Iinit}}$ (43% versus 101%): intralaminar crack propagation is independent of $V_2$ fibres (Fig. 5.13c).

The tendencies observed in LV2$_{G_{IC}}$ are contrary to standard-ply studies where the veil fibres with higher adhesion provide the lower $G_{IC}$ values. Saz-Orozco *et al.* [126] reported that a 45 g/m$^2$ polyethylene terephtalate veil deviated crack initiation from the resin interlayer (full of veil) to the interfacial region between resin and structural fibres (depleted of veil), which had no effect on $G_{\text{Iprop}}$ and decreased $G_{\text{Iinit}}$ by 32%. The difference is that LV2$_{G_{IC}}$ deviated crack propagation not to the interfacial but to the intralaminar region (i.e. the 0° plies in Fig 5.13c), which increased the initiation energy. We speculate that this is the consequence of several factors such as the smaller interface thickness of thin-plies, the shape distortions induced by NCF stitches and the low fibre areal weight and fibre diameter of $V_2$

preventing resin accumulation in the interfaces (there is no such resin layer depleted of veil).

For the veil configurations studied, interleaving $V_2$, the veil with lower fibre diameter, minimized the impairment of interface thickness and resulted in a reasonable trade-off between mode-I interlaminar fracture toughness and in-plane properties. We believe this trade-off could be further improved if, for the given veil fibre areal weight, fibre diameter was reduced (which means increasing the surface area covered by veil fibres while minimizing their impact on interface thickness) [15]. For example, Beylergil *et al.* [197] enhanced interlaminar fracture toughness along with certain impact, flexural and compressive properties by interleaving 1 g/m$^2$ PA nano-fibre veils (the mean fibre diameter was 110 nm). However, toughening nano-fibre veils entailed an evident disadvantage: the manufacturing costs. In this sense, light CoPA micro-fibre veils (in particular $V_2$) offer the perfect balance between price, properties, commercial availability and ease of manufacture, ideal to toughen thin-ply laminates.

## 5.5 Conclusions

We manufactured a thin-ply quasi-isotropic baseline laminate and laminates interleaved with two types of 4 g/m$^2$ co-polyamide veils (named $V_1$ and $V_2$). The combination of the low veil fibre areal weight and a resin transfer mould was crucial to preserve laminate thickness and fibre volume fraction: baseline and interleaved configurations fitted within the same mould. None of the laminates displayed porosity, evidencing that light veils allow through-the-thickness resin flow.

Given the similar laminate thickness, the veil fibre diameter was the key parameter in determining the tensile properties. The veil with thicker fibres ($V_1$) increased the thickness of the resin interfaces and reduced the tensile properties (elastic modulus and ultimate strength were reduced by 4% and 5%). The veil with the smaller diameter fibres ($V_2$) avoided resin accumulation in the interfaces and displayed the same tensile strength, strain-to-failure and longitudinal modulus as the baseline laminate did. Both types of veil decreased compressive strength by up to 9% because of an increase in the ductile phase surrounding the carbon plies, which favours fibre buckling.

Mode-I interlaminar crack propagation was mainly controlled by the adhesion between fibres (the non-crimp fabric yarn fibres, the $V_1$ fibres and the $V_2$ fibres) and the resin. Fibres with a low adhesion (the yarn fibres and the $V_1$ fibres) promoted crack growth by debonding from the resin. Fibres with a higher adhesion (the $V_2$ fibres) deviated crack growth away from the veil. In the non-interleaved laminate,

the crack deviated from the 0°/0° interface through debonding of the stitching yarn fibres. In the laminate interleaved with $V_1$, the crack confined into the 0°/0° interface through interaction with the $V_1$ fibres (fracture toughness was not improved because the veil $V_1$ contained few fibres). In the laminate interleaved with $V_2$, the crack jumped from the 0°/0° interface to the surrounding 0° plies which, in the material system studied, resulted in the highest mode-I initiation and propagation interlaminar fracture toughness (101% and 43% increase compared to the baseline).

# Paper D

# 6

## The effect interleaving has on thin-ply non-crimp fabric laminate impact response: X-ray tomography investigation

S.M. García-Rodríguez[a,*], J. Costa[a], V. Singery[b], I. Boada[c], J. A. Mayugo[a]

[a]AMADE, Polytechnic School, University of Girona, Av. Universitat de Girona, 4. 17003 Girona, Spain

[b]Chomarat, 39 Avenue de Chabannes, 07160, Le Cheylard, France

[c]Graphics and Imaging Laboratory, University of Girona, Av. Universitat de Girona, 4. 17003 Girona, Spain

Published in *Composites Part A: Applied Science and Manufacturing* 107 409-420 (2018). doi: https://doi.org/10.1016/j.compositesa.2018.01.023

* Corresponding author

**Overview**

Paper D compares the impact resistance, tolerance and damage sequence of the thin-ply baseline laminate and laminates interleaved with with $V_1$ and $V_2$ veils ($LTHIN_{LVI}$, $LV1_{LVI}$ and $LV2_{LVI}$, Table 1.2). The aim of this paper is to fulfil the objective 4 in Section 1.2 as well as addressing the corresponding open question in Table 1.1. Impact resistance and tolerance are characterized with the drop-weight impact and compression after impact experiments, while damage sequence is elucidated by combining QSI testing with X-ray micro-computed tomography (μCT) inspections.

Paper D also compares the microstructure of baseline and interleaved configurations. However, there are several contradictions between the conclusions reached by papers C and D (the preliminary μCT inspections of paper D were carried out prior to the more detailed sub-micron resolution acquisitions of paper C). Firstly, paper D claims that $V_1$ fibres accumulate resin at the interfaces because they do not melt during manufacturing. However, paper C clearly evidences that this is a consequence of the higher diameter of $V_1$ fibres compared to their $V_2$ counterparts ($37\pm4$ μm and $11\pm2$ μm for $V_1$ and $V_2$). Secondly, paper D claims that interleaving $V_1$ veils causes porosity during manufacturing (Fig. 6.5). However, paper C demonstrates that all the laminates are free of porosity (Figs. 5.4-5.5 and 5.7). (Paper D confused the debonding between $V_1$ fibres and resin with porosity, Figs. 5.5 and 6.5). Neglecting these microstructural aspects, paper D provides comprehensive insight into the impact response of baseline and interleaved laminates.

**Abstract**

To improve the damage resistance and tolerance of thin laminates manufactured with thin-ply non-crimp-fabrics, we interleaved non-woven veils into the interlaminar regions (two different types of co-polyamide veil were studied). We devised a low velocity impact and compression after impact (CAI) experimental campaign, where quasi-static indentation (QSI) tests at increasing loading displacements gave insight into the damage initiation and growth. For impact and QSI, the damage area was inspected using C-scan and X-ray micro-computed tomography. We observed that the melting temperature of the co-polyamide fibres has a key role on the impact response of thin-ply NCFs. Veils that melt during manufacturing avoided resin accumulation at the interfaces, decreased the damage area by more than 100% for a 14 J impact and improved CAI strength by up to 28%.

*Keywords*: Thin-ply, Interleaving B. Compression after impact, D. CT analysis

## 6.1 Introduction

In an effort to reduce costs, the airline industry is increasingly considering thinner carbon fibre reinforced composite laminates manufactured using cost-efficient resin infusion (RI) methods. Both facts accentuate the out-of-plane susceptibility of such types of components. For instance, bending stiffness decreases when laminate thickness is reduced [198] and RI is limited to low viscosity resins that are inherently brittle [10]. In service, accidental impacts may reduce the load-carrying capacity as a result of matrix cracking, delamination and fibre breakage [76, 88].

New manufacturing approaches, such as the tow spreading method, allow plies thinner than 125 µm (so-called "thin-plies") to be produced [2] and, in turn, these are attracting growing interest because in-situ strength is increased [21, 25] and certain in-plane mechanical properties are improved [2, 3, 54, 60, 62]. During impact, matrix cracking and delamination are delayed in the thin-plies [98, 113]. Despite the evident contributions in terms of laminate strength, decreasing ply-thickness deteriorates the translaminar fracture toughness [68, 199] and consequently, designing damage-tolerant components using thin-ply laminates requires the incorporation of toughening methods.

Many investigations have added toughening agents during the manufacturing process to improve the interlaminar fracture toughness. Reinforcements can be incorporated through-the-thickness (e.g. Z-pins), mixed within the matrix (e.g. soluble rubber particles) or incorporated in the interlaminar regions (e.g. thermoplastic films) [16].

Yet other studies have hybridized carbon and glass to improve translaminar fracture toughness [88, 200]. In our investigation, we focus on a relatively unexplored interlaminar toughening approach: interleaving with non-woven veils [10]. We selected this type of additive because of its cost effectiveness, its suitability for RI and its potential to arrest delamination [10, 16, 143].

Walker *et al.* [122] interleaved polyamide (PA) veils in every interface of carbon/epoxy layups and found the thermoplastic webs were able to localise impact damage without any flexural stiffness deterioration. Nash *et al.* [16] toughened quasi-isotropic carbon/benzoxazine non-crimp fabric (NCF) laminates with non-woven PA veils. As the number of interleaved interfaces increased, the projected delamination area decreased and the specimens presented a lower difference between residual and undamaged compressive strength. Hogg [143] and Zhu [117] improved the CAI strength of carbon/epoxy laminates (unidirectional and woven fabrics, respectively) by interleaving different types of thermoplastic veils.

The objective of this investigation is to (a) understand the impact damage mechanisms of carbon/epoxy thin layups manufactured with thin-ply NCFs and (b) characterize the effect interleaving co-polyamide (CoPA) non-woven veils has on damage resistance and tolerance. We considered laminates thinner than the standard (i.e. approximately 2 mm rather than 4-6 mm [93]) because they are closer to the thickness of the skins currently used in aircraft components. We carried out low-velocity impact, quasi-static indentation (QSI) and compression after impact testing. Damage caused by impact and QSI was inspected through ultrasonic C-scans and X-ray micro-computed tomography (μCT). The latter provided comprehensive insights into the effect interleaving has on the pattern of impact damage.

## 6.2 Materials and methods

### 6.2.1 Materials

We used T700 GC carbon in the form of bi-axial NCFs (C-PLY$^{TM}$ from Chomarat, material reference C-PLY SP0/(±)45 67/67 CT3,4 12KT700GC X125CM). (0°/45°) and (0°/−45°) blankets of 134 g/m$^2$ fibre areal weight (67 g/m$^2$ per unidirectional ply) were used. NCFs combine the perfect placement of the reinforcing fibres with an easy-to-handle, cost-effective, automated fabrication i.e., an ideal combination when manufacturing plies of reduced thickness [48]. C-PLY$^{TM}$ fabrics were infused with HexFlow® RTM6 epoxy resin.

Quasi-isotropic $[(45°/0°)/(-45°/90°)]_{4s}$ laminates (LTHIN$_{LVI}$) were manufactured with the carbon C-PLY$^{TM}$ reinforcement, where the bi-angle NCF layers are indicated by parenthesis. Additionally, quasi-isotropic $[(45°/V_i/0°)/V_i/(-45°/V_i/90°)/\bar{V}_i]_{4s}$

($i$ = 1,2) laminates were considered: $LV1_{LVI}$ and $LV2_{LVI}$, where the bar sign signifies only one veil in the symmetry plane. $V_1$ and $V_2$ were two confidential low-density web-like materials made of dispersed CoPA fibres ("non-woven veils"). Their melting point was higher ($V_1$) and lower ($V_2$) than the post-curing temperature (180 °C). In addition, while they both had the same fibre areal weight (4 g/m$^2$), $V_1$ presented a more open-web architecture formed of fibres with a greater diameter than those of $V_2$.

Laminates were manufactured using resin transfer moulding (RTM). A single interlayer was incorporated in every interlaminar region of interleaved systems (NB: Chomarat incorporated the veils between the carbon plies of the NCFs during the stitching process, whereas the rest of interleafs were cut/placed manually during the pre-forming). The layups were pre-formed in a vacuum hot-press set at 85 °C for 10 min. Prior to infusion, the resin was degassed for 5 min in a vacuum oven set at 80 °C and 900 mbar (absolute value). Afterwards, the resin was heated to 120 °C and infused at low pressure (maximum of 8 bars) into the dry fabric preform, which had been previously placed on a heated aluminium mould. The infusion temperature, pressure and vacuum were controlled to ensure a resin flow of 20-30 g/min for 20 min. To cure the resin, the mould was heated to 170 °C for 90 min. During the first 30 min of curing, the heat was maintained along with the infusion pressure, which ceased for the remainder of the process. Once cooled, the laminates were removed from the tool and post-cured, i.e. heated from room temperature to 180 °C at 1 °C/min, followed by 120 min of dwell time, and then cooled to room temperature at 1 °C/min. The average thickness values of $LTHIN_{LVI}$, $LV1_{LVI}$ and $LV2_{LVI}$ tested specimens were 2.24±0.07, 2.21±0.04 and 2.17±0.03 mm, where ± means standard deviation. Their average fibre volume fractions were 54.81±1.97%, 54.40±1.68% and 54.04±1.57%, respectively (five samples were measured per laminate according to the standard EN 2564:1998 [163]). For the same type of material, specimens with a higher thickness presented the lowest fibre volume fraction values.

### 6.2.2 Experimental tests

Impact testing was performed in a CEAST Fractovis Plus 7536 drop-weight tower with a 16 mm diameter hemispherical impactor. Specimens 100 mm wide x 150 mm long were positioned over a metallic fixture base with a 75 mm x 125 mm rectangular cut-out and restrained with four rubber-tipped clamps. For further details of the test configuration, refer to González *et al.* [88]. The data provided by the drop-weight tower were the impactor's force (the former was instrumented with a load cell) and initial impact velocity (measured with an optical sensor). This

data was used to calculate the displacement and velocity of the impactor during the test [88]. A sampling rate of 1000 kHz was considered. From a preliminary study, the experiments were conducted at 10 and 14 J impact energy to ensure that a considerable amount of damage (i.e. development of visible back-face fibre breakage) occurred in all the samples.

QSI tests were performed using an electromechanical MTS INSIGHT®100 testing machine with a 10 kN load-cell. The same boundary conditions and hemispherical indenter were used during the impact and QSI experiments because the purpose of the latter was to imitate the sequence of damage mechanisms that take place during impact events [92, 95, 96]. Indentation was conducted at a rate of 0.5 mm/min to avoid dynamic effects. The energy applied to the system was obtained by integrating the area below the force-displacement curve. Three specimens per material system were indented to a different deflection, defined as the displacement of the indenter during the test. The smaller deflections (d = 4 and 4.4 mm) were chosen based on the onset of acoustic emissions heard during testing of the $\text{LTHIN}_{\text{LVI}}$ baseline. The higher deflection (d = 5.24 mm) was selected based on the load drop observed in the same material. These deflections resulted in energies of approximately 4, 5.5 and 8 J. The combination of QSI displacements and impact energies provided insight into the damage initiation and damage growth.

CAI tests were performed using an electromechanical MTS INSIGHT®300 testing machine with a 300 kN load cell. A non-standard CAI device based on the design

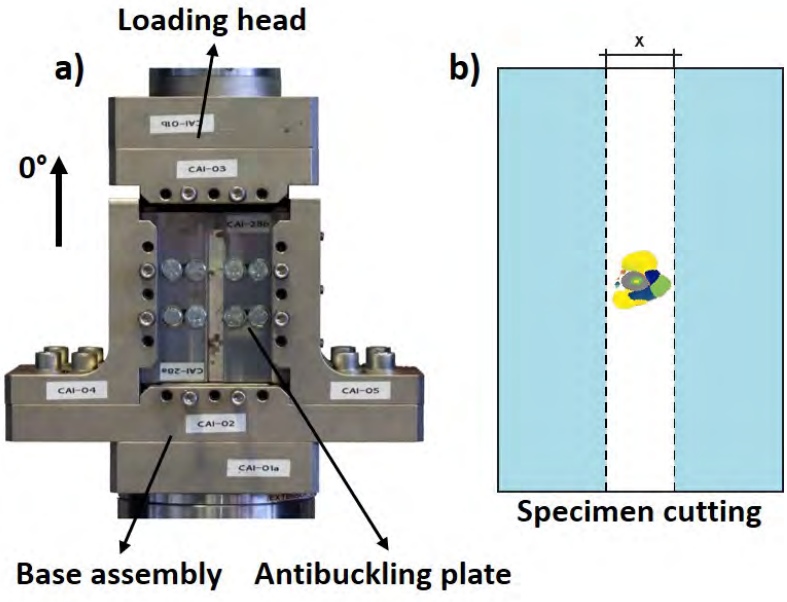


**Figure 6.1:** a) Non-standard compression after impact (CAI) test fixture (adopted from [112]). 1b) Cutting of indented specimens prior to inspection with X-ray micro-computed tomography (μCT).

**Table 6.1:** Test matrix. For details of the stacking sequence of $LTHIN_{LVI}$, $LV1_{LVI}$ and $LV2_{LVI}$ refer to Table 1.2.

| Name | Number of specimens tested | | | | | | | |
|---|---|---|---|---|---|---|---|---|
| | Impact | | CAI | | | QSI | | |
| | 10 J | 14 J | 0 J | 10 J | 14 J | d = 4 mm | d = 4.4 mm | d= 5.24 mm |
| $LTHIN_{LVI}$ | 3 | 5 | 2 | 3 | 5 | 1 | 1 | 1 |
| $LV1_{LVI}$ | 3 | 4 | 2 | 3 | 4 | 1 | 1 | 1 |
| $LV2_{LVI}$ | 3 | 5 | 2 | 3 | 5 | 1 | 1 | 1 |

from Remacha *et al.* [112] (Fig. 6.1a) was used. This fixture enabled the testing of laminates thinner than those recommended by the standard ASTM 7137/D7137M [93], which would otherwise fail by structural global buckling [112, 178, 179]. It consisted of two anti-buckling plates with equally spaced vertical ribs to stabilize the specimen on the vertical plane. The central rib included a cut-out to prevent any interference with the damaged zone, ensuring local buckling-induced failure and allowing for damage propagation during compression. A load rate of 0.5 mm/min was considered.

The impact, QSI and CAI test matrix is presented in the Table 6.1. The entire campaign was performed at 23±2 °C temperature and 50±5% relative humidity in the mechanical testing laboratory at the University of Girona. The laboratory is ISO17025 and NADCAP (non-metallic materials) accredited.

### 6.2.3 Damage inspection

A small piece from each of the $LTHIN_{LVI}$, $LV1_{LVI}$ and $LV2_{LVI}$ (non-impacted) laminates was embedded into a two-component epoxy and inspected using an epi-fluorescence microscope, whereas impacted and indented specimens were inspected by ultrasonic C-scan. Prior to inspection, the samples were submerged in a tank with distilled water, where the Pulso-Echo technique was employed using a 5 MHz piezoelectric probe and a reflective glass. The movement of the probe inside the pool was automatized using a robotic arm. Data was acquired using an OLYMPUS OMNI MX C-scan system.

Representative impacted specimens and each indented sample were inspected by µCT. Besides this, non-damaged samples (10 mm wide x 20 mm long) were also inspected to assess the microstructure of the $LTHIN_{LVI}$, $LV1_{LVI}$ and $LV2_{LVI}$ specimens. The inspection equipment consisted of an X-Ray source (20 W and 5 µm maximum power and focal spot) and a 2400 x 2400 pixel detector. Both were manufactured by HAMAMATSU and assembled by Novadep Scientific Instruments.

**Table 6.2:** µCT inspection parameters depending on the width of the inspected samples.

| Type of specimen | Sample width (mm) | Exposure time (ms) | V (kV) | I (µA) | Voxel size (µm) | Field of view (mm) |
|---|---|---|---|---|---|---|
| Non-tested and QSI at d = 4/4.4 mm | 9-10 | 1500 | 55 | 80 | 5 | 11.2 |
| QSI at d= 5.24 mm | 30 | 1200 | 60 | 70 | 7 | 15.7 |
| Impact at 10 J | Not cut | 2500 | 70 | 75 | 11/6.5 | 24.6/14.6[a] |
| Impact at 14 J | Not cut | 2500 | 70 | 75 | 14/10 | 31.4/22.4[a] |

[a] Global or detailed inspections to asses the entire damage scenario or a representative zone centred at the site of impact.

Contrast agents (i.e. penetrant dies) were avoided to ensure that matrix cracking and delamination were observed regardless of their interconnection. Prior to inspection, indented specimens were cut (see Fig. 6.1b) to reduce the aspect ratio of the cross-sections normal to the axis of rotation and thus improve the signal-to-noise ratio [180]. The inspection parameters are summarized in Table 6.2. In all cases, 1401 projections (3 integrations per projection) were acquired as the sample rotated over 360°. From a previous C-scan, it was decided to examine the entire damage scenario of the indented specimens. In the case of the impacted specimens, two inspections were carried out; one to capture the whole damaged area and the other to detail a representative region centred at the site of impact. In some cases, 2D slices were rendered in 3D using the medical software Starviewer [182].

## 6.3 Results

### 6.3.1 Structural response

Fig. 6.2 presents the load-displacement curves of representative specimens impacted at 10 and 14 J. All the materials exhibited a similar flexural stiffness until a local maximum was reached ($F_i$), followed by a load drop and a change in the bending response. Table 6.3 summarizes the average values of $F_i$ and the magnitude of the associated load drops. In the $LTHIN_{LVI}$ and $LV1_{LVI}$ specimens impacted at both energy levels, $F_i$ oscillated approximately between 3.2 and 3.4 kN. In contrast, $LV2_{LVI}$ increased the former load range to approximately 3.5-4 kN, the $LV2_{LVI}$ coupons impacted at 14 J presenting the highest standard deviation of all the batches (Table 6.3). In the $LTHIN_{LVI}$ baseline impacted at both energies, the force dropped approximately between 20 and 23% relative to the local maximum. In contrast, interleaving reduced this value; in particular the $LV2_{LVI}$ sample impacted at 10 J displayed the minimum drop (approximately 8%). Finally, we observed that

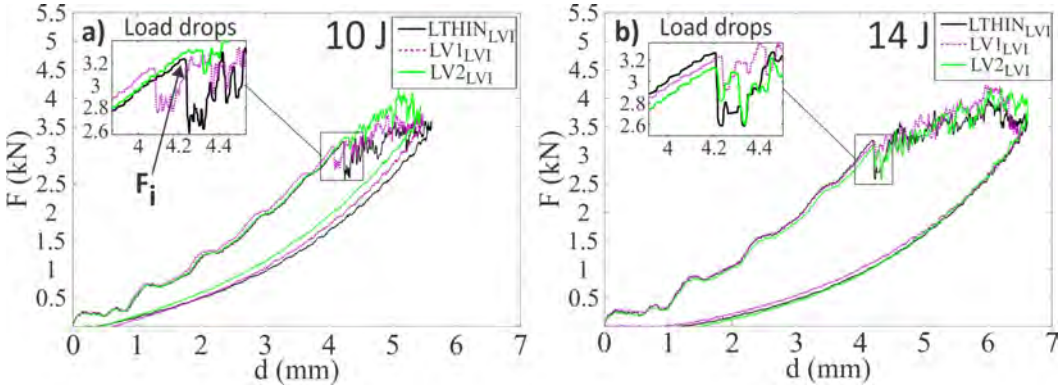


**Figure 6.2:** Load-displacement curves of representative LTHIN$_{LVI}$, LV1$_{LVI}$ and LV2$_{LVI}$ specimens impacted at a) 10 J and b) 14 J. (For interpretation of the references to colour in this figure legend, the reader is referred to the web version of this article.)

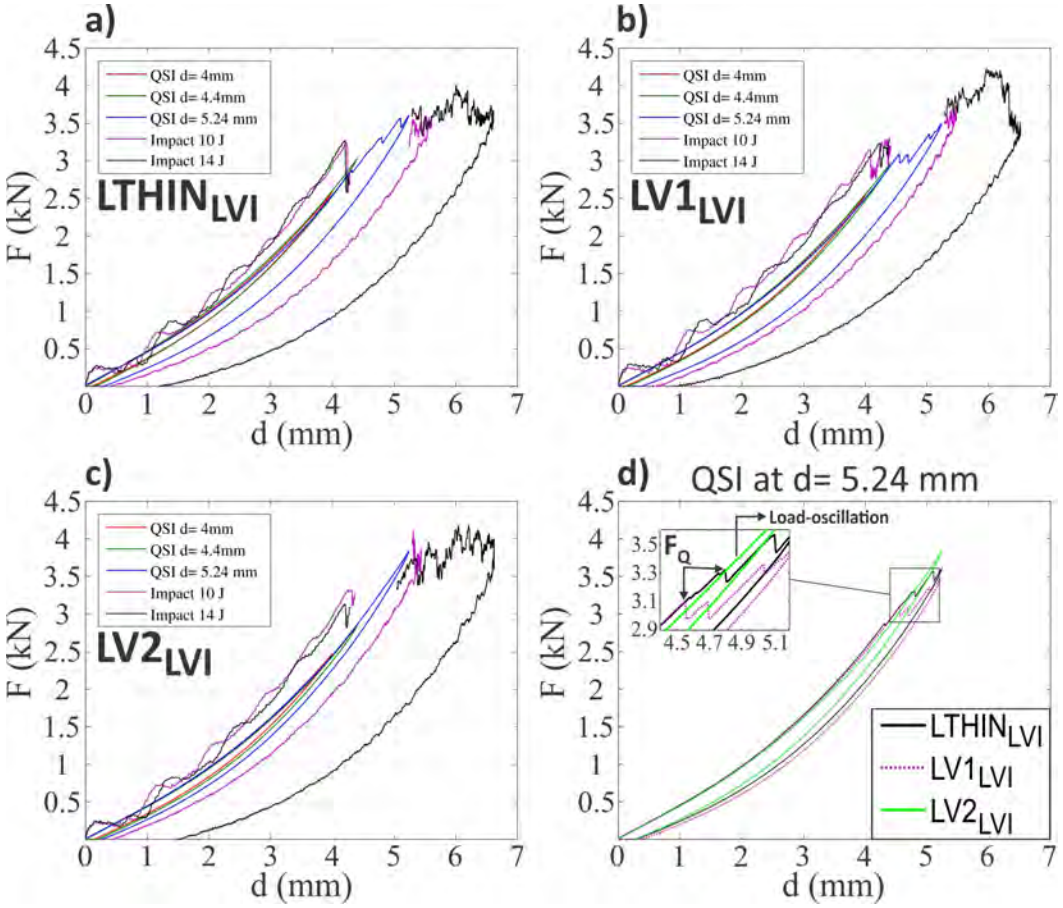


**Figure 6.3:** Load-displacement curves of representative impacted and indented specimens a) LTHIN$_{LVI}$ b) LV1$_{LVI}$ c) LV2$_{LVI}$. For visualization purposes, the region of the impact curves that overlapped with that of the indented samples was suppressed. 3d) Load-displacement curves of indented LTHIN$_{LVI}$, LV1$_{LVI}$ and LV2$_{LVI}$ specimens indented at d = 5.24 mm.

interleaving veils increased the scatter in terms of the magnitude of the load drop (Table 6.3).

Fig. 6.3 compares the load-displacement curves of the indented and representative impacted specimens of a particular system. In all cases, the curves of the indented specimens overlapped each other at every incremental displacement level. The load on the $LTHIN_{LVI}$ and $LV1_{LVI}$ specimens was increased non-linearly until a local maximum was reached ($F_Q$). This was followed by several load drops and a change in the bending stiffness (Fig. 6.3d). In contrast, $LV2_{LVI}$ exhibited a non-linear response followed by a small load-oscillation without concomitant reduction of the flexural stiffness (approximately 3.4 kN in the zoomed region of the Fig. 6.3d). Despite the scatter presented by impacted specimens of the same test batch, $F_i$ and $F_Q$ (impact and QSI) agreed reasonably well for the $LTHIN_{LVI}$ and $LV1_{LVI}$ specimens. For $LV2_{LVI}$, we observed that the severity of the load drop reduced in QSI with respect to low-velocity impact (i.e. between 8-11% for impact and negligible for QSI at d = 5.24 mm).

**Table 6.3:** Value of the force local maximums ($F_i$ and $F_Q$) and magnitude of the associated load drops observed in the load-displacement curves of impacted and indented $LTHIN_{LVI}$, $LV1_{LVI}$ and $LV2_{LVI}$ specimens, ± refers to the standard deviation between experiments.

| Material | Test | | | | | |
|---|---|---|---|---|---|---|
| | Impact at 10 J | | Impact at 14 J | | QSI | |
| | $F_i$ (kN) | Load drop (%) | $F_i$ (kN) | Load drop (%) | $F_Q$ (kN) | Load drop (%) |
| $LTHIN_{LVI}$ | 3.24 ± 0.02 | 19.75 ± 0.55 | 3.41 ± 0.25 | 22.80 ± 1.40 | 3.32 | Multiple |
| $LV1_{LVI}$ | 3.19 ± 0.04 | 14.64 ± 2.55 | 3.24 ± 0.22 | 11.34 ± 4.46 | 3.10 | Multiple |
| $LV2_{LVI}$ | 3.51 ± 0.15 | 8.17 ± 2.36 | 3.95 ± 0.51 | 10.80 ± 1.28 | None | None |

### 6.3.2 Non-destructive inspection

We performed time-of-flight (TOF) C-scans to evaluate the global profile of the damage, the distribution through-the-thickness, and the projected area (Fig. 6.4a). Because of the TOF gate configuration, no depth-information was provided for the first 500 µm below the centre of impact. Additionally, in the indented profiles that were concave enough, the ultrasonic wave may have dispersed and hidden part of the results (see white and grey regions of specimens impacted at 14 J, Fig. 6.4a).

Ultrasonic inspection of specimens indented at d = 4 and d = 4.4 mm featured no or very small amounts of damage (Fig. 6.4a). At d = 5.24 mm, the interleaved samples presented a circular damage profile, whereas the profile of the $LTHIN_{LVI}$ samples elongated in the longitudinal direction. Additionally, $LV2_{LVI}$ exhibited the highest

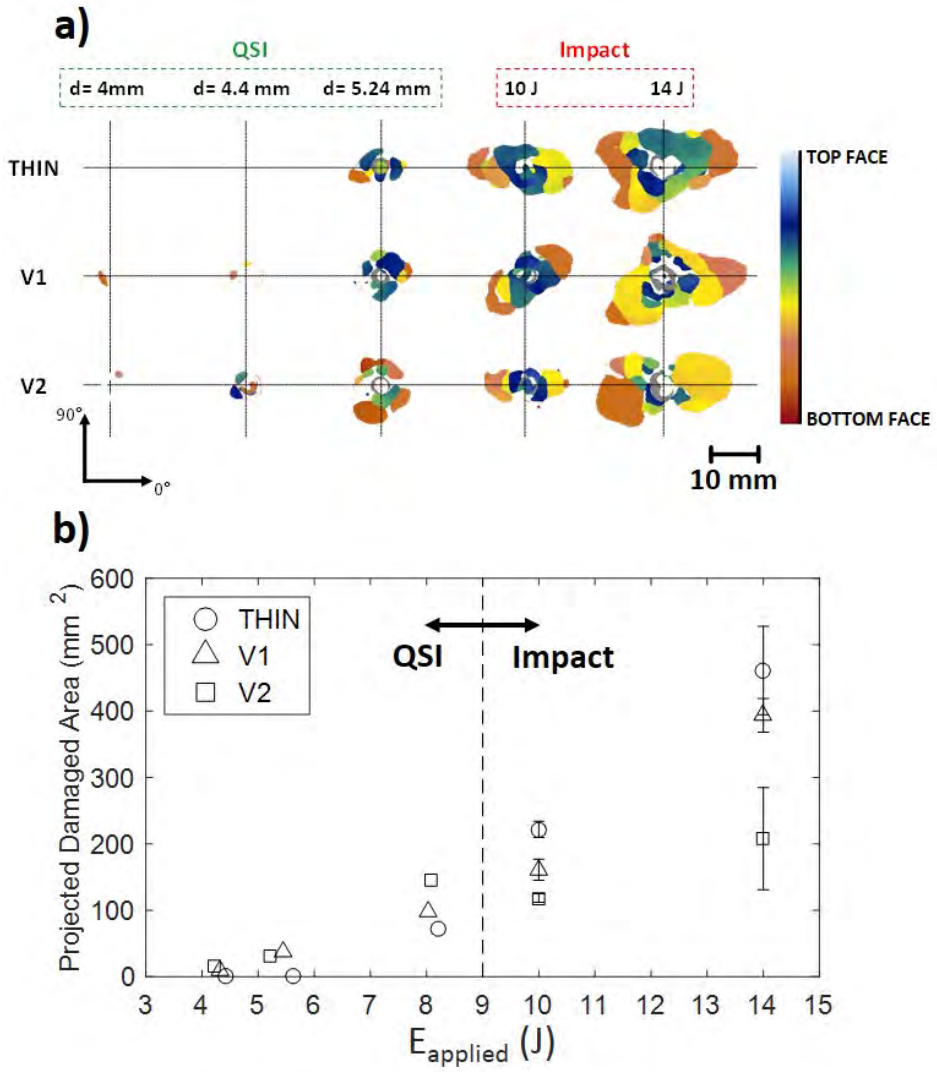


**Figure 6.4:** a) Ultrasonic C-scan images with a depth scale to the right part of the picture. 4b) Corresponding average C-scan projected damaged area plotted against the energy applied during impact and quasi-static indentation (QSI) tests - vertical bars refer to the standard deviation between measurements.

projected damage area with an approximate 100% increase in respect to the average between the $\text{LTHIN}_{\text{LVI}}$ and $\text{LV1}_{\text{LVI}}$ specimens (Fig. 6.4b).

For the specimens impacted at 10 and 14 J, the damage propagated largely below the mid-plane, leading to global profiles oriented at 0°, albeit with the exception of $\text{LV1}_{\text{LVI}}$ impacted at 10 J, which was oriented at 45° (Fig. 6.4a). At 10 J, every material featured damage distributed through-the-thickness. At 14 J, the $\text{LTHIN}_{\text{LVI}}$ specimens exhibited more severe damage in the top-half of the laminate than their interleaved counterparts. Meanwhile, $\text{LV2}_{\text{LVI}}$ presented the lowest projected damaged area (for the highest impact energy, it decreased by 55% compared to the $\text{LTHIN}_{\text{LVI}}$ baseline, Fig. 6.4b).

Figs. 6.5 and 6.6 present the microstructure of pristine $LTHIN_{LVI}$, $LV1_{LVI}$ and $LV2_{LVI}$ laminates obtained with μCT and epifluorescence microscopy. In every system, inspection detected resin-accumulated areas (so-called resin pockets) dispersed throughout the volume of specimens. After manufacturing, $V_1$ veils conserved their 'fibrous' architecture, increased the thickness of the interface between the plies and caused porosity within resin-rich areas (Figs. 6.5b and 6.6a). In contrast, $LV2_{LVI}$

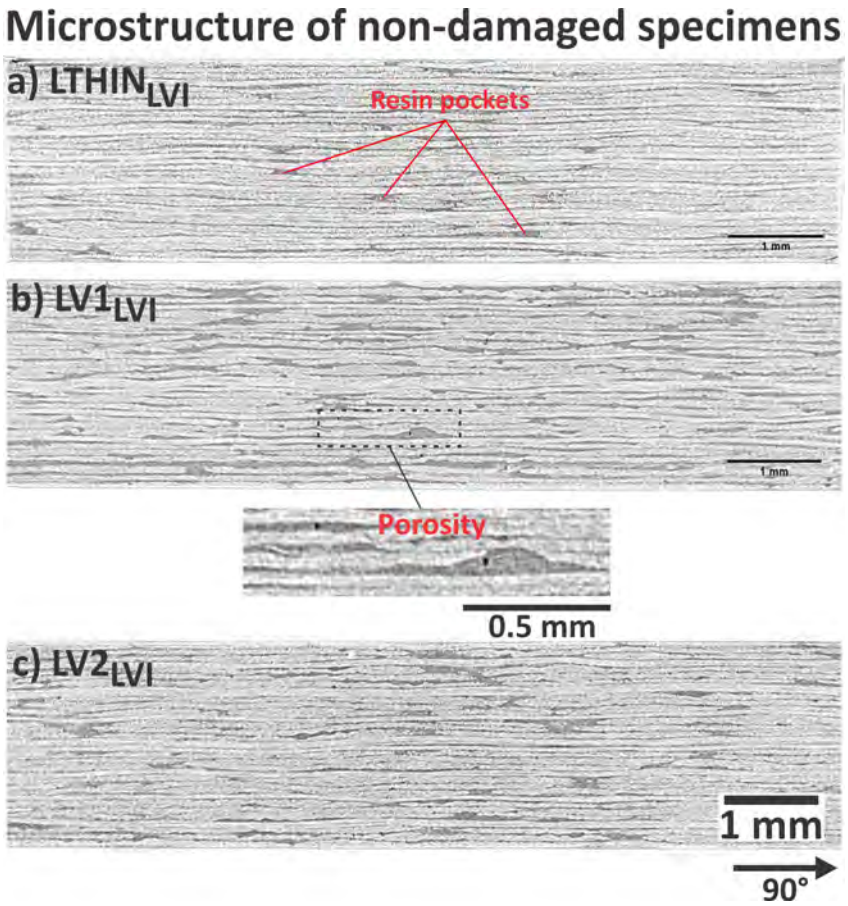


**Figure 6.5:** μCT cross-sections of non-damaged $LTHIN_{LVI}$, $LV1_{LVI}$ and $LV2_{LVI}$ specimens.

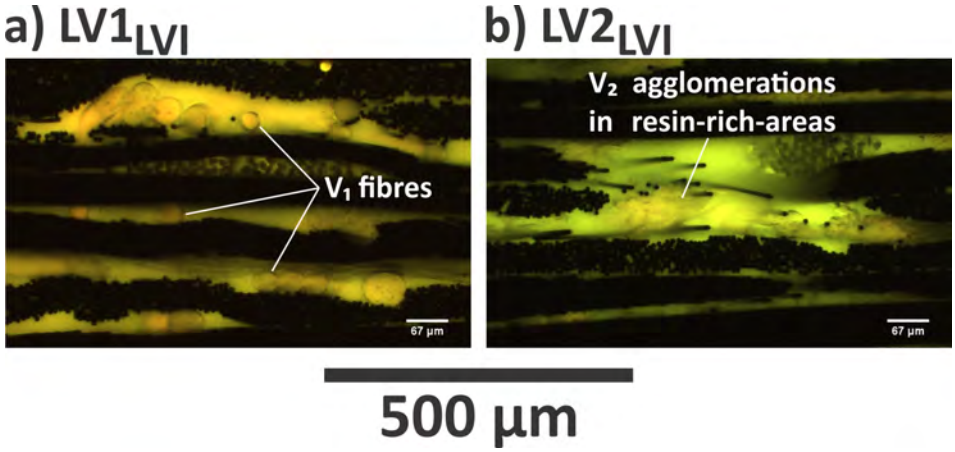


**Figure 6.6:** Epifluorescence cross-sections of non-damaged $LV1_{LVI}$ and $LV2_{LVI}$ specimens.

specimens exhibited a greater number of resin accumulations than the $LTHIN_{LVI}$ specimens and less porosity than the $LV1_{LVI}$ laminates (Fig. 6.5c). We observed that, during manufacturing, $V_2$ veils agglomerated within resin pockets (Fig. 6.6b).

µCT slices of specimens indented at d = 4 mm illustrate the onset of damage propagation resulting from quasi-static indentation loading (Fig. 6.7). In all cases, most of the damage was confined to under the mid-plane and propagated a few

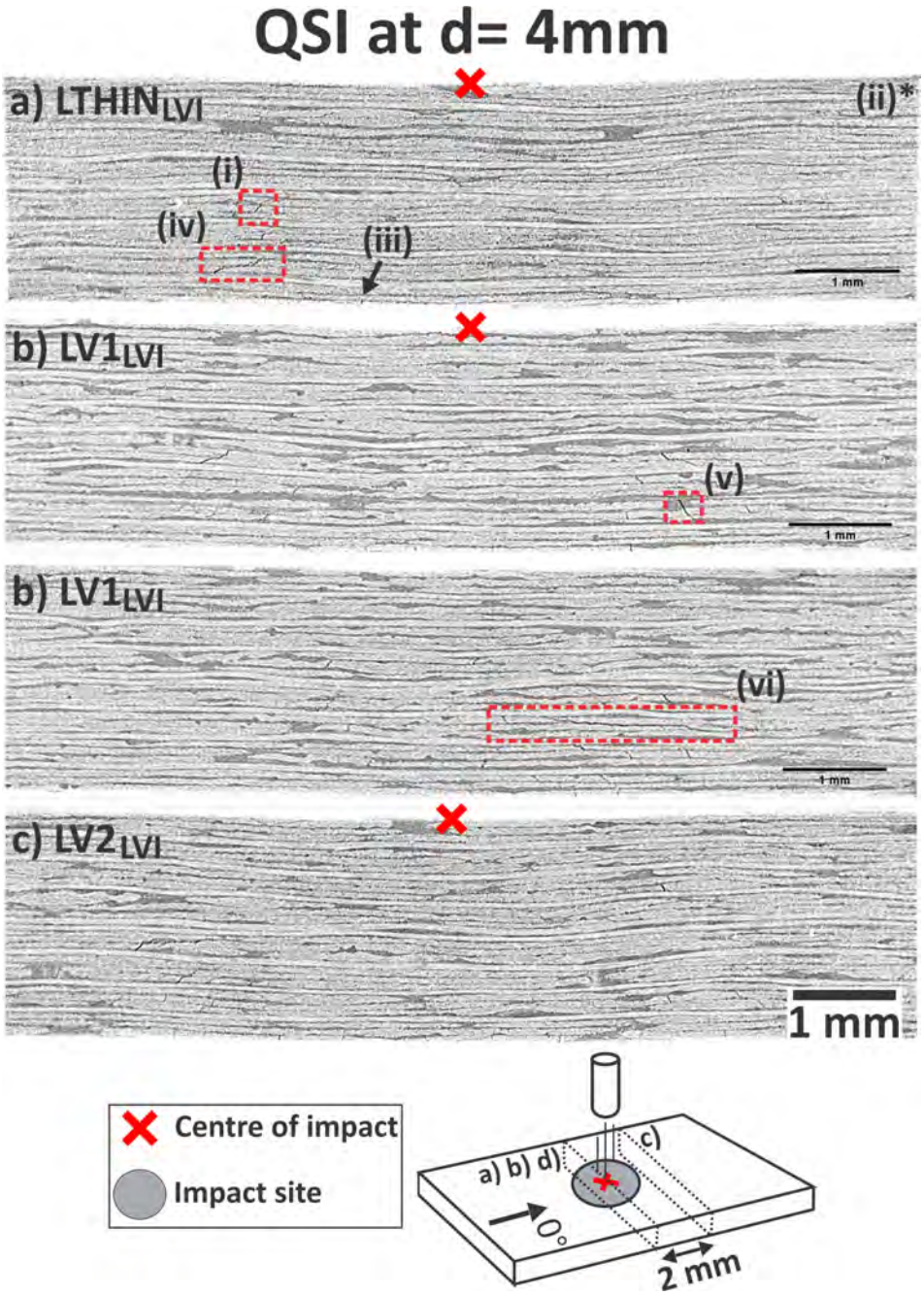


**Figure 6.7:** µCT cross-sections of $LTHIN_{LVI}$, $LV1_{LVI}$ and $LV2_{LVI}$ specimens indented at d = 4 mm. The centre of impact is indicated with a cross, (iii) is the tensile crack, whereas the rest of damage mechanisms are detailed in Fig. 6.8.

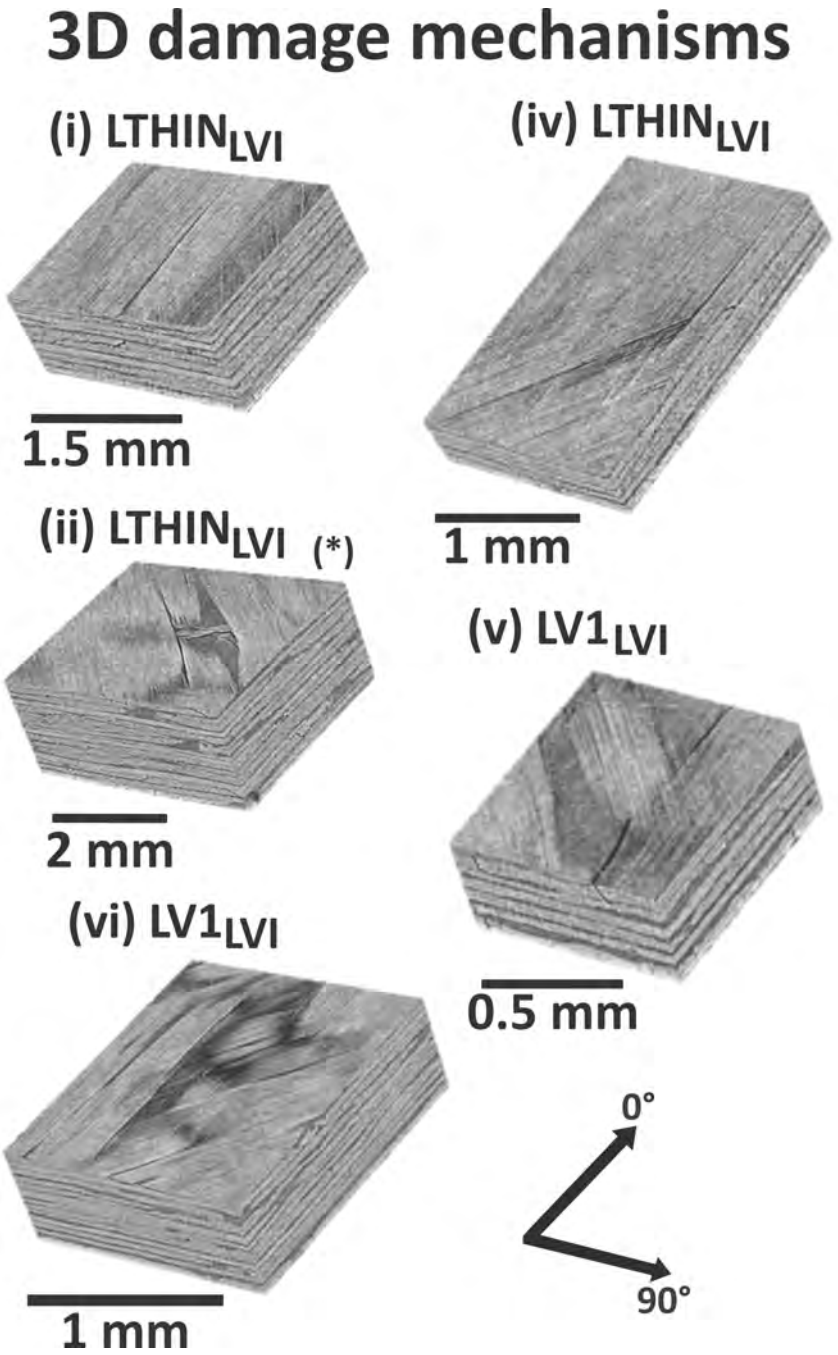


**Figure 6.8:** 3D representations of the damage mechanisms of $LTHIN_{LVI}$, $LV1_{LVI}$ and $LV2_{LVI}$ specimens indented at d = 4 mm, (i) is the shear crack, (ii) is the crack initiated near NCF stitching locations (*) (NB: As this mechanism is located well away from the centre of impact it is not indicated in the Fig. 6.7a, (iv) is the small delamination below the centre of impact, (v) is the intra-resin crack and (vi) is the delamination away from the centre of impact.

millimetres away from each side of the centre of impact. The $LTHIN_{LVI}$ specimen exhibited several types of matrix cracking, i.e. (i) in Figs. 6.7a and 6.8 are the 45° cracks that propagate parallel to the fibre direction ('shear cracks' [99]), (ii) in Fig. 6.8 are the cracks initiated at fibre-free zones where the NCF yarn stitch two consecutive plies [185] and (iii) in Fig. 6.7a are the 90° cracks induced by tensile stresses at the bottom-plies of the laminate ('tensile cracks' [96]). We also observed delaminations less than 1 mm wide propagating at the intersection between two matrix cracks ((iv) in Figs. 6.7a and 6.8). The interleaved systems exhibited all the previous damage mechanisms, with $LV1_{LVI}$ showing increased crack density and new forms of damage propagation (Fig. 6.7b,c and 6.8). In $LV1_{LVI}$, we also observed cracks tunnelling resin-rich areas ((v) in Figs. 6.7b and 6.8) and delaminations 1-2 mm long propagating away from the impact centre ((vi) in Figs. 6.7c and 6.8). Finally, $LV2_{LVI}$ presented a higher density of cracks than the $LTHIN_{LVI}$ laminate and comparable to that of $LV1_{LVI}$ (Fig. 6.7d).

Increasing the deflection of the $LTHIN_{LVI}$ plate to 4.4 mm incremented both the crack-openings and density of tensile cracks (Fig. 6.9a). In the $LV1_{LVI}$ specimen indented at d = 4.4 mm, matrix cracks and matrix crack-induced delaminations ('MCID' [201]) extended through-the-thickness of the sample (Fig. 6.9b). The

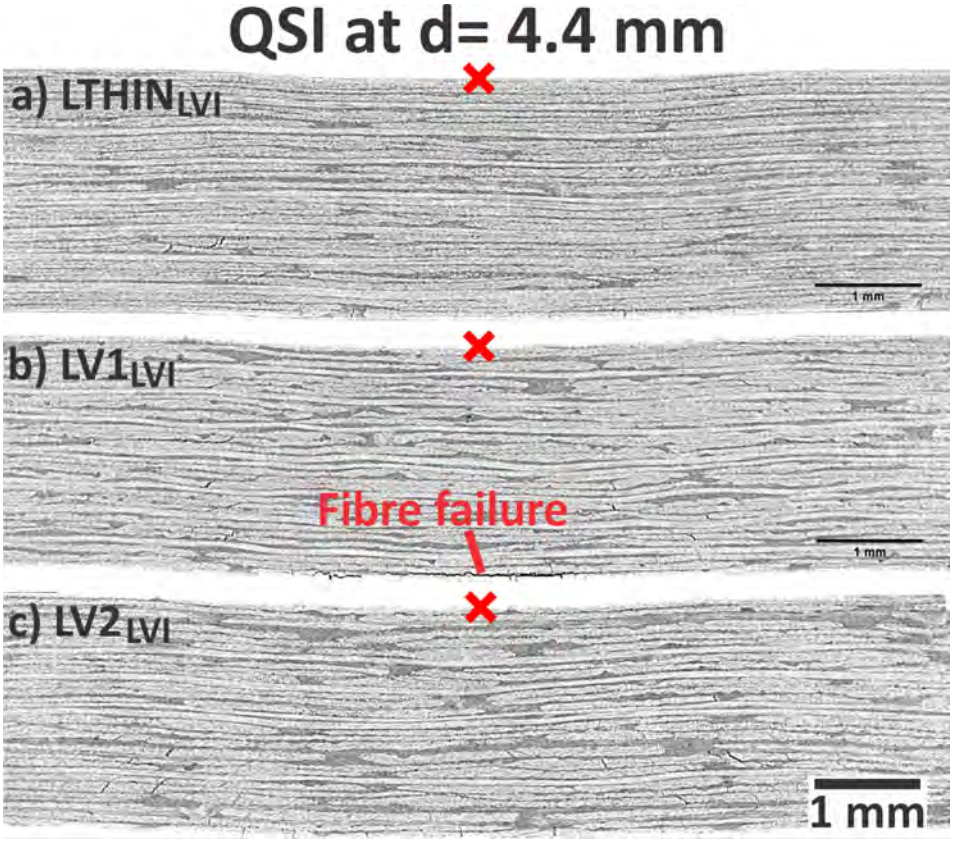


**Figure 6.9:** µCT cross-sections of $LTHIN_{LVI}$, $LV1_{LVI}$ and $LV2_{LVI}$ specimens indented at d = 4.4 mm. The centre of impact is indicated with a cross.

bottom-ply of the plate featured fibre failure due to tensile stresses induced by bending. In contrast, $LV2_{LVI}$ presented a high density of matrix cracks in the lower-half of the laminate along with delaminations 1-2 mm long propagating away from the centre of impact (Fig. 6.9c).

The $LTHIN_{LVI}$ specimen indented at d = 5.24 mm developed fibre failure in all the plies in the lower third of the laminate ((viii) in Fig. 6.10a). Additionally, matrix cracks and MCID extended from the bottom to the top of the plate (Figs. 6.7a, 6.9 and 6.10a). $LV1_{LVI}$ also presented localized fibre breakage accompanied by cracks/MCID (Fig. 6.10b). In contrast, $LV2_{LVI}$ limited fibre failure to the bottom-ply of the sample (Fig. 6.10c). In this system, delaminations developed through-the-thickness with a characteristic "cone-shape" [5], i.e. they grew larger at the bottom-half of the laminate. Besides this, we observed that crack ligaments

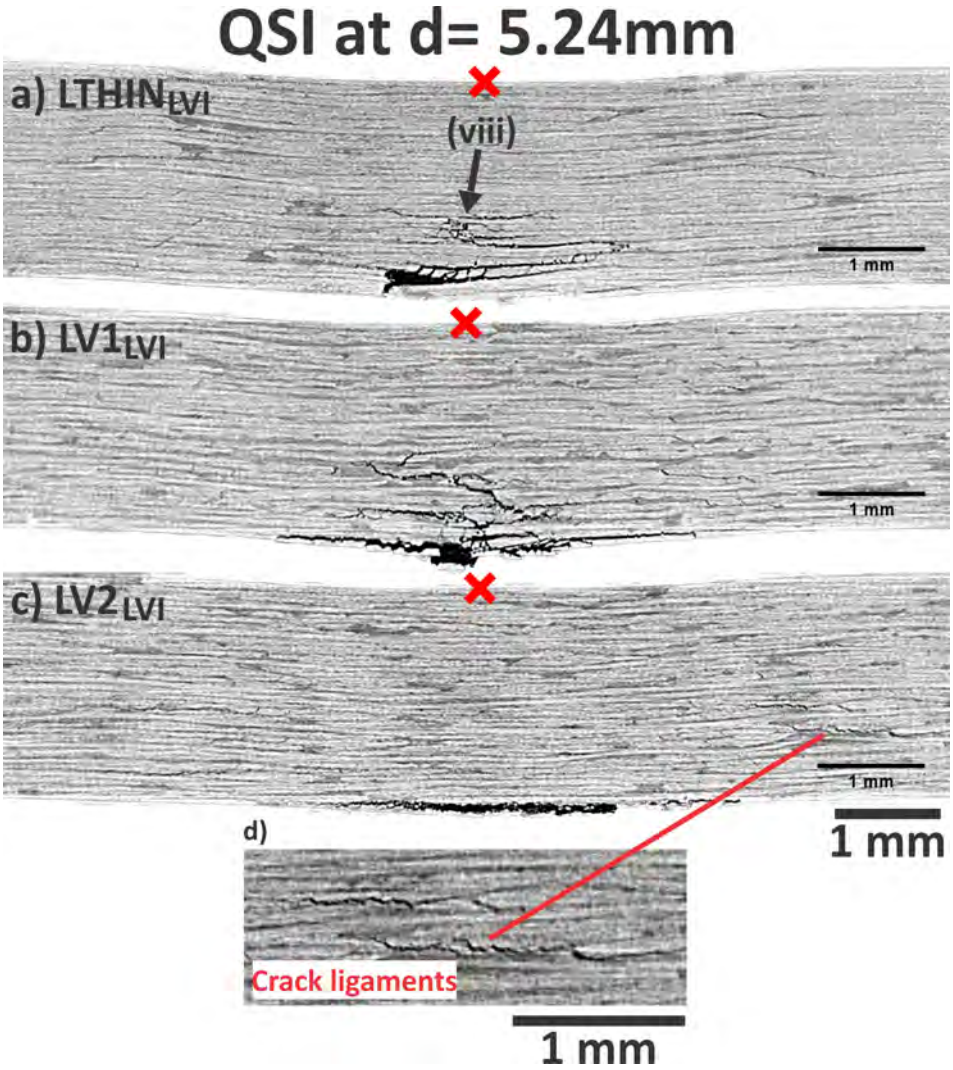


**Figure 6.10:** µCT cross-sections of $LTHIN_{LVI}$, $LV1_{LVI}$ and $LV2_{LVI}$ specimens indented at d = 5.24 mm. The centre of impact is indicated with a cross, (viii) is fibre failure.

developed when delaminations propagated through resin-rich areas (Fig. 6.10d).

The main difference in the damage scenario between the $LTHIN_{LVI}$ specimens impacted at 10 J or indented at d = 5.24 mm (corresponding energy of 8 J) was that, during impact, fibre failure extended to all the plies within the boundaries of the contact zone (Figs. 6.10a and 6.11a). Away from this region, fibre breakage localized under the mid-plane. $LV1_{LVI}$ exhibited similar damage features to the $LTHIN_{LVI}$ samples, albeit with slightly reduced severity (Fig. 6.11b). In contrast, $LV2_{LVI}$ limited fibre breakage to almost the bottom-half of the laminate and presented reduced delamination propagation (Fig. 6.11c).

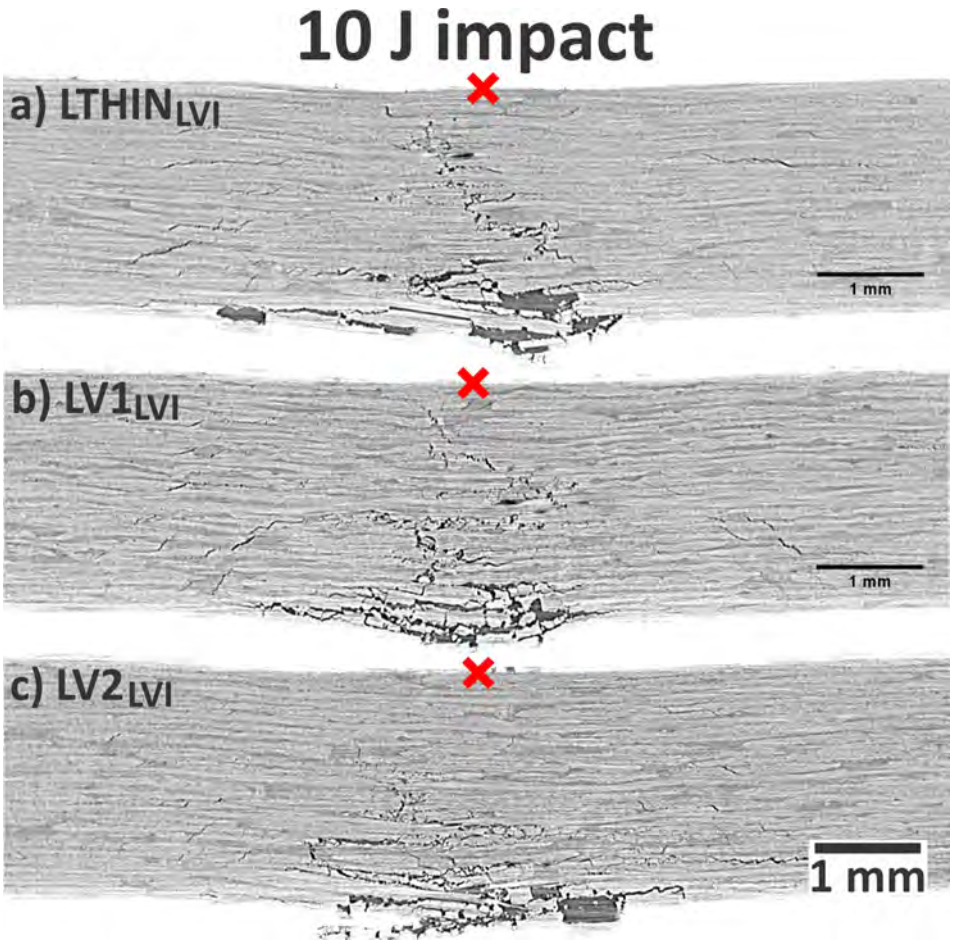


**Figure 6.11:** µCT cross-sections of $LTHIN_{LVI}$, $LV1_{LVI}$ and $LV2_{LVI}$ representative specimens impacted at 10 J. The centre of impact is indicated with a cross.

The $LTHIN_{LVI}$ and $LV1_{LVI}$ specimens impacted at 14 J presented catastrophic fibre breakage through-the-thickness and delamination propagation largely away from each side of the centre of impact (Fig. 6.12a and b). In contrast, $LV2_{LVI}$ constrained most of the damage to a 2 mm wide region centred at the point of impact, where all the plies presented fibre failure without significant associated delamination (Fig.

6.12c). Interestingly, in $LV2_{LVI}$ the propagation of delaminations was induced during indentation, but not during impact events (Figs. 6.10-6.12c).

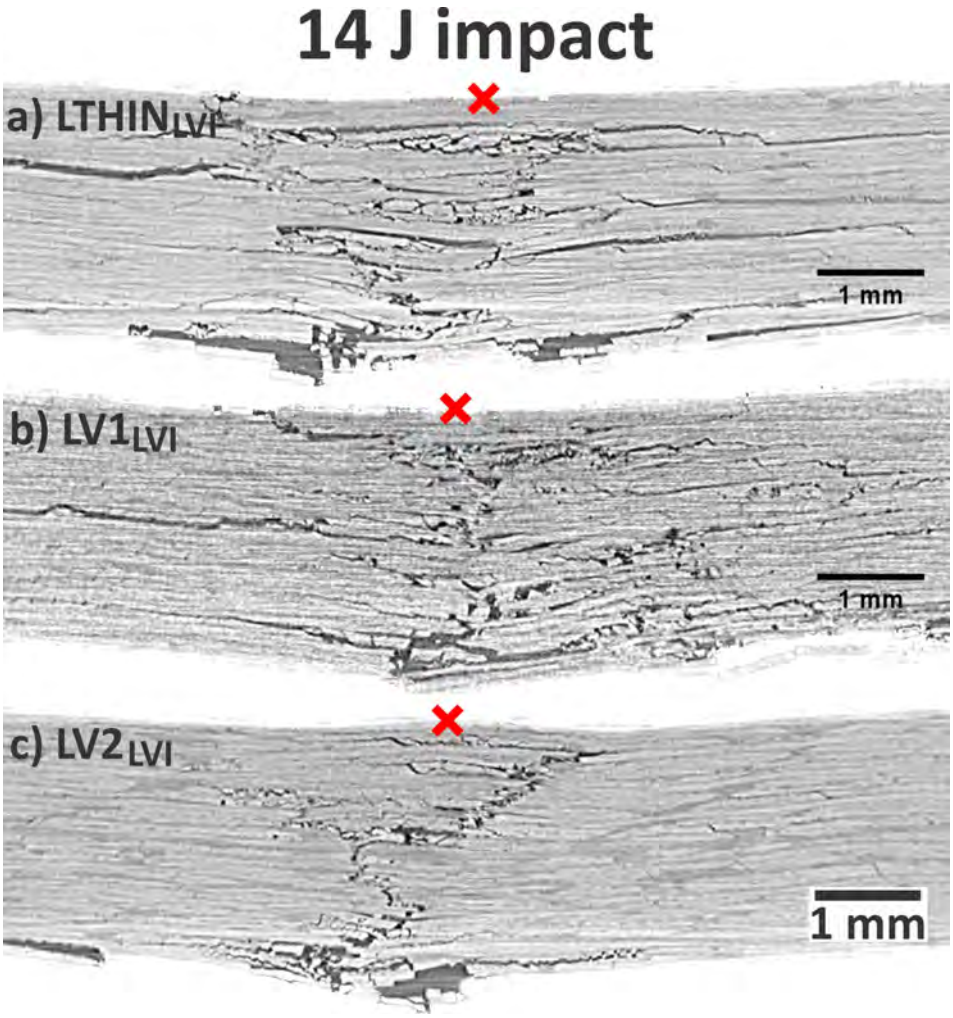


**Figure 6.12:** µCT cross-sections of $LTHIN_{LVI}$, $LV1_{LVI}$ and $LV2_{LVI}$ representative specimens impacted at 14 J. The centre of impact is indicated with a cross.

### 6.3.3 Compression after impact

All the impacted coupons displayed the same failure mechanisms, local buckling at the impact site followed by damage propagation perpendicular to the applied load (Fig. 6.13a). In contrast, the pristine samples presented through-the-width damage localized at the topmost clamping region, suggesting that global buckling occurred during compression [112]. Consequently, the CAI results of pristine specimens are considered to be of a lower strength threshold. Regarding the CAI strength of impacted specimens, $LV2_{LVI}$ improved the residual strength of the baseline by 7% and 28% for 10 and 14 J (Fig. 6.13b).

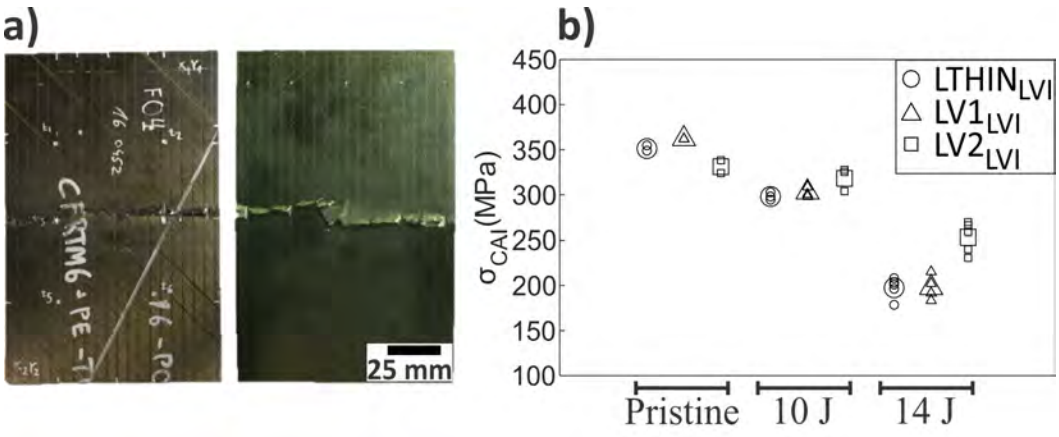


**Figure 6.13:** a) Across-the-width failure of a 2.16 mm thick specimen impacted at 10 J. 13b) CAI strength of pristine and impacted $LTHIN_{LVI}$, $LV1_{LVI}$ and $LV2_{LVI}$ specimens. The smaller markers refer to the strength of individual coupons, whereas the bigger ones stand for the average values.

## 6.4 Discussion

### 6.4.1 Effect interleaving has on the microstructure

NCF laminates present resin pockets because the stitching deviates carbon tows from their uniform directions [185] (see 3D representation number (ii) in Fig. 6.8). Focusing on the effect of interleaving, $V_1$ veils conserve their "fibre-like" integrity because their melting point is higher than the manufacturing temperature (Fig. 6.6a). Since the non-woven veils have a higher permeability than the tightly packed carbon tows, the resin accumulates at the interlayers (i.e. increases the interface thickness) and leads to voids [16] (Fig. 6.5b). In contrast, the melting temperature of $V_2$ corresponds approximately to the RTM post-curing temperature. This type of veil melts partially/completely and diffuses with the resin during the infusion process (Fig. 6.6b), leading to an interface with non-increased thickness (Fig. 6.5c).

### 6.4.2 Force-displacement curves

The impact load-displacement curves of the $LTHIN_{LVI}$, $LV1_{LVI}$ and $LV2_{LVI}$ specimens evidence that all systems exhibit a similar flexural stiffness (Fig. 6.2). Walker *et al.* [122] observed a similar response when interleaving 2.2 g/m$^2$ PA veils at every interlayer. However, other studies considering 34 g/m$^2$ PA veils report penalties of approximately 20% in flexural stiffness [16], highlighting the trade-off between areal weight and bending stiffness or other mechanical properties of the material [10].

We observed a single load drop following $F_i$ and a series of consecutive load drops following $F_Q$ (Figs. 6.2-6.3). Comparing the load-displacement curves in Fig. 6.3

with the μCT slices in Figs. 6.9-6.11, we conclude that $F_i$ and $F_Q$ correspond to the development of fibre failure localized in the lower half of the specimen (in the specimen $LV2_{LVI}$ indented at d = 5.24 mm, the load oscillation may correspond to fibre breakage at the bottom-ply, see Fig. 6.10c). Additionally, the magnitude of the load drop associated to $F_i$ scales with the severity of the observed fibre fracture (Table 6.3, and Figs. 6.11-6.12) [92]. On the other hand, $LV1_{LVI}$ and $LV2_{LVI}$ decreased the repeatability of $F_i$ and the magnitude of the load drop compared to the non-interleaved baseline (Table 6.3), which is attributed to their less homogeneous microstructure. Optimizing the manufacturing process to minimize agglomeration of the veils and porosity could have a positive effect on this aspect [16].

The fact that the load-displacement curves of the $LTHIN_{LVI}$, $LV1_{LVI}$ and $LV2_{LVI}$ specimens exhibit a non-linear behaviour until fibre damage occurs is a consequence of the thickness-to-length ratio of the plate (thin versus thick laminates [114]). The impact response of thick laminates is dominated by shear and delamination [107]. Accordingly, the load-displacement curve presents two consecutive load drops, attributed respectively to the onset of delamination and to fibre failure processes [92, 95, 96]. In contrast, the response of thin laminates is dominated by bending and associated non-linear membrane effects, which reduce or suppress the evidence of delamination onset in the force-displacement curve (i.e. the first load drop; see, for example, the load-displacement curves of the impacted/indented thin laminates studied by Sutherland *et al.* [107], Yokozeki *et al.* [98] and Abisset *et al.* [96]).

### 6.4.3 Sequence of damage events

Based on the μCT observations of the indented and impacted specimens (Figs. 6.7a and 6.9-6.12a), the damage sequence of the $LTHIN_{LVI}$ specimens is summarized as follows:

- development of multiple tensile cracks at the bottom-ply of the laminate and growth of shear cracks/induced delaminations up to 3 mm wide from the bottom to the top,
- fibre failure localized to the lower sublaminate groups,
- growth of bottom-up fibre failure and enlargement of existing delaminations.

This is in agreement with the damage sequence proposed by Yokozeki et al. (2010) [13], who considered carbon/toughened epoxy $[45°/0°/-45°/90°]_{4s}$ 2.2 mm thick layups with 70 μm thin-plies. Since bending dominates the out-of-plane response of thin laminates, damage starts at the bottom interfaces and extends progressively towards the top surface [5].

The effect of interleaving on the onset of damage clearly depends on how the veils modify the microstructure. $LV1_{LVI}$ delaminated prematurely as the excess of resin counteracted the reinforcing mechanisms that $V_1$ fibres were able to provide at the interfaces (i.e. fibre pull-out or plastic deformation [115, 137]) (Figs. 6.6a and 6.7c). Besides this, $V_1$ has a relatively open structure with few fibres available to interact with the crack front. In contrast, $V_2$ veils increase the density of fibre-free regions compared to the thin-ply baseline without modifying the thickness of the interface (Figs. 6.5c and 6.6b). Consequently, $LV2_{LVI}$ presents a higher density of matrix cracks than $LTHIN_{LVI}$ and delays the initiation of delaminations relative to $LV1_{LVI}$ (Fig. 6.7d).

### 6.4.4 Structural response: damage resistance and damage tolerance

From the C-scans, μCT, and CAI tests of the impacted specimens, interleaving $V_2$ enhances impact resistance and tolerance (Figs. 6.4 and 6.11-6.13). Nash *et al.* [14, 17] reported that polyamide non-woven veils improve damage resistance and certain CAI properties because they increase mode I and II interlaminar fracture toughness.

$LV2_{LVI}$ specimens indented at d = 5.24 mm present large delaminations contrary to their impacted counterparts (Figs. 6.10c and 6.11c). Additionally, the severity of their load drop decreases from 8-11% during impact to negligible during indentation at d = 5.24 mm (Table 6.3 and Figs. 6.2 and 6.3d). Both facts indicate that, as the strain rate decreases, a higher proportion of energy dissipates through delamination propagation rather than through fibre failure. The reason why delaminations propagate at the lowest loading rate could be related to the micromechanisms of crack propagation. At low rates, the thermoplastic polymer has enough time to accommodate part of the stresses through viscoplastic deformation ("shear yielding" [202]). Then, successive crack "ligaments" form when the crack front encounters a resin-rich area (Fig. 6.10d). At higher loading rates, the thermoplastic become more resistant, reducing the initiation of delaminations and localizing the damage under the impactor (Fig. 6.12c). Bull *et al.* [92] observed an analogous effect in particle-toughened carbon/epoxy laminates where thermoplastic particles bridged the crack tip during QSI but did not do so during impact experiments.

In view of our study, non-woven veils are promising and cost-effective candidates for improving the damage tolerance of carbon/epoxy aircraft components. Manufacturing layups with this type of toughening agent only requires one extra-step, cutting the veils and placing them between the carbon layers. In addition, the open structure of the interlayers allows the resin to flow through-the-thickness, as

opposed to other conventional approaches (e.g. interleaving thermoplastic films) [10]. Apart from reducing impact damage, non-woven veils could be used as scarf repairs [134], to reduce delamination induced by pull-off loads or to improve the conductivity of the laminate (e.g. functionalizing the veils with silver nano-wires [135] or graphite/graphene particles [120]).

## 6.5 Conclusions

Thin laminates manufactured with thin-ply NCFs accumulate matrix cracks and delaminations 1-3 mm wide until fibre failure causes the damage to extend further. Their load-displacement curves present load drops corresponding to the development of fibre breakage, which subsequently evolves from the bottom to the top parts of the laminate. In addition, the NCF stitching yarns induce resin pockets that favour the development of matrix cracks.

Interleaving non-woven CoPA veils of approximately 4 g/m$^2$ fibre areal weight at every interface does not penalise the bending stiffness. However, the melting temperature and architecture of veil fibres play a key role in the laminate's microstructure and impact performance. Veils that do not melt during manufacturing accumulate resin at the interfaces and reduce the effect of interleaving on damage resistance and CAI strength (i.e. $V_1$ veils). In contrast, interleaving veils with a melting temperature lower than the post-curing temperature ($V_2$) arrest the onset of delamination during impact and improve the damage tolerance of thin-ply NCF systems. In particular, by interleaving this type of veil the damage area is reduced by 55% for a 14 J impact and the CAI strength is improved by up to 28%. The opposite trends that $LV2_{LVI}$ presents during impact and QSI loading (i.e. it arrests or favours the initiation of delaminations compared to the thin-ply baseline) indicate that the strain rate is a crucial parameter governing the structural response of the interleaved material.

# Discussion

# 7

This chapter brings together the main results and conclusions of papers A-D. For details of the nomenclature and stacking sequence of the laminates used in this study refer to Table 1.2

The damage sequence evolution of $\text{LSTANDARD}_{\text{ILSS}}$ and $\text{LTHIN}_{\text{ILSS}}$ specimens provides a straightforward reply to some of the open questions raised in Table 1.1 (Fig. 7.1). For detailed explanations of the ILSS experimental and numerical campaigns the reader is referred to Chapter 3. Regardless ply-thickness, failure was initiated by a shear crack tunnelling across central $90^{\circ}_2$ ply-cluster. The intersection of this crack with the ones developing in the adjacent $-45°$ layers induced a delamination which, in turn, penalized the load-carrying capacity (Figs. 3.1, 3.4-3.5 and 7.1). What is also interesting is that, for a similar maximum principal stress distribution across the width of the $90^{\circ}_2$ ply-cluster, the thin-plies required a 32% higher interlaminar shear stress to initiate the catastrophic crack (for further insight into the stress distribution refer to Fig. 3.6). In other words, the thinner $90^{\circ}_2$ ply-cluster has a 32% higher ply-strength under transverse shear, attributed to the in-situ effect [20, 21, 25]. To the author's knowledge, this is the first unambiguous proof of the in-situ effect under transverse shear, i.e. $\tau_{23}$ in the coordinate system of the 90° plies (Fig. 7.1).

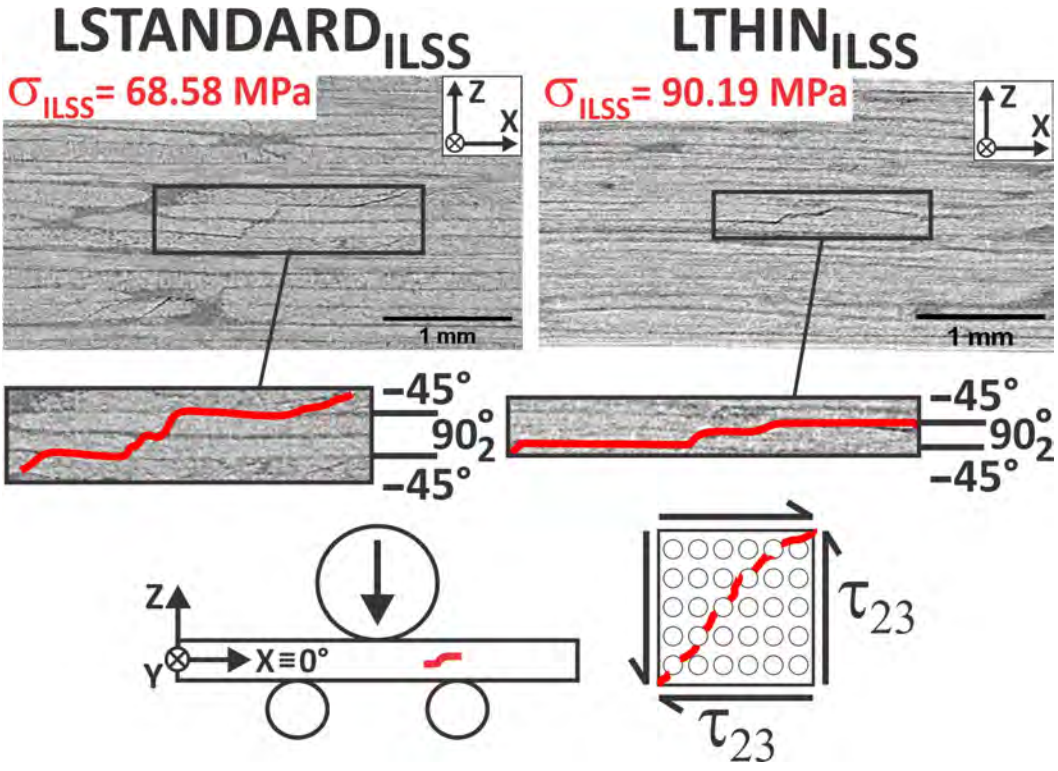


**Figure 7.1:** Damage scenario of $\text{LSTANDARD}_{\text{ILSS}}$ and $\text{LTHIN}_{\text{ILSS}}$ specimens loaded until the onset of ultimate failure (points $C_S$ and $C_T$ in Figs. 3.1, 3.4-3.5).

The higher strength of $\text{LTHIN}_{\text{ILSS}}$'s $90^{\circ}_{2}$ ply-cluster is quantitatively consistent with the predictions of existing 3D failure criteria [38]. Catalanotti *et al.* [38] assumed that the in-situ transverse shear strength $S_T^{is}$ is proportional to the in-situ strength under in-plane shear $S_L^{is}$ with the fracture angle under pure compression $\alpha_0$ and a friction coefficient in the longitudinal direction $\eta_L$:

$$S_T^{is} = \frac{(2sin^2\alpha_0 - 1)}{\eta_L sin2\alpha_0} S_L^{is} \tag{7.1}$$

Assuming linear stress-stain behaviour, the in-situ in-plane shear strength follows [21]:

$$S_L^{is} = \sqrt{\frac{8G_{12}G_{\text{IIc}}}{\pi t}} \tag{7.2}$$

where $G_{12}$ is the shear modulus, $G_{\text{IIc}}$ is the mode-II ply-fracture toughness and $t$ is the ply-thickness. That is, for a material system with constant $\alpha_0$, $\eta_L$, $G_{12}$ and $G_{\text{IIc}}$, the in-situ transverse shear strength $S_T^{is}$ is inversely proportional to the square-root of ply-thickness. Considering the interlaminar shear strength of $\text{LSTANDARD}_{\text{ILSS}}$ (68.58±4.20 MPa) and the ply-thickness values of $\text{LSTANDARD}_{\text{ILSS}}$ and $\text{LTHIN}_{\text{ILSS}}$ (134 and 67 μm), the theoretical strength of $\text{LTHIN}_{\text{ILSS}}$ is 96.99 MPa, which is only 7% higher than the measured value (90.19±1.64 MPa) and, given the standard deviation, compliant with the experimental results.

The observation of shear cracks inducing delamination in quasi-isotropic ILSS specimens can be generalized to other loading scenarios where out-of-plane shear stresses prevail e.g., the unfolding test or a T-joint subjected to bending [172, 203, 204] (Fig. 7.2). The unfolding test loads a curved laminate in four-point bending. Failure of unidirectional laminates is typically attributed to delamination caused by $\sigma_{33}$ stresses [171], a case in which the strength is independent of the laminate thickness. However, when the stacking sequence includes off-axis plies, analytical models fail to explain why and how the strength may vary with the thickness of the sample (the off-axis plies are subjected to shear stresses) [172]. González-Cantero *et al.* [172] postulated that this is because damage starts as an intralaminar crack that further propagates to a delamination and causes instantaneous failure (Fig. 7.2a), which is in agreement with the experimental observations of Huchette *et al.* [203]. Regarding the T-joint, Burns *et al.* [204] reported that failure initiated in the radius bend region (i.e. the only region displaying a shear crack, Fig. 7.2b). Based on the ILSS results, González-Cantero's postulation and Burn's observations, the author of this document believes that, in all of these loading scenarios, it is the shear crack which triggers the delamination and controls the ultimate strength of the samples. Improved analytical models should account for the propagation of the initial shear crack.

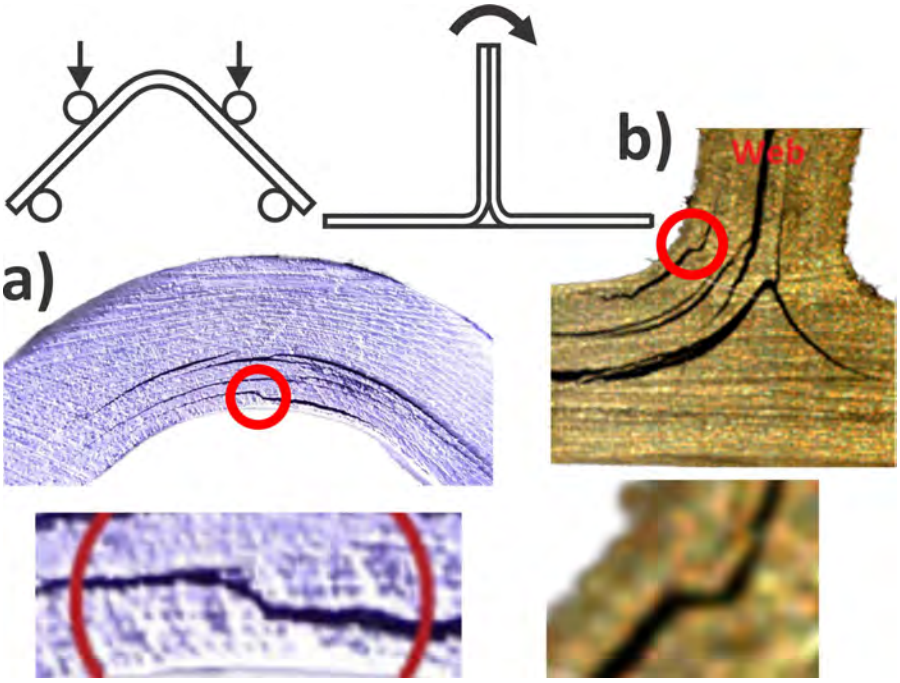


**Figure 7.2:** Damage scenario of two types of quasi-isotropic specimen: a) a curved specimen subjected to four-point bending and b) a T-joint sample subjected to pure bending, adapted from [172, 204].

The same concept applies to out-of-plane loading cases where delamination develops away from the free-edges: low-velocity impact and quasi-static indentation. Section 2.3.1 raised the open question whether shear cracks precede delamination during impact as well as which damage mechanism penalizes the load-carrying capacity [49, 85, 92, 95, 96, 107] —this questions refers to conventional-ply quasi-isotropic thick and thin laminates. Comparing the failure scenario of ILSS and impact specimens (Figs. 2.11 and 7.1), we infer that it is most likely the shear cracks that induce delamination which, in turn, account for the first load drop in the load-displacement curve of thick laminates (refer to the force drop-off following $F_{threshold}$, Fig. 2.13). While this hypothesis is widely accepted [5, 49, 85, 92, 96, 107], separating the shear crack from the delamination would require either prohibitively expensive experimental campaigns (impact specimens are too big for try-and-error testing) or coupling QSI devices with sophisticated in-situ µCT fixtures —Sandhu *et al.* [205] are giving the first steps towards this challenging objective.

The µCT inspections of ILSS specimens provide information that goes beyond the described damage sequence. Fig 7.3 depicts the damage scenario developed in a $-45°/90_2°$ ply-group of the $LSTANDARD_{ILSS}$ specimen tested until failure. The XY image corresponds to a 3D segmentation of the damage area highlighted in the YZ slice (refer to the coordinate system defined in Fig. 7.1). Delamination was surrounded by a single shear crack in the $90^{\circ}_2$ ply-cluster and multiple shear cracks in the adjacent $-45°$ layer (the shear crack in the $90^{\circ}_2$ ply-cluster is not visible from

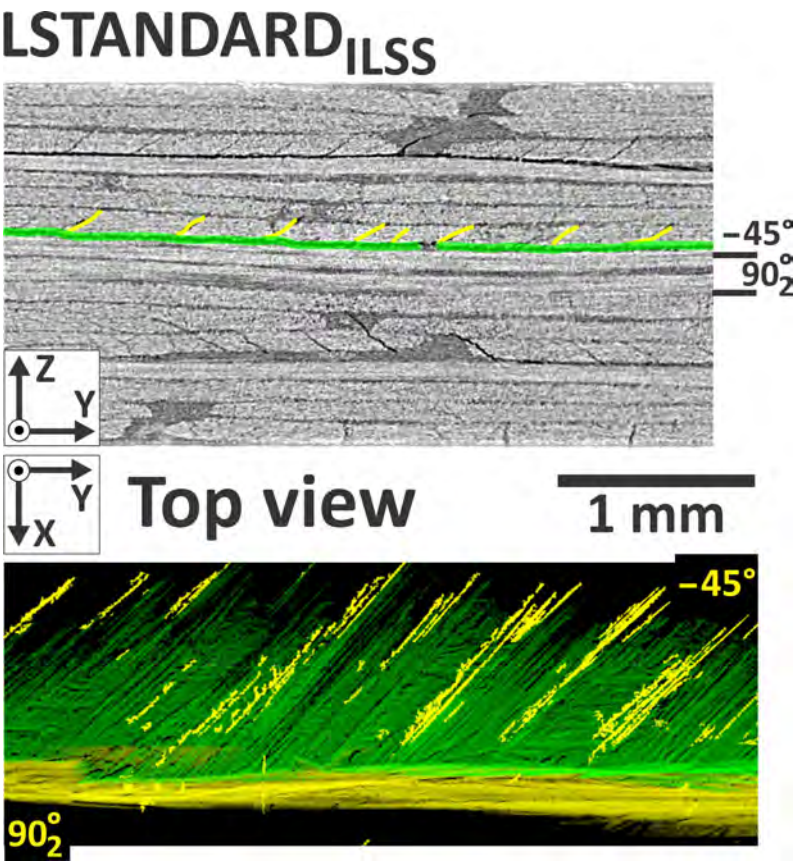


**Figure 7.3:** Delamination constrained between a single shear crack in the $90^\circ_2$ ply-cluster and multiple shear cracks in the adjacent $-45°$ layer. The shear crack in the $90^\circ_2$ ply-cluster is not visible from the YZ plane because this plane is parallel to the crack's length (refer to the coordinate system defined in Fig. 7.1). The yellow and green colours stand for the shear cracks and the delamination.

the YZ plane because this plane is parallel to the crack's length). Among these damage mechanisms, the shear crack in the $90^\circ_2$ ply-cluster was the first one to initiate (Chapter 3). Therefore, it is plausible that delamination develops as a result of the progressive intersection of the initial shear crack in the $90^\circ_2$ ply-cluster with the multiple shear cracks in the $-45°$ layer (for a comprehensive sketch refer to Fig 7.4). This tendency is supported by impacted specimens, where we observed delamination confined between two "main-cracks" with dissimilar orientation and multiple "micro-cracks" developing in the adjacent 45° layers (e.g. Fig. A.3). Choi *et al.* also observed multiple micro-cracks growing in the off-axis plies of impacted specimens [183]. In summary, our observations (a) demonstrate that shear cracks induce delamination during ILSS experiments and (b) suggest that delamination grows progressively as a result of the intersection of multiple shear crack with dissimilar orientation.

The in-situ effect also governs the damage sequence evolution of LSTANDARD$_{LVI}$ and LTHIN$_{LVI}$ specimens (for detailed explanations of the impact and QSI experi-

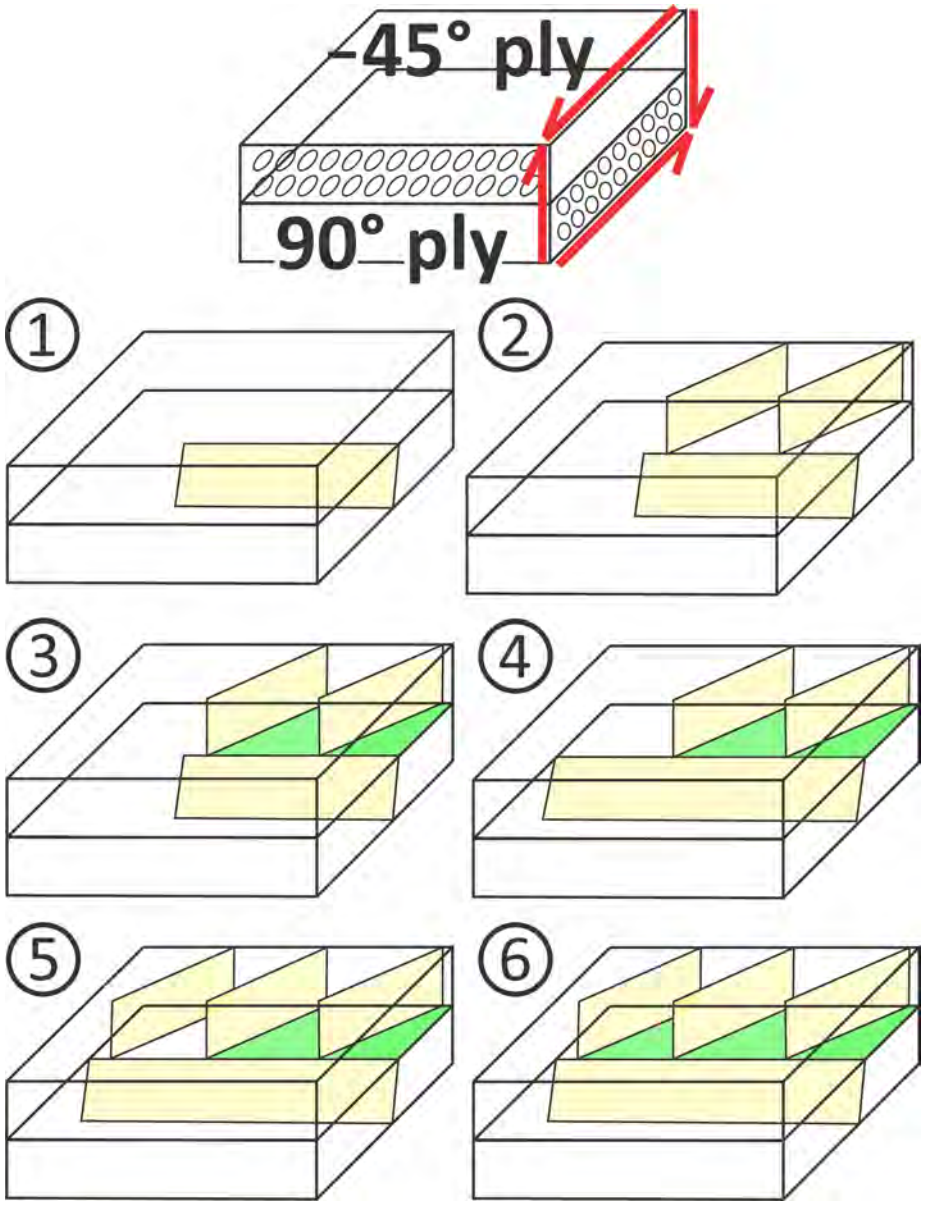


**Figure 7.4:** Suspected damage sequence evolution of the damage scenario highlighted in Fig 7.3. The yellow and green colours stand for the shear cracks and the delamination. whereas the red arrows represent the applied load (for further insight refer to the sketch of Fig. 7.1).

mental campaigns refer to Chapter 4). While both materials displayed qualitatively similar damage mechanisms, the thin-plies delayed the onset of shear cracks and delaminations to higher applied energies (Figs. 4.4a-b and 4.5a-b). What is surprising is that, for thin laminates, damage mitigation is connected with a poorer impact tolerance. The combination of low energy dissipation and high bending deflections (inherent to thin laminates) resulted in premature fibre failure in the non-impacted surface of $\text{LTHIN}_{\text{LVI}}$ (Fig. 7.5) [3, 98]. Besides this, the intensity of fibre failure increased with improved impact energy resulting, for impact at 14 J, in a lower load-carrying capacity and CAI strength compared to $\text{LSTANDARD}_{\text{LVI}}$

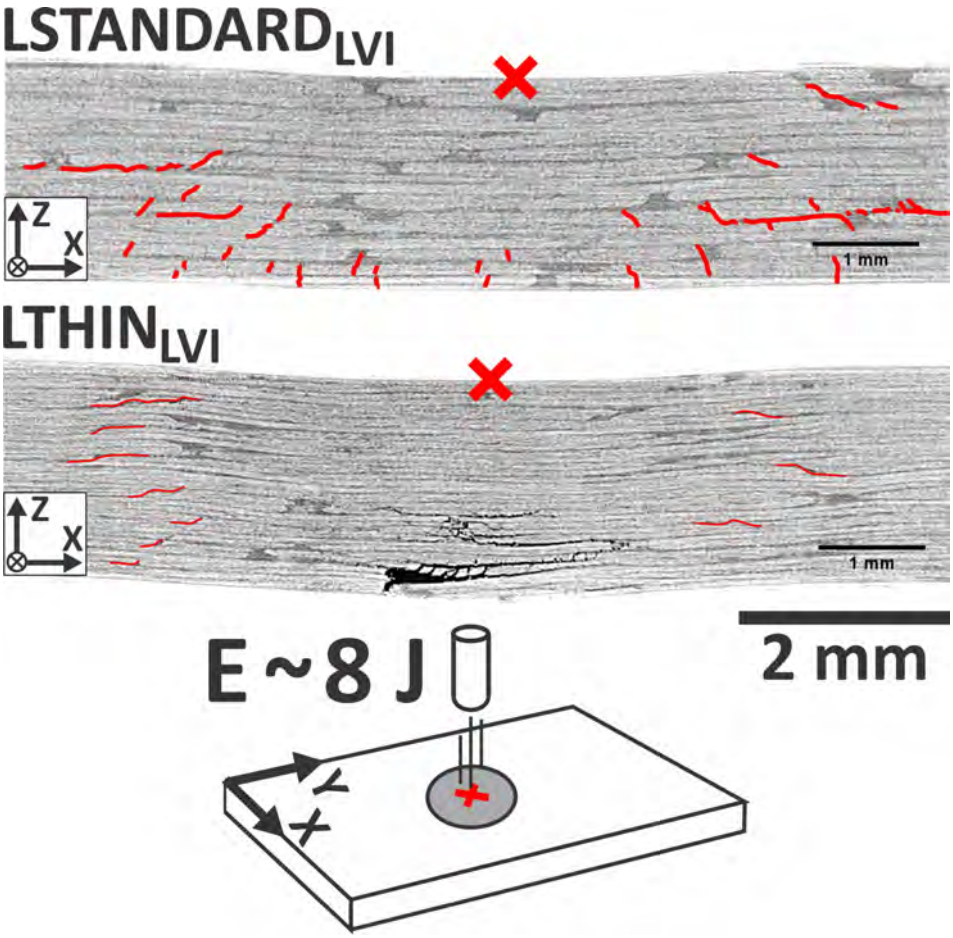


**Figure 7.5:** Damage scenario of LSTANDARD$_{LVI}$ and LTHIN$_{LVI}$ after quasi-static indentation at approximately 8 J. Shear cracks and delamination are coloured red, while the fibre failure in the non-impacted surface of LTHIN$_{LVI}$ is black.

(Figs. 4.2 and 4.9). Therefore, it is clear that the thin-plies impair thin laminate's impact tolerance, which justifies the use of toughening methods such as non-woven veils.

The author speculates that the CAI tendency displayed by LSTANDARD$_{LVI}$ and LTHIN$_{LVI}$ could be reversed for impact energies higher than 14 J. The CAI strength of the thin-ply laminates is expected to level-off after laminate penetration, whereas the CAI strength of LSTANDARD$_{LVI}$ will keep decreasing with improved impact energy because of the higher delamination extension. Therefore, we believe that, for a certain energy range above 14 J, the thin-ply specimens may exhibit a higher CAI strength than the standard-ply counterparts (this is currently investigation). In any case, based on recent works at the University of Girona, an optimal balance between the damage suppression and CAI strength can be achieved by mixing standard- and thin-plies within the same laminate [206–208] —whereas ply-hybridization is out-of-the-scope of this thesis, the University of Girona is exploring both approaches, interleaving veils and ply-hybridization, to maximize the CAI strength of thin

laminates.

Interleaving CoPA veils, the toughening approach selected to improve the CAI strength of $LTHIN_{LVI}$, enhances the interlaminar fracture toughness, impact resistance and impact tolerance (the improvement accentuates with increased veil fibre areal weight) [14, 15, 18, 115, 123, 137]. However, an excessive veil fibre areal weight severely compromises laminate thickness and certain in-plane mechanical properties [15, 18, 19]. To minimize this trade-off, we selected two types of light CoPA veils named $V_1$ and $V_2$. Fig. 7.6 illustrates the effect interleaving has on interface thickness, while Fig. 7.7 summarizes the mechanical properties of the thin-ply baseline and interleaved configurations (for the sake of comparison, the available mechanical properties of the standard-ply laminate were also included in the figure). The success of the initial objective is evident: interleaving $V_2$ veils improves impact resistance, tolerance and mode-I interlaminar fracture toughness with minimum reduction of tensile and compressive properties.

Interleaving both types of veil into the interfaces of the thin-ply laminate did not

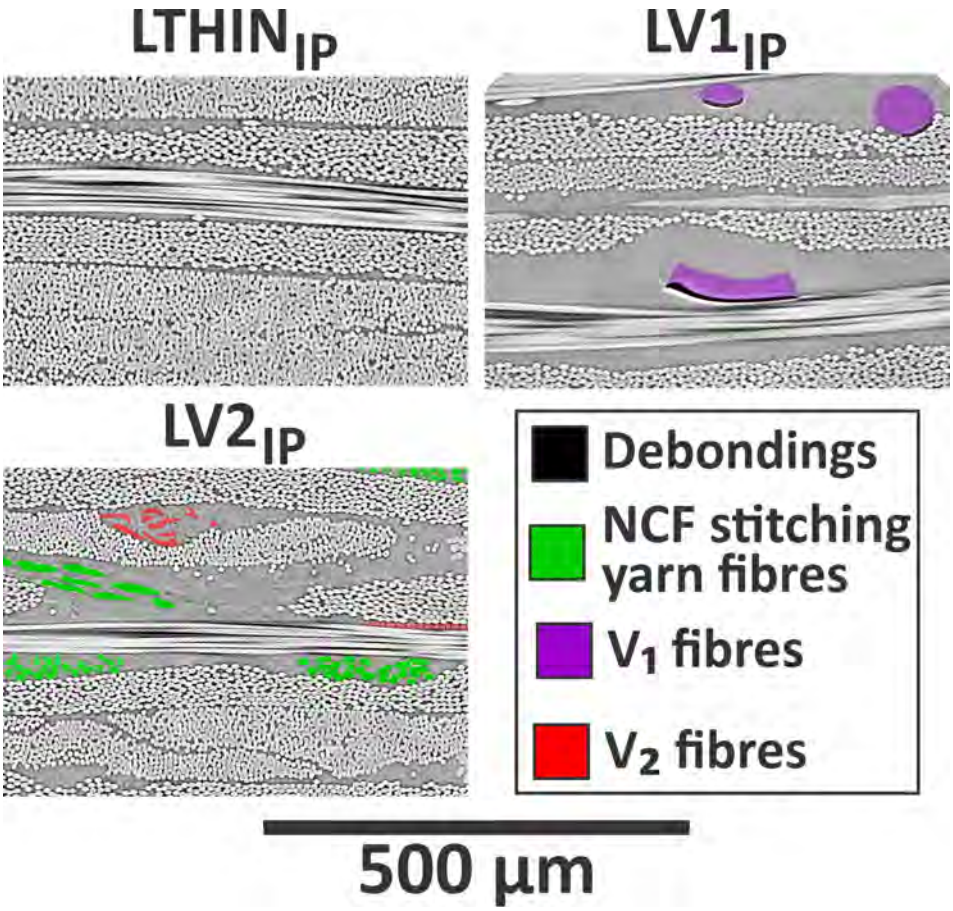


**Figure 7.6:** Sub-micron resolution µCT cross-sections depicting the microstructure of $LTHIN_{IP}$, $LV1_{IP}$ and $LV2_{IP}$. (For a enlarged version of the images, the reader is referred to Figs. 5.4-5.5 and 5.7).

increase the baseline laminate thickness because of the combination of low veil fibre areal weight (4 g/m$^2$) and resin transfer moulding manufacturing (all the laminates fitted within the same mould). The lack of porosity is also attributed to the low fibre areal weight of the veils: light veils allow through-the-thickness resin flow [16, 19]. Regarding the adhesion between veil fibres and resin, the sub-micron resolution µCT inspections demonstrated consistent debonding between $V_1$ fibres and the surrounding resin (refer to $LV1_{IP}$ in Fig. 7.6). In contrast, the $V_2$ fibres displayed almost no decohesion with the resin (Figs. 5.7-5.8). Therefore, $V_2$ fibres have better adhesion with HexFlow® RTM6 epoxy than $V_1$ fibres do.

The level of detail displayed by the microstructural slices of Fig. 7.6 demonstrate that high-resolution µCT is an outstanding tool to gain insight into the state of veil fibres after manufacturing as well as to qualitatively assess the adhesion between veil fibres and matrix. The advantages compared to scanning electron microscopy, contact angle measurements or Fourier-transform infrared spectroscopy analyses are countless (the two latter techniques are used to quantify veil fibre-resin adhesion [125, 126, 129], Section 2.4.1). In contrast, high-resolution µCT is more time- and money-consuming.

The tensile modulus and strength of $LV1_{IP}$ and $LV2_{IP}$ are closely connected to the veil fibre diameter (Figs. 7.6-7.7). The tensile properties of $LV2_{IP}$ are similar to those of $LTHIN_{IP}$ because both laminates have the same nominal thickness, fibre volume fraction and (overall) interface thickness (the $V_2$ fibres did not increase the interface thickness except for the regions where they agglomerated, Fig. 7.6). Provided that $LV1_{IP}$ also has a similar nominal thickness and fibre content, the mild decrease of tensile properties can only be attributed to the higher diameter of $V_1$ fibres (the thick $V_1$ fibres increased the interface thickness, compacted locally the carbon plies and reduced carbon uniformity across the thickness, Fig. 7.6).

$LV1_{IP}$ and $LV2_{IP}$ decreased the compressive strength of $LTHIN_{IP}$ by 4% and 9% (and yet most of $LV2_{IP}$ values lay within the standard deviation of $LTHIN_{IP}$, Fig. 5.9). Compressive strength depends on the ability of the matrix to prevent fibre buckling [19]. Compressive loads rotate the carbon fibres and generate shear stresses that, in turn, further kink the fibres until catastrophic buckling occurs [209]. Therefore, we postulate that interleaving ductile veils reduces the pristine shear strength of the matrix (at least at the low strain-rate of the test [92]). This hypothesis was validated using the ILSS methodology developed in Chapter 3 (the test measuring the resistance of the matrix under transverse shear). Unpublished results demonstrate that the interlaminar shear strength of $LV1_{ILSS}$ and $LV2_{ILSS}$ specimens is 11% and 14% lower than that of $LTHIN_{ILSS}$, which is coherent with the tendencies displayed by $LV1_{IP}$ and $LV2_{IP}$. Further work will be devoted to correlate veil properties (veil

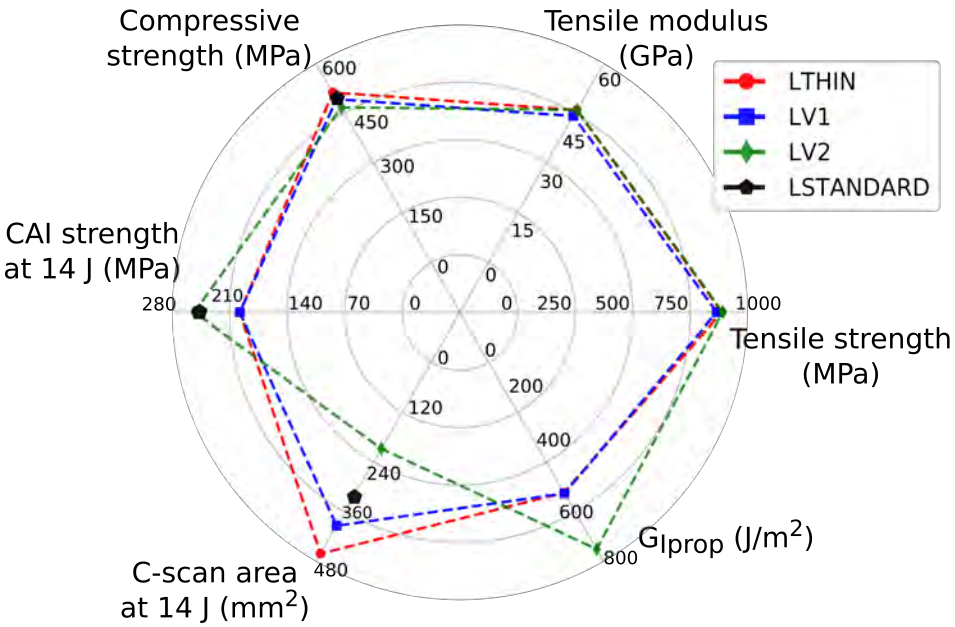


**Figure 7.7:** Mechanical properties of the standard- and thin-ply laminates (LSTANDARD and LTHIN) as well as of the thin-ply systems interleaved with $V_1$ or $V_2$ veils (LV1 and LV2). (For more detailed charts including standard deviations, the reader is referred to Figs. 4.3, 4.9, 5.9, 5.11, 6.4, 6.13).

fibre diameter, veil fibre adhesion...) with matrix shear strength.

Regarding mode-I interlaminar fracture toughness, crack propagation is mainly controlled by the adhesion between veil fibres and resin. Fibres with a low adhesion (the $V_1$ fibres) promote crack growth by debonding from the resin. Fibres with a higher adhesion (the $V_2$ fibres) deviate crack growth away from the veil (Fig. 7.8) [124]. In $LV1_{GIC}$, the mode-I crack confined itself into the 0°/0° interface through interaction with the $V_1$ fibres. In $LV2_{GIC}$, the crack deviated from the 0°/0° interface to the surrounding 0° plies.

$LV2_{G_{IC}}$ enhanced $G_{Iinit}$ and $G_{Iprop}$ by 101% and 43% compared to $LTHIN_{G_{IC}}$, while $LV1_{G_{IC}}$ only enhanced $G_{Iinit}$ by 12% (Fig. 5.11). The relation between mode-I interlaminar fracture toughness and veil fibre-resin adhesion is contrary to the one observed in conventional-ply laminates [126]. In those systems, the veil with higher adhesion ($V_2$) results in the lower $G_{IC}$ values because it deviates crack propagation from the resin interface (full of veil) to the interfacial region between resin and structural fibres (depleted of veil, Fig. 2.20). The difference is that $V_2$ deviated crack propagation not to the interfacial region but into the 0° plies (Fig. 7.8), which obviously increased the initiation energy (the crack required extra-energy to circumvent the $V_2$ fibres and penetrate into the tows). The reason why $V_2$ deviated crack propagation into the intralaminar region is probably a combination of several factors such us the small interface thickness of thin-plies, the shape distortions induced by the NCF stitches and the low veil fibre diameter preventing

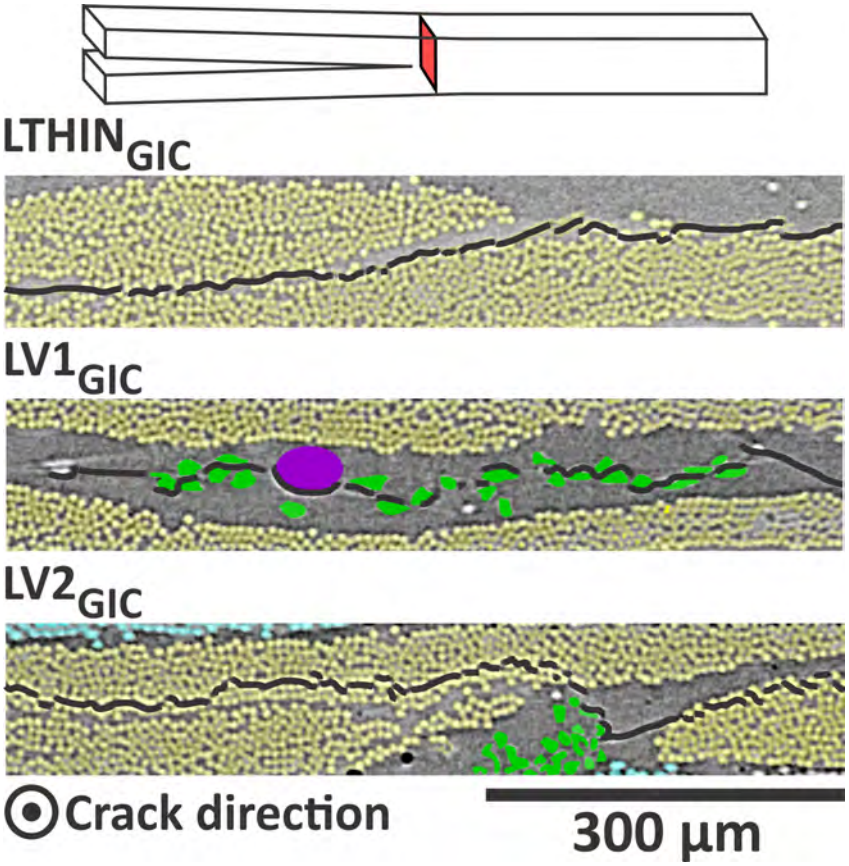


**Figure 7.8:** Sub-micron resolution µCT cross-sections depicting the fracture process zone of LTHIN$_{GIC}$, LV1$_{GIC}$ and LV2$_{GIC}$ double cantilever beam specimens. The crack grows towards the reader. (For the colour legend of this figure, refer to Fig. 5.2).

resin accumulation in the interfaces. Regarding LV1$_{GIC}$, $G_{Iprop}$ was unaffected because of the low surface area covered by $V_1$ fibres (22%): the crack encountered few veil fibres during its propagation (for details of the fibre architecture of $V_1$ and $V_2$ refer to Section 5.2.1).

The positive and subtle effects that $V_2$ and $V_1$ veils have on mode-I interlaminar fracture toughness are also replicated on impact resistance: LV2$_{LVI}$ and LV1$_{LVI}$ reduced LTHIN$_{LVI}$'s C-scan damage area by 55% and 15% for impact at 14 J. Besides this, LV2$_{LVI}$ enhanced the baseline CAI strength by 28% (Figs 7.7). (For the complete details of LTHIN$_{LVI}$, LV1$_{LVI}$ and LV2$_{LVI}$'s impact and CAI experimental campaigns, the reader is referred to Chapter 6). What is even more interesting is that, compared to LSTANDARD$_{LVI}$, LV2$_{LVI}$ also reduced C-scan damage area (by 36% for impact at 14 J) as well as recovered the full CAI strength (Fig. 7.7). Therefore, interleaving $V_2$ veils overcomes the weak impact tolerance of thin laminates made with thin-plies (for more information concerning LSTANDARD$_{LVI}$ and LTHIN$_{LVI}$'s impact responses refer to Chapter 4). The impact damage scenario of LV2$_{LVI}$ evidences that $V_2$ veils mitigated delamination initiation compared to the non-

interleaved laminate (Fig. 7.9). In particular, they arrested delamination induced during the fibre failure event since $LTHIN_{LVI}$ develops minimum delamination prior to fibre failure (Fig. 7.5). This fact was captured by the load-displacement curves: $LV2_{LVI}$ reduced the magnitude of the load drop attributed to failure failure damage (i.e. the load drop after $F_i$ in Fig. 6.2, Table 6.3) [92] —for further information regarding the load-displacement curves of thin laminates and the damage mechanisms underlying the observed load drops refer to Section 2.3.1. The reason for the damage suppression is probably that $V_2$ veils enhance the pristine shear strength of the matrix under high-strain rates of the test, which is in agreement with the shear strength reduction under static compression because thermoplastic materials (the veils) suffer strain-rate hardening [92, 210].

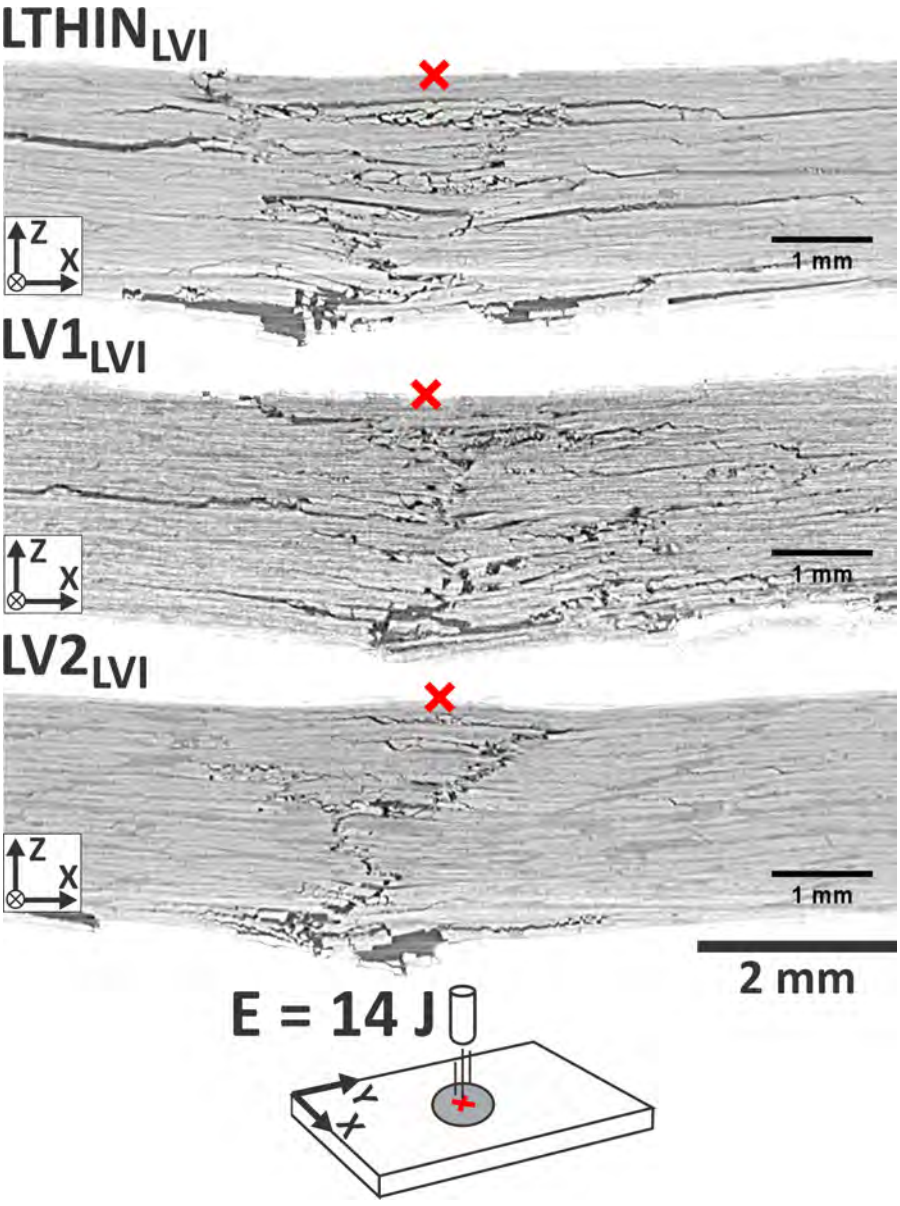


**Figure 7.9:** Damage scenario of $LTHIN_{LVI}$, $LV1_{LVI}$ and $LV2_{LVI}$ after impact at 14 J.

$LV1_{LVI}$ featured an impact scenario comparable to that of $LTHIN_{LVI}$, albeit with slightly reduced intensity (Fig. 7.9). This is once again attributed to the low surface area covered by $V_1$ fibres: there is a few number of fibres available to interact with the delamination front.

Most of the mechanical properties of interleaved laminates present a common denominator: they would benefit from thinner veil fibres. The benefits of reducing veil fibre diameter are two-fold: minimizing the increase of interface thickness and improving the surface area covered by veil fibres. This is supported by the experimental observations of Ramírez *et al.* [15] and Tsotsis *et al.* [13]: they improved interlaminar fracture toughness and CAI strength by, for a given veil configuration, increasing the surface area covered by veil fibres. Reducing veil fibre diameter means changing the scale of the fibres from the micro- to the nano-scale: "nano-fibre veils" may result in synergetic improvements of impact, flexural, compressive properties, etc. [197, 211, 212]. However, they entail an evident disadvantage: manufacturing costs. In this sense, $V_2$, the light micro-fibre veil proposed in this study, offers a reasonable balance between price, commercial availability, mechanical properties and ease of manufacture, optimal for toughening thin-plies.

The final discussion concerns the comparison between low-velocity impact and quasi-static indentation experiments. In the non-interleaved laminates ($LSTANDARD_{LVI}$ and $LTHIN_{LVI}$), both tests displayed a good coherence in terms of the force local maxima preceding the load drops, the C-scan projected damage area and the damage mechanisms observed using μCT (Section 4.3). Therefore, the quasi-static test can be used to infer qualitative information about the damage mechanisms taking place during impact. In contrast, $LV2_{LV1}$ displayed inconsistent impact and quasi-static indentation damage scenarios. For LVI at 14 J, $LV2_{LV1}$ arrested delamination propagation compared to the non-interleaved laminate (Fig. 7.9) while, for QSI at 8 J, $LV2_{LV1}$ displayed more extended delaminations than $LTHIN_{LV1}$ (Fig. 6.10). This is in line with the typical strain-hardening behaviour of thermoplastics and highlights the fact that the correlation between LVI and QSI is a material dependent problem [85]. The results of Lawrence *et al.* [213], where a glass/epoxy laminate displayed conflicting projected damage areas but similar CAI strength after LVI and QSI at equivalent applied energies, evidences the complexity of the topic (they tested both impacted and indented specimens under compression).

In a nutshell, the experimental results of this thesis provide insight into the interaction between shear cracks and delamination under transverse shear (it is the shear cracks which induces delamination) as well as furnish evidence of the corresponding in-situ effect (the thin-plies have a higher resistance to matrix cracking under $\tau_{23}$

stress). It is precisely the in-situ effect which, during impact, delays the development of shear cracks and delamination in thin laminates made with thin-plies. However, the damage suppression results into premature fibre failure and a reduced impact tolerance compared to their standard-ply counterparts (CAI strength decreased by 27% for impact at 14 J). To improve impact tolerance, we interleaved two types of co-polyamide micro-fibre non-woven veil into the interfaces. One of the veils recovered the CAI strength of the standard-ply laminate (the relatively low veil fibre areal weight and veil fibre diameter were crucial to minimize the penalty of tensile and compressive properties). Therefore, if non-woven micro-fibre veils are used to improve the impact tolerance of thin laminates made with thin-plies, we recommend the lightest and thinnest veil configuration that is commercially available —this recommendation could not be valid for other types of veil such us those made with nano-fibres. Besides reducing impact damage, the veils could have other applications such as scarf repairs [134], reducing delamination induced by pull-off loads or improving the conductivity of the laminate (by functionalizing the veils with silver nano-wires [135] or graphite/graphene particles [120])

# Conclusions and future work

# 8

## 8.1 Conclusions

Combining interlaminar shear strength (ILSS) and quasi-static indentation (QSI) experiments with X-ray micro-computed tomography (μCT) inspections, we elucidated the low-velocity impact damage sequence of thin quasi-isotropic laminates made with standard- or thin-plies. (The ILSS test provided insight into the interaction between shear cracks and delamination, whereas the QSI experiment is a replica of the impact scenario). Impact resistance and tolerance was subsequently characterized with the drop-weight impact and compression after impact (CAI) tests. Besides this, we enhanced the CAI strength of the thin-ply laminate by interleaving thermoplastic non-woven veils (two types of co-polyamide veil were studied: $V_1$ and $V_2$). The veil that improved CAI strength also improved mode-I interlaminar fracture toughness with minimum impairment of in-plane mechanical properties. For interleaved laminates, some of the experiments were accompanied by sub-micron resolution μCT inspections.

The force-displacement curves of ILSS specimens displayed monotonous load growth until a catastrophic load drop developed. The damage sequence evolution of standard- and thin-ply samples exhibited common qualitative trends. A few newtons before the drop-off, a shear crack tunnelled across from one of the free-edges of the central $90^\circ_2$ ply-cluster. The intersection of this crack with multiple shear cracks in the adjacent $-45^\circ$ layers induced delamination which, in turn, triggered the load drop. Eventually, the stress redistribution extended the damage through the thickness of the coupons. The main difference between the standard- and thin-ply systems was the stress at which the initial shear crack developed (for a similar maximum principal stress, the thinner $90^\circ_2$ ply-cluster displayed a 32% higher strength). Based on the observations, we conclude that (a) it is the shear cracks that trigger delamination under transverse shear ($\tau_{23}$ in the local coordinates of the $90^\circ$ plies) (b) it is the delamination which impairs the load-carrying capacity (c) decreasing ply-thickness increases ply-strength because of the in-situ effect.

The sequence of damage events developed in the standard- and thin-ply laminates also exhibited common qualitative trends. First, shear cracks and delamination concatenated from the non-impacted to the impacted surface of the specimens. Then, fibre failure developed in the non-impacted surface and subsequently evolved towards the impactor causing further damage propagation. The difference was that, owing to the in-situ effect, the thin-plies delayed the onset of matrix cracks and delaminations. Lessening the energy dissipated through delamination propagation resulted in premature fibre breakage, decreased load-carrying capacity (by 25% and

55% for impact at 10 and 14 J) and lower CAI strength for impact at 14 J (by 27%). The reason why impact damage propagated from the non-impacted to the impacted surfaces is the low thickness-to-length ratio of the specimens: thin laminates suffer high deflections an associated bending stresses.

The key aspect to preserve laminate thickness was the combination of low veil fibre areal weight (4 g/m$^2$) and resin transfer moulding manufacturing (baseline and interleaved configuration configurations fitted within the same mould). Given the similar laminate thickness, the veil fibre diameter was the crucial in determining the tensile properties. The veil with thicker fibres ($V_1$) increased the thickness of the resin interfaces and reduced the tensile properties (elastic modulus and ultimate strength were reduced by 4% and 5%). The veil with the thinner fibres ($V_2$) avoided resin accumulation in the interfaces and displayed the same tensile strength, strain-to-failure and longitudinal modulus as the baseline laminate did.

Mode-I interlaminar crack propagation was mainly controlled by the adhesion between fibres (the non-crimp fabric yarn fibres, the $V_1$ fibres and the $V_2$ fibres) and the resin. Fibres with a low adhesion (the yarn fibres and the $V_1$ fibres) promoted crack growth by debonding from the resin. Fibres with a higher adhesion (the $V_2$ fibres) deviated crack growth away from the veil. In the non-interleaved laminate, the crack deviated from the 0°/0° interface through debonding of the stitching yarn fibres. In the laminate interleaved with $V_1$, the crack confined into the 0°/0° interface through interaction with the $V_1$ fibres (fracture toughness was not improved because the veil $V_1$ contained few fibres). In the laminate interleaved with $V_2$, the crack migrated from the 0°/0° interface to the surrounding 0° plies which, in the material system studied, resulted in the highest mode-I initiation and propagation interlaminar fracture toughness (101% and 43% increase compared to the baseline).

Both types of veil decreased compressive strength by up to 9% because of an increase in the ductile phase surrounding the carbon plies, which favours fibre buckling. However, $V_2$ arrested the initiation of delamination during impact (damage area was reduced by 55%) and recovered the CAI strength of the standard-ply system.

The last conclusion of this thesis concerns the comparison between the drop-weight impact and QSI experiments. In the non-interleaved laminates, both tests displayed a good coherence in terms of the force-level of the load drops, the projected damage area (which grew linearly with the incremental energy applied in both tests) and the observed damage mechanisms. Therefore, for the type of materials and range of energies considered in this study, the quasi-static test can be used to infer qualitative information about the failure mechanisms developing during low-velocity impact. In contrast, the laminate interleaved with $V_2$ veils displayed inconsistent impact

and QSI damage scenarios. For impact at 14 J, it arrested delamination propagation compared to the non-interleaved laminate whereas, for QSI at 8 J, it displayed larger delaminations than the baseline system. In other words, the strain rate is a crucial parameter governing the structural response of laminates toughened with thermoplastic veils.

From the airline's industry point of view, interleaving $V_2$ veils is a potential toughening technique to enhance the CAI strength of thin laminates made of thin-plies; not only because they arrest impact damage, but also because they are relatively cheap, commercially available and easy to manufacture (the only extra-step is cutting and incorporation of the veils during the lay-up). $V_2$ entails a 9% reduction of pristine compressive strength. However, this deterioration is less relevant when compared to the compressive strength of the standard-ply laminates (6%).

## 8.2 Future work

Chapter 3 proposes a novel experimental methodology to characterize in-situ strength under transverse shear. Two quasi-isotropic laminates were studied, one with standard-, and other with thin-plies. The next step should be testing a wider range of ply-thicknessess. The design of such experimental campaign should depart from a numerical analysis to ensure that, in all the laminates, ply-failure is caused by a similar principal stress distribution. A second experimental campaign should be devoted to characterize how in-situ strength depends on the orientation of the adjacent plies (the in-situ strength depends not only on ply thickness, but also, in second order, on the orientation of the surrounding plies [21, 23]). The last and most important step of this work package should be developing an analytical expression able to connect transverse shear in-situ strength ($S_T^{is}$) with ply-thickness ($t$) in order to enrich existing 3D failure criteria (this analytical expression should be experimentally validated).

Chapter 4 reports a detailed experimental study of the impact and CAI responses of thin laminates made with standard- and thin-plies. For impact at 14 J, the $\text{LTHIN}_{\text{LVI}}$ specimens displayed increased amounts of fibre failure compared to their $\text{LSTANDARD}_{\text{LVI}}$ counterparts which, in turn, resulted in a lower CAI strength. Further work should be devoted to verify if the same tendency applies for impact at higher energies (the author believes that the CAI strength of $\text{LTHIN}_{\text{LVI}}$ coupons impacted at higher energies will reach a plateau value because of laminate penetration).

Recent studies by Sasikumar *et al.* [207, 208] (University of Girona) and a previous study by Sebaey *et al.* [206] demonstrate that a promising balance between damage

supression and CAI strength can be achieved by mixing conventional- and thin-plies within the same laminate. The success of those studies along with the large design space of thin-plies suggest that there is still a lot of room for improvement. To further improve the CAI strength of thin laminates, ply-hybridization could be combined with the use of veils in selected interfaces.

Chapters 5-6 deal with the characterization and analysis of the thin-ply baseline laminate and the configurations interleaved with $V_1$ or $V_2$ veils. Interleaving $V_2$ improves CAI strength and mode-I interlaminar fracture toughness with reduced impairment of in-plane mechanical properties. To further reduce this trade-off, the first step should be minimizing the impact that $V_2$ veils have on the microstructure. A "heat bonding" step prior to resin infusion (i.e. carefully heating the laminate pre-form to improve the adhesion between veils and dry fabrics) will be performed to avoid agglomeration of $V_2$ fibres (Fig. 5.7a) [13, 117]. In addition to this, $V_2$ fibre diameter should be reduced as much as possible in order to (a) minimize the increase of interface thickness and (b) improve the surface area covered by veil fibres. After assessing which of the veil fibre architectures provides the better mechanical properties, the veil fibre areal weight will also be optimized (the studied veils remaining relatively light). To reduce costs, the veils should be fabricated using industrial processes.

Another aspect that captured the attention of this investigation was assesing the adhesion between veil fibres and resin. To this purpose, we accomplished insightful but costly sub-micron resolution X-ray micro-computed tomography inspections. Further efforts should be devoted to develop a mechanical procedure able to characterize the adhesion force between veil fibres and resin. This procedure will provide quick insight into the adhesion between veil fibres and different types of industrial resin.

Using $V_2$ veils in aircraft laminate design requires knowledge about the effect moisture and temperature conditioning has on mechanical properties (polyamide is hydrophilic [14, 17, 123]). Besides this, other mechanical properties such as mode-II and mixed-mode interlaminar fracture toughness, the intralaminar fracture toughness, dynamic-mechanical properties, flexural properties, creep performance, etc. should be tested under dry and humid conditions.

The contradictory impact and quasi-static indentation damage scenarios displayed by the specimens interleaved with $V_2$ veils evidence that their matrix properties depend on the strain-rate (Chapter 6). Strain-rate effects should be the concern of an additional experimental campaign. This campaign should include not only the usual composite coupons, but also specimens formed by only resin and veil (e.g. tensile, single-edge-notch bending specimens, etc.).

# Bibliography


[1] J. Llorca, C. González, J. M. Molina-Aldareguía, C. S. Lópes, Multiscale modeling of composites: Toward virtual testing ... and beyond, The Journal of The Minerals, Metals & Materials Society (TMS) 65 (2) (2013) 215–225. doi:10.1007/s11837-012-0509-8.

[2] S. Sihn, R. Kim, K. Kawabe, S. Tsai, Experimental studies of thin-ply laminated composites, Composites Science and Technology 67 (6) (2007) 996–1008. doi:10.1016/j.compscitech.2006.06.008.

[3] R. Amacher, J. Cugnoni, J. Botsis, L. Sorensen, W. Smith, C. Dransfeld, Thin ply composites: Experimental characterization and modeling of size-effects, Composites Science and Technology 101 (2014) 121–132. doi:10.1016/j.compscitech.2014.06.027.

[4] J. Cugnoni, R. Amacher, S. Kohler, J. Brunner, E. Kramer, C. Dransfeld, W. Smith, K. Scobbie, L. Sorensen, J. Botsis, Towards aerospace grade thin-ply composites: Effect of ply thickness, fibre, matrix and interlayer toughening on strength and damage tolerance, Composites Science and Technology 168 (10) (2018) 467–477. doi:10.1016/j.compscitech.2018.08.037.

[5] S. Abrate, Impact on composite structures (1998). URL: www.cambridge.org/9780521473897.

[6] S. Rivallant, C. Bouvet, E. Abi Abdallah, B. Broll, J. J. Barrau, Experimental analysis of CFRP laminates subjected to compression after impact: The role of impact-induced cracks in failure, Composite Structures 111 (1) (2014) 147–157. doi:10.1016/j.compstruct.2013.12.012.

[7] C. Bouvet, S. Rivallant, Damage tolerance of composite structures under low-velocity impact, Elsevier, 2016. doi:10.1016/b978-0-08-100080-9.00002-6.

[8] G. Davies, R. Olsson, Impact on composite structures, The Aeronautical Journal 108 (1089) (2004) 541–563. doi:10.1017/S0001924000000385.

[9] R. Bogenfeld, J. Kreikemeier, T. Wille, Review and benchmark study on the analysis of low-velocity impact on composite laminates, Engineering Failure Analysis 86 (2018) 72–99. doi:10.1016/j.engfailanal.2017.12.019.

[10] N. H. Nash, T. M. Young, P. T. McGrail, W. F. Stanley, Inclusion of a thermoplastic phase to improve impact and post-impact performances of carbon fibre reinforced thermosetting composites - A review, Materials and Design 85 (2015) 582–597. doi:10.1016/j.matdes.2015.07.001.

[11] N. Hongkarnjanakul, Modélisation numérique pour la tolérance aux dommages d'impact sur stratifié composite : de l'impact à la résistance résiduelle en compression. Ph.D. dissertation submitted to the University of Toulouse (2013).
URL http://depozit.isae.fr/theses/2013/2013_Hongkarnjanakul_Natthawat.pdf

[12] R. Talreja, N. Phan, Assessment of Damage Tolerance Approaches for Composite Aircraft with Focus on Barely Visible Impact Damage, Composite Structures 219 (January) (2019) 1–7. doi:10.1016/J.COMPSTRUCT.2019.03.052.

[13] T. Tsotsis, Interlayer toughening of composite materials, Polymer Composites 30 (1) (2009) 70–86. doi:10.1002/pc.20535.

[14] N. Nash, D. Ray, T. Young, W. Stanley, The influence of hydrothermal conditioning on the Mode-I, thermal and flexural properties of Carbon/Benzoxazine composites with a thermoplastic toughening interlayer, Composites Part A: Applied Science and Manufacturing 76 (2015) 135–144. doi:10.1016/j.compositesa.2015.04.023.

[15] V. Ramírez, P. Hogg, W. Sampson, The influence of the nonwoven veil architectures on interlaminar fracture toughness of interleaved composites, Composites Science and Technology 110 (2015) 103–110. doi:10.1016/j.compscitech.2015.01.016.

[16] N. H. Nash, T. M. Young, W. F. Stanley, An investigation of the damage tolerance of carbon/Benzoxazine composites with a thermoplastic toughening interlayer, Composite Structures 147 (2016) 25–32. doi:10.1016/j.compstruct.2016.03.015.

[17] N. H. Nash, T. Young, W. Stanley, The influence of a thermoplastic toughening interlayer and hydrothermal conditioning on the Mode-II interlaminar fracture toughness of Carbon/Benzoxazine composites, Composites Part A: Applied Science and Manufacturing 81 (2016) 111–120.

doi:10.1016/j.compositesa.2015.11.010.

[18] B. Beylergil, M. Tanoğlu, E. Aktaş, Effect of polyamide-6,6 (PA 66) nonwoven veils on the mechanical performance of carbon fiber/epoxy composites, Composite Structures 194 (2018) 21–35. doi:10.1016/j.compstruct.2018.03.097.

[19] S. Miller, G. Roberts, L. Kohlman, P. Heimann, J. Pereira, R. Ruggeri, R. Martin, L. McCorkle, Impact behavior of composite fan blade leading edge subcomponent with thermoplastic polyurethane interleave. 20th International Conference on Composite Materials (Copenhagen, 19-24th July 2015).

[20] G. J. Dvorak, N. Laws, Analysis of Progressive Matrix Cracking In Composite Laminates II. First Ply Failure, Journal of Composite Materials 21 (April 1987) (1987) 309–329. doi:10.1177/002199838702100402.

[21] P. Camanho, C. Dávila, S. Pinho, L. Iannucci, P. Robinson, Prediction of in situ strengths and matrix cracking in composites under transverse tension and in-plane shear, Composites Part A: Applied Science and Manufacturing 37 (2) (2006) 165–176. doi:10.1016/j.compositesa.2005.04.023.

[22] P. Maimí, E. V. González, P. P. Camanho, Comment to the paper 'Analysis of Progressive Matrix Cracking in Composite Laminates II. First Fly Failure' by George J Dvorak and Norman Laws, Journal of Composite Materials 48 (9) (2014) 1139–1141. doi:10.1177/0021998313483986.

[23] G. Catalanotti, Prediction of in situ strengths in composites: some considerations, Composite Structures 207 (2018) 889–893. doi:10.1016/j.compstruct.2018.09.075.

[24] A. Arteiro, G. Catalanotti, A. R. Melro, P. Linde, P. P. Camanho, Micromechanical analysis of the in situ effect in polymer composite laminates, Composite Structures 116 (1) (2014) 827–840. doi:10.1016/j.compstruct.2014.06.014.

[25] P. Maimí, P. Rodriguez, N. Blanco, J. Mayugo, Numerical modeling of matrix cracking and intralaminar failure in advanced composite materials. In "Numerical Modelling of Failure in Advanced Composite Materials". Eds.: Camanho, P.P. and Hallet, S.R., 2015. doi:10.1016/B978-0-08-100332-9.00007-4.

[26] A fatigue damage and residual strength model for unidirectional carbon/epoxy composites under on-axis tension-tension loadings, International Journal of Fatigue 103 (2017) 508–515. doi:10.1016/j.ijfatigue.2017.06.026.

[27] P. Camanho, A. Arteiro, G. Catalanotti, A. Melro, M. Vogler, Three-dimensional invariant-based failure criteria for transversely isotropic fibre-reinforced composites. In "Numerical Modelling of Failure in Advanced Composite Materials". Eds.: Camanho, P.P. and Hallet, S.R., 2015. doi:10.1016/B978-0-08-100332-9.00005-0.

[28] T. A. Sebaey, J. Costa, P. Maimí, Y. Batista, N. Blanco, J. A. Mayugo, Measurement of the in situ transverse tensile strength of composite plies by means of the real time monitoring of microcracking, Composites Part B: Engineering 65 (2014) 40–46. doi:10.1016/j.compositesb.2014.02.001.

[29] A. Wang, Fracture mechanics of sublaminate cracks in composite materials, Journal of Composites, Technology and Research 6 (2) (1984) 5–62. doi:10.1520/CTR10817J.

[30] F. Crossman, A. Wang, The dependence of transverse cracking and delamination on ply thickness in graphite/epoxy laminates (1982). doi:10.1520/STP34324S.

[31] I. García, J. Justo, A. Simon, V. Mantič, Experimental study of the size effect on transverse cracking in cross-ply laminates and comparison with the main theoretical models, Mechanics of Materials 128 (May 2018) (2019) 24–37. doi:10.1016/j.mechmat.2018.09.006.

[32] A. Parvizi, J. Bailey, On multiple transverse cracking in glass fibre epoxy cross-ply laminates, Journal of Materials Science 13 (10) (1978) 2131–2136. doi:10.1007/BF00541666.

[33] D. L. Flaggs, M. H. Kural, Experimental Determination of the In Situ Transverse Lamina Strength in Graphite/Epoxy Laminates, Journal of Composite Materials 16 (2) (1982) 103–116. doi:10.1177/002199838201600203.

[34] J. Mayugo, P. P. Camanho, P. Maimí, C. Dávila, Analytical modelling of transverse matrix cracking of [$\pm\theta$/ 90n]s composite laminates under multiaxial loading, Mechanics of Advanced Materials and Structures 17 (4) (2010) 237–245. doi:10.1080/15376490903056577.

[35] H. Saito, H. Takeuchi, I. Kimpara, Experimental evaluation of the damage growth restraining in 90° layer of thin-ply CFRP cross-ply laminates, Advanced Composite Materials 21 (1) (2012) 57–66. doi:10.6089/jscm.37.121.

[36] H. Saito, H. Takeuchi, I. Kimpara, A study of crack suppression mechanism of

thin-ply carbon-fiber-reinforced polymer laminate with mesoscopic numerical simulation, Journal of Composite Materials 48 (17) (2014) 2085–2096. doi:10.1177/0021998313494430.

[37] P. Maimí, P. P. Camanho, J. A. Mayugo, C. G. Dávila, A continuum damage model for composite laminates: Part I - Constitutive model, Mechanics of Materials 39 (10) (2007) 897–908. doi:10.1016/j.mechmat.2007.03.005.

[38] G. Catalanotti, P. P. Camanho, A. T. Marques, Three-dimensional failure criteria for fiber-reinforced laminates, Composite Structures 95 (2013) 63–79. doi:10.1016/j.compstruct.2012.07.016.

[39] K. Kawabe, H. Sasayama, S. Tomoda, New carbon fiber tow spread technology and applications to advanced composite materials, SAMPE journal 45 (2009) 6–17.

[40] H. El-Dessouky, C. Lawrence, Ultra-lightweight carbon fibre/thermoplastic composite material using spread tow technology, Composites Part B: Engineering 50 (50) (2013) 91–97. doi:10.1016/j.compositesb.2013.01.026.

[41] V. Singery, T. Roure, P. Sanial, J. Drean, J. Osselin, Comparison of C-Ply™ SP (thin ply) with woven fabric and UD performances. ICCM-20, 20th International Conference on Composite Materials (2015).

[42] https://www.thinplytechnology.com/products/thin-ply-prepreg.

[43] K. Kawabe, S. Tomoda, United States Patent, number 6,032,342 (2000).

[44] R. Amacher, W. Smith, C. Dransfeld, J. Botsis, J. Cugnoni, Thin Ply: From size-effect characterization to real life design. CAMX 2014 - Composites and Advanced Materials Expo: Combined Strength (2014).

[45] T. Tsai, Theory of Composites Design. Think Composites (1992).

[46] A. Arteiro, G. Catalanotti, J. Xavier, P. Camanho, Notched response of non-crimp fabric thin-ply laminates, Composites Science and Technology 79 (2013) 97–114. doi:10.1016/j.compscitech.2013.02.001.

[47] N. Hongkarnjanakul, C. Bouvet, S. Rivallant, Validation of low velocity impact modelling on different stacking sequences of CFRP laminates and influence of fibre failure, Composite Structures 106 (2013) 549–559. doi:10.1016/j.compstruct.2013.07.008.

[48] M. Papila, Design of and with thin-ply non-crimp fabric (NCF) as building

blocks for composites, Science and Engineering of Composite Materials 25 (3) (2016) 1–16. doi:doi.org/10.1515/secm-2015-0386.

[49] A. Sasikumar, J. Costa, D. Trias, E. González, S. García-Rodríguez, P. Maimí, Unsymmetrical stacking sequences as a novel approach to tailor damage resistance under out-of-plane impact loading, Composites Science and Technology 173 (2019) 125–135. doi:10.1016/J.COMPSCITECH.2019.02.002.

[50] B. Rodini, J. Eisenmann, An Analytical and Experimental Investigation of Edge Delamination in Composite Laminates. In: Lenoe E.M., Oplinger D.W., Burke J.J. (eds) Fibrous Composites in Structural Design. Springer, Boston, MA (1980). doi:10.1007/978-1-4684-1033-4_25.

[51] P. Roure, P. Sanial, C-PLY™, a new structural approach to multiaxials in composites. JEC Composites Maganize no. 68. Special JEC Asia, pgs. 53-54 (2001).

[52] C. Huang, M. He, Y. He, J. Xiao, J. Zhang, S. Ju, D. Jiang, Exploration relation between interlaminar shear properties of thin-ply laminates under short-beam bending and meso-structures, Journal of Composite Materials 52 (17) (2017) 1–12. doi:10.1177/0021998317745586.

[53] S. Pinho, R. Gutkin, S. Pimenta, N. Carvalho, P. Robinson, Fibre-dominated compressive failure in polymer matrix composites. In "Failure Mechanisms in Polymer Matrix Composites" (eds. P. Robinson, E. Greenhalgh, and S. Pinho), Woodhead Publishing Series in Composites Science and Engineering, 2012. doi:10.1533/9780857095329.1.183.

[54] T. Yokozeki, Y. Aoki, T. Ogasawara, Experimental characterization of strength and damage resistance properties of thin-ply carbon fiber/toughened epoxy laminates, Composite Structures 82 (3) (2008) 382–389. doi:10.1016/j.compstruct.2007.01.015.

[55] A. Arteiro, G. Catalanotti, J. Xavier, P. Linde, P. P. Camanho, Effect of tow thickness on the structural response of aerospace-grade spread-tow fabrics, Composite Structures 179 (2017) 208–223. doi:10.1016/j.compstruct.2017.06.047.

[56] Y. Nishikawa, K. Okubo, T. Fujii, K. Kawabe, Fatigue crack constraint in plain-woven CFRP using newly-developed spread tows, International Journal of Fatigue 28 (2006) 1248–1253. doi:10.1016/j.ijfatigue.2006.02.010.

[57] J. Moon, M. Kim, C. Kim, S. Bhowmik, Improvement of tensile properties

of CFRP composites under LEO space environment by applying MWNTs and thin-ply, Composites Part A: Applied Science and Manufacturing 42 (6) (2011) 694–701. doi:10.1016/j.compositesa.2011.02.011.

[58] Y. Ho, H. Sasayama, J. Yanagimoto, Mechanical properties and drawing process of multilayer carbon-fiber-reinforced plastic sheets with various prepreg thicknesses, Advances in Mechanical Engineering 9 (3) (2017) 1–12. doi:10.1177/1687814017692695.

[59] K. Mouane, Polyimide thin-ply composite. M.Sc. dissertation submitted to Luleå University of Technology, Sweeden, 2018.
URL http://ltu.diva-portal.org/smash/get/diva2:1232831/FULLTEXT02.pdf

[60] G. Guillamet, A. Turon, J. Costa, J. Renart, P. Linde, J. Mayugo, Damage occurrence at edges of non-crimp-fabric thin-ply laminates under off-axis uniaxial loading, Composites Science and Technology 98 (2014) 44–50. doi:10.1016/j.compscitech.2014.04.014.

[61] P. Camanho, A. Turon, J. Costa, G. Guillamet, A. Arteiro, E. González, Structural integrity of thin-ply laminates, JEC Composites Magazine (71) (2012) 49–50.

[62] G. Guillamet, A. Turon, J. Costa, P. Linde, A quick procedure to predict free-edge delamination in thin-ply laminates under tension, Engineering Fracture Mechanics 168 (2016) 28–39. doi:10.1016/j.engfracmech.2016.01.019.

[63] C. Furtado, A. Arteiro, G. Catalanotti, J. Xavier, P. P. Camanho, Selective ply-level hybridisation for improved notched response of composite laminates, Composite Structures 145 (2016) 1–14. doi:10.1016/j.compstruct.2016.02.050.

[64] C. Huang, S. Ju, M. He, Q. Zheng, Y. He, J. Xiao, J. Zhang, D. Jiang, Identification of failure modes of composite thin-ply laminates containing circular hole under tension by acoustic emission signals, Composite Structures 206 (2018) 70–79. doi:10.1016/j.compstruct.2018.08.019.

[65] E. Kalfon-Cohen, R. Kopp, C. Furtado, X. Ni, A. Arteiro, G. Borstnar, M. Mavrogordato, I. Sinclair, S. Spearing, P. Camanho, B. Wardle, Synergetic effects of thin plies and aligned carbon nanotube interlaminar reinforcement in composite laminates, Composites Science and Technology 166 (2018) 160–168. doi:10.1016/j.compscitech.2018.01.007.

[66] G. Frossard, Fracture of thin-ply composites: effects of ply thickness. Ph.D. dissertation submitted to the École Polytechnique Fédérale de Laussane, Switzerland. (November 2010).
URL https://infoscience.epfl.ch/record/232437/files/EPFL_TH8032.pdf?version=1

[67] G. Frossard, J. Cugnoni, T. Gmür, J. Botsis, Mode I Interlaminar Fracture of Carbon Epoxy Laminates: Effects of Ply Thickness, Composites Part A: Applied Science and Manufacturing 91 (1) (2016) 1–8. doi:10.1016/j.compositesa.2016.09.009.

[68] R. Teixeira, S. Pinho, P. Robinson, Thickness-dependence of the translaminar fracture toughness: Experimental study using thin-ply composites, Composites Part A: Applied Science and Manufacturing 90 (2016) 33–44. doi:10.1016/j.compositesa.2016.05.031.

[69] G. Frossard, J. Cugnoni, T. Gmür, J. Botsis, Ply thickness dependence of the intralaminar fracture in thin-ply carbon-epoxy laminates, Composites Part A: Applied Science and Manufacturing 109 (2018) 95–104. doi:10.1016/j.compositesa.2018.03.001.

[70] W. Cantwell, J. Morton, The impact resistance of composite materials - a review, Composites 22 (5) (1991) 347–362. doi:10.1016/0010-4361(91)90549-V.

[71] M. Richardson, M. Wisheart, Review of low-velocity of composite materials, Composites Part A: Applied Science and Manufacturing 27A (1996) 1123–1131. doi:10.1016/1359-835X(96)00074-7.

[72] H. Abdulhamid, C. Bouvet, L. Michel, J. Aboissiere, C. Minot, Numerical simulation of impact and compression after impact of asymmetrically tapered laminated CFRP, International Journal of Impact Engineering 95 (2016) 154–164. doi:10.1016/j.ijimpeng.2016.05.002.

[73] N. Dubary, C. Bouvet, S. Rivallant, L. Ratsifandrihana, Damage tolerance of an impacted composite laminate, Composite Structures 206 (2018) 261–271. doi:10.1016/j.compstruct.2018.08.045.

[74] S. R. Swanson, Limits of quasi-static solutions in impact of composite structures, Composites Engineering 2 (4) (1992) 261–267. doi:10.1016/0961-9526(92)90009-U.

[75] R. Olsson, Analytical model for delamination growth during small mass impact on plates, International Journal of Solids and Structures 47 (21)

(2010) 2884–2892. doi:10.1016/j.ijsolstr.2010.06.015.

[76] E. González, P. Maimí, P. P. Camanho, C. S. Lopes, N. Blanco, Effects of ply clustering in laminated composite plates under low-velocity impact loading, Composites Science and Technology 71 (6) (2011) 805–817. doi:10.1016/j.compscitech.2010.12.018.

[77] R. Olsson, Analytical prediction of damage due to large mass impact on thin ply composites, Composites Part A: Applied Science and Manufacturing 72 (2015) 184–191. doi:10.1016/j.compositesa.2015.02.005.

[78] A. Wagih, P. Maimí, N. Blanco, E. González, Scaling effects of composite laminates under out-of-plane loading, Composites Part A: Applied Science and Manufacturing 116 (2019) 1–12. doi:10.1016/j.compositesa.2018.10.001.

[79] Y. Aoki, H. Suemasu, T. Ishikawa, Damage propagation in CFRP laminates subjected to low velocity impact and static indentation, Advanced Composite Materials 16 (1) (2007) 45–61. doi:10.1163/156855107779755318.

[80] N. Dubary, G. Taconet, C. Bouvet, B. Vieille, Influence of temperature on the impact behavior and damage tolerance of hybrid woven-ply thermoplastic laminates for aeronautical applications, Composite Structures 168 (2017) 663–674. doi:10.1016/j.compstruct.2017.02.040.

[81] A. Soto, E. V. González, P. Maimí, F. Martín de la Escalera, J. R. Sainz de Aja, E. Alvarez, Low velocity impact and compression after impact simulation of thin ply laminates, Composites Part A: Applied Science and Manufacturing 109 (2018) 413–427. doi:10.1016/j.compositesa.2018.03.017.

[82] A. Sasikumar, J. Costa, D. Trias, E. González, S. García-Rodríguez, P. Maimí, Unsymmetrical stacking sequences as a novel approach to tailor damage resistance under out-of-plane impact loading, Composites Science and Technology 173 (2019) 125–135. doi:10.1016/J.COMPSCITECH.2019.02.002.

[83] ASTM Standard D7136/D7136M-15, Standard Test Method for Measuring the Damage Resistance of a Fiber-Reinforced Polymer Matrix Composite to a Drop-Weight Impact Event. ASTM International, West Conshohocken, PA, 2015. doi:10.1520/D7136_D7136M-15.

[84] G. Davies, X. Zhang, Impact damage prediction in carbon composite structures, International Journal of Impact Engineering 16 (1) (1995) 149–170. doi:10.1016/0734-743X(94)00039-Y.

[85] A. Nettles, M. J. Douglas, A comparison of quasi-static indentation to low-

velocity impact, NASA Technical Report, NASA/TP-2000-210481, Langley Research Center, Virginia, USA (2000).
URL https://ntrs.nasa.gov/archive/nasa/casi.ntrs.nasa.gov/20000109864.pdf

[86] T. A. Sebaey, E. V. González, C. S. Lopes, N. Blanco, J. Costa, Damage resistance and damage tolerance of dispersed CFRP laminates: Effect of ply clustering, Composite Structures 106 (2013) 96–103. doi:10.1016/j.compstruct.2013.05.052.

[87] T. A. Sebaey, E. V. González, C. S. Lopes, N. Blanco, P. Maimí, J. Costa, Damage resistance and damage tolerance of dispersed CFRP laminates: Effect of the mismatch angle between plies, Composite Structures 101 (2013) 255–264. doi:10.1016/j.compstruct.2013.01.026.

[88] E. González, P. Maimí, J. R. Sainz de Aja, P. Cruz, P. P. Camanho, Effects of interply hybridization on the damage resistance and tolerance of composite laminates, Composite Structures 108 (1) (2014) 319–331. doi:10.1016/j.compstruct.2013.09.037.

[89] Y. Liv, G. Guillamet, J. Costa, E. González, L. Marín, J. Mayugo, Experimental study into compression after impact strength of laminates with conventional and nonconventional ply orientations, Composites Part B: Engineering 126 (2017) 133–142. doi:10.1016/j.compositesb.2017.05.074.

[90] X. Sun, S. Hallett, Failure mechanisms and damage evolution of laminated composites under compression after impact (CAI): Experimental and numerical study, Composites Part A: Applied Science and Manufacturing 104 (2018) 41–59. doi:10.1016/j.compositesa.2017.10.026.

[91] J. Prichard, P. Hogg, The role of impact damage in post-impact compression testing, Composites 21 (6) (1990) 503–511. doi:10.1016/0010-4361(90)90423-T.

[92] D. Bull, S. Spearing, I. Sinclair, Investigation of the response to low velocity impact and quasi-static indentation loading of particle-toughened carbon-fibre composite materials, Composites Part A: Applied Science and Manufacturing 74 (2015) 38–46. doi:10.1016/j.compositesa.2015.03.016.

[93] ASTM Standard D7137/D7137M-17, Standard Test Method for Compressive Residual Strength Properties of Damaged Polymer Matrix Composite Plates. ASTM International, West Conshohocken, PA, 2017. doi:10.1520/D7137_D7137M-17.

[94] J. Zhang, X. Zhang, An efficient approach for predicting low-velocity impact force and damage in composite laminates, Composite Structures 130 (2015) 85–94. doi:10.1016/j.compstruct.2015.04.023.

[95] A. Wagih, P. Maimí, N. Blanco, J. Costa, A quasi-static indentation test to elucidate the sequence of damage events in low velocity impacts on composite laminates, Composites Part A: Applied Science and Manufacturing 82 (2016) 180–189. doi:10.1016/j.compositesa.2015.11.041.

[96] E. Abisset, F. Daghia, X. Sun, M. Wisnom, S. Hallet, Interaction of inter- and intralaminar damage in scaled quasi-static indentation tests: Part 1 - Experiments, Composite Structures 136 (2016) 712–726. doi:10.1016/j.compstruct.2015.09.061.

[97] T. Nettles, J. Douglas, Scaling Effects in Carbon / Epoxy Laminates Under Transverse Quasi-Static Loading. NASA Technical Report, NASA/TM-1999-209103, Langley Research Center, Virginia, USA (1999).

[98] T. Yokozeki, A. Kuroda, A. Yoshimura, T. Ogasawara, T. Aoki, Damage characterization in thin-ply composite laminates under out-of-plane transverse loadings, Composite Structures 93 (1) (2010) 49–57. doi:10.1016/j.compstruct.2010.06.016.

[99] A. Wagih, P. Maimí, E. González, N. Blanco, J. Sainz de Aja, F. de la Escalera, R. Olsson, E. Alvarez, Damage sequence in thin-ply composite laminates under out-of-plane loading, Composites Part A: Applied Science and Manufacturing 87 (2016) 66–77. doi:10.1016/j.compositesa.2016.04.010.

[100] W. Jackson, C. Poe, The use of impact force as a scale parameter for the impact response of composite laminates, NASA Technical Memorandum 104189, Langley Research Center, Virginia, USA (1992).

[101] P. Sjoblom, J. Hartness, T. Cordell, On Low-Velocity Impact Testing of Composite Materials, Journal of Composite Materials 22 (1) (1988) 30–52. doi:10.1177/002199838802200103.

[102] S. Lee, P. Zahuta, Instrumented Impact and Static Indentation of Composites, Journal of Composite Materials 25 (2) (1991) 204–222. doi:10.1177/002199839102500205.

[103] H. Kaczmarek, S. Maison, Comparative ultrasonic analysis of damage in CFRP under static indentation and low-velocity impact, Composites Science and Technology 51 (1) (1994) 11–26. doi:10.1016/0266-3538(94)

90152-X.

[104] E. Abdallah, C. Bouvet, S. Rivallant, B. Broll, J. Barrau, Experimental analysis of damage creation and permanent indentation on highly oriented plates, Composites Science and Technology 69 (7-8) (2009) 1238–1245. doi:10.1016/j.compscitech.2009.02.029.

[105] D. Symons, Characterisation of indentation damage in 0/90 lay-up, Composite Science and Technology 60 (2000) 391–401. doi:10.1016/S0266-3538(99)00139-6.

[106] T. Allen, S. Ahmed, W. Hepples, P. Reed, I. Sinclair, S. Spearing, A comparison of quasi-static indentation and low velocity impact on composite overwrapped pressure vessels, Journal of Composite Materials 52 (29) (2018) 4051–4060. doi:10.1177/0021998318774401.

[107] L. Sutherland, C. Guedes Soares, Impact characterisation of low fibre-volume glass reinforced polyester circular laminated plates, International Journal of Impact Engineering 31 (1) (2005) 1–23. doi:10.1016/j.ijimpeng.2003.11.006.

[108] F. Aymerich, L. Francesconi, Damage mechanisms in thin stitched laminates subjected to low-velocity impact, Procedia Engineering 88 (2014) 133–140. doi:10.1016/j.proeng.2014.11.136.

[109] Y. Liv, A contribution to the understanding of compression after impact of composite laminates. Ph.D. dissertation submitted to the Doctoral Programme in Technology, University of Girona (2017).
URL https://dugi-doc.udg.edu/bitstream/handle/10256/15006/tyl_20171026.pdf?sequence=1&isAllowed=y

[110] F. A. Habib, A new method for evaluating the residual compression strength of composites after impact, Composite Structures 53 (3) (2001) 309–316. doi:10.1016/S0263-8223(01)00015-0.

[111] S. Sanchez-Saez, E. Barbero, R. Zaera, C. Navarro, Compression after impact of thin composite laminates, Composites Science and Technology 65 (13) (2005) 1911–1919. doi:10.1016/j.compscitech.2005.04.009.

[112] M. Remacha, S. Sánchez-Sáez, B. López-Romano, E. Barbero, A new device for determining the compression after impact strength in thin laminates, Composite Structures 127 (2015) 99–107. doi:10.1016/j.compstruct.2015.02.079.

[113] H. Saito, M. Morita, K. Kawabe, M. Kanesaki, H. Takeuchi, M. Tanaka,

I. Kimpara, Effect of ply-thickness on impact damage morphology in CFRP laminates, Journal of Reinforced Plastics and Composites 30 (13) (2011) 1097–1106. doi:10.1177/0731684411416532.

[114] S. Timoshenko, S. Woinowsky-Krieger, Theory of Plates and Shells Second Edition. McGraw-Hill International Edition (1959).

[115] M. Kuwata, P. J. Hogg, Interlaminar toughness of interleaved CFRP using non-woven veils: Part 1. Mode-I testing, Composites Part A: Applied Science and Manufacturing 42 (10) (2011) 1551–1559. doi:10.1016/j.compositesa.2011.07.016.

[116] V. Ramírez, Effect of nonwoven veil architectures on interlaminar fracture toughness of interleaved composites. Ph.D. dissertation submitted to the Faculty of Engineering and Physical Sciences, University of Manchester (2015).
URL https://www.research.manchester.ac.uk/portal/files/61848942/FULL_TEXT.PDF

[117] L. Zhu, Investigations on damage resistance of carbon fiber composite panels toughened using veils, Chinese Journal of Aeronautics 26 (3) (2013) 807–813. doi:10.1016/j.cja.2013.05.006.

[118] https://www.castrocompositesshop.com/gb/fibre-reinforcements/1691-optiveil-20301a-carbon-veil-17-gm2-1350-mm-width.html.

[119] M. Sohn, X. Hu, Processing of carbon-fibre/epoxy composites with cost-effective interlaminar reinforcement, Composites Science and Technology 58 (2) (1998) 211–220. doi:10.1016/S0266-3538(97)00114-0.

[120] E. Barjasteh, C. Sutanto, T. Reddy, J. Vinh, A graphene/graphite-based conductive polyamide 12 interlayer for increasing the fracture toughness and conductivity of carbon-fiber composites, Journal of Composite Materials 51 (20) (2017) 2879–2887. doi:10.1177/0021998317705707.

[121] B. Yuan, B. Tan, Y. Hu, J. Shaw, X. Hu, Improving impact resistance and residual compressive strength of carbon fibre composites using un-bonded non-woven SAF veil, Composites Part A 121 (2019) 439–448. doi:10.1016/j.compositesa.2019.04.006.

[122] L. Walker, M. Sohn, X. Hu, Improving impact resistance of carbon-fibre composites through interlaminar reinforcement, Composites - Part A: Applied Science and Manufacturing 33 (6) (2002) 893–902. doi:10.1016/S1359-835X(02)00010-6.

[123] N. H. Nash, T. M. Young, W. F. Stanley, The reversibility of Mode-I and -II interlaminar fracture toughness after hydrothermal aging of Carbon/Benzoxazine composites with a thermoplastic toughening interlayer, Composite Structures 152 (2016) 558–567. doi:10.1016/j.compstruct.2016.05.086.

[124] M. Kuwata, Mechanisms of interlaminar fracture toughness using non-woven veils as interleaf materials. Ph.D. dissertation submitted to the School of Engineering and Materials Science, Queen Mary, University of London (February 2010).
URL https://qmro.qmul.ac.uk/xmlui/handle/123456789/2220

[125] A. Duarte, I. Herszberg, R. Paton, Impact resistance and tolerance of interleaved RTM laminates. International Conference on Composite Materials (ICCM, 1999).
URL http://www.iccm-central.org/Proceedings/ICCM12proceedings/site/papers/pap1032.pdf

[126] B. Saz-Orozco, D. Ray, W. F. Stanley, Effect of Thermoplastic Veils on Interlaminar Fracture Toughness of a Glass Fiber/Vinyl Ester Composite, Polymers and Polymer Composites 16 (2) (2015) 101–113. doi:10.1002/pc.23840.

[127] K. Fitzmaurice, D. Ray, M. McCarthy, PET interleaving veils for improved fracture toughness of glass fibre/low-styrene-emission unsaturated polyester resin composites, Journal of Applied Polymer Science 133 (3) (2015) 1–8. doi:10.1002/app.42877.

[128] K. O'Donovan, D. Ray, M. McCarthy, Toughening effects of interleaved nylon veils on glass fabric/low-styrene-emission unsaturated polyester resin composites, Journal of Applied Polymer Science 132 (2014) 1–9. doi:10.1002/app.41462.

[129] Nash N.H., Improving the Performance of Out-of-Autoclave Composite Laminates Using an Interlaminar Toughening Technique. Ph.D. dissertation submitted to the Faculty of Science and Engineering, University of Limerick (March 2016).
URL https://ulir.ul.ie/handle/10344/5229

[130] T. Reddy, Interlayer toughening of carbon-fiber/benzoxazine composite laminates. Master thesis submitted to the Department of Mechanical and Aerospace Engineering, California State University, Long Beach, California, 2017.

URL https://pqdtopen.proquest.com/doc/1906281563.html?FMT=ABS

[131] S. Eichhorn, W. Sampson, Relationships between specific surface area and pore size in electrospun polymer fibre networks, Journal of the Royal Society Interface 7 (45) (2010) 641–649. doi:10.1098/rsif.2009.0374.

[132] W. Sampson, Modelling Stochastic Fibrous Materials with Mathematica, Springer-Verlag London Limited, 2009. doi:10.1007/978-1-84800-991-2.

[133] G. Borstnar, M. N. Mavrogordato, L. Helfen, I. Sinclair, S. M. Spearing, Interlaminar fracture micro-mechanisms in toughened carbon fibre reinforced plastics investigated via synchrotron radiation computed tomography and laminography, Composites Part A: Applied Science and Manufacturing 71 (2015) 176–183. doi:10.1016/j.compositesa.2015.01.012.

[134] D. Tzetzis, P. J. Hogg, Bondline toughening of vacuum infused composite repairs, Composites Part A: Applied Science and Manufacturing 37 (9) (2006) 1239–1251. doi:10.1016/j.compositesa.2005.09.008.

[135] M. Guo, X. Yi, G. Liu, L. Liu, Simultaneously increasing the electrical conductivity and fracture toughness of carbon-fiber composites by using silver nanowires-loaded interleaves, Composites Science and Technology 97 (2014) 27–33. doi:10.1016/j.compscitech.2014.03.020.

[136] N. Ni, Y. Wen, D. He, X. Yi, T. Zhang, Y. Xu, High damping and high stiffness CFRP composites with aramid non-woven fabric interlayers, Composites Science and Technology 117 (2015) 92–99. doi:10.1016/j.compscitech.2015.06.002.

[137] M. Kuwata, P. J. Hogg, Interlaminar toughness of interleaved CFRP using non-woven veils: Part 2. Mode-II testing, Composites Part A: Applied Science and Manufacturing 42 (10) (2011) 1560–1570. doi:10.1016/j.compositesa.2011.07.017.

[138] D. Wong, H. Zhang, E. Bilotti, T. Peijs, Interlaminar toughening of woven fabric carbon/epoxy composite laminates using hybrid aramid/phenoxy interleaves, Composites Part A: Applied Science and Manufacturing 101 (2017) 151–159. doi:10.1016/j.compositesa.2017.06.001.

[139] http://www.matweb.com/.

[140] Mark JE. Polymer data handbook. Oxford University Press Inc.; 1999.

[141] W. Cantwell, M. Blyton, Influence of Loading Rate on the Interlaminar Fracture Properties of High Performance Composites - A Review, Applied Mechanics Reviews 52 (6) (1999) 199. doi:10.1115/1.3098934.

[142] J. E. Masters, Improved impact and delamination resistance through interleafing, Key Engineering Materials 37 (1989) 317–347. doi:10.4028/www.scientific.net/KEM.37.317.

[143] P. J. Hogg, Toughening of thermosetting composites with thermoplastic fibres, Materials Science and Engineering A 412 (2005) 97–103. doi:10.1016/j.msea.2005.08.028.

[144] A. Duarte, I. Herszberg, R. Paton, Impact resistance and tolerance of interleaved tape laminates, Composite Structures 47 (1999) 753–758. doi:10.1016/S0263-8223(00)00049-0.

[145] M. Sohn, X. Hu, J. Kim, L. Walker, Impact damage characterisation of carbon fibre/epoxy composites with multi-layer reinforcement, Composites Part B: Engineering 31 (8) (2000) 681–691. doi:10.1016/S1359-8368(00)00028-7.

[146] R. Ritchie, The conflicts between strength and toughness, Nature Materials 10 (11) (2011) 817–822. doi:10.1038/nmat3115.

[147] Y. Wang, C. Soutis, Fatigue Behaviour of Composite T-Joints in Wind Turbine Blade Applications, Applied Composite Materials 24 (2) (2017) 461–475. doi:10.1007/s10443-016-9537-9.

[148] Y. Wang, C. Soutis, A Finite Element and Experimental Analysis of Composite T-Joints Used in Wind Turbine Blades, Applied Composite Materials 165 (2018) 953–964. doi:10.1007/s10443-018-9711-3.

[149] European standard DIN EN 2563:1997, Aerospace series, Carbon fibre laminates, Determination of the apparent interlaminar shear strength; Deutsches Institut für Normung (DIN), Berlin, Germany, 1997.

[150] S. C. Garcea, Y. Wang, P. J. Withers, X-ray computed tomography of polymer composites, Composites Science and Technology 156 (2018) 305–319. doi:10.1016/j.compscitech.2017.10.023.

[151] D. Adams, L. Carlsson, R. Byron Pipes, Experimental Characterization of Advanced Composite Materials. Third Edition. CRC Press LLC (2003).

[152] A. Arteiro, G. Catalanotti, A. R. Melro, P. Linde, P. P. Camanho, Micro-mechanical analysis of the effect of ply thickness on the transverse compres-

sive strength of polymer composites, Composites Part A: Applied Science and Manufacturing 79 (2015) 127–137. doi:10.1016/j.compositesa.2015.09.015.

[153] F. París, M. L. Velasco, E. Correa, Micromechanical study on the influence of scale effect in the first stage of damage in composites, Composites Science and Technology 160 (2018) 1–8. doi:10.1016/j.compscitech.2018.03.004.

[154] A. Arteiro, G. Catalanotti, J. Reinoso, P. Linde, P. P. Camanho, Simulation of the Mechanical Response of Thin-Ply Composites: From Computational Micro-Mechanics to Structural Analysis, Archives of Computational Methods in Engineering 2. doi:10.1007/s11831-018-9291-2.

[155] P. P. Camanho, A. Arteiro, A. R. Melro, G. Catalanotti, M. Vogler, Three-dimensional invariant-based failure criteria for fibre-reinforced composites, International Journal of Solids and Structures 55 (2015) 92–107. doi:10.1016/j.ijsolstr.2014.03.038.

[156] A. Quintanas-Corominas, P. Maimí, E. Casoni, A. Turon, J. Mayugo, G. Guillamet, M. Vázquez, A 3D transversally isotropic constitutive model for advanced composites implemented in a high performance computing code, European Journal of Mechanics, A/Solids 71 (2018) 278–291. doi:10.1016/j.euromechsol.2018.03.021.

[157] J. M. Whitney, C. E. Browning, On short-beam shear tests for composite materials, Experimental Mechanics 25 (3) (1985) 294–300. doi:10.1007/BF02325100.

[158] W. C. Cui, M. R. Wisnom, Contact finite-element analysis of 3-point and 4-point short-beam bending of unidirectional composites, Composites Science and Technology 45 (4) (1992) 323–334. doi:10.1016/0266-3538(92)90047-7.

[159] W. C. Cui, M. R. Wisnom, M. Jones, Effect of Specimen Size on Interlaminar Shear-Strength of Unidirectional Carbon Fiber-Epoxy, Composites Engineering 4 (3) (1994) 299–307. doi:10.1016/0961-9526(94)90080-9.

[160] D. Adams, J. Busse, Suggested Modifications of the Short Beam Shear Test Method, Proceedings of the 49th International SAMPE Symposium (Long Beach, Calif., 2004).

[161] A. Makeev, Y. He, H. Schreier, Short-beam Shear Method for Assessment of Stress-Strain Curves for Fibre-reinforced Polymer Matrix Composite Materi-

als, Strain 49 (5) (2013) 440–450. doi:10.1111/str.12050.

[162] S. M. García-Rodríguez, J. Costa, V. Singery, I. Boada, J. A. Mayugo, The effect interleaving has on thin-ply non-crimp fabric laminate impact response: X-ray tomography investigation, Composites Part A: Applied Science and Manufacturing 107 (2018) 409–420. doi:10.1016/j.compositesa.2018.01.023.

[163] European standard DIN EN 2564:1998, Aerospace series, Carbon fibre laminates, Determination of the fibre-, resin- and void contents, Deutsches Institut für Normung (DIN), Berlin, Germany, 1998.

[164] ASTM D2344/D2344M-13, Standard Test Method for Short-Beam Strength of Polymer Matrix Composite Materials and Their Laminates. ASTM International, West Conshohocken, PA, 2013. doi:10.1520/D2344_D2344M-13.

[165] S. García-Rodríguez, J. Costa, A. Bardera, V. Singery, D. Trias, A 3D tomographic investigation to elucidate the low-velocity impact resistance, tolerance and damage sequence of thin non-crimp fabric laminates: effect of ply-thickness, Composites Part A: Applied Science and Manufacturing 113 (2018) 53–65. doi:10.1016/j.compositesa.2018.07.013.

[166] Abaqus Analysis User's Manual. In: Abaqus documentation 6.11. Providence, RI 02909 2499, USA: Simulia World Headquarters; 2011.

[167] P. Maimí, P. P. Camanho, J. A. Mayugo, A. Turon, Matrix cracking and delamination in laminated composites. Part I: Ply constitutive law, first ply failure and onset of delamination, Mechanics of Materials 43 (4) (2011) 169–185. doi:10.1016/j.mechmat.2010.12.003.

[168] C. Mittelstedt, W. Becker, Free-Edge Effects in Composite Laminates, Applied Mechanics Reviews 60 (5) (2007) 217. doi:10.1115/1.2777169.

[169] W. Tan, F. Naya, L. Yang, T. Chang, B. G. Falzon, L. Zhan, J. M. Molina-Aldareguía, C. González, J. Llorca, The role of interfacial properties on the intralaminar and interlaminar damage behaviour of unidirectional composite laminates: Experimental characterization and multiscale modelling, Composites Part B: Engineering 138 (2018) (2018) 206–221. doi:10.1016/j.compositesb.2017.11.043.

[170] S. Kohler, Multiscale experimental characterisation and modelling of transverse cracking in thin-ply composites. Ph.D. dissertation submitted to the École Polytechnique Fédérale de Laussane, Switzerland. (February 2019).

URL https://infoscience.epfl.ch/record/263781/files/EPFL{_}TH9132.pdf

[171] S. Avalon, S. L. Donaldson, Strength of composite angle brackets with multiple geometries and nanofiber-enhanced resins, Journal of Composite Materials 45 (9) (2011) 1017–1030. doi:10.1177/0021998310381538.

[172] J. M. González-Cantero, E. Graciani, B. López-Romano, F. París, Competing mechanisms in the unfolding failure in composite laminates, Composites Science and Technology 156 (2018) 223–230. doi:10.1016/j.compscitech.2017.12.022.

[173] X. Sun, M. Wisnom, S. Hallett, Interaction of inter- and intralaminar damage in scaled quasi-static indentation tests: Part 2 - Numerical simulation, Composite Structures 136 (2016) 727–742. doi:10.1016/j.compstruct.2015.09.062.

[174] H. Yu-Chien, H. Sasayama, J. Yanagimoto, Mechanical properties and drawing process of multilayer carbon-fiber-reinforced plastic sheets with various prepreg thicknesses, Advances in Mechanical Engineering 9 (3) (2017) 1–12. doi:10.1177/1687814017692695.

[175] Y. Kim, S. Ko, W. Lay, T. Jingmeng, P. Chang, S. Thielk, Effects of Shallow Biangle, Thin-Ply Laminates on Structural Performance of Composite Wings, AIAA Journal 55 (6) (2017) 2086–2092. doi:10.2514/1.J055465.

[176] J. Zghal, A. Ammar, F. Chinesta, C. Binetruy, E. Abisset-Chavanne, High-resolution elastic analysis of thin-ply composite laminates, Composite Structures 172 (2017) 15–21. doi:10.1016/j.compstruct.2017.03.083.

[177] ASTM Standard D6641/D6641M-14, Standard Test Method for Compressive Properties of Polymer Matrix Composite Materials Using a Combined Loading Compression (CLC) Test Fixture. ASTM International, West Conshohocken, PA, 2014. doi:10.1520/D6641_D6641M-16E01.

[178] M. Abir, T. Tay, M. Ridha, H. Lee, On the relationship between failure mechanism and compression after impact (CAI) strength in composites, Composite Structures 182 (15) (2017) 242–250. doi:10.1016/j.compstruct.2017.09.038.

[179] D. Ghelli, G. Minak, Low velocity impact and compression after impact tests on thin carbon/epoxy laminates, Composites Part B: Engineering 42 (7) (2011) 2067–2079. doi:10.1016/j.compositesb.2011.04.017.

[180] N. O'Brien, R. Boardman, I. Sinclair, T. Blumensath, Recent advances in

X-ray Cone-beam Computed Laminography, Journal of X-Ray Science and Technology 24 (5) (2016) 691–707. doi:10.3233/XST-160581.

[181] F. Léonard, J. Stein, C. Soutis, P. Withers, The quantification of impact damage distribution in composite laminates by analysis of X-ray computed tomograms, Composites Science and Technology 152 (2017) 139–148. doi:10.1016/j.compscitech.2017.08.034.

[182] http://starviewer.udg.edu/.

[183] H. Choi, R. Downs, F. Chang, A New Approach toward Understanding Damage Mechanisms and Mechanics of Laminated Composites Due to Low-Velocity Impact: Part I-Experiments, Journal of Composite Materials 25 (1991) 992–1011. doi:10.1177/002199839102500803.

[184] H. Choi, R. Downs, F. Chang, A New Approach toward Understanding Damage Mechanisms and Mechanics of Laminated Composites Due to Low-Velocity Impact: Part II-Analysis, Journal of Composite Materials 25 (1991) 1012–1038. doi:10.1177/002199839102500804.

[185] I. Verpoest, S. Lomov, Virtual textile composites software WiseTex: Integration with micro-mechanical, permeability and structural analysis, Composites Science and Technology 65 (2005) 2563–2574. doi:10.1016/j.compscitech.2005.05.031.

[186] J. Nairn, Matrix Microcracking in Composites, Chapter 13 in Polymer Matrix Composites (edited by R. Talreja and J.-A. E. Månson), Comprehensive Composite Materials, Elsevier Science, Vol. 2, 2000, pp. 403–432.

[187] A. Wagih, P. Maimí, N. Blanco, S. García-Rodríguez, G. Guillamet, R. Issac, A. Turon, J. Costa, Improving damage resistance and load capacity of thin-ply laminates using ply clustering and small mismatch angles, Composites Part A: Applied Science and Manufacturing 117 (April 2018) (2019) 76–91. doi:10.1016/j.compositesa.2018.11.008.

[188] Image J: Image Processing and Analysis in Java, URL: https://imagej.nih.gov/ij/.

[189] ASTM Standard D5528/D5528M-13, Standard Test Method for Mode I Interlaminar Fracture Toughness of Unidirectional Fiber-Reinforced Polymer Matrix Composites. ASTM International, West Conshohocken, PA, 2013. doi:10.1520/D5528-13.

[190] ISO Standard 15024, Fibre-reinforced plastic composites - Determination of mode II fracture resistance for unidirectionally reinforced materials us-

ing the calibrated end-loaded split (C-ELS). Geneva, Switzerland. URL: www.iso.org.

[191] ASTM Standard D3039/D3039M-14, Standard Test Method for Tensile Properties of Polymer Matrix Composite Materials. ASTM International, West Conshohocken, PA, 2014. doi:10.1520/D3039_D3039M-14.

[192] J. Renart, N. Blanco, E. Pajares, J. Costa, S. Lazcano, G. Santacruz, Side Clamped Beam (SCB) hinge system for delamination tests in beam-type composite specimens, Composites Science and Technology 71 (8) (2011) 1023–1029. doi:10.1016/j.compscitech.2010.10.005.

[193] ISO Standard 15024, Fibre-reinforced plastic composites - Determination of mode I interlaminar fracture toughness, Gic, for unidirectionally reinforced materials. Geneva, Switzerland (2011). URL: www.iso.org.

[194] Trainable Weka Segmentation plugin, URL: https://imagej.net/Trainable_Weka_Segmentation.

[195] S. Lomov, E. Belov, T. Bischoff, S. Ghosh, T. Chi, I. Verpoest, Carbon composites based on multiaxial multiply stitched preforms . Part 1. Geometry of the preform, Composites - Part A: Applied Science and Manufacturing 33 (2002) 1171–1183. doi:10.1016/S1359-835X(02)00090-8.

[196] C. Lekakou, S. Edwards, G. Bell, S. C. Amico, Computer modelling for the prediction of the in-plane permeability of non-crimp stitch bonded fabrics, Composites Part A: Applied Science and Manufacturing 37 (2006) 820–825. doi:10.1016/j.compositesa.2005.04.002.

[197] B. Beylergil, M. Tanoğlu, E. Aktaş, Enhancement of interlaminar fracture toughness of carbon fiber–epoxy composites using polyamide-6,6 electrospun nanofibers, Journal of Applied Polymer Science 134 (35) (2017) 1–12. doi:10.1002/app.45244.

[198] K. N. Shivakumar, W. Elber, W. Illg, Prediction of Impact Force and Duration Due to Low-Velocity Impact on Circular Composite Laminates, Journal of Applied Mechanics 52 (3) (1985) 674–680. doi:10.1115/1.3169120.

[199] G. Bullegas, S. T. Pinho, S. Pimenta, Engineering the translaminar fracture behaviour of thin-ply composites, Composites Science and Technology 131 (2016) 110–122. doi:10.1016/j.compscitech.2016.06.002.

[200] A. Ortega, P. Maimí, E. V. González, J. R. Sainz de Aja, F. M. de la Escalera, P. Cruz, Translaminar fracture toughness of interply hybrid laminates under tensile and compressive loads, Composites Science and Technology 143

(2017) 1–12. doi:10.1016/j.compscitech.2017.02.029.

[201] L. Zubillaga, A. Turon, J. Renart, J. Costa, P. Linde, An experimental study on matrix crack induced delamination in composite laminates, Composite Structures 127 (2015) 10–17. doi:10.1016/j.compstruct.2015.02.077.

[202] M. Launey, R. Ritchie, On the Fracture Toughness of Advanced Materials, Advanced Materials 21 (20) (2009) 2103–2110. doi:10.1002/adma.200803322.

[203] C. Huchette, T. Vandellos, F. Laurin, Influence of Intralaminar Damage on the Delamination Crack Evolution. In Damage Growth in Aerospace Composites. Ed: Riccio, A., 2015. doi:10.1007/978-3-319-04004-2.

[204] L. Burns, A. P. Mouritz, D. Pook, S. Feih, Bio-inspired hierarchical design of composite T-joints with improved structural properties, Composites Part B: Engineering 69 (2015) 222–231. doi:10.1016/j.compositesb.2014.09.041.

[205] A. Sandhu, A. Rhead, X-ray computed tomography of damage formation under in-situ loading. 20th International Conference on Composite Materials (ICCM 20), Copenhaguen, Denmark (2015).
URL https://researchportal.bath.ac.uk/en/publications/x-ray-computed-tomography-of-damage-formation-under-in-situ-loadi

[206] T. A. Sebaey, E. Mahdi, Using thin-plies to improve the damage resistance and tolerance of aeronautical CFRP composites, Composites Part A: Applied Science and Manufacturing 86 (2016) 31–38. doi:10.1016/j.compositesa.2016.03.027.

[207] A. Sasikumar, D. Trias, J. Costa, N. Blanco, J. Orr, P. Linde, Effect of ply thickness and ply level hybridization on the compression after impact strength of thin laminates, Composites Part A 121 (2019) 232–243. doi:10.1016/j.compositesa.2019.03.022.

[208] A. Sasikumar, D. Trias, J. Costa, V. Singery, P. Linde, Mitigating the weak impact response of thin-ply based thin laminates through an unsymmetrical laminate design incorporating intermediate grade plies, Composite Structures 220 (2019) 93–104. doi:10.1016/j.compstruct.2019.03.069.

[209] S. Pinho, L. Iannucci, P. Robinson, Physically based failure models and criteria for laminated fibre-reinforced composites with emphasis on fibre kinking. Part I: Development, Composites Part A: Applied Science and Manufacturing 37 (5) (2006) 63–73. doi:10.1016/j.compositesa.2005.

04.016.

[210] D. A. Şerban, G. Weber, L. Marşavina, V. V. Silberschmidt, W. Hufenbach, Tensile properties of semi-crystalline thermoplastic polymers: Effects of temperature and strain rates, Polymer Testing 32 (2) (2013) 413–425. doi:10.1016/j.polymertesting.2012.12.002.

[211] G. W. Beckermann, Nanofiber interleaving veils for improving the performance of composite laminates, Reinforced Plastics 61 (5) (2017) 289–293. doi:10.1016/j.repl.2017.03.006.

[212] R. Palazzetti, A. Zucchelli, Electrospun nanofibers as reinforcement for composite laminates materials – A review, Composite Structures 182 (2017) 711–727. doi:10.1016/j.compstruct.2017.09.021.

[213] B. Lawrence, R. Emerson, A Comparison of Low-Velocity Impact and Quasi-Static Indentation, Army Research Laboratory, Aberdeen, USA (2012).
URL https://apps.dtic.mil/dtic/tr/fulltext/u2/a579696.pdf